Experimental Investigation of the Mixing of an Axial Jet Within a Swirling Flow, Utilizing Laser Doppler Velocimetry and Particle Image Velocimetry

by

David Joseph Danitz

Submitted to the Department of Mechanical Engineering
in partial fulfillment of the requirements for the degree of

Master of Science in Mechanical Engineering

at the

MASSACHUSETTS INSTITUTE OF TECHNOLOGY

January 1995

Author ....
Department of Mechanical Engineering
January 20, 1995

Certified by ....
Professor Douglas P. Hart
Department of Mechanical Engineering
Thesis Supervisor

Accepted by ....
Professor Ain A. Sonin
Chairman, Departmental Committee on Graduate Studies
Department of Mechanical Engineering

Experimental Investigation of the Mixing of an Axial Jet Within a Swirling Flow, Utilizing Laser Doppler Velocimetry and Particle Image Velocimetry

by

David Joseph Danitz

Submitted to the Department of Mechanical Engineering on
January 20, 1995, in partial fulfillment of the requirements for the
degree of Master of Science in Mechanical Engineering

Abstract

Swirl is a common way to stabilize the flame in industrial and jet engine combustion chambers. It provides a means by which the mixing of the fuel and oxidizer can be controlled. The present study uses water to model the flow inside a combustion chamber, and examine the mixing of a vortex with an axial jet. By excluding many of the parameters involved in the study of combustible swirling flows, the basic mechanisms that affect this simplified flow can be understood and quantified.

A swirl chamber is designed and constructed to model the flow inside a combustion chamber. Using dimensional analysis, the swirl chamber is scaled to common combustion chamber characteristics. The swirl number, Reynolds number and the jet to mainstream momentum flux ratio are the primary non-dimensional numbers used. Laser Doppler velocimetry is implemented to obtain one-dimensional, time averaged velocity profiles of the flow in the axial and tangential directions. Particle image velocimetry is also used to obtain two-dimensional velocity fields. The mixing between the jet and swirling flow in the swirl chamber is quantified using flow visualization techniques. Finally, flow trends in the one-dimensional velocity profiles are discovered for different boundary conditions.

The information gained from this study aids in understanding the basic phenomena of this complex flow. Once the flow is better understood, more efficient combustors with reduced nitrogen oxide emissions can be designed and constructed.

Thesis Supervisor: Douglas P. Hart
Title: Assistant Professor, Department of Mechanical Engineering

Acknowledgments

First and foremost, I would like to thank my advisor Professor Doug Hart for his guidance and support throughout my stay at MIT. His constant words of encouragement and suggested paths to follow, guided me through the rigors of research. In the past year and a half, he has become much more than a mentor, he has become a dear friend.

I want to thank my parents for believing in me, even when I did not. Because of them, I have been given the opportunity to obtain a Masters Degree. Their perpetual love is, and always will be, greatly cherished. You are truly the best parents in the world.

There are many people who lent a helpful hand in the design and construction of the swirl chamber, particularly Dick Fenner and Norm Berube. Dick provided crucial advise during the design stage, and made my transition to MIT very smooth. He also took me sailing in the Boston harbor, which I will always remember. Norm shared his expertise in the machine shop and made the construction of the swirl chamber possible. Tim Hopp designed the plumbing and helped put the swirl chamber together. Andy Yablon, Edwin Ozawa, Arthur Sit, Youssef Marzouk, Peter Noymer, Paul Farrell, Matt Hyre, James Moran, Kurt Roth and Shay, gave up time to help in the construction and to fire the laser during the experiments.

There are several friends in the Fluids lab who made my stay enjoyable: Edwin Ozawa, Arthur Sit, Gregg Duthaler, James Shin, Matteo Pedercini, Doug Crawford, Benjamin Sun, Amit Dhadwal, Naomi Chesler, Serhat Yesilyurt, Mariano Enrique Gurfinkel, Jim McGrath, Steffano Schiaffino, Frank Espinosa, Hugo Ayala, Barbara Hamer, Sanjay Patel, John Otto, and last but not least, John Dzenitis. Special thanks go out to Arthur, Edwin and Gregg for upholding the integrity of Edgerton House by not letting people sleep in the courtyard, and to Naomi for proof-reading work my. Oops, she missed one.

Also, thanks to Amit, Mariano, and Arthur for convincing me to invest in MITEC. Ten-grand in four month? Yeah right!

Finally and most importantly, I would like to dedicate this thesis to my fiancée. Debbie, your understanding and sacrifice during the last year and a half have made this work possible. The daily phone calls and uplifting words of encouragement inspired me during the long nights in the lab. Thank you for your love and friendship.

Table of Contents

List of Figures

List of Tables

Chapter 1

Introduction

Atmospheric pollutants such as nitrous oxide (NO) and nitrous dioxide (NO_2) present a threat to human health and the Earth's ecosystem [1]. These pollutants have been linked to acute sickness, impairment of growth, alteration of important physiological functions and impairment of athletic performance [2]. Because of this, emphasis has been placed on reducing the emissions of nitrous oxides (NO_x) before environmental changes become irreversible, and the effects on personal health escalate. Two principal sources of NO_x emissions are jet aircraft engines and industrial burners. The goal of this research is to investigate a method by which NO_x emissions from these sources can be minimized.

1.1 Goals

Through the use of swirl, the rate of mixing between the fuel and oxidizer in a combustion chamber can be controlled, thereby controlling the formation and reaction of NO_x. However, the fundamental physics of this mixing process is poorly understood [3]. Therefore, the elemental mechanisms that affect the mixing rate of two fluids under conditions of swirl must be understood and quantified before combustion chambers with reduced NO_x emissions can be properly designed.

The goal of the present work is to understand the fundamental physics of the swirl mixing process and how it differs from non-swirling processes. An investigation was made of the changes in the velocity profiles of the primary and secondary flows in a simulated coaxial combustor for different boundary conditions, thus providing insight into the mechanisms which govern these complex flows. Water was used as the working fluid in the simulated coaxial combustion chamber. With this simplified configuration, the effects of varying the swirl and injection rates could be analyzed without the complications compressible fluids introduced. In particular, one-dimensional and two-dimensional, time-averaged axial and tangential velocity profiles were measured for different swirl rates, primary flow injection rates and axial positions. Using these measurements, the importance of swirl and injection rate was explored. In addition, measurements of the mixing of the jet and swirling flow for different swirl rates, primary injection rates and axial positions were made, to aid in the understanding of the effects swirl and injection rate have on mixing.

The investigations presented in this thesis aid in understanding the fundamental mechanisms that influence the swirl mixing process. This understanding is an important first step toward designing low emission combustion chambers.

1.2 Historical Research

Over the past several decades, swirl has become a common way to stabilize the flame in industrial and jet engine combustion chambers. It was found that swirling flows allow better control of the flame by increasing or decreasing the mixing of the fuel (primary flow) and oxidizer (secondary flow). The change in the flame length was the first sign that swirl was affecting the mixing. When the flame length increased, the mixing decreased, and when the flame length decreased, the mixing increased.

In 1967 Emmons conducted a study on the fire whirl [4]. He found that the fire whirl consisted of a fuel rich core and a lean exterior. The study also showed that the surrounding air was in a free vortex motion except for a finite size vortex core in solid body rotation. The flame length, in the fire whirl, increased because of an increase in the supply of fuel, which was caused by buoyancy effects, and because of the rotating secondary flow.

Beer et al. conducted a similar experiment in 1971 [5]. However, the fuel was supplied by a constant velocity jet along the axis of the swirling secondary flow. The flame length was still increased despite the constant fuel supply rate, which showed that the increase in flame length was due entirely to the aerodynamic effect of swirling the secondary flow. In other words, the decrease in the rate of mixing between the jet fluid and the surrounding swirling air resulted in a considerable increase in flame length.

The explanation of this decrease in mixing was made with the aid of Rayleigh's stability criterion [6]. Rayleigh stated that a system is stable if the angular momentum increases with the radius. This occurs in solid body rotation. A system is neutrally stable if the angular momentum is constant for any radius. This occurs in a free vortex. Finally, a system is unstable if the angular momentum decreases with the radius. Beer et al. [5], with the aid of Rayleigh's criterion, explained that for a system with a jet injected into the axis of a cylindrical swirling flow, the centrifugal forces have a stabilizing effect and decrease the radial motion of the fluid. The centrifugal forces act against the turbulent viscous forces and reduce the turbulent mixing. If the jet is burning, a strong density gradient is set up which influences the stability of the flow. When the density increases radially outward within the centrifugal force field, a stable density stratification is formed which decreases the turbulent mixing. The combination of these two mechanisms greatly decreased the mixing of the fuel and the air, which increased the flame length.

Chigier and Beer [7] also demonstrated that when swirl was imparted on the jet and the secondary flow was stagnant, the flame length decreased. This study additionally showed that closed vortices were present along the axis and the strength of the vortices increased with increasing swirl. These vortices became known as recirculation.

Finally, Chigier et al. [8] noted that the rotation of the air led to an increase in the stability limits of the flame and an increase in flame length. Chigier et al. coupled their results with the work of Chigier and Beer to demonstrate that decreasing and increasing the flame length was possible. This coupling confirmed that total control of the flame could be achieved.

A good summary of the work performed on combustion in swirling flows was written by Syred and Beer in 1974 [9]. The paper describes the lack of understanding of swirling flows in combustion chambers because of their complexity.

1.3 Recent Research

Over the years it became accepted that recirculation zones are needed for flame stabilization. As the axial flow velocity is increased, larger and stronger recirculation zones are needed to stabilize the flame [3]. However, the extent to which swirl is needed is still unclear.

The focus of recent research has been to obtain benchmark data to verify computational fluid dynamic codes. These codes are used to model specific combustion chambers. The data consists of velocity, temperature and pressure profiles, in and around the recirculation zone. The trend has shifted away from understanding the fundamental mechanisms that increase or decrease the mixing of the fluids. Kihm et al. [3], Halpin [10], Ogawa and Kasuki [11], Ahmed and Nejad [12], Singh et al. [13], and Kok et al. [14] demonstrate this shift.

1.4 Thesis Organization

This chapter introduces the goals of the thesis, and presents a historical overview of how swirl became important to combustion chambers. Chapter 2 discusses the theory needed to understand swirling flows in combustion and swirl chambers. Chapter 3 explains the swirl chamber and instrumentation used to obtain the data. Chapter 4 explains the experimental procedures used to obtain the LDV, PIV and flow visualization data. Chapter 5 presents the data. Chapter 6 discusses the findings of the data. Finally, Chapter 7 presents the conclusions of this research.

Detailed CAD drawings of the swirl chamber, the hardware and software needed for the experimental instrumentation, are given in the Appendices.

Chapter 2

Theory

The previous chapter demonstrated that swirling the flow in a combustion chamber can be used as a means of controlling the flame; and, by controlling the flame, NO_x emissions can be reduced. This chapter explains the theory needed to understand the swirling flow phenomena.

2.1 Swirling Flows

Swirling flows are found in many natural phenomena such as tornados, hurricanes, dust-devils, fire whirls, and vortex shedding from aircraft wings. Swirl has also found its way into several practical applications such as vortex amplifiers, cyclone separators, and combustion chambers. In the context of this thesis we will focus on the theory needed to understand swirling flows in combustion chambers.

2.1.1 Swirl Number

The primary non-dimensional number used to characterize swirling flows is the swirl number, S. The swirl number is defined as the angular momentum flux divided by the axial momentum flux times the equivalent nozzle radius,

$$S = \frac{\int_0^{\frac{D}{2}} (vr)\,\rho u 2\pi r dr}{\frac{D}{2}\int_0^{\frac{D}{2}} u\rho u 2\pi r dr}, \tag{2.1}$$

where:

D is the diameter of the test section, or combustion chamber,

v is the tangential velocity,

u is the axial velocity,

ρ is the density of the fluid,

r is the radial variable.

The swirl number is a good characterization of a swirling flow because both of the momentum fluxes are conserved. Experiments have shown that the swirl number is the significant similarity variable of swirling jets produced by geometrically similar swirl generators [16]. There are other definitions of the swirl number that include a pressure term and a turbulent normal stress term. However, the added complication only leads to a downstream conservation of the swirl number [17], which is not useful for the small scale of the swirl chamber.

2.1.2 Rankine's Vortex

The tangential velocity component in guide vane swirl chambers can often be modeled as a Rankine's vortex. The Rankine's vortex consists of a core where viscosity dominates. An inviscid vortex exists outside of the core. The size of the core radius is determined by tangential velocities, viscosity, turbulence and the introduction of a nonrotating fluid at the vortex center [18]. The critical radius that divides the viscid and inviscid regions is denoted by R. A diagram of the Rankine's vortex is given in Figure 2.1. The tangential velocity component, v, and the pressure, p, are plotted as a function of the radius. Within the core the velocity is given by,

$$v = \omega r = \frac{\zeta r}{2}, \tag{2.2}$$

where:

v is the tangential velocity,

ω is the angular velocity $\left(\omega = \frac{1}{2} (\nabla \times \underline{V}) \right)$,

r is the radial coordinate,

ζ is the vorticity $(\zeta = 2\omega)$.

By Stoke's theorem, circulation, Γ, is the integral of ζ over the area of the circle of radius R, so $\Gamma = \pi R^2 \zeta$. From this, the vorticity as a function of an equivalent vortex with strength K is,

$$\zeta = \frac{2K}{R^2}. \tag{2.3}$$

Then, the velocity inside the core as a function of K is,

$$v = \frac{Kr}{R^2}. \tag{2.4}$$

Which is continuous with the velocity outside of the core,

$$v = \frac{K}{r}. \tag{2.5}$$

These velocity relations are plotted in Figure 2.1.

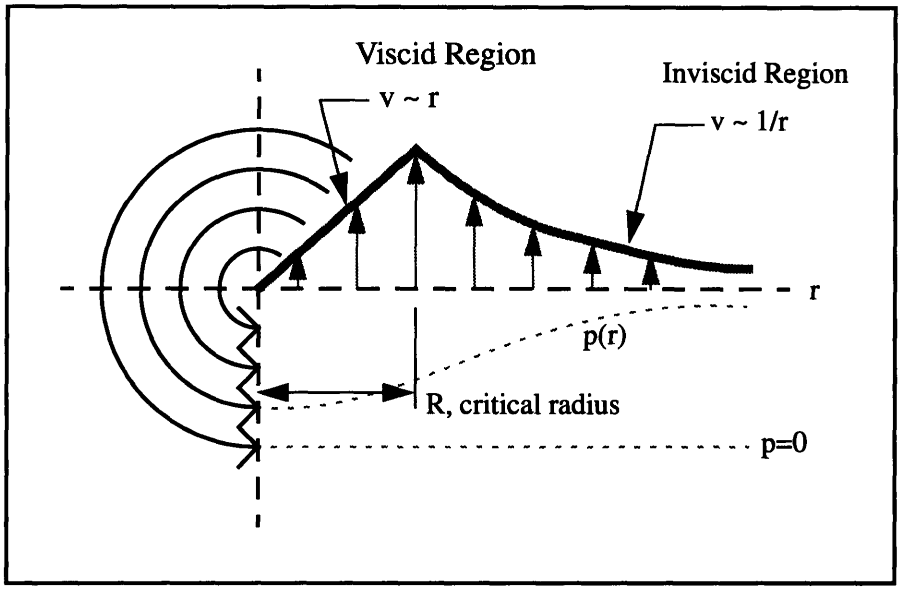

Figure 2.1: Pressure profile and tangential velocity profile in a Rankine's Vortex [18].

The pressure is continuous with radius also [18]. Inside the core the radial pressure gradient is equal to the density times centripetal acceleration, $\frac{dp}{dr} = \rho r \omega^2$. Using equation 2.3, the pressure gradient becomes,

$$\frac{dp}{dr} = \frac{\rho r K^2}{R^4}. \tag{2.6}$$

This integrates to,

$$p_1 = p_o + \frac{\rho r^2 K^2}{2R^2}, \tag{2.7}$$

where:

p_1 is the pressure inside the core, and

p_o is the pressure at the center.

Bernoulli's equation can be applied in the inviscid vortex. Taking a point at infinity where v= 0, and a point at an arbitrary radius within the inviscid vortex yields,

$$p_2 = p_\infty - \frac{\rho K^2}{2r^2}, \tag{2.8}$$

where:

p_2 is the pressure outside the core.

Finally, by equating equations 2.7 and 2.8 at R, p_o can be eliminated from equation 2.7 leaving the pressure inside the core as a function of the pressure at infinity, as in equation 2.8,

$$p_1 = p_\infty - \frac{\rho K^2}{R^2}\left(1 - \frac{r^2}{2R^2}\right). \tag{2.9}$$

2.1.3 Axial and Tangential Components of Vorticity

In a swirling flow with an axial jet there are two components of vorticity that interact. The axial component is created by swirling the secondary flow. Its direction is positive with the flow. The tangential component of vorticity is created by the shear layer set up between the primary and secondary flows. The two components are shown schematically in Figure 2.2. These two vorticity components are responsible for creating the recirculation zone which is sometimes found in swirling flows.

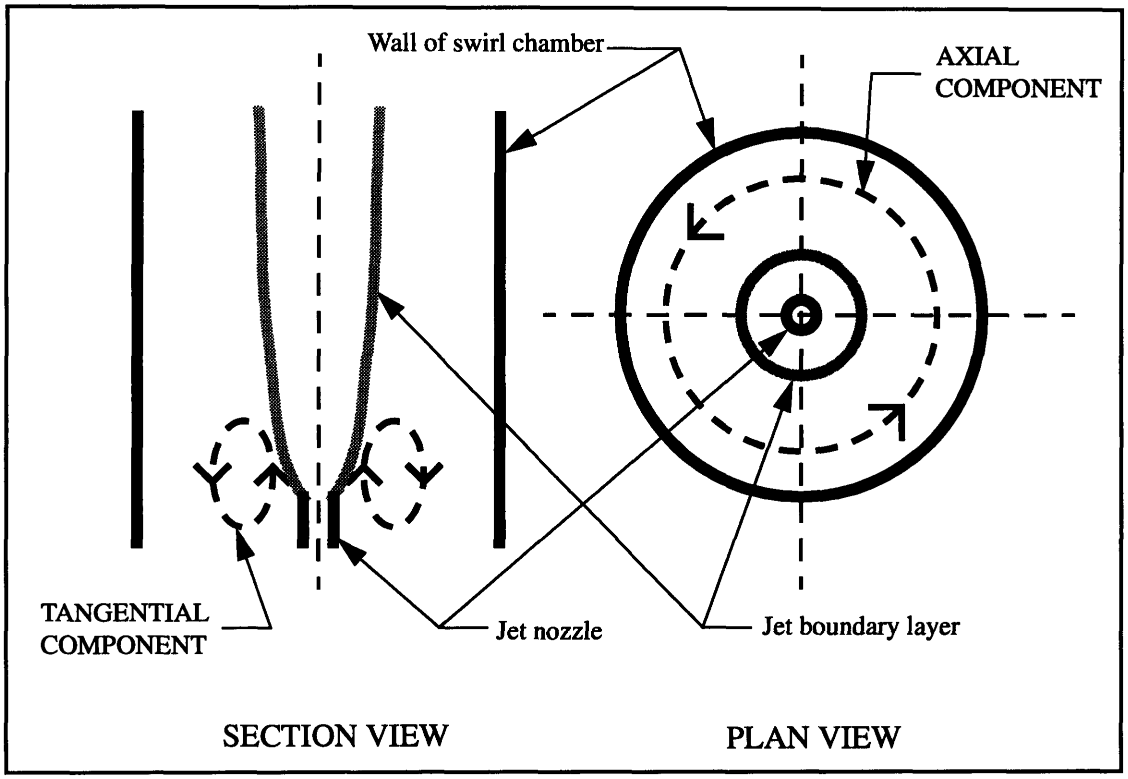

Figure 2.2: The axial and tangential components of vorticity present in a swirling flow with an axial jet.

2.1.4 The Recirculation Zone

At high degrees of swirl strong radial and axial pressure gradients are created near the nozzle exit, resulting in axial recirculation in the form of a toroidal recirculation zone (TRZ) or recirculation zone. The recirculation zone is not found in flows with weak swirl. It is widely known that the recirculation zone is formed when the swirl number is greater than 0.6 [17]. However, researchers have shown that divergent exit nozzles reduce the swirl number needed to induce the recirculation zone [9]. The formation of the recirculation zone is also known to depend on the size of enclosure, the method used to generate swirl and the initial velocity profile. A diagram of the recirculation zone is given in Figure 2.3.

The size and shape of the recirculation zone affects the stability, intensity and performance of the flame. For example, the recirculation zone reduces the velocity requirements for flame stabilization by recirculating heat and active chemical species to the base of the flame [9]. Because of this, the recirculation zone is often modelled as a well stirred reactor. Finally, recirculation zones in swirling jets are similar to those created by bluff bodies. However, there is one important difference. For bluff bodies, the size of the recirculation zone depends on the diameter of the bluff body. Therefore it is constant. For swirling flows, the size of the recirculation zone depends on the swirl number, and thus can be controlled. Although much is known about the recirculation zone, it still can not be controlled to the point that NO_x is minimized.

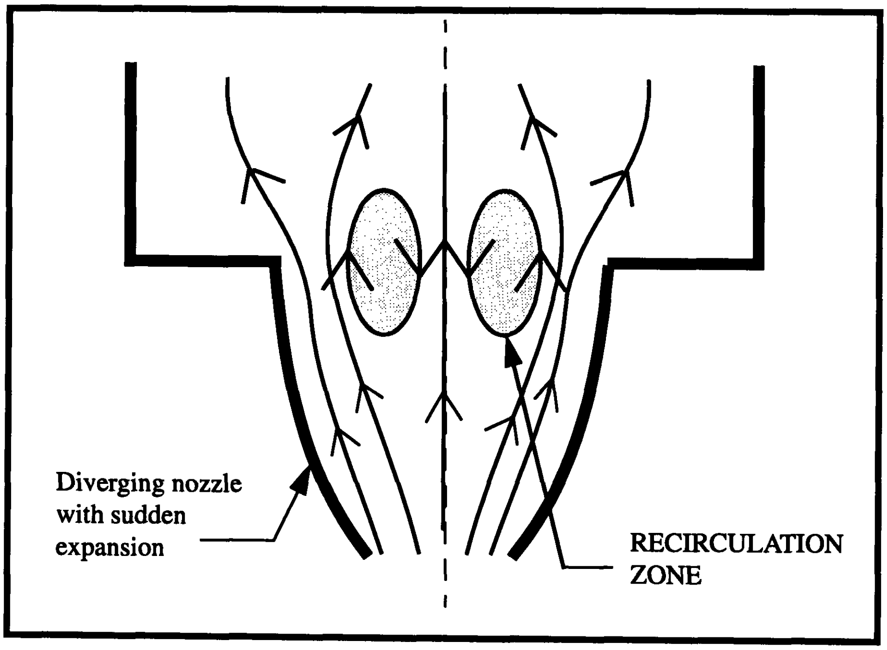

Figure 2.3: Sketch of the recirculation zone in a diverging nozzle with a sudden expansion.

2.1.5 Generation of Swirl

Swirl is generated by three primary methods: guide vanes, tangential entry and direct rotation. First, in guide vane swirl chambers, the flow is redirected as it passes through an array of vanes. The vanes can be set at different angles, thus dictating the amount of swirl. The vanes can also be rotated, or remain stationary. Several factors affect the efficiency of the vane array: the profile of the individual vanes, the number of vanes in the array, the diameter of the vane array, and the angle of attack. Because of the ease of manufacturing and a large swirl range, guide vanes where chosen for the swirl chamber design. Second, tangential entry swirl chambers create a swirling flow by injecting the secondary flow tangential into the chamber. High swirl numbers can be achieved, however, the total pressure requirements of the system are high [17]. Finally, direct rotation creates swirl by rotating the walls of the swirl chamber at thousands of revolutions per minute. This type of swirl chamber produces solid body rotation.

Chapter 3

Experimental Setup

A swirl chamber and particle image velocimetry system were designed and constructed to conduct the experiments. The first part of this chapter describes how the swirl chamber works and the characteristics of the swirl chamber. The second part of the chapter explains the particle image velocimetry system. Laser Doppler velocimetry and flow visualization are also discussed.

3.1 Swirl Chamber

The swirl chamber creates a simplified model of a jet engine combustion chamber within a cylindrical glass test section. The test section allows easy viewing of the axial or longitudinal cross-sections. The test section is 2 ft long and 4 inches in diameter. The simple geometry of the test section reduces the complexity of the flow in order to isolate the fundamental mechanisms of mixing. Water is used to simulate the primary and secondary flows. With water, Reynolds numbers on the order of 10^4 to 10^5 can be achieved at axial velocities of 1 to 3 m/s. These lower velocities lead to highly accurate measurements. Water also diminishes compressibility effects, which simplifies the flow field, also bringing out the fundamental mechanisms. The primary flow is injected into the secondary flow axis with a nozzle 0.305 inches in diameter. The velocity of the jet can be varied from 0 to 10 m/s. The secondary flow is swirled using stationary guide vanes. The swirl number can be varied from 0 to 1.

Detailed CAD drawings of the swirl chamber are included in Appendix A. However, an assembly drawing of the swirl chamber is given on the next page. The parts are drawn to scale.

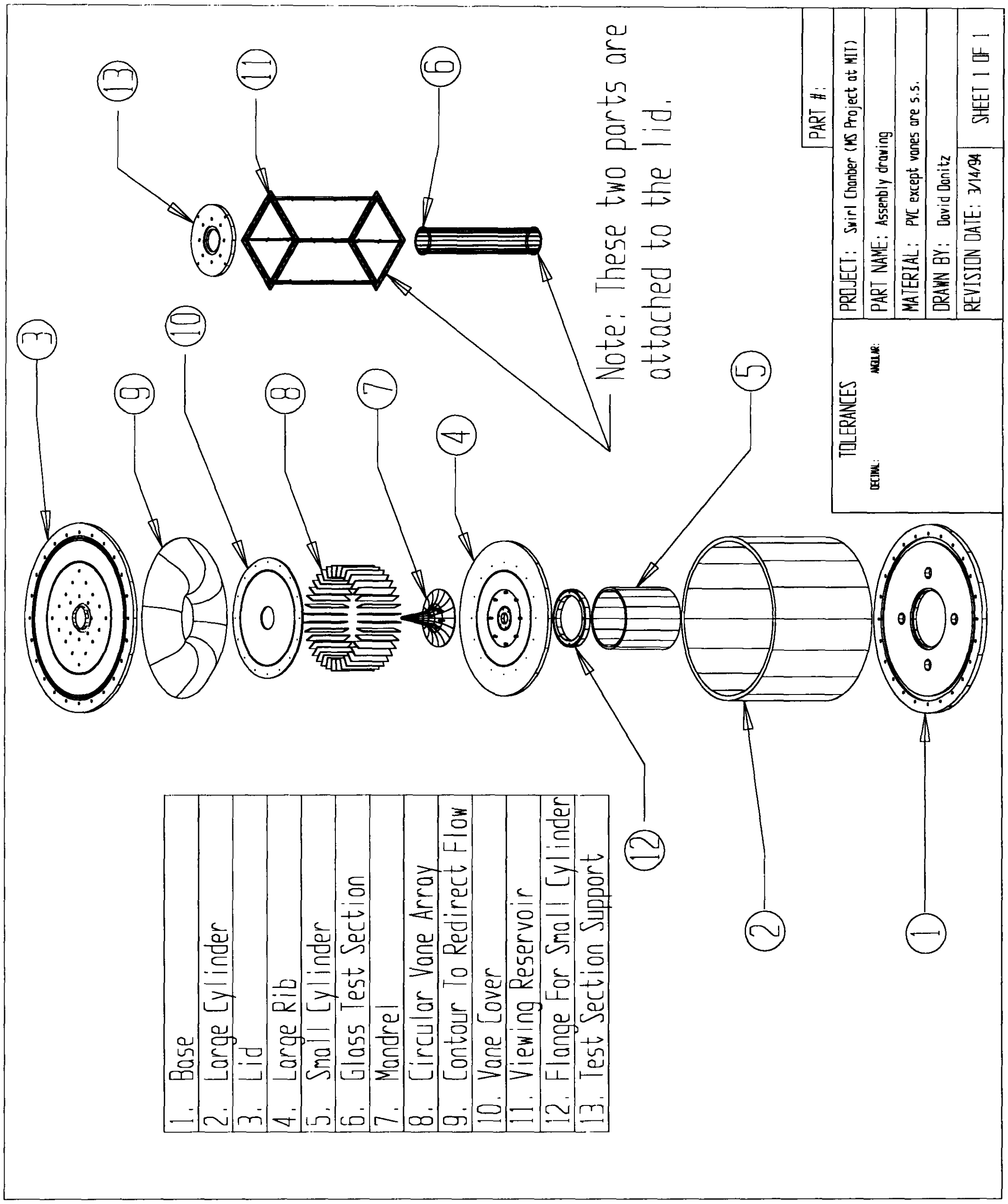

Figure 3.1: Assembly drawing of the swirl chamber. The parts are drawn to scale.

3.1.1 How the Swirl Chamber Works

The swirl chamber creates a clean vortex in the test section and allows a jet to be injected along the axis of the vortex. A picture of the swirl chamber is given below in Figure 3.2. A scaled cross-section of the swirl chamber is given on the next page in Figure 3.3.

Figure 3.2: The swirl chamber and the secondary flow reservoirs.

The secondary flow is pumped from the starting reservoir to a distributor consisting of 3 inch polyvinylchloride (PVC) pipe. As seen in Figure 3.2, all junctions of the distributor exhaust into a toroidal shaped settling chamber at the base of the swirl chamber, desig-

nated (a) in Figure 3.3. The toroidal shaped settling chamber damps out any vortices created by the pump. The secondary flow is then passed through 500 half-inch holes drilled along the periphery of the central rib, location (b). These holes act as a flow straightener. The water is then forced radially inward through a second flow straightener located directly ahead of the leading edges of the vanes. The flow straightener consists of a brillo pad filter.

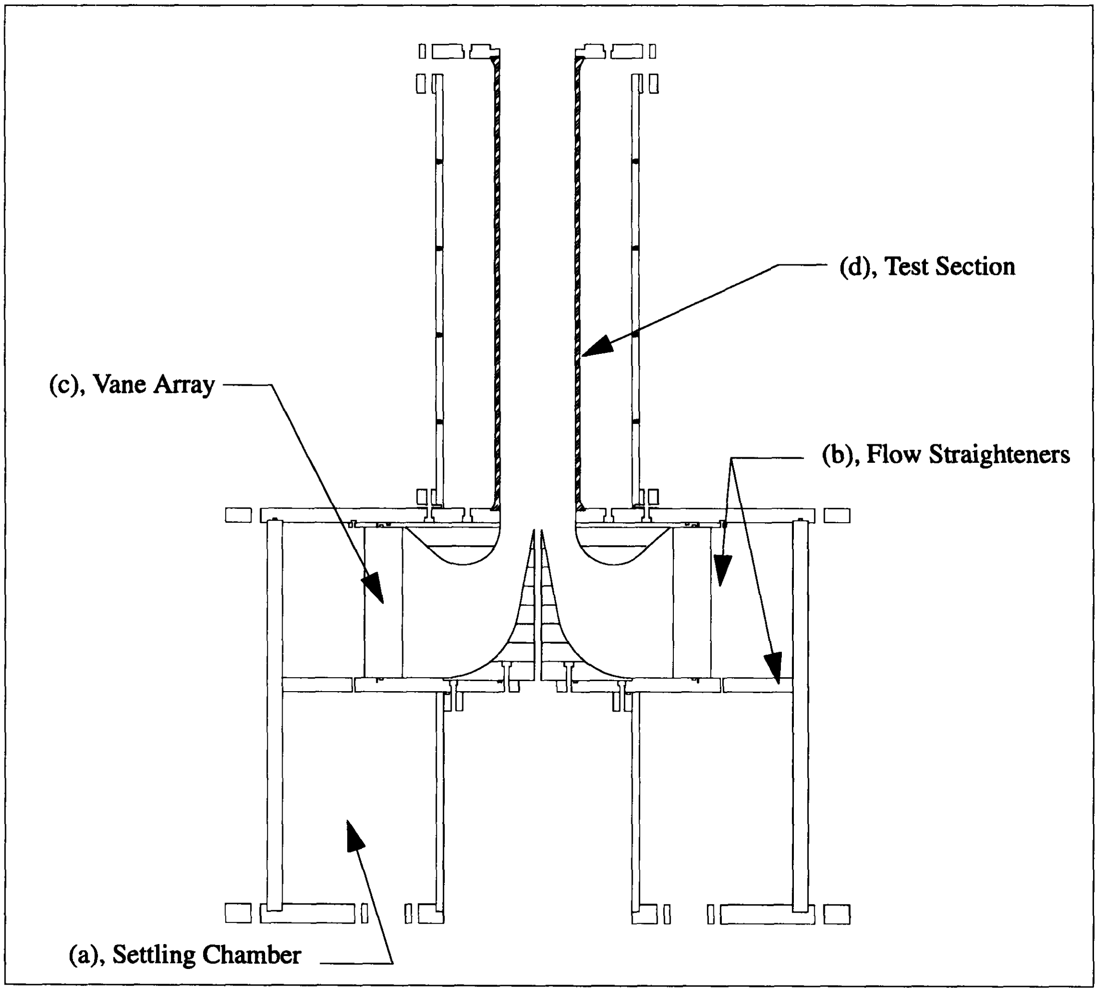

Figure 3.3: Scaled cross-section of the swirlchamber.

The laminar flow then passes through a circular array of vanes, labeled (c). These vanes impart swirl on the flow. The swirling water is then accelerated and turned 90 degrees by

smooth contours. The acceleration dampens any unsteadiness, and the contours aid in preventing separation. The swirling secondary flow then enters the test section, area (d), where the primary flow is injected through a nozzle located at the axis of the secondary flow. The combined flows pass by an orifice plate for velocity readings, seen at the top of Figure 3.2, and then exhaust back into the starting reservoir or into a second reservoir. The exhaust uses 4 inch PCV pipe. A separate plumbing circuit controls the primary flow. The primary flow is pumped from a separate starting reservoir directly to the axis of the swirling secondary flow. The primary plumbing circuit is shown below in Figure3.4.

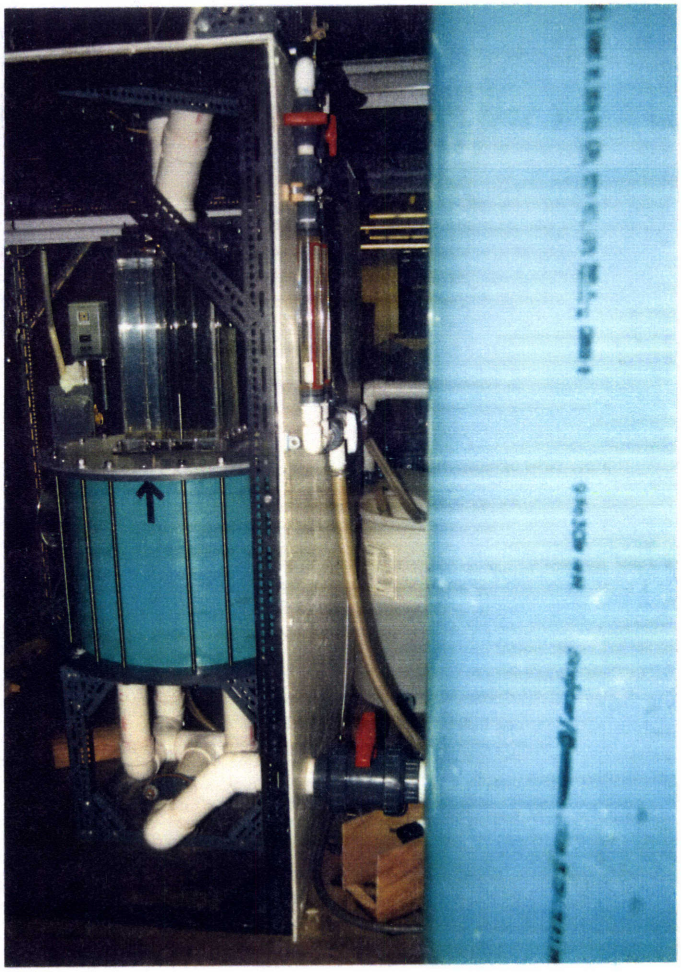

Figure 3.4: The primary plumbing circuit is mounted on the wall of the swirl chamber enclosure. The white primary flow reservoir can be seen in the background.

3.1.2 Modes of Operation and Controlling Axial Flow Rates

The swirl chamber is capable of running in an open or closed circuit mode. The closed circuit mode recirculates the flow by exhausting the water back into the starting reservoir once it has left the test section. The open circuit mode dumps the flow into a second reservoir after the flow has left the test section. This allows for a one time blow down of the starting reservoir.

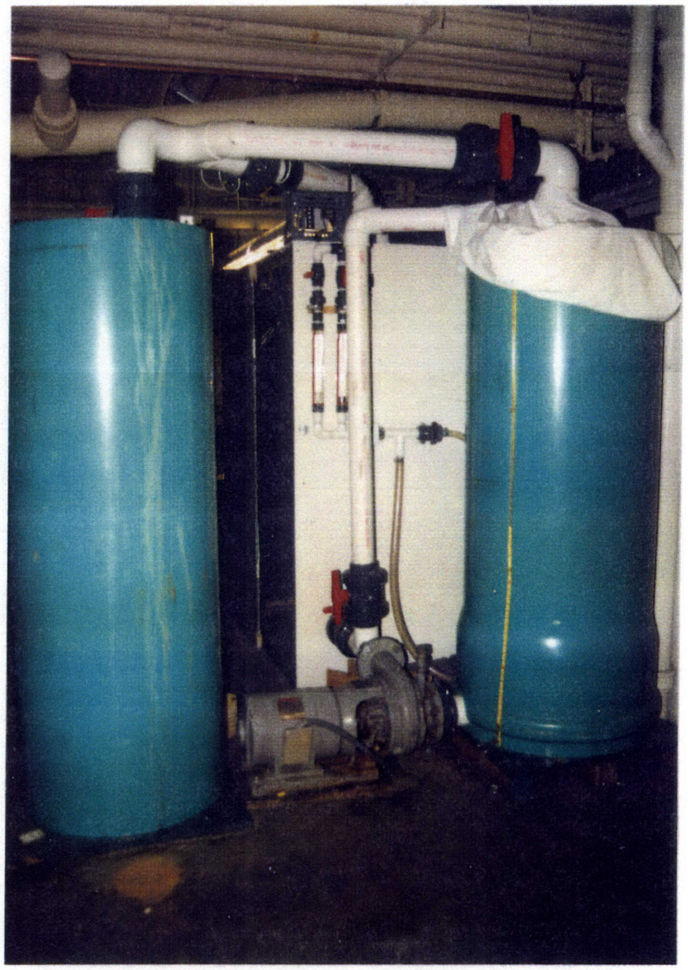

Figure 3.5: The secondary flow plumbing can be seen clearly in this picture. The valves immediately downstream of the secondary pump regulate the flow through the test section. The valves directly above the green reservoirs are used to switch between the open and closed circuit modes.

The open circuit is used when the primary flow is seeded with particles or dye, and contaminates the secondary flow after mixing. In the open circuit mode, a test run can only

last about 90 seconds with steady state being reached in about 15 seconds. The closed circuit mode is used when the secondary flow is seeded with particles or dye, and the mixing with the primary flow dilutes the concentration slightly. The swirl chamber can be run in the closed circuit mode indefinitely, the only limitation is overheating of the pump.

The volume flow rate into the swirl chamber can be controlled using the bypass line, seen in Figure 3.5. The 3 inch ball valves located immediately after the pump are used to regulate the amount of water sent to the swirl chamber. By changing the configuration of the valves, an axial velocity range from 0 m/s to 3 m/s is possible. The 4 inch ball valves located directly above the starting and finishing reservoirs are used to switch between open and closed circuit modes. They can also be used to regulate the back pressure.

The axial velocity in the test section is monitored by an orifice plate mounted downstream of the test section. Eight pressure ports, four evenly spaced every 90 degrees, a distance of 2 inches from each side of the plate, measure the pressure drop across the orifice plate. This pressure differential is used to assure the axial velocity is consistent between different experimental runs.

3.1.3 Changing the swirl number

The swirl number can be altered by changing the angle of the vanes. There are 36 rectangular vanes 8 in. x 2 in. x 1/8 in., evenly spaced on a 17.00 inch diameter circle. A cross-section of the vane array is given below in Figure 3.6. The actual vane configuration is shown in Figure 3.7. The vanes are held in place between the vane cover and the central rib. The frictional force created by squeezing the two plates together with tension rods keeps the vanes stationary. O-rings are mounted between the vanes and the two plates to

increase the coefficient of friction.

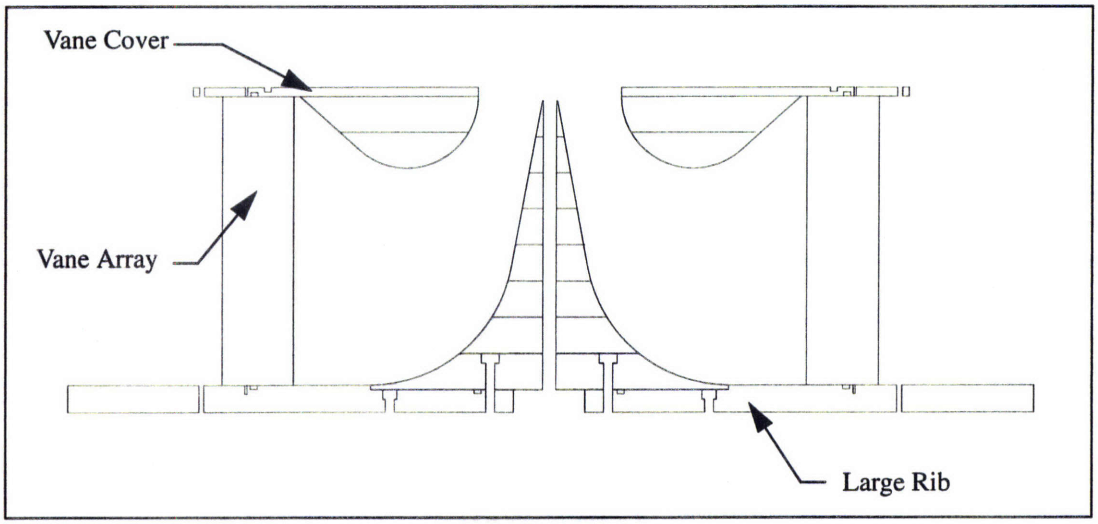

Figure 3.6: Cross section of the swirl chamber vane array.

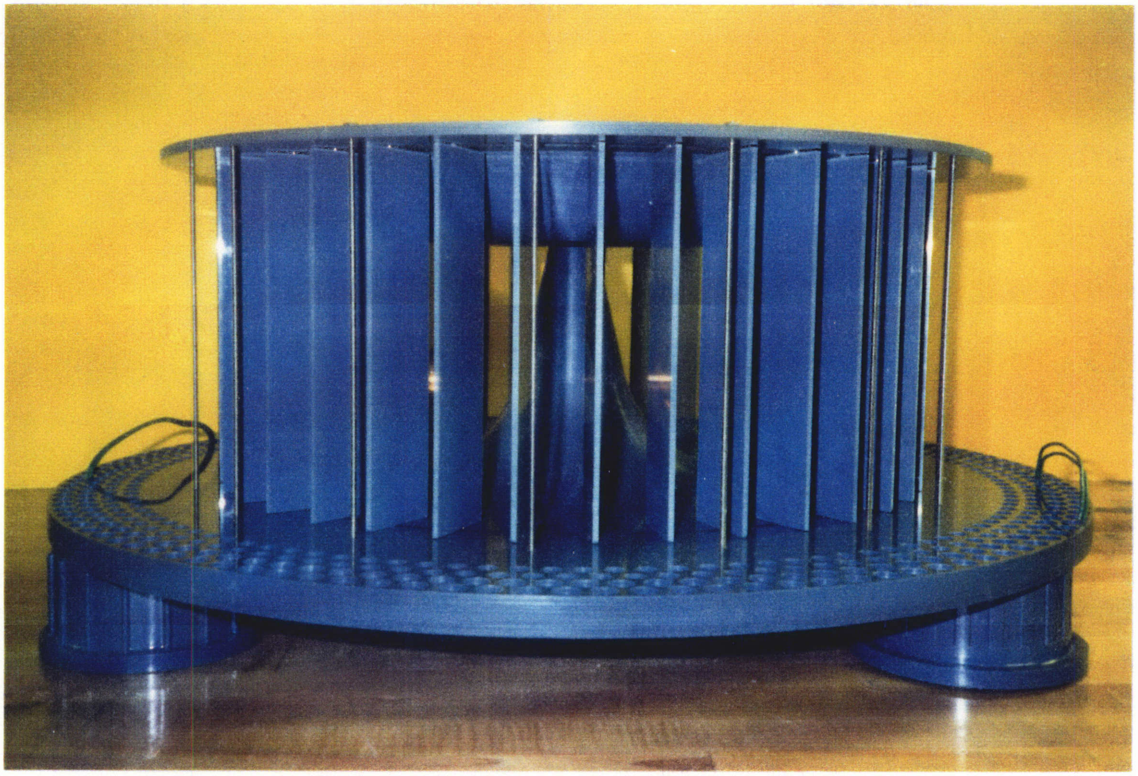

Figure 3.7: The vane array, vane cover and large rib.

The vanes are aligned using a precision machined vane aligner. The aligner uses a triangulation technique to assure the proper orientation of the vanes. An example of the alignment of one vane is given in Figure 3.8.

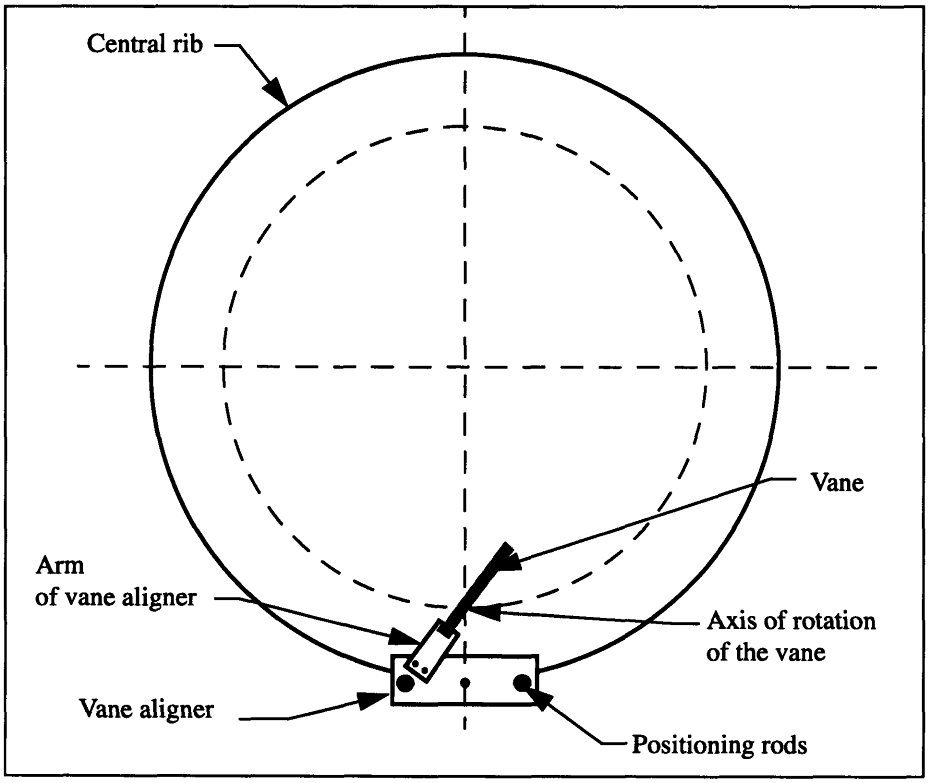

Figure 3.8: Precision machined vane aligner

A groove is machined in the arm of the vane aligner that is the same width as the vane. The arm is mounted onto the vane aligner to position the vane at the desired angle. First, the vane is snugly placed in the groove. Second, the vane aligner is positioned so that its center is along the same radius of the central rib as the axis of rotation of the vane, and both positioning rods on the vane aligner make contact with the central rib. Finally with the vane aligner properly positioned, the arm assures the vane is located at the desired angle.

3.1.4 Optical Viewing Box and Viewing Orientations

When an object is seen through a flat piece of glass the image is not deformed because the refraction of light in the glass is small. However, when an object is viewed through a circular piece of glass, the deformation of light is greater due to the radius of curvature of the glass. Because of this, a clear acrylic waterproof box, the optical viewing box, surrounds the test section. The box has a 10 in. by 10 in. base. Water is used to fill the space between the acrylic box and the glass test section. Because the index of refraction of water is similar to that of glass, the round test section does not refract the light, and the flow field is not deformed when viewed from the outside. A close-up of the optical viewing box is given below in Figure 3.9.

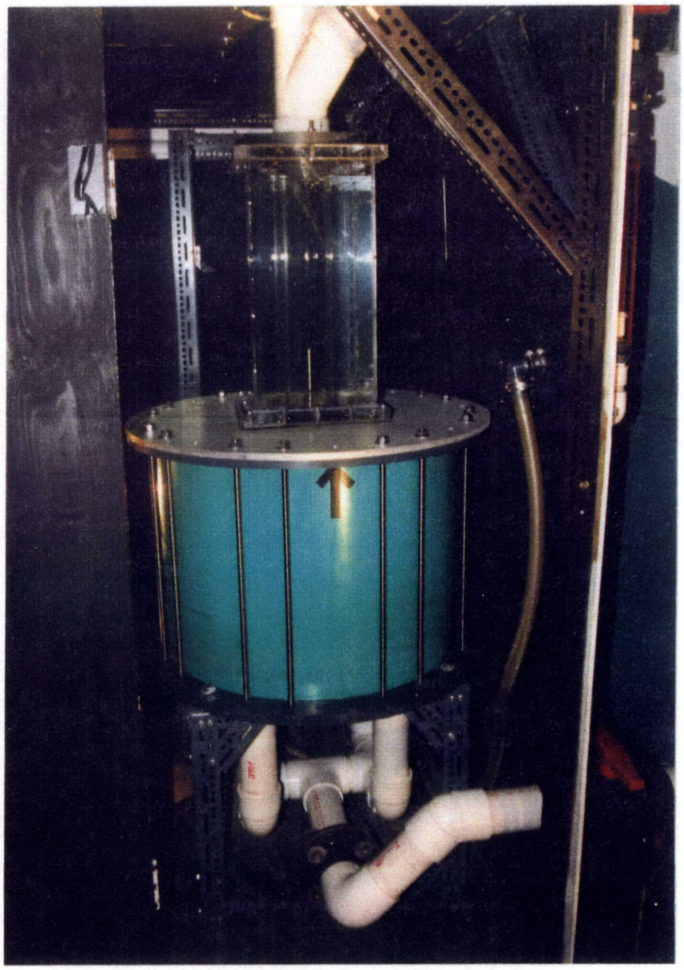

Figure 3.9: Swirl chamber optical viewing box.

3.1.5 Robustness of Swirl Chamber

The versatility of the experimental facility allows many different combustion chamber configurations to be modelled. For example, air could also be used as the working fluid, or with minor modifications, fuel could be burned.

The central hub is the contour that turns the swirling flow 90 degrees into the test section. The primary flow nozzle is mounted along the axis of this hub. The hub has been designed to be interchanged with other hubs. For example, a bluff body hub could be inserted to study the effects of swirl combined with a bluff body. Also, a hub that allows for off axis injection could be inserted.

3.2 Design of the Swirl Chamber

3.2.1 Scaling

The early aspects of the design deal with scaling the flow characteristics of several combustion chambers to a dynamically similar swirl chamber. The first step is to use the Buckingham Pi Theorem to calculate the non-dimensional parameters that are important to the flow. From the work of Beer, Chigier, Gupta, Lilley..., [4] to [17], it is found that the parameters needed to characterize swirling flows in combustion chambers are:

ρ, the density of the fluids,

μ, the viscosity of the fluids,

x, the axial distance from the primary flow nozzle exit,

r, the radial position,

D_j, the diameter of the primary flow nozzle,

D_s, the diameter of the swirl chamber,

$\int_0^{\frac{D_s}{2}} (\rho u_s v_s)\, r^2\, dr$, the angular momentum flux of the secondary flow,

$\int_0^{\frac{D_s}{2}} \left(\rho u_s^2 \right) r dr$, the axial momentum flux of the secondary flow,

$\int_0^{\frac{D_j}{2}} \left(\rho u_j^2 \right) r dr$, the axial momentum flux of the primary flow.

After applying the Buckingham Pi Theorem, the non-dimensional groups needed to dynamically scale a combustion chamber to the swirl chamber are found to be:

The ratio of the two diameters, which characterizes the size of the swirl chamber,

$$\frac{D_s}{D_j}. \tag{3.1}$$

This number is found to range from 3 to 15 in most combustion chambers.

The non-dimensionalized axial position,

$$\frac{x}{D_j}. \tag{3.2}$$

The non-dimensionalized radial position,

$$\frac{r}{D_j}. \tag{3.3}$$

The non-dimensionalized viscosity, which is similar to a Reynolds number,

$$\frac{\mu}{\rho^{\frac{1}{2}}\left(\int_0^{\frac{D_s}{2}}\left(\rho u_s^2\right)rdr\right)^{\frac{1}{2}}}. \tag{3.4}$$

Because the Reynolds number is commonly used in most research on swirling flows, it is utilized in the scaling of the swirl chamber to common combustion chambers, instead of the non-dimensionalized viscosity. The Reynolds number is found to range from 15,000 to 300,000 in typical combustion chambers.

The swirl number, S, which is discussed in Section 2.1.1,

$$\frac{\int_0^{\frac{D_s}{2}} (\rho u_s v_s)\, r^2 dr}{\frac{D_s}{2}\int_0^{\frac{D_s}{2}}\left(\rho u_s^2\right)rdr}. \tag{3.5}$$

The swirl number is found to range from 0 to 3 in most combustion chambers.

The primary to secondary momentum flux ratio, M, which characterizes the rate of injection of the primary flow is,

$$\frac{\int_0^{\frac{D_j}{2}}\left(\rho u_j^2\right)rdr}{\int_0^{\frac{D_s}{2}}\left(\rho u_s^2\right)rdr}. \tag{3.6}$$

The primary to secondary momentum flux ratio is found to range from 3 to 60 in typical applications.

Beer and Chigier have shown that the swirl number, Reynolds number and the primary to secondary momentum flux ratio are the most important numbers used to characterize the flow. The swirl chamber is designed to operate in the ranges of each nondimensional number above. A 10 cm diameter cylinder is chosen to represent the walls of a combustion chamber. The primary flow nozzle is chosen to be 0.77 cm in diameter. These dimensions lead to a diameter ratio of 13.0. With a secondary pump capable of supplying 120 gmp, and a primary pump capable of supplying 7 gpm, the primary to secondary momentum flux ratio can be varied from 0 to 80. Also, the Reynolds number can be varied from 0 to 350,000.

In order to match the range of the swirl number in combustion chambers a vane type swirler is chosen to impart swirl onto the flow. A calculation is performed below to ensure the entire range of the swirl number can be achieved. A schematic of the model is given in Figure 3.10. Water enters the vane array normal to the control volume at location 1 with a velocity v_1. The vanes then turn the water to an angle θ as shown in Figure 3.10. The water leaves normal to the control volume at location 2 with a velocity v_2.

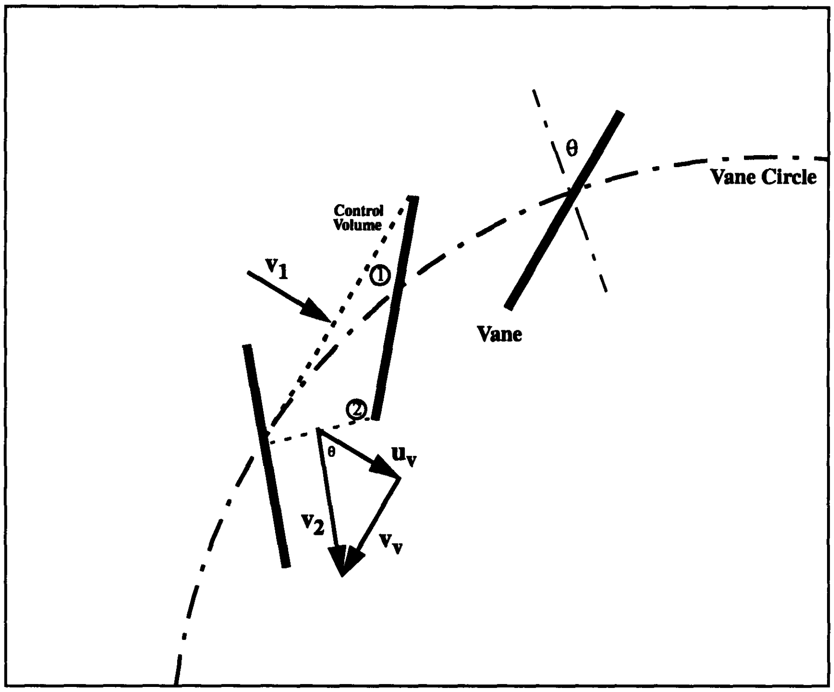

Figure 3.10: The vane configuration used to calculate the swirl number range. A control volume is taken between two vanes. The variables are defined in the paragraph below.

All of the vanes are centered on a vane circle of diameter, D. Each vane makes an angle θ with a radius of the vane circle. The following symbols are used in the calculation:

Q is the volume flow rate of the secondary pump,

v_1 is the velocity of the water as it enters the control volume,

v_2 is the velocity of the water as it leaves the control volume,

u is the axial velocity in the test section,

u_v is the radial velocity at the vane array,

v is the tangential velocity in the test section,

v_v is the tangential velocity at the vane array,

D is the diameter of the vane circle,

D_s is the diameter of the test section,

θ is the angle the vanes make with a radius of the vane circle,

h is the height of the vanes.

The velocity of the water entering the control volume at surface 1 is,

$$v_1 = \frac{Q}{\pi D h}. \tag{3.7}$$

By using the conservation of mass v_1 is found to be roughly equal to the radial velocity at the vane array, u_v, because both velocities are in the radial direction and are at similar radial distances. Therefore, the tangential velocity at the vane array is,

$$v_v = u_v \tan\theta = \frac{Q}{\pi D h}\tan\theta. \tag{3.8}$$

However, we are interested in the axial and tangential velocities in the test section, not at the vane array. Assuming solid body rotation, v equals ωr, and from equation 3.8 the tangential velocity in the test section is,

$$v = \frac{2Q\tan\theta}{\pi D^2 h} r. \tag{3.9}$$

The axial velocity, u, can be found assuming a parabolic profile in the test section so, $u = ar^2 + b$, where a and b are constants. The boundary conditions are $u = \frac{6Q}{\pi D_s^2}$ at $r = 0$, and $u = 0$ at $r = D_s/2$. This leads to,

$$u = \frac{6Q}{\pi D_s^2}\left\{1 - \left(\frac{2r}{D_s}\right)^2\right\}. \tag{3.10}$$

Substituting these values into the swirl number, equation 3.5, and integrating gives,

$$S = \frac{D_s^3}{12hD^2}\tan(\theta)\ . \tag{3.11}$$

The values of D_s, h and D, after many iterations were chosen to be 4 inches, 8 inches and 17 inches respectively. Therefore, the vane angle must range from 0 to 89 degrees in order to achieve a swirl number from 0 to 3.

3.2.2 Cavitation Prevention

To prevent bubbles from expanding within the test section, the axial pressure was designed to be above atmospheric pressure. This is the region in which the lowest pressure occurs, see Figure 2.1 in Section 2.1.2. Equation 2.9 in Section 2.1.2 was used to calculate the pressure along the axis of the test section. Equation 2.9 is repeated here as equation 3.12,

$$p_1 = p_\infty - \frac{\rho K^2}{R^2}\left(1 - \frac{r^2}{2R^2}\right). \tag{3.12}$$

The pressure at infinity, in equation 3.12, is assumed to be the pressure at the entrance to the swirl chamber. Therefore, in order to find the pressure at the axis of the test section, the closed circuit plumbing needs to be analyzed. Figure 3.11 gives the model of the plumbing circuit. Because the pressure at point (c) can be found with fluid statics, Bernoullis equation can be used to find the pressure at point (b), which can be used to find the pressure at point (a), which is assumed to be the same as the pressure at the entrance of the swirl chamber. Equation 3.12 can then be used to find the pressure along the axis.

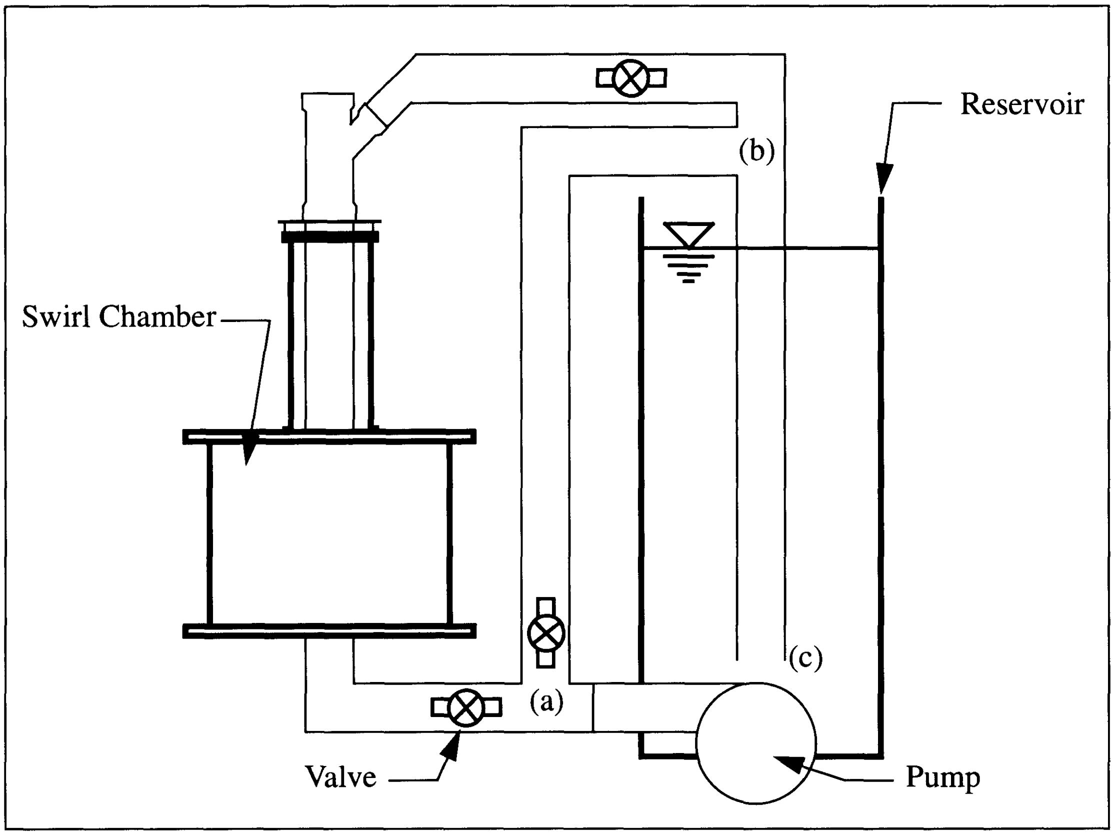

Figure 3.11: Sketch of the swirl chamber and the closed circuit plumbing. The flow is pumped from the reservoir to point (a) where some of the flow returns to the reservoir via a bypass line and the rest of the flow goes to the swirlchamber.

The pressure at (b) is found using Bernoulli's equation from (c) to (b),

$$\frac{P_b}{\rho}+\frac{v_b^2}{2}+gz_b=\frac{P_c}{\rho}+\frac{v_c^2}{2}+gz_c+f\left(\frac{L}{D}+\frac{L_e}{D}\right), \qquad (3.13)$$

where:

$P_{b,c}$ is the pressure at point (b) or (c),

$v_{b,c}$ is the velocity at point (b) or (c),

$z_{b,c}$ is the height at point (b) or (c),

g is the gravity constant,

ρ is the density,

f is the friction factor,

L is the length between (b) and (c),

L_e is the equivalent length for all minor head losses,

D is the diameter of the pipe.

The volume flow rate supplied by the pump is 120 gpm and the pipe between points (b) and (c) is 4 inches in diameter, which means that the average velocity in the pipe is 0.91 m/s. The height of point (b) is 1.83 m, and the height of point (c) is 0 m. The Reynolds number at (b) is 85,103, which yields a friction factor of 0.0185. Because the pipe between points (b) and (c) is straight, there are no minor head losses. Using equation 3.13 the pressure at (b) is found to be 1.65 kPa.

Apply Bernoullis equation from point (b) to point (a), and assuming low headloss in the swirl chamber, the following relation is found,

$$\frac{P_a}{\rho} + \frac{v_a^2}{2} + gz_a = \frac{P_b}{\rho} + \frac{v_b^2}{2} + gz_b + f\left(\frac{L}{D} + \frac{L_e}{D}\right). \tag{3.14}$$

There are two paths from point (a) to (b), through the swirl chamber and through the bypass line, given that all the valves are open. Assuming that half of the volume flow rate, 60 gpm, goes through the swirl chamber., the velocity at (a) is 0.83 m/s, since 3 inch diameter pipe is used for the bypass line and the entrance to the swirl chamber. The Reynolds number is then 56,735 and the coefficient of friction is 0.2 at point (a). The swirl chamber is assumed to produce an equivalent length of 38.1 m. The five elbows, four 45 degree turns and the orifice plate, which are also in the circuit, produce an equivalent length of 55.9 m. The length of pipe between points (a) and (b) is 6.1 m. Substituting these values into equation 3.14, solving for v_a and converting to a volume flow rate at (a) gives,

$$Q_a = 0.11186 A_a \left(\frac{1}{r} (P_a - P_b) + g (z_a - z_a) \right)^{\frac{1}{2}}, \tag{3.15}$$

where:

Q_a is the volume flow rate through the swirl chamber,

A_a is the area of the pipe at (a),

P_a is the pressure at (a),

P_b is the pressure at (b),

z_a is the elevation of (a),

z_b is the elevation of (b).

Next the volume flow rate through the bypass line is determined. The length of the pipe is 2.7 m, and the diameter is 3 inches. The Reynolds number is 56,735 so the friction coefficient is roughly 0.2. Therefor, the volume flow rate through the bypass is,

$$Q_t = 0.3892 A_a \left(\frac{1}{r} (P_a - P_b) + g (z_a - z_a) \right)^{\frac{1}{2}}. \tag{3.16}$$

By using equations 3.15 and 3.16 it is found that 22.3% of the flow goes through the swirl chamber, and 77.7% of the flow goes through the bypass line. Therefore, if the pump provides 120 gpm, the velocity of the fluid entering the swirl chamber in the 3 inch diameter pipe is traveling at 0.37 m/s. Also, the veloctiy of the water in the bypass line is 1.29 m/s.

With a better approximation of the velocities at point (a) and (b), a second iteration to obtain a better estimate of the two velocities is performed. The Reynolds number at the entrance of the swirl chamber is 20,717, which gives a friction factor of 0.025. The Reynolds number in the bypass line is 97,548, which gives a friction coefficient of 0.0185. Using the same minor headlosses for the swirl chamber path and the bypass line, it is found that 20% of the flow goes through the swirl chamber, and 80% of the flow goes through the bypass line. Which means the velocity in the bypass line is 1.33 m/s, and the velocity at the entrance to the swirl chamber is 0.33 m/s.

Now that the velocities at (a) and (b) have been found and the pressure at (b) is known, equation 3.14 can be applied to obtain the pressure at (a). This is found to be 20.7 kPa gage. Assuming there are no losses between point (a) and the entrance of the swirl chamber, the pressure at the entrance of the swirl chamber is 20.7 kPa gage.

Finally, equation 3.12 is used to find the pressure along the axis of the test section. At the axis, equation 3.12 becomes,

$$p_1 = p_\infty - \frac{\rho K^2}{2R^2} \quad , \tag{3.17}$$

where P_∞ is 20.7 kPa. Taking the critical radius, R, as 1 cm corresponds to a small core, which results in a conservative solution. Also, assuming the highest swirl number of 3 resuts in a vortex strength, K, of 0.028 m^2/s. Using these values and equation 3.17, the pressure along the axis, P_1, is found to be 17.5 kPa gage, which is above atmospheric pressure. So, under the worst conditions the pressure along the axis will not drop bellow atmospheric pressure. Thus, air will not come out of solution within the flow.

3.2.3 Orifice Plate Calculation

An orifice plate was designed and constructed in order to measure the average axial velocity through the test section. Experimental data was used that empirically found the pressure drop across different orifice plates. The pressure drop could be calculated by,

$$\frac{\Delta P}{\rho} = \zeta \frac{v^2}{2}, \qquad \text{(C.18)}$$

where:

ΔP is the pressure drop across the orifice plate,

ρ is the density of the fluid,

ζ is a constant found experimentally and given in Table 3.1,

v is the velocity of the fluid.

Table 3.1 gives the values of z for different size orifice plates. D_1 is the diameter of the pipe, and D_2 is the diameter of the hole in the orifice plate.

•

Table 3.1: Experimental data of the pressure drop constant for different size orifice plates.

D_2/D_1	ζ
0.3	300
0.4	85
0.5	30
0.6	12
0.7	4.5
0.8	2.0

Because a small pressure drop was desired to keep air from expanding in the flow, a diameter ratio of 0.8 was chosen. Figure 3.12 shows a drawing of the orifice plate.

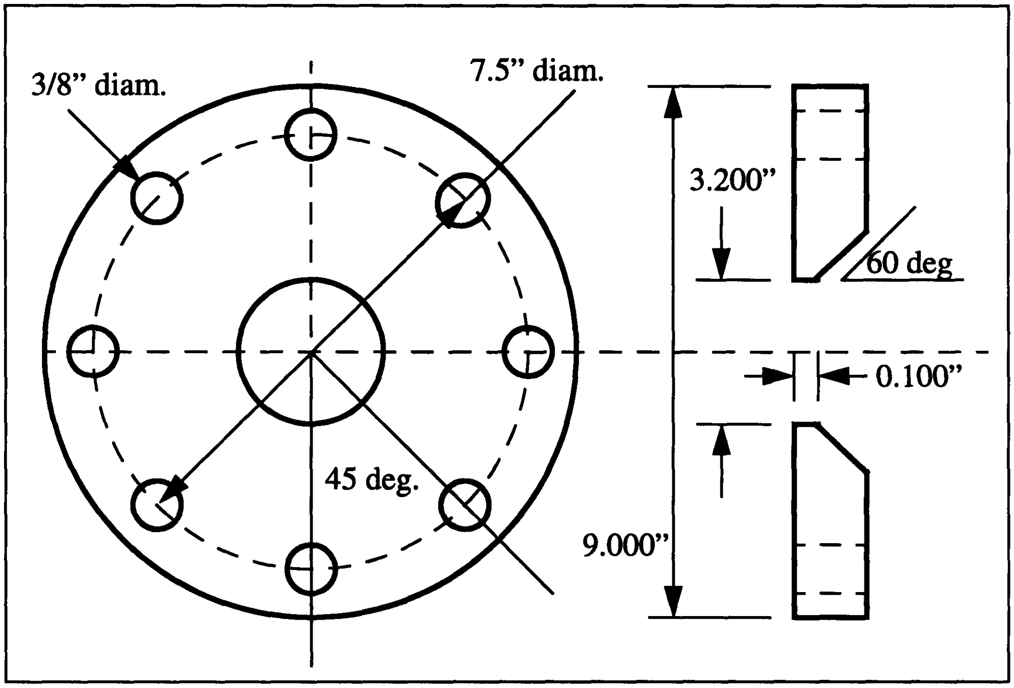

Figure 3.12: Drawing of the orifice plate

3.2.4 Hoop Stress Calculation

Figure 3.13 shows the internal stresses in the swirl chamber's large cylinder.

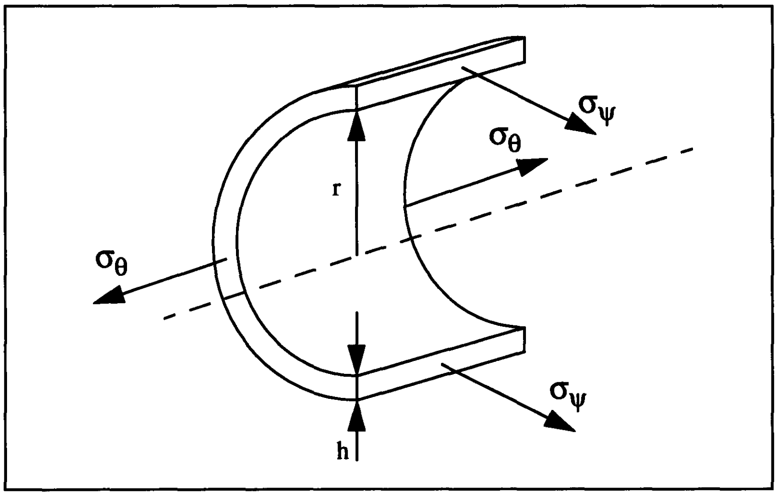

Figure 3.13: Cross-section of the large cylinder showing the hoop stress, σ_ψ,and the axial stress, σ_θ.

The hoop stress can be calculated by,

$$\sigma_\psi = \frac{Pr}{h}, \tag{3.19}$$

where:

σ_ψ is the hoop stress,

P is the pressure acting on the cylinder from the water,

r is the mean radius,

h is the wall thickness.

The axial stress can be calculated by,

$$\sigma_\theta = \frac{Pr}{2h}, \tag{3.20}$$

where:

σ_θ is the axial stress.

The maximum pressure the pump can supply is 206.8 kPa, which corresponds to a 60 ft head. The radius of the large cylinder is 0.353 m, and the wall thickness of the large cylinder is 0.02 m. Using these values and equations 3.19 and 3.20, the hoop stress is calculated to be 3.59 MPa, and the axial stress is calculated to be 1.79 MPa. The Young's modulus of PVC is 1.4 to 4.1 MPa. The tensile strength of PVC is 34.4 to 62.0 MPa. The yield strength is unknown, however, the hoop stress is an order of magnitude smaller than the tensile strength. Therefore, the internal stresses in the large cylinder under the worst conditions should not exceed the yield strength of PVC.

3.2.5 Deformation of Top Plate

When the swirl chamber was turned on for the first time, the pressure inside the large cylinder caused the top plate to deform. The top plate bulged to the point that the o-ring seal between the top plate and the large cylinder failed. An aluminum support plate was designed and built to take up the force on the top plate due to the internal pressure. Marks' Standard Handbook for Mechanical Engineers [19] was used to design the aluminum plate, so that the maximum deformation of the top plate was 5 mm. Figure 3.14 shows the model of the aluminum plate.

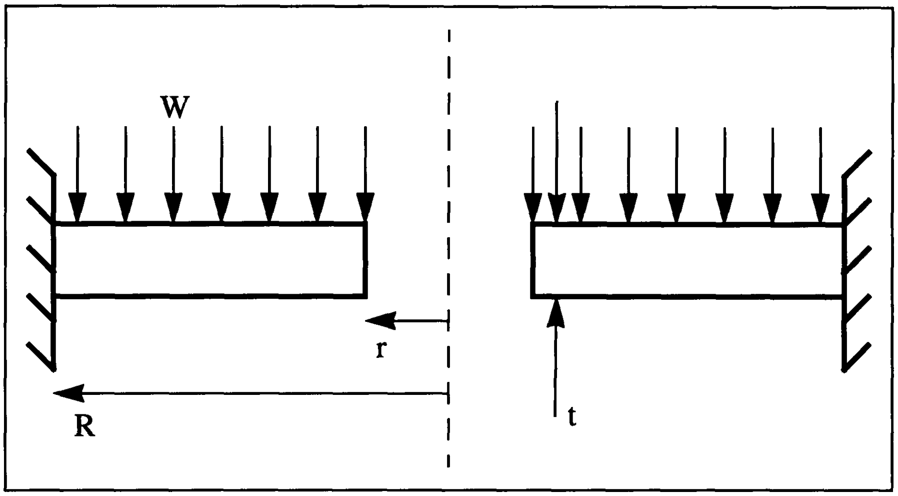

Figure 3.14: Circular aluminum plate with a central hole of radius r, and a outside radius R. The plate is rigidly fixed along the outside perimeter. W is the applied load, and t is the thickness of the plate.

The maximum internal stress in the plate is,

$$S_m = k_1 \frac{wr^2}{t^2}, \tag{3.21}$$

where:

S_m is the maximum internal stress,

w is the applied load,

r is the radius of the hole,

t is the thickness of the plate,

k_1 is an empirical constant found in [19] on page 5-53, Table 5.2.19.

The maximum deflection in the plate is,

$$Y_m = k_2 \frac{wr^4}{Et^3}, \tag{3.22}$$

where:

E is the Young's modulus,

k_2 is an empirical constant found in [19] on page 5-53, Table 5.2.19.

With an outside radius of 0.375 m, a hole radius of 0.102 m, a load of 0.207 MPa, a plate thickness of 1.25 cm and a Young's modulus of 2 GPa, k_1 and k_2 are 0.15 and 0.675 respectively. This yields a maximum deflection of 4 mm and a maximum internal stress of 17.7 kPa. So the maximum deflection is less than 5 mm and the maximum internal stress is well below the yield strength of aluminum.

3.2.6 Buckling of Vanes

Because friction is used to keep the vanes in place, the vane array is designed not to buckle under the normal force required to provide the frictional force which keeps the vanes stationary. If the pump provides 120 gpm, the vane array has a radius of 17.00 in. and the vanes are 8.00 in. high, the velocity of the water as it enters the vane array is 2.75 cm/s. If the vanes are 2.00 in. long, the area of a vane side is 16.00 in^2, or 103.22 cm^2. In the worse case scenario, the stagnation pressure of the flow would be applied to this area. With a velocity of 2.75 cm/s the stagnation pressure is 0.38 Pa. So the entire distributed force on the one vane is 3.9 mN. The coefficient of friction of PVC on PVC is around 0.2. It would take a normal force of 0.02 N to overcome the torque applied on the vane. This is insignificant. However, lets calculate the buckling force required to see if the weight of the vane cover will cause a vane to buckle.

Figure 3.15 shows a model of the loading of a vane. Euler buckling occur when,

$$P_{cr} = \frac{\pi^2 EI}{L^2}, \tag{3.23}$$

where:

P_{cr} is the critical stress applied to the vane,

I is the area moment of inertia and is equal to $\frac{bh^3}{12}$,

E is the Young's modulus of PVC and is equal to 1.4 MPa,

L is the length of the vane.

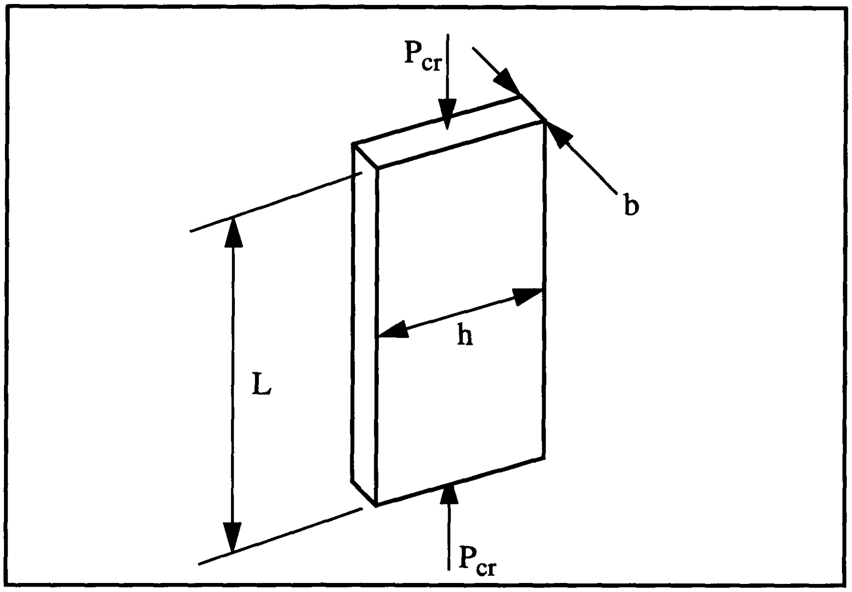

Figure 3.15: Model of a vane under an applied stress.

The area moment of inertia is calculated to be 3.255 x 10^{-4} in.^{4}, the Young's modulus of PVC is at worst 200,000 psi and the length, L, of the vane is 8.00 in. So the vane will buckle under a critical stress of 53 psi. Since a cross-section of the vane is 0.25 in.^{2}, the applied force that would cause the vane to buckle is 13.25 lbf. The weight of the vane cover is only 4 lbf. Therefore, one vane can withstand the weight of the vane cover. There are at least 8 vanes in the array. Therefore, the vanes will not buckle.

3.3 Particle Image Velocimetry System

3.3.1 Overview

Particle image velocimetry (PIV) is an experimental method used to measure instantaneous velocity vector fields in turbulent fluid flows. In theory, the method is fairly simple. First, the flow is seeded with fluorescent particles about 50 μm in diameter. While taking a time elapsed photograph, a cross-section of the flow field is illuminated by a sheet of laser light. By double pulsing this sheet during one photograph, each particle appears twice on the same picture. The velocity field can be obtained by measuring the distance the particles traveled and recording the time between laser pulses.

An auto-correlation program written by Doug Hart is used to measure the distances the particles travel. The program thresholds the picture and compares each pixel to other pixels. The correlation value between the pixels is recorded in a matrix that remembers the relative distances between each pixel. The correlation at each distance is added for every pixel and the maximum is recorded. The maximum corresponds to the distance the particle traveled. If the laser is triple pulsed, and the time between pulses is altered, then the autocorelation program can decipher what direction the particles are traveling. The acceleration of the particles can also be found.

A pulsed Nd:YAG laser is used to create the sheet of light. The laser produces 15 J per pulse during a 20 ms pulse length and a 10 Hz repetition rate at 1064 nm. The frequency of the pulses can range from 10 to 300 Hz. The infrared light is frequency doubled to produce a laser sheet with a wavelength of 532 nm, which is in the green range of the visible

spectrum. The details of frequency doubling the laser is discussed in Section 3.2.2. The power output of the laser after being frequency doubled is unknown at this time. However, the pulse length is estimated to be around 10 to 50 ns. The number of pulses and time between pulses are controlled by a program and an electronic circuit. The program is given in Appendix C. Two or three pulses can be created at any time interval by the program. A picture of the laser system is given below in Figure 3.16.

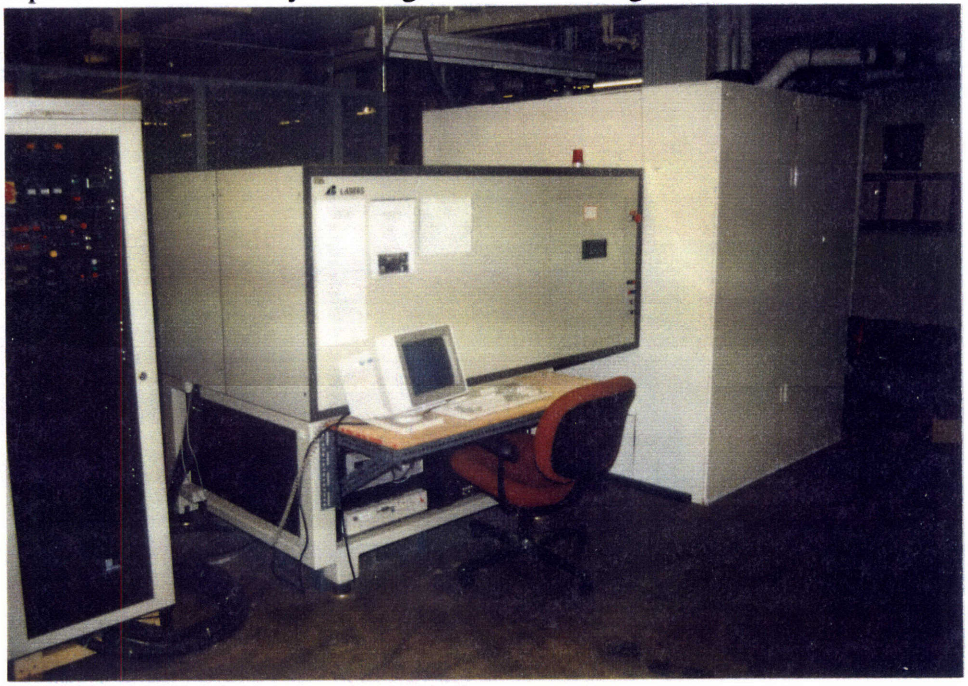

Figure 3.16: The Nd:YAG laser system. The laser control box can be seen in the far right of the picture. The computer that controls the q-switch is mounted at the base of the laser enclosure. The laser sheet passes through a clear acrylic window built into the swirl chamber enclosure.

The initial diameter of the beam is 0.5 mm. A cylindrical lens is used to transform the circular beam into a sheet. Detailed drawings of the lens mount is given in appendix D. The sheet is 0.5 cm thick and about 1 m wide when it passes through the test section. The lens can be oriented to create an axial or a longitudinal sheet. The orientation of the beam is controlled with a pair of galvanometers that can move the beam in a two dimensional

plane. Also, the entire laser head is mounted on a rail and can be moved up and down. A picture of the optical setup is given in Figure 3.17.

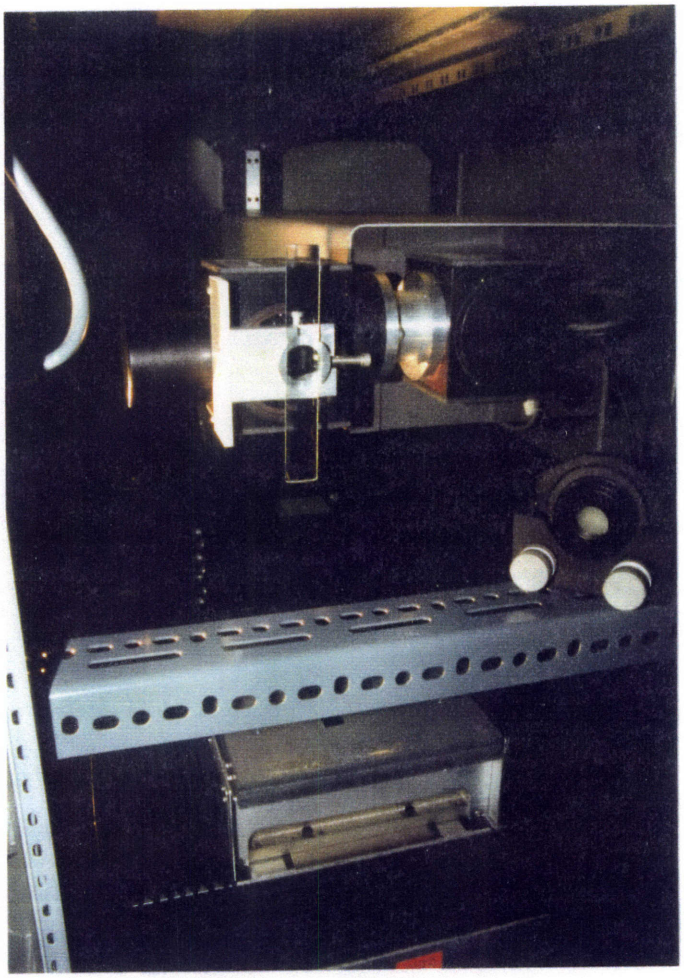

Figure 3.17: The cylindrical lens and galvanometers of the Nd:YAG laser. The galvanometers are used to fine tune the position of the laser sheet. The cylindrical lens can be rotated 90 degrees to produce an axial or longitudinal laser sheet.

The PIV pictures are taken with a Nikon 2000 still camera. For axial cross-sections, the camera is mounted on top of the swirl chamber encloser. For longitudinal cross-sections the camera is mounted on a tripod next to the swirl chamber.

3.3.2 Frequency Doubling the Nd:YAG Laser, Hardware

Several components are needed to frequency double the Nd:YAG laser. First, a CD*A crystal is used to actually perform the doubling. The frequency doubler is held in place with a custom built mount. A mirror, positioned immediately after the frequency doubler, reflects the remaining infrared beam into an aluminum light absorber. Both the frequency doubler and mirror are located after the front mirror.

A q-switch is required to increase the instantaneous power of the infrared beam in order to achieve a higher conversion efficiency in the frequency doubler. The q-switch is a KD*P. The q-switch is positioned between the rear mirror and the laser head and is held in place by a custom built mount. When the Nd:YAG laser is fired, the q-switch prevents lasing by disrupting the oscillation of the photons between the front and back mirrors. Power must be supplied to the q-switch in order to prevent the oscillation. When the power to the q-switch is turned off, the built up population inversion is dumped all at once, creating a pulse with power on the order of a megawatt and a pulse length on the order of 10 nanoseconds. The infrared beam must be polarized in order for the q-switch to prevent lasing. A 500:1, linear, high power polarizing cube was used to polarize the beam. The polarizer is mounted on the same carriage as the q-switch.

The alignment of each component is performed with the aid of a diode laser that is mounted to the optical rail. The backscatter created from the reflection of the diode laser beam off the components is used to assure that each component is aligned. The diode laser is also used to align the laser sheet to the proper location in the test section.

3.3.3 Frequency Doubling the Nd:YAG Laser, Electronics

A timing circuit controls the q-switch and allows up to three pulses to be fired at variable intervals. The circuit, presented in Figures 3.20 and 3.21, massages the outputs from a

CTM05 timing card which is run from the IBM PS2 mounted at the base of the laser encasing. A program, written by Professor Hart and presented in Appendix C, controls the timing card. The circuit consists of two one-shots, two AND gates and two transistors.

The Nd:YAG laser outputs a -15 V pulse when it is fired. This pulse is converted to a +5 V pulse by the first transducer. The +5 V pulse is sent to the one-shot which triggers a +5 V signal that is outputted to the timing card thus starting four separate counters. The output from the one-shot is also sent to the first and second AND gates. The one-shot is used as a safety precaution to assure that the q-switch is not left on. The one-shot pulse is set to be a maximum of 20 ms by the choice of the resistor and capacitor connected to pins 1 and 2 of the one-shot. Figure 3.18 illustrates the signal.

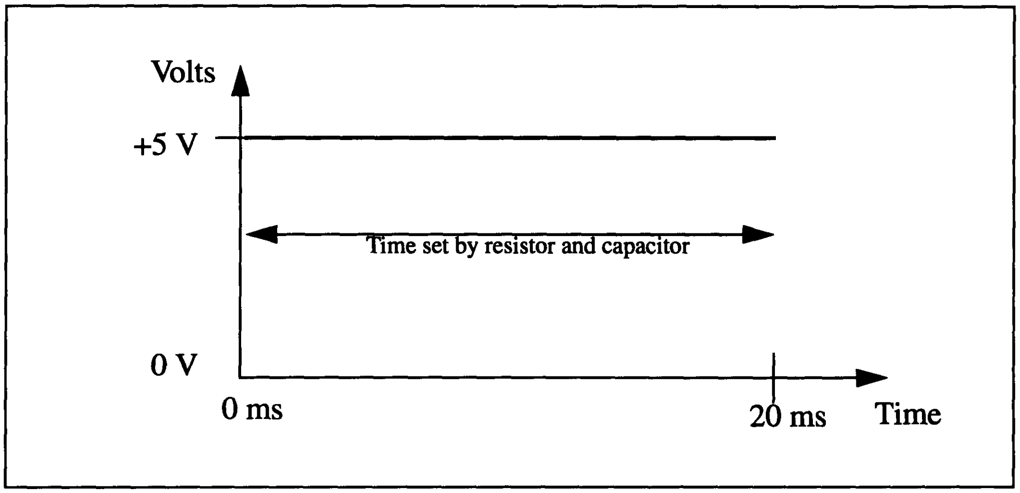

Figure 3.18: Output from first one-shot. The length of the signal is determined by the resistor and capacitor connected to the one-shot

The output from counters 2 through 4 are also sent to the first AND gate. The counter outputs are always high except for a low pulse when a counter reaches a preprogrammed time. Therefore, once the laser is fired, and all counters start, the output from the first AND gate is high. The output from the first AND gate is sent to the second one-shot. When one of the three timers reaches its preprogrammed time and flashes low, the AND gate also flashes low which fires the second one-shot outputting a second +5 V signal, shown in Figure 3.19.

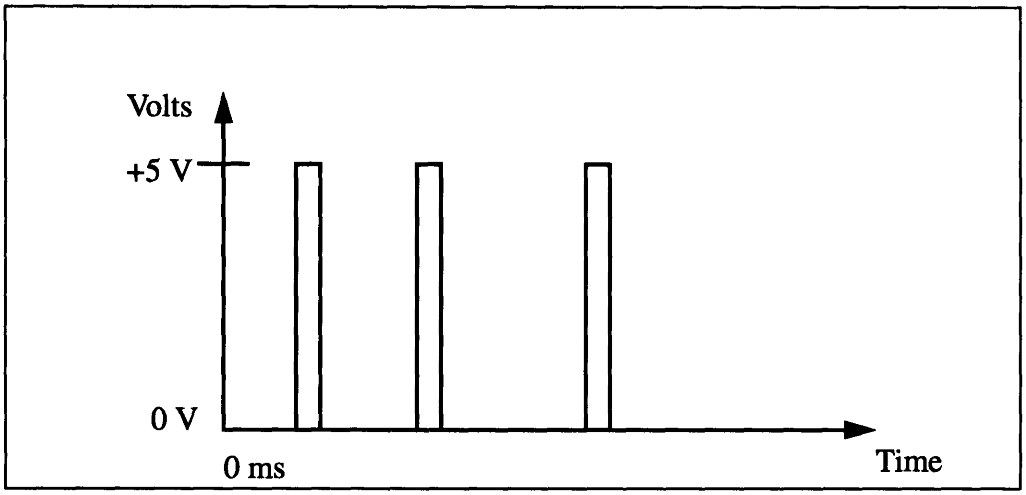

Figure 3.19: Output from second one-shot. The length of each pulse is determined from the resistor and capacitor connected to the one-shot. The starting time for each pulse is determined by the program.

The length of the output from the second one-shot is controlled by a variable resistor. The +5 V signals from the first and second one-shots trigger the second AND gate which sends a +5 V signal, that is amplified by the second transducer, to the q switch. The q-switch is turned off releasing the laser energy and creating a laser pulse. The preprogrammed times from timer 3 and 4 produce a similar set of events creating pulses at variable times, shown in Figure 3.20. The output from timer 1 is connected to the reset button on the first one-shot. When timer 1 is activated the entire circuit is reset for the next PIV run.

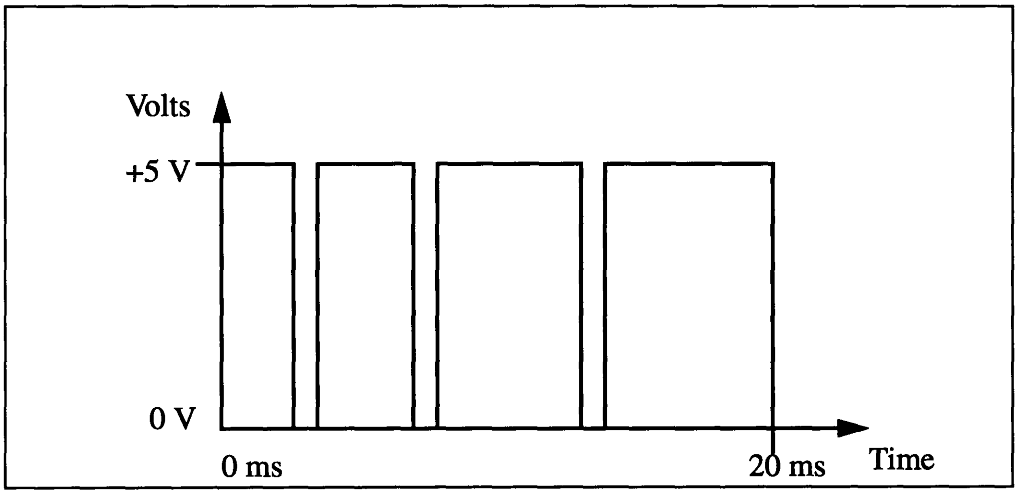

Figure 3.20: Signal sent to the q-switch. The q-switch is turned on at 0 ms. It is then turned off for the three pulses which allows the laser to fire. The q-switch is turned off automatically at 20 ms unless timer 1 resets the system.

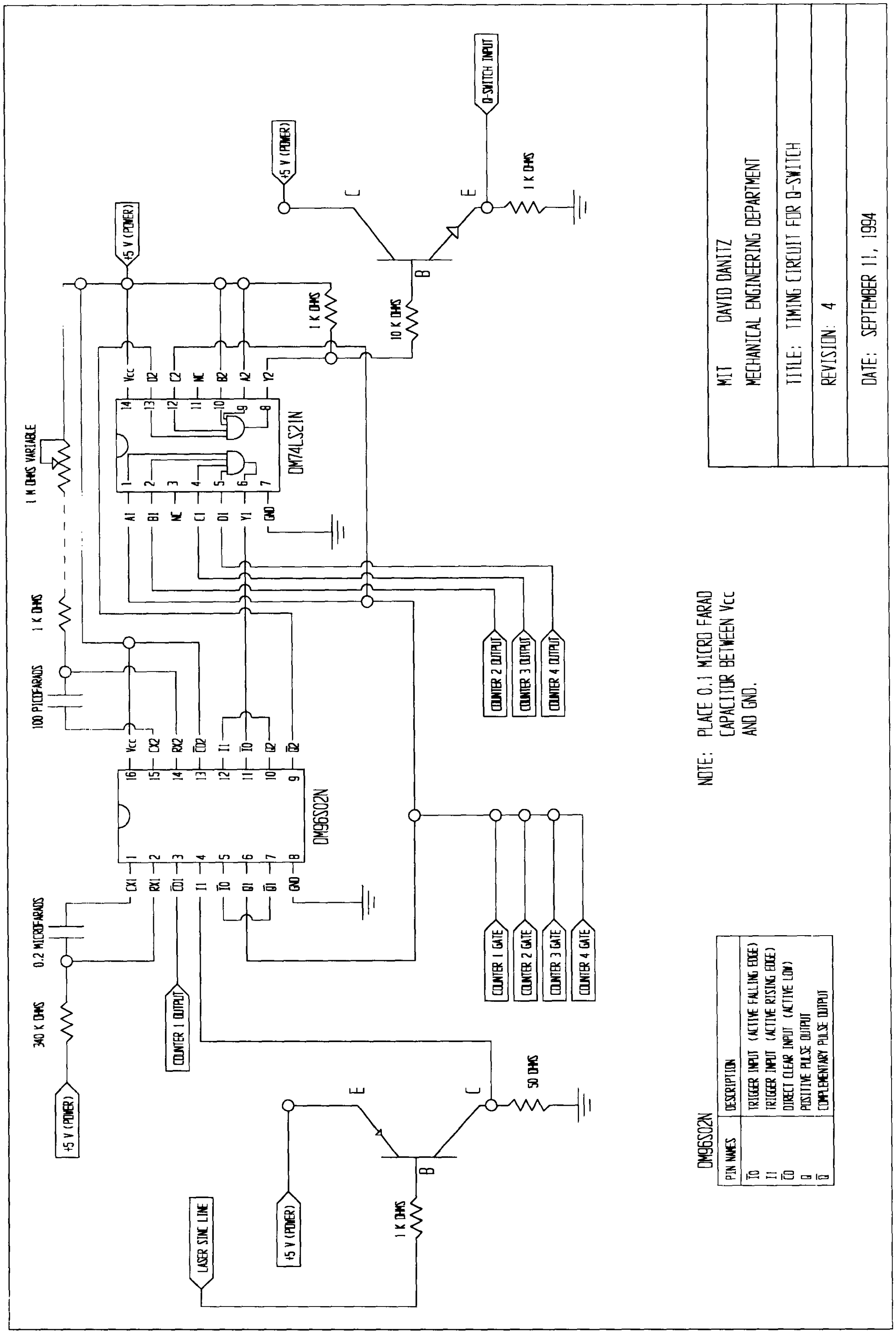

Figure 3.21: Schematic of the q-switch timing circuit controller.

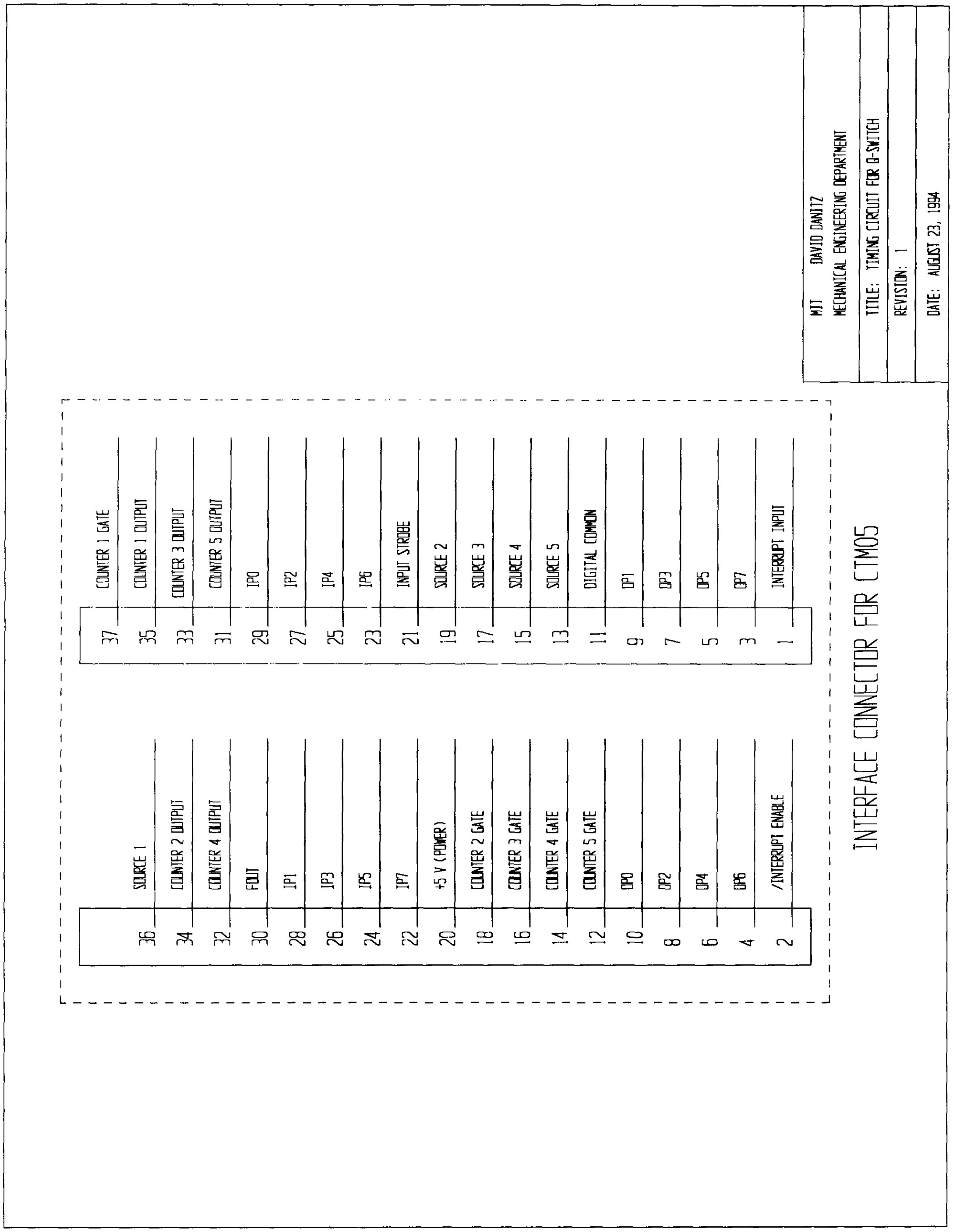

Figure 3.22: Continuation of the q-switch timing circuit controller.

3.4 Laser Doppler Velocimetry

The laser Doppler velocimetry (LDV) system was built by Aerometrics, Inc. The system uses an Argon-Ion laser to create the test volume, and a personal computer to perform the analysis. A picture of the system is given in Figure 3.23.

Figure 3.23: The laser Doppler velocimetry system. The emitter and sensor are connected to the laser via fiber optics.

The transmitter and receiver are mounted to an aluminum base, which is held in place by a truss structure, shown in Figure 3.24. The base slides on two rails that can be moved to different axial positions. Markers on the base and the rail allow for accurate movement of the laser test volume in the radial direction.

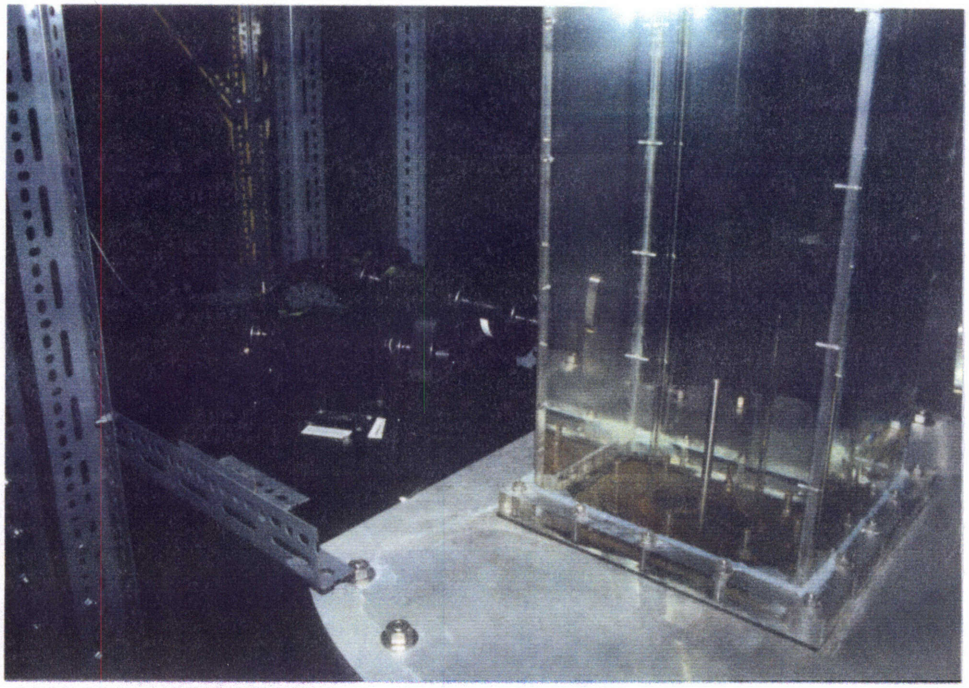

Figure 3.24: Picture of the truss structure that the LDV sensors are mounted to. Marks are inscribed onto the truss to allow accurate movement of the sensor in the radial direction.

3.5 Flow Visualization

Flow visualization pictures are taken with a Nikon 2000 camera. The primary flow is dyed with fluorescein sodium salt. An argon-ion laser and a cylindrical lens is used to create a sheet of laser light. This sheet can be oriented in the axial or longitudinal directions. The camera can be mounted in two positions for axial or longitudinal cross-sections. The axial viewing position is shown in Figure 3.25. A picture of the argon-ion laser creating a laser sheet is shown in Figure 3.26.

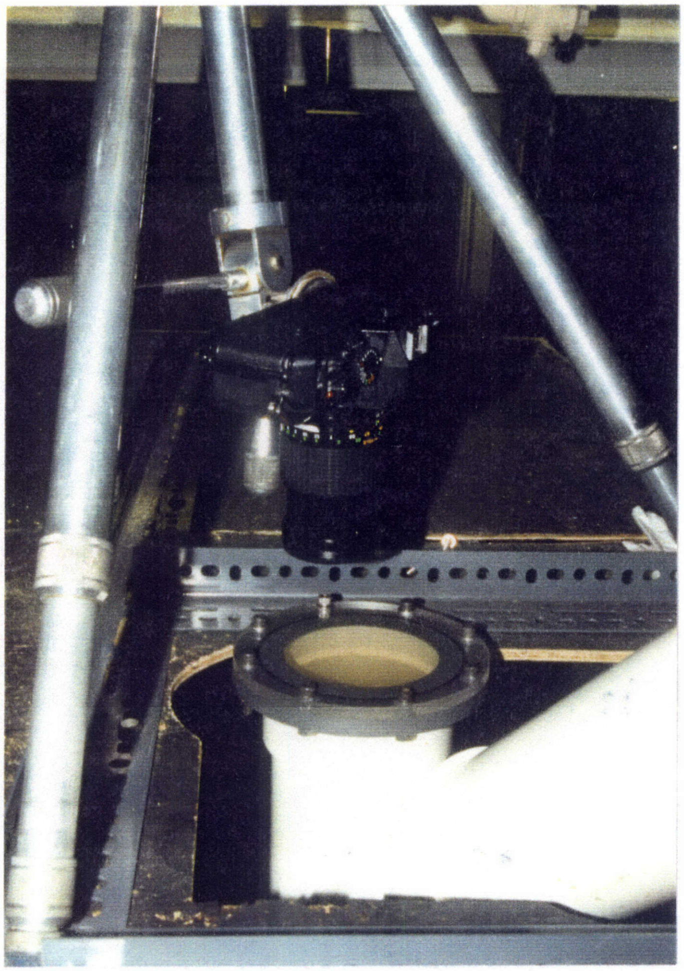

Figure 3.25: Camera mount for viewing axial cross-section. An axial viewing window allows an unobstructed view of the axis of the test section.

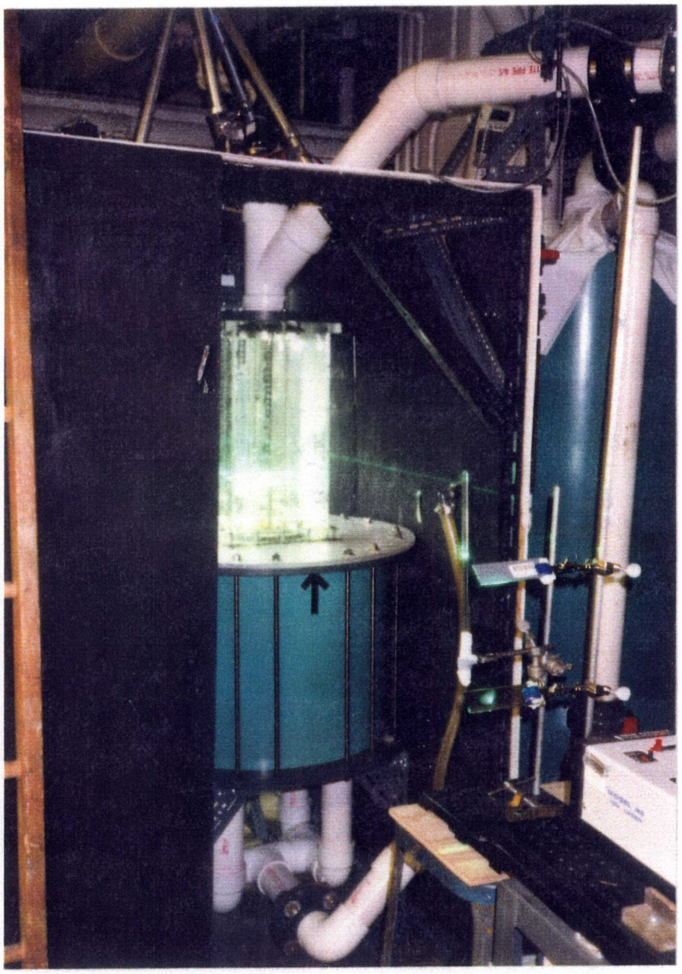

Figure 3.26: The argon-ion laser is creating a sheet of laser light with the aid of a cylindrical lens. The lens can be moved to different axial locations by sliding up or down on the rail. An axial cross-section is being taken in this photograph.

Chapter 4

Experimental Procedures

To obtain data to investigate the effect of swirl and injection rate on the mixing process, LDV was used to acquire one-dimensional, timed averaged velocity profiles in the axial and tangential directions. This data will also be used to verify CFD codes. Flow visualization was performed to obtain data for quantifying the rate of mixing between the primary and secondary flows. Axial and longitudinal cross-sections of the flow were taken using the coordinate system defined in Figure 4.1. Finally, PIV was performed to obtain two-dimensional, instantaneous velocity profiles in the axial and longitudinal planes. The swirl chamber was run in closed circuit mode for every experiment.

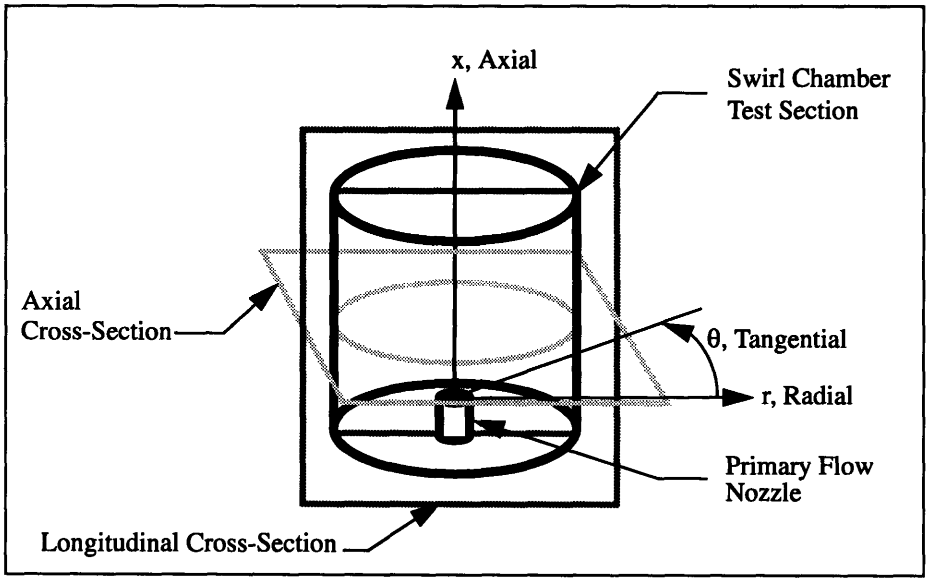

Figure 4.1: Definition of swirl chamber coordinate system.

4.1 Laser Doppler Velocimetry

The swirl chamber was run in closed circuit mode for all LDV experiments. Measurements were taken for three different swirl numbers. For each swirl number, the axial and tangential velocity profiles were obtained at different axial locations. Each profile consists of nine data points along the radial direction, at each axial location.

4.1.1 Calibration of the LDV System

The LDV system was calibrated in the following way. First, the flow meter, used to measure the velocity of the primary flow, was calibrated by measuring how long it took the primary flow pump to exhaust the primary flow reservoir. The time to exhaust 15 gallons of water was measured for primary flow velocities ranging from 1 to 10 gpm. The maximum error of the flow meter was 1.8%. The calibrated flow meter was then used to measure the velocity of the primary flow jet. LDV readings were taken in the potential core of the jet, where the velocity was accurately known. The average error in the LDV readings over a range from 0 to 9 m/s was found to be 6.4% as measured against the flow meter standard.

4.1.2 First Set of LDV Experiments

The first set of LDV experiments was run with two inch long vanes set at 73 degrees. There were 36 vanes evenly spaced every 10 degrees in the array. The flow was adjusted until the pressure drop across the orifice plate produced a pressure transducer reading of 11mV, which corresponded to an average axial velocity of 1.16 m/s. At an axial distance of 0.5 cm above the primary flow nozzle, the axial and tangential velocity profiles were recorded. Each profile consisted of nine data points at a radial distance of: 0.0, 0.3, 0.9, 1.6, 2.3, 3.0, 3.7, 4.3 and 5.0 cm. Both axial and tangential profiles were recorded for primary flow injection velocities of: 0.0, 2.7, 6.7 and 9.4 m/s. A total of 24 profiles were recorded at this axial position.

The same process was repeated at an axial distance of 5.6 and 10.7 cm.

4.1.3 Second Set of LDV Experiments

The second set of LDV experiments was run with four inch long vanes set at 63 degrees. There were 36 vanes evenly spaced every 10 degrees in the array. The flow was adjusted until the pressure drop across the orifice plate produced a pressure transducer reading of 30 mV, which corresponded to an average axial velocity of 2.39 m/s. At an axial distance of 0.25 cm above the primary flow nozzle, the axial and tangential velocity profiles were recorded. Each profile consisted of nine data points at a radial distance of: 0.0, 0.6, 1.2, 1.8, 2.5 3.1 3.7 4.4 and 5.0 cm. Both axial and tangential profiles were recorded for primary flow injection velocities of: 0.0, 2.7, 6.7 and 9.4 m/s. A total of 32 profiles were recorded at this axial position.

The same process was repeated at an axial distance of 1.95, 4.2 and 5.9 cm.

4.1.4 Third Set of LDV Experiments

The third set of LDV experiments was run with four inch long vanes set at 75 degrees. There were 18 vanes evenly spaced every 20 degrees in the array. The flow was adjusted until the pressure drop across the orifice plate produced a pressure transducer reading of 30 mV, which corresponded to an average axial velocity of 2.37 m/s. At an axial distance of 0.25 cm above the primary flow nozzle, the axial and tangential velocity profiles were recorded. Each profile consisted of nine data points at a radial distance of: 0.0, 0.6, 1.2, 1.8, 2.5 3.1 3.7 4.4 and 5.0 cm. Both axial and tangential profiles were recorded for primary flow injection velocities of: 0.0, 2.7, 6.7 and 9.4 m/s. A total of 32 profiles were recorded at this axial position.

The same process was repeated at an axial distance of 4.2, 7.6 and 30.0 cm.

4.2 Flow Visualization

Flow visualization pictures were taken for two swirl number, 0 and 0.82. The first set of flow visualization experiments was run with four inch long vanes set at 75 degrees. Fluorescein sodium salt was used to dye the primary flow. Cross-sections of the flow were created with an argon-ion laser. Once again, there were 18 vanes spaced 20 degrees apart. The average axial velocity was set at 2.37 m/s. Pictures of the axial cross-section of the flow were taken at 0.25, 4.2, 7.6 and 30.0 cm. At each axial position, pictures were taken for primary flow velocities of 2.7, 6.7 and 9.4 m/s. The process was repeated with the vanes set at zero degrees.

Pictures of a longitudinal cross-section were also taken with 18 four inch vanes set at 75 degrees. However, no quantifiable data was obtained with these pictures.

Once the pictures were developed they were digitized using a 300 dpi scanner. The area of the test section and the area of the interface between the primary and secondary flows was then measured using NIH Image V1.54, a share-ware image analysis package. To remain consistent in the measurement process a thresholding technique was used. Each picture was thresheld to distinguish the walls of the test section and the interface of the primary and secondary flows.

4.3 Particle Image Velocimetry

One set of PIV experiments were performed for a vane angle of 75 degrees with 18 vanes and an average axial velocity of 2.37 m/s. Vector fields were obtained at an axial positions of 0.25, 4.2 and 30.0 cm above the primary flow jet nozzle. At these axial position the primary flow was injected at 2.7, 6.7 and 9.4 m/s. The sheet of laser light was about 0.5 cm thick. Three pulses were taken with intervals of 0.4 and 0.5 ms between the pulses. The photographs were taken through the axial viewing port. Black and white, 3200 ASA film was used at an f-stop of 3.3. A 78 mm lens allowed for magnification of the cross-section. The pictures were developed at a local camera shop. Each picture was then digitized and analyzed by the auto-correlation program.

Chapter 5

Results

This chapter presents the data taken during the different experiments. Section 5.1 presents the one-dimensional velocity profiles taken with the LDV system. Section 5.2 presents the results of the flow visualization experiments. Finally, Section 5.3 displays the PIV photographs.

5.1 LDV Velocity Profiles

The profiles given in Figures 5.1 to 5.31 are the velocity profiles at different axial locations and for different swirl numbers within the swirl chamber. The time averaged velocity profiles, taken with the LDV system, are one-dimensional. Each data point is averaged over a period of about 1 to 2 minutes. The following symbols are used in the plots:

x is the axial position with the nozzle exit taken as x equal to 0,

r is the radial position with the axis taken as r equal to 0. The wall of the test section is located at an r of 5.08 cm,

u is the velocity in the axial direction,

v is the velocity in the tangential direction,

U_{avg} is the average velocity in the axial direction,

V_{avg} if the average velocity in the tangential direction,

U_j is the velocity of the primary flow at the nozzle exit,

D_j is the diameter of the primary flow nozzle (0.77 cm for all experiments),

S is the swirl number.

All variables are nondimensionalized to allow comparison of results between experiments. The axial and tangential velocities are nondimensionalized by the average axial and tangential velocities respectively. The velocity of the primary flow jet is nondimensionalized by the average axial velocity. All distances are nondimensionalized by the diameter of the primary flow nozzle.

5.1.1 Axial Velocity with a Swirl Number of 0.51

Figures 5.1 to 5.3 show axial velocity profiles for a swirl number of 0.51, Reynolds number of 118,000 and average axial velocity of 1.16 m/s. The profiles for different injection rates but similar axial positions are given on the same plot. Near the wall of the test section, r/D_j of 6.5, the axial profiles resemble fully developed flow in pipes. With no injection of the primary flow, deviation from the fully developed profile occurs at an r/D_j between 4.5 and 5.5. For smaller values of r/D_j, the velocity decreases as you get closer to the axis. However, when the primary flow is injected, the velocity increases close to the axis and the velocity decreases for r/D_j greater than 3.

The increase in the axial velocity close to the axis due to the primary flow is sometimes called the jet boundary layer.

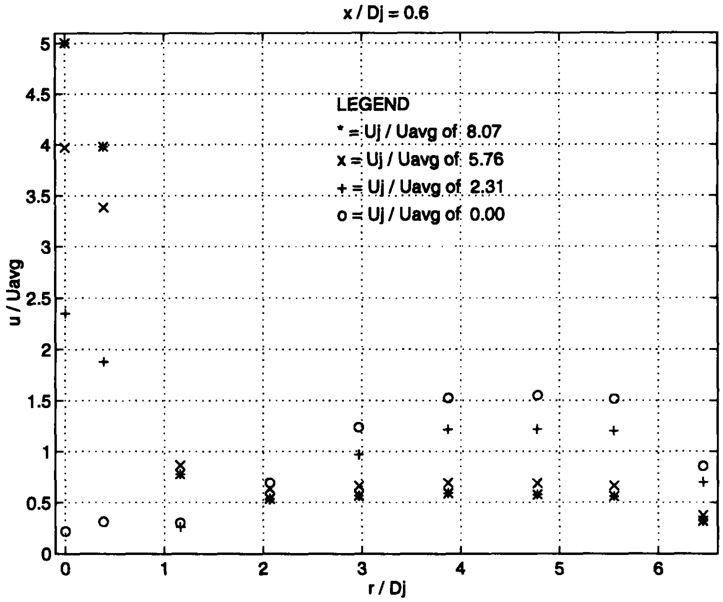

Figure 5.1: Axial velocity is plotted versus radial position for x / D_j = 0.6.

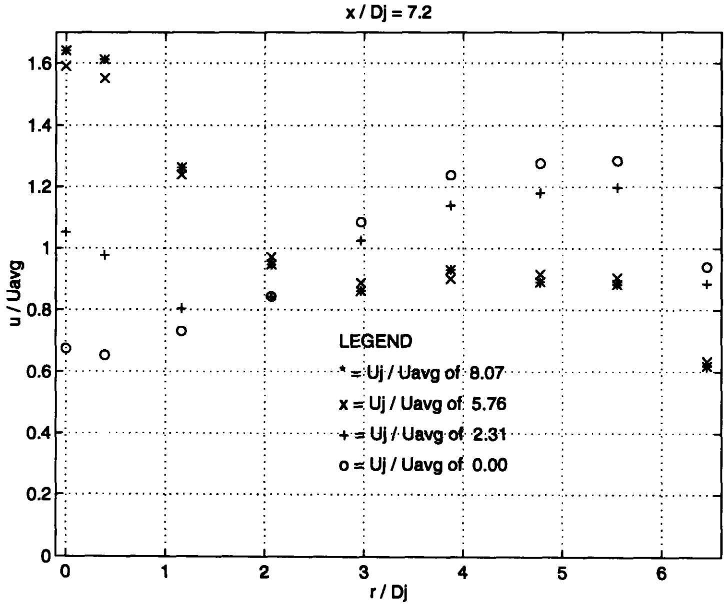

Figure 5.2: Axial velocity is plotted versus radial position for x / D_j = 7.2.

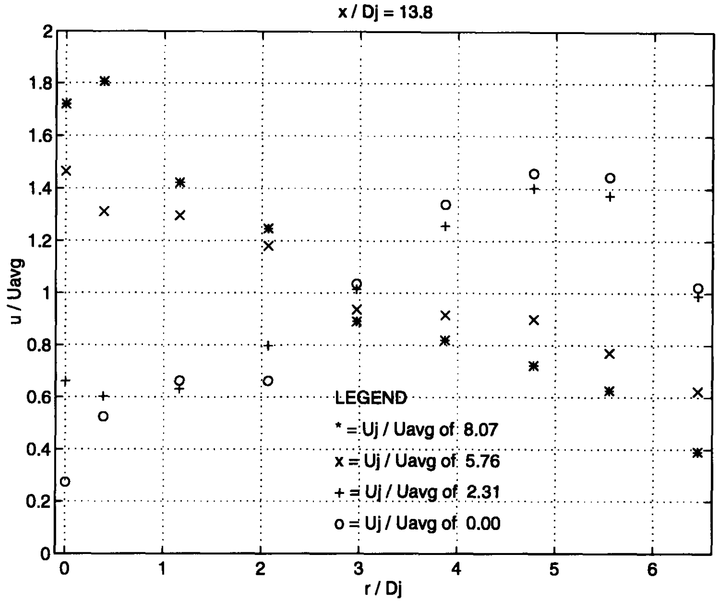

Figure 5.3: Axial velocity is plotted versus radial position for x / D_j = 13.8.

Lets look at Figures 5.1 to 5.3 a little closer. First, in Figure 5.1, the axial velocity increases for increasing injection rate. For a U_j/U_{avg} equal to 8.07 the axial velocity is greater than for a U_j/U_{avg} of 5.76, which is greater than for a U_j/U_{avg} of 2.31. Second, the growth of the jet boundary layer can be seen by comparing Figure 5.1 with 5.2. The jet boundary layer has spread in the radial direction at an x/D_j of 7.2. Also, the magnitude of the different velocity profiles still increases for increasing U_j/U_{avg}. Finally, the profiles in Figure 5.3 are similar to the profiles in Figure 5.2 except the boundary layer of the jet has grown slightly.

5.1.2 Axial Velocity with a Swirl Number of 0.59

Figures 5.4 to 5.7 show the axial velocity profiles for a swirl number of 0.59, Reynolds number of 242,000 and average axial velocity of 2.39 m/s. There are many things to note. First, all of the profiles share the same form. They are similar to fully developed flow in pipes until an r/D_j of about 5. The velocity then decreases as you move closer to the axis until the effect of the primary flow jet increases the velocity. Second, the higher the primary flow injection rate the higher the velocity near and on the axis. Third, as the axial distance is increased, the boundary layer of the jet grows in the radial direction. Fourth, the shape of the profiles are very similar outside of the jet boundary layer. Note that the only difference in the profiles outside of the jet boundary layer is that for higher primary flow injection, the magnitude of the axial velocity decreases. Finally, the velocity at the axis decreases for increasing axial distances.

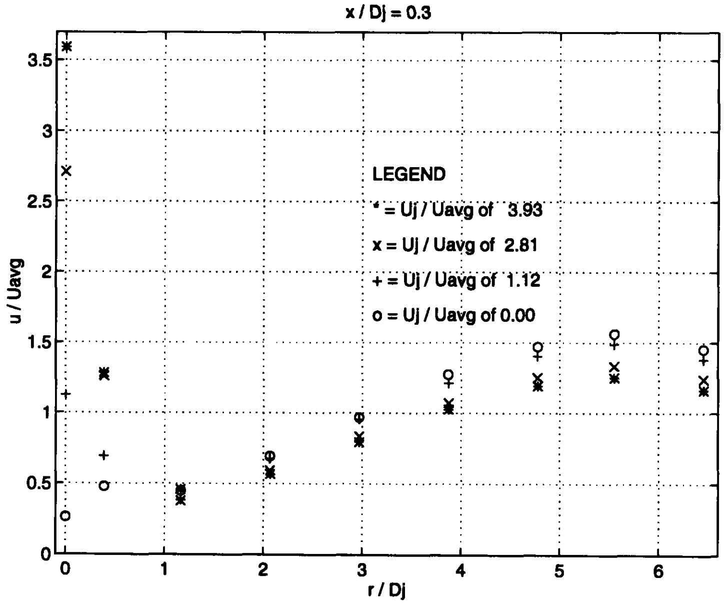

Figure 5.4: Axial velocity is plotted versus radial position for $x / D_j = 0.3$.

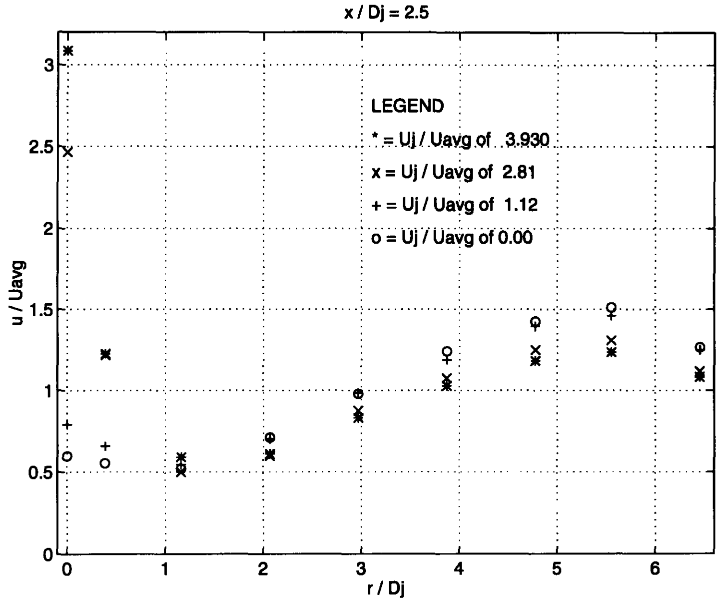

Figure 5.5: Axial velocity is plotted versus radial position for x / D_j = 2.5.

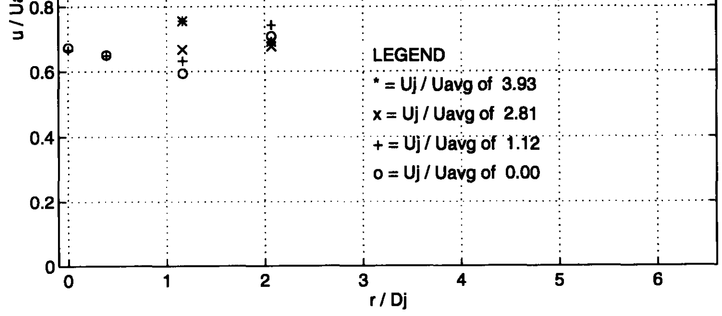

Figure 5.6: Axial velocity is plotted versus radial position for x / D_j = 5.4.

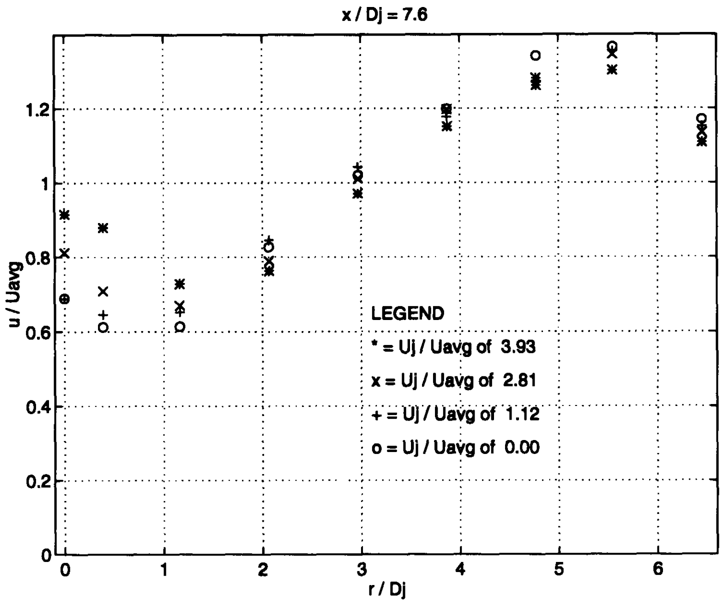

Figure 5.7: Axial velocity is plotted versus radial position for x / D_j = 7.6.

5.1.3 Axial Velocity with a Swirl Number of 0.82

Figures 5.8 to 5.11 present the axial velocity profiles for a swirl number of 0.82, Reynolds number of 241,000 and average axial velocity of 2.37. Once again, the profiles for different injection rates but similar axial positions are given on the same plot. These plots show similar trends to the previous profiles. First, the profiles are similar to fully developed flow in pipes until an r/Dj of about 5. The velocity then decreases until the effect of the primary flow injection increases the axial velocity close to the axis. Second, the jet boundary layer grows in the radial direction as the axial distance increases. Third, outside of the jet boundary layer, the shape of the profiles are similar. The only difference in the profiles is the axial velocity decreases as the primary flow injection rate increases. Finally, the velocity close to the axis, with no injection, increases as the axial distance increases.

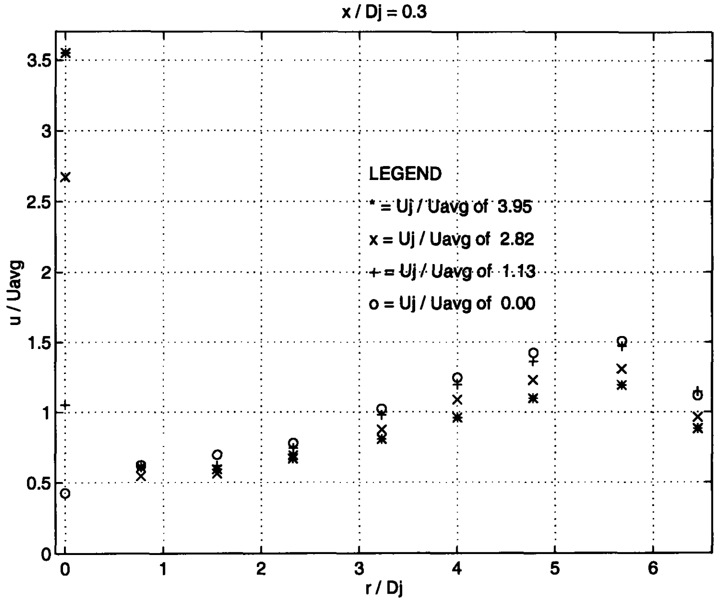

Figure 5.8: Axial velocity is plotted versus radial position for x / D_j = 0.3.

In Figure 5.9, note that the velocity close to the axis is greatest when U_j/U_{avg} is equal to 2.82. This is the only time that a lower primary flow injection rate produces a higher axial velocity than a higher primary flow injection rate.

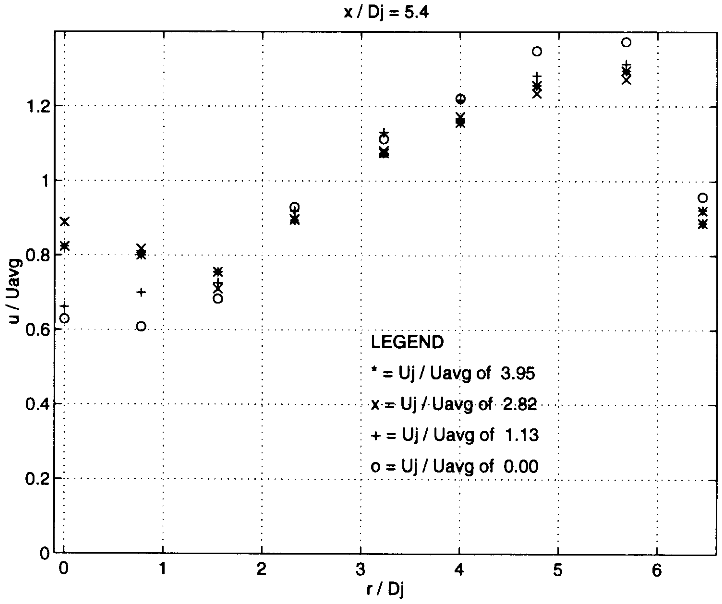

Figure 5.9: Axial velocity is plotted versus radial position for x / D_j = 5.4.

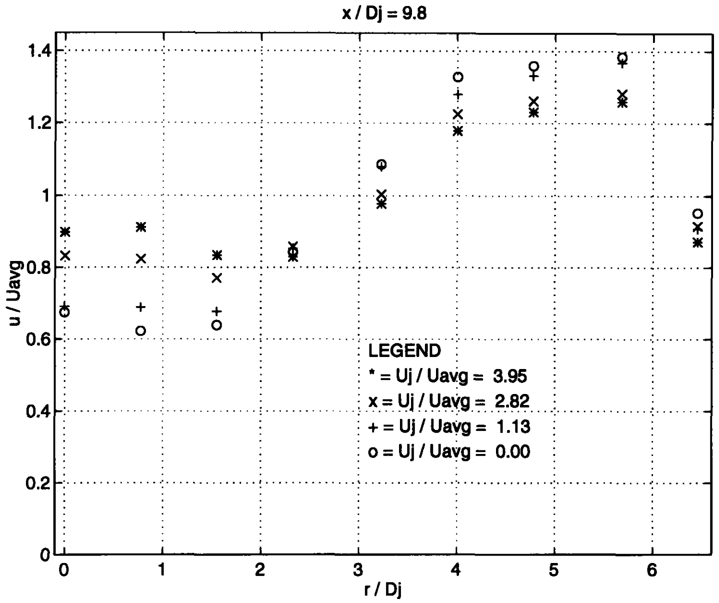

Figure 5.10: Axial velocity is plotted versus radial position for x / D_j = 9.8.

In Figure 5.11, note that the velocity close to the axis is highest when the primary flow is not injected. This is the only time this occurred. It is also the only time a velocity profile is taken so far downstream.

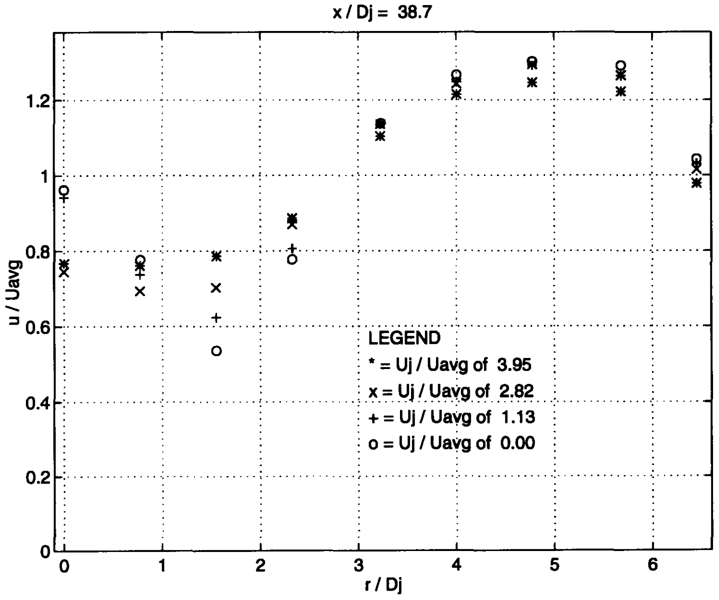

Figure 5.11: Axial velocity is plotted versus radial position for x / D_j = 38.7.

5.1.4 Tangential Velocity with a Swirl Number of 0.51

The tangential velocity profiles for a swirl number of 0.51, Reynolds number of 118,000, average axial velocity of 1.16 m/s and average tangential velocity of 0.88 m/s, are given in Figures 5.12 to 5.14. Each figure shows the profiles for different injection rates but the same axial distance. The profiles have the same shape as a Rankine's vortex. In Figures 5.12 and 5.13, the core of the Rankine's vortex, when U_j/U_{avg} is 2.31 or less, extends to an r/D_j of about 2. When U_j/U_{avg} is 5.76 or greater, the core of the Rankine's vortex extends to a r/D_j of about 1. This is the only time that a difference in injection rate produced a shrinking of the vortex core.

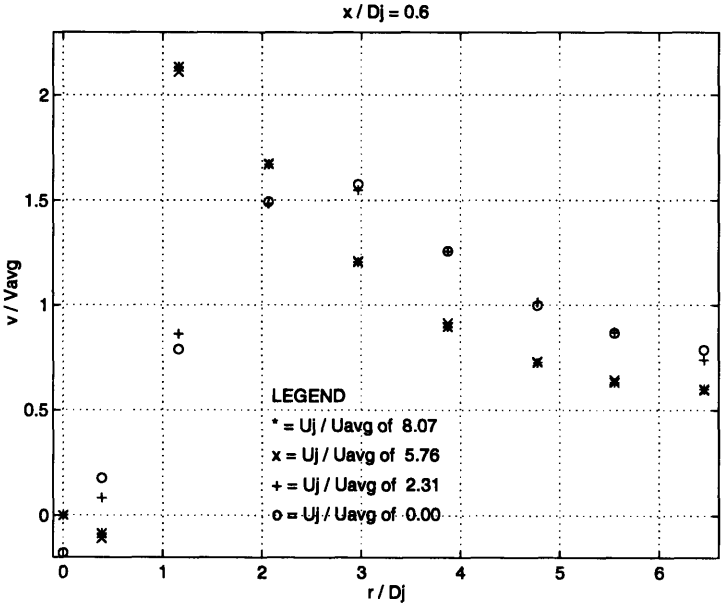

Figure 5.12: Tangential velocity is plotted versus radial position for $x / D_j = 0.6$.

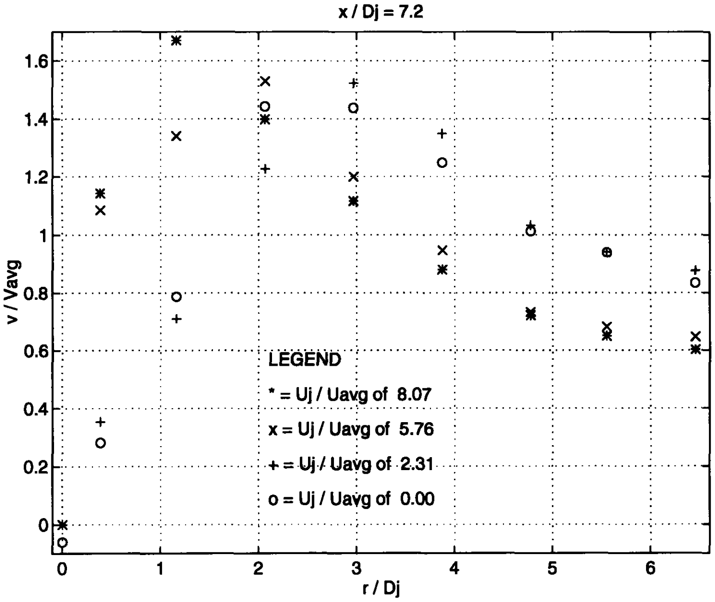

Figure 5.13: Tangential velocity is plotted versus radial position for x / D_j = 7.2.

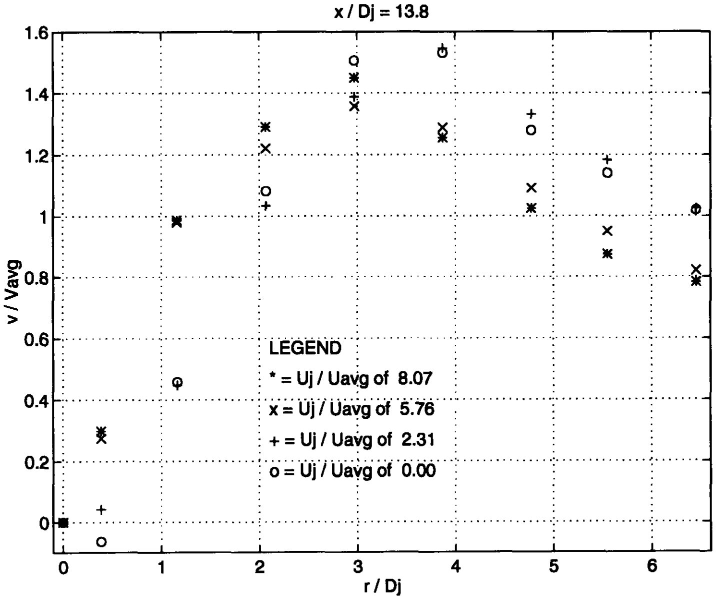

Figure 5.14: Tangential velocity is plotted versus radial position for x / D_j = 13.8.

5.1.5 Tangerntial Velocity with a Swirl Number of 0.59

The tangential velocity profiles for a swirl number of 0.59, Reynolds number of 242,000, average axial velocity of 2.39 m/s and average tangential velocity of 2.20, are presented in Figures 5.15 to 5.18. The core of the Rankine's vortex is around 2.5 nozzle diameters for all tangential velocity profiles except Figure 5.18, where the core radius is around 3 nozzle diameters. The only other thing to notice in these plots is that each profile is similar in shape and magnitude no matter what injection rate or axial position.

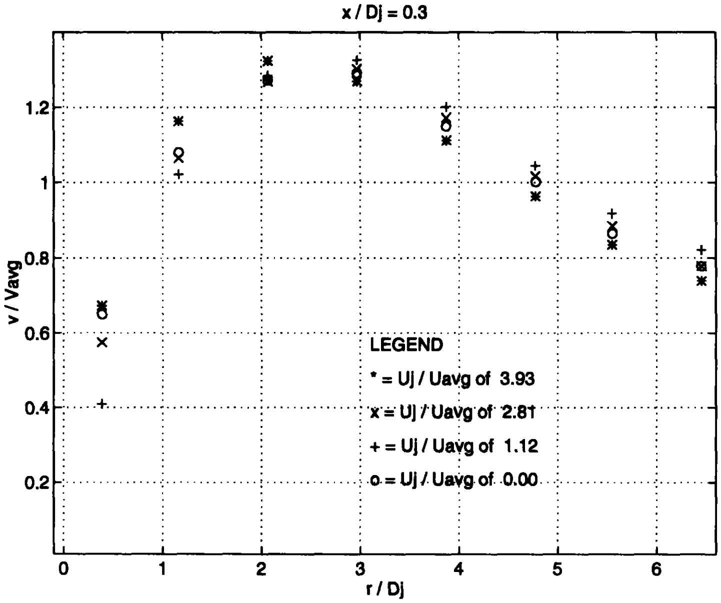

Figure 5.15: Tangential velocity is plotted versus radial position for x / D_j = 0.3.

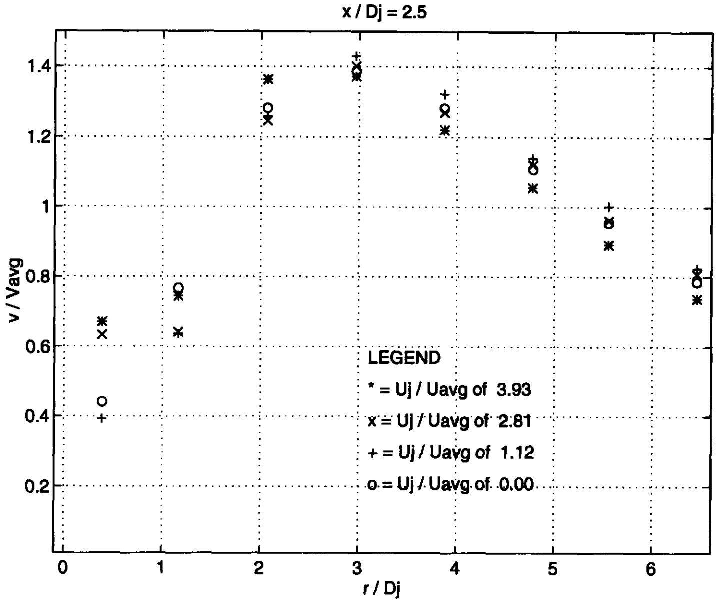

Figure 5.16: Tangential velocity is plotted versus radial position for x / D_j = 2.5.

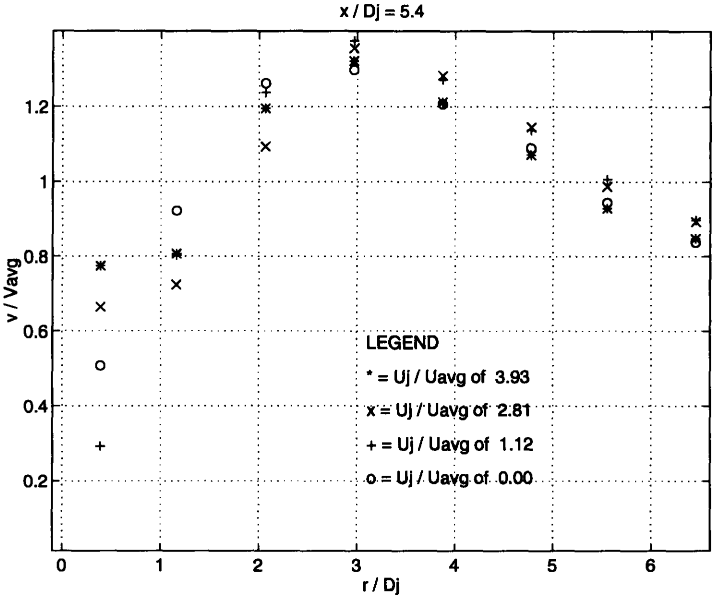

Figure 5.17: Tangential velocity is plotted versus radial position for x / D_j = 5.4.

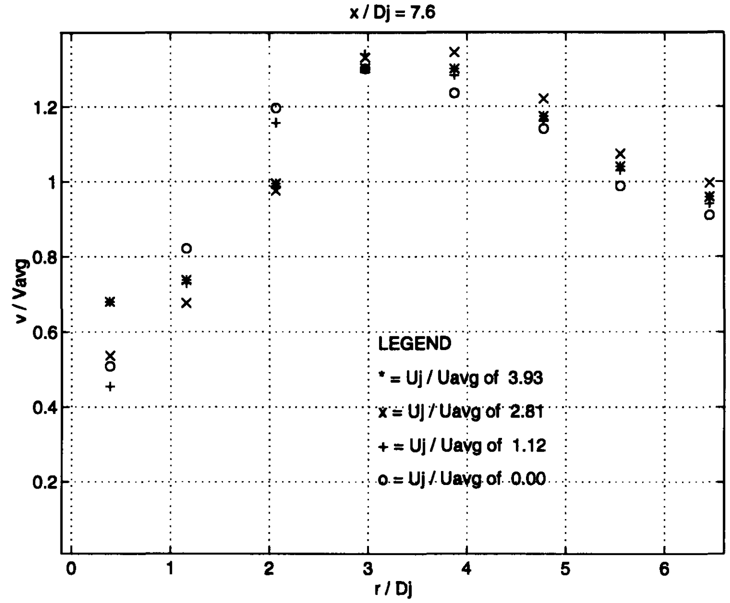

Figure 5.18: Tangential velocity is plotted versus radial position for x / D_j = 7.6.

5.1.6 Tangential Velocity with a Swirl Number of 0.82

Finally, Figures 5.19 through 5.20 present the tangential velocity profiles for a swirl number of 0.89, Reynolds number of 241,000, average axial velocity of 2.37 m/s and average tangential velocity of 2.68 m/s. As in the tangential velocity profiles for a swirl number of 0.59, each profile is very similar in shape and magnitude. In every plot the vortex core has a radius of around 2.5 nozzle diameters. In Figure 5.20 the datapoints taken at a r/Dj of 6.5 seem to wander from the Rankine's vortex velocity profile. This data set is most likely in the boundary layer of the test section walls.

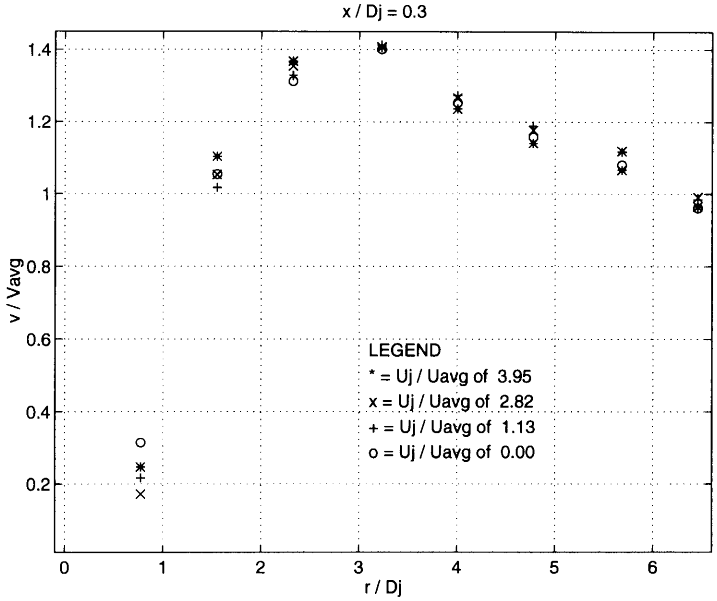

Figure 5.19: Tangential velocity is plotted versus radial position for x / D_j = 0.3.

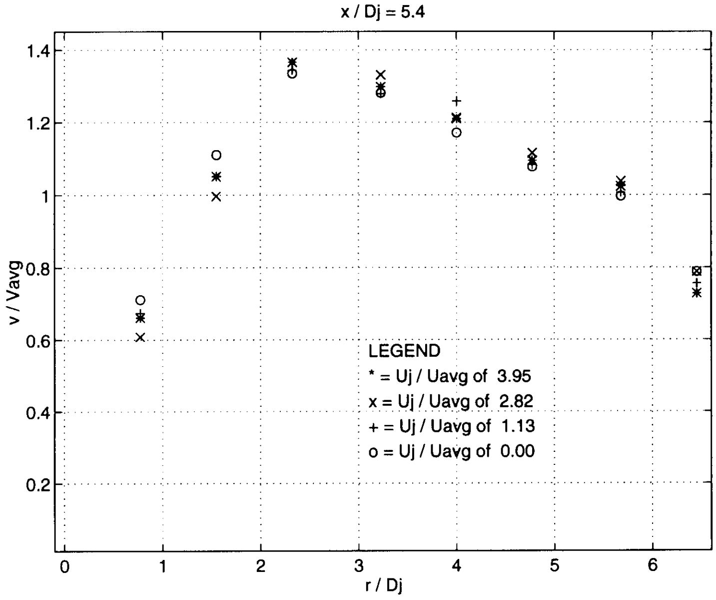

Figure 5.20: Tangential velocity is plotted versus radial position for x / D_j = 5.4.

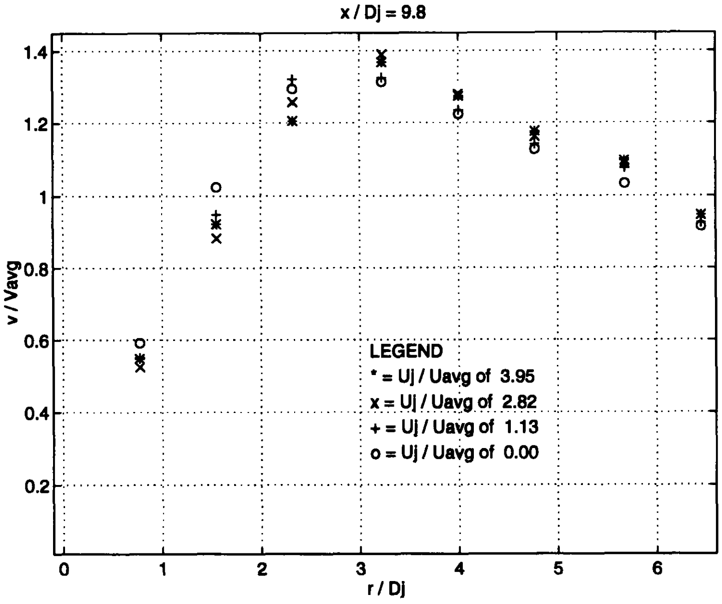

Figure 5.21: Tangential velocity is plotted versus radial position for x / D_j = 9.8.

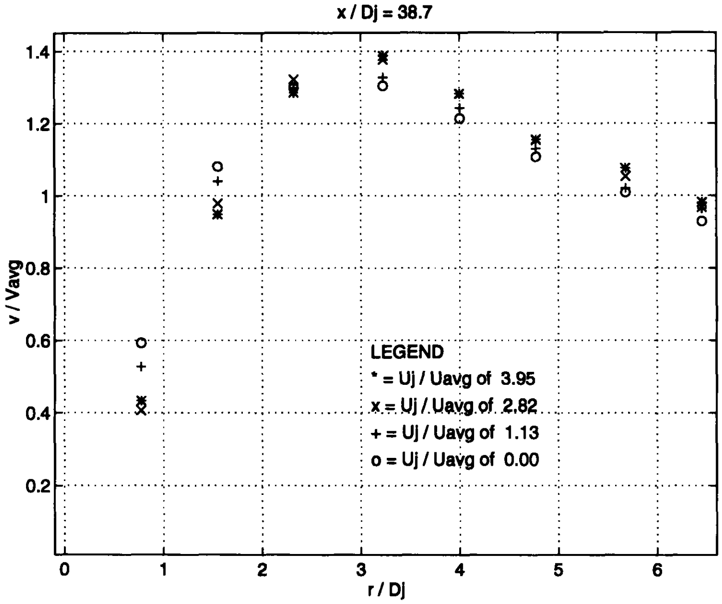

Figure 5.22: Tangential velocity is plotted versus radial position for x / D_j = 38.7.

5.1.7 Axial Velocity for all Swirl Numbers

In Figures 5.23 to 5.30, some of the axial and tangential velocity profiles are plotted again. However, this time profiles for different swirl numbers are plotted on the same graph.

In Figure 5.23, the axial velocity begins to decrease at an r/D_j of 4, when the swirl number is 0.51. However, for larger swirl numbers, the decrease in velocity begins at an r/D_j of 5.5.

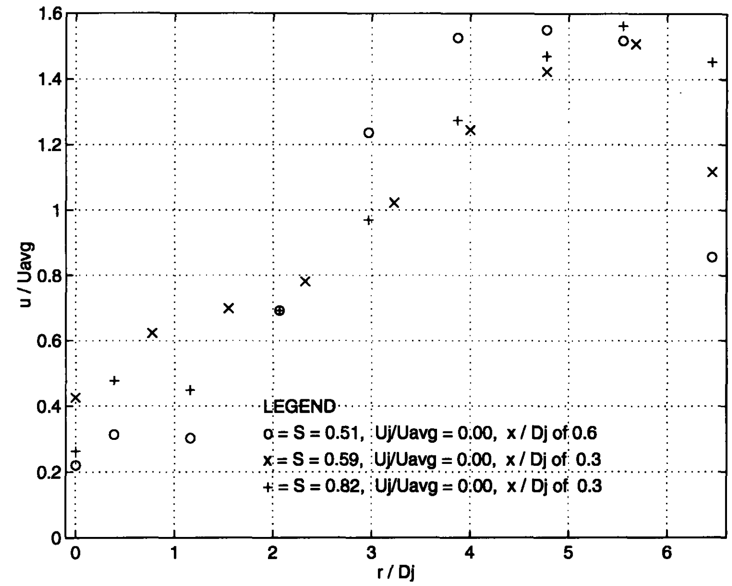

Figure 5.23: Axial velocity is plotted versus radial position for different swirl numbers.

Figure 5.25 demonstrates that when the primary flow is injected along the axis of the secondary flow, the axial profiles close to the nozzle do not seem to change for different swirl numbers. The velocity at the axis increases due to the injection of the primary flow, the velocity at larger radii decreases.

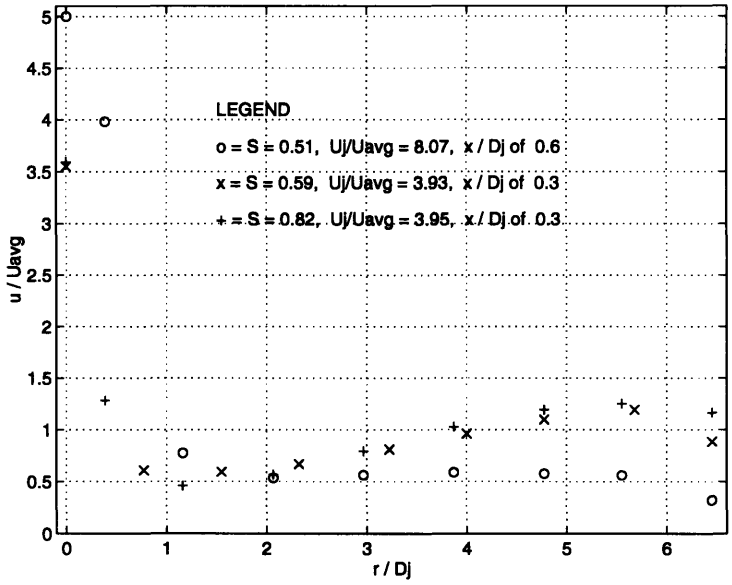

Figure 5.24: Axial velocity is plotted versus radial position for different swirl numbers.

Further downstream the velocity profiles are similar despite the change in swirl number. This can be seen in Figure 5.25. With no injection, the axial velocity profiles only diverge from similarity at the axis. The velocity at the axis increases with larger swirl numbers.

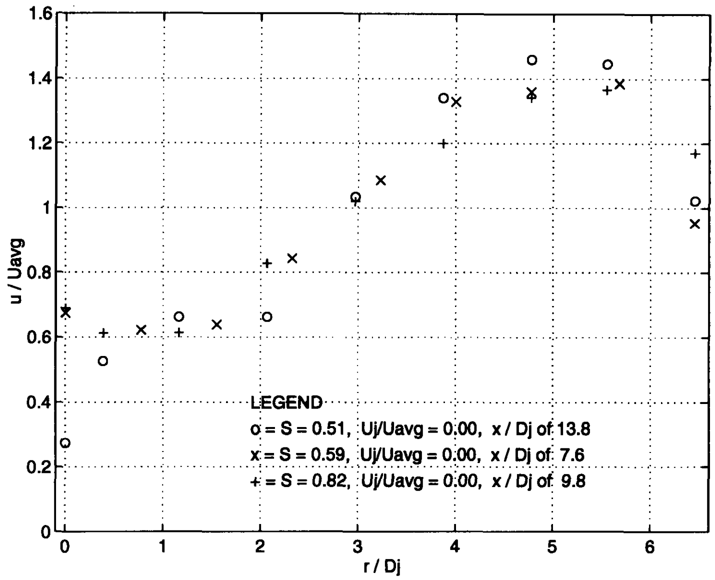

Figure 5.25: Axial velocity is plotted versus radial position for different swirl numbers.

The trends in the axial velocity profiles in Figure 5.26 are the same as those in Figure 5.25. The profiles are similar for a swirl number of 0.59 and 0.81, and the profile for a swirl number of 0.51 is influenced by the large injection rate.

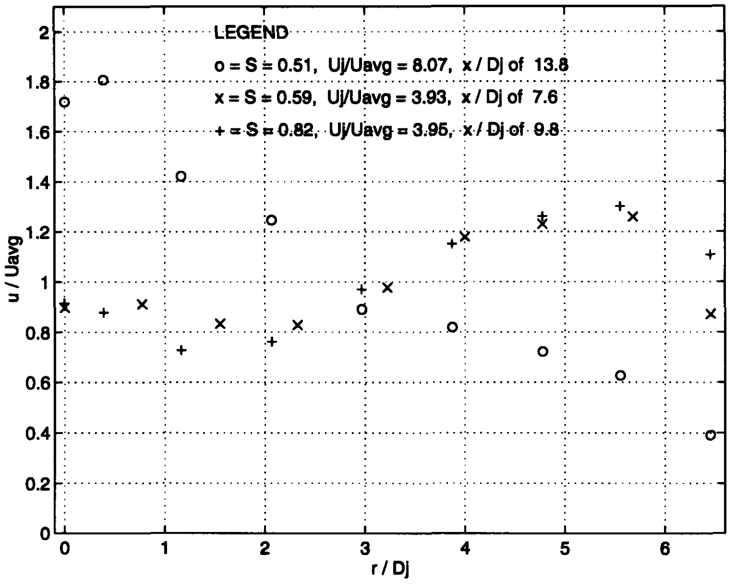

Figure 5.26: Axial velocity is plotted versus radial position for different swirl numbers.

5.1.8 Tangential Velocity for all Swirl Numbers

The tangential velocity profiles for different swirl numbers are plotted in Figures 5.27 to 5.30. However, plotting the data in this form does not show anything different than the previous plots of the tangential velocity profiles. The profiles do not change in shape or magnitude despite changes in swirl number, axial position and primary flow injection rate.

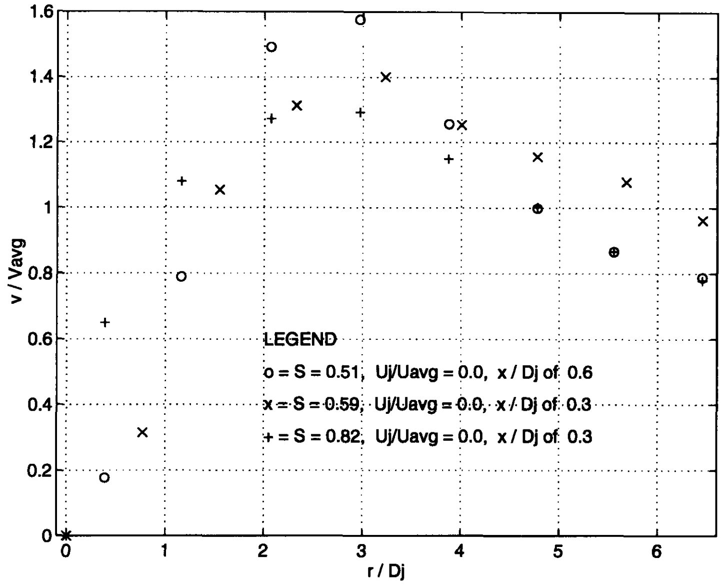

Figure 5.27: Tangential velocity is plotted versus radial position for different swirl numbers.

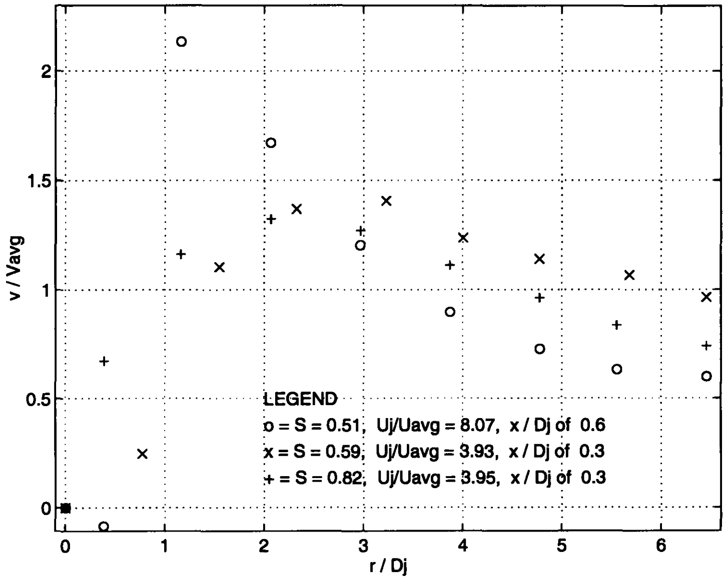

Figure 5.28: Tangential velocity is plotted versus radial position for different swirl numbers.

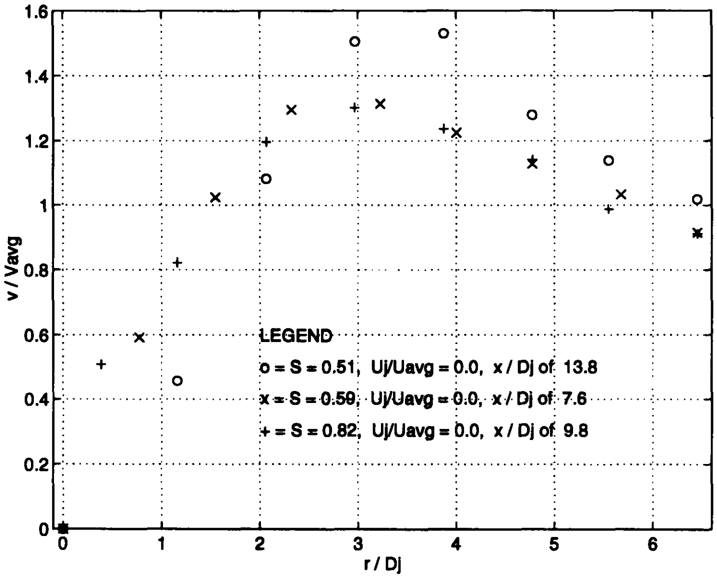

Figure 5.29: Tangential velocity is plotted versus radial position for different swirl numbers.

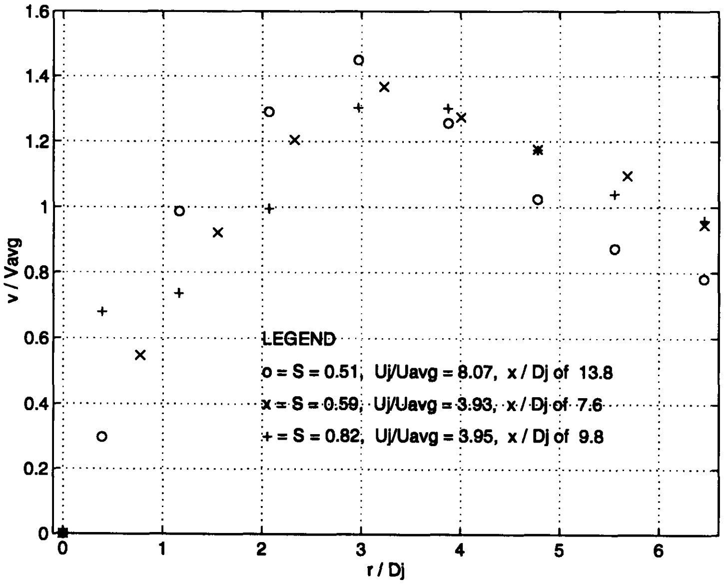

Figure 5.30: Tangential velocity is plotted versus radial position for different swirl numbers.

5.1.9 Axial Velocity Profile with No Swirl

The last of the one-dimensional velocity profiles is plotted in Figure 5.31. The axial velocity is plotted for no primary flow injection and no swirl. Different axial positions are represented with different symbols. The profiles increase from the wall of the swirl chamber and then level off between an r/D_j from 4 to 1. The axial velocity then decreases slightly at the axis.

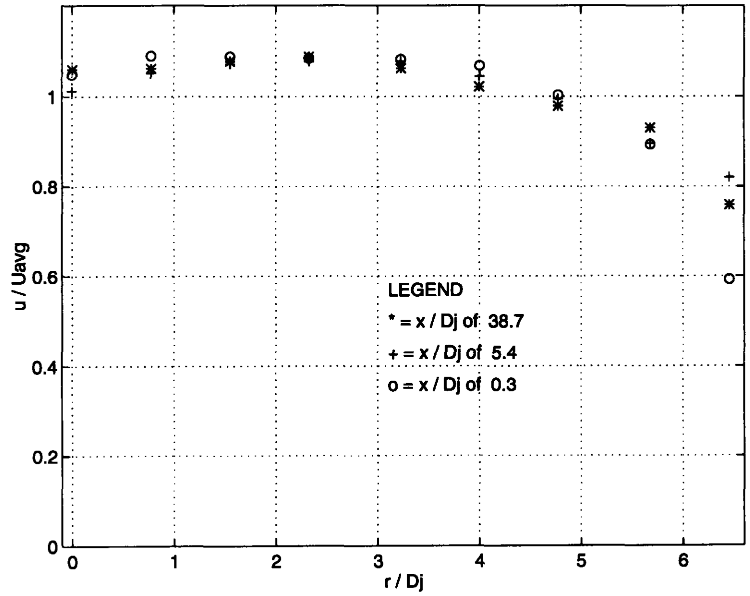

Figure 5.31: Axial velocity is plotted versus radial position for a swirl number of 0.0. Note that the profile is similar to fully developed, turbulent flow in pipes.

5.2 Flow Visualization Data

5.2.1 Quantifying the Rate of Mixing

The growth of the primary flow jet boundary layer can be seen in Figure 5.32. The radius of the jet boundary layer is shown at different axial positions. Both the radius, r, and the axial positions, x, are nondimensionalized by the diameter of the primary flow jet nozzle, D_j.

When the secondary flow is not swirled, the radius of the jet boundary layer is equal for an x/D_j of 0.3, 5.4 and 9.8. Also, by examining Figure 5.32, it can be seen that the growth of the jet boundary layer, when there is no swirl, can be fitted with a straight line. With a U_j/U_{avg} of 3.67, the equation of the line is $x/D_j = 21.7r/D_j - 11.6$. The average error for this curve fit is 13%.

As seen in the figure below, with a swirl number of 0.82, the jet boundary layer grows quickly close to the nozzle exit. After about 10 nozzle diameters downstream, the growth rate of the jet boundary layer decreases dramatically. Finally, and most importantly, the radius of the jet boundary layer with swirl is larger, at every axial position, than the radius of the jet boundary layer without swirl.

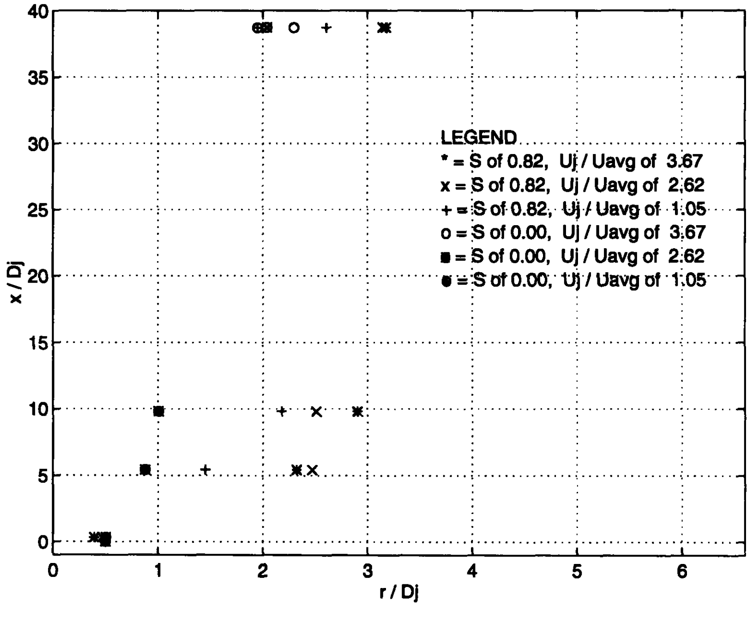

Figure 5.32: Radius of the primary flow jet is plotted versus axial position. All variables are nondimensionalized. The swirl number is 0.0 and 0.82, the Reynolds number is 241,000, the average axial velocity is 2.37 m/s and the diameter of the primary flow nozzle is 0.77 cm

5.2.2 Longitudinal Cross-sections

The following pictures, Figures 5.33 to 5.35, are longitudinal cross-sections of the flow. The swirl number is 0.82, the average axial velocity is 2.37 m/s and the Reynolds number is 241,000. The walls of the test section can be seen at the sides of each photograph. The primary flow nozzle can be seen in the bottom-middle of each photograph. The primary flow jet has been died with fluorescein sodium salt and appears yellow.

In Figure 5.33, U_j/U_{avg} equals 1.13, in Figure 5.34, U_j/U_{avg} equals 2.82 and in Figure 5.35, U_j/U_{avg} equals 3.95. These pictures were taken to get a visual representation of the flow. Only qualitative information can be obtained with these pictures. By examining the three pictures, it can be seen that increasing the primary flow injection rate increases the intensity of the fluoresced jet. The radius of the jet boundary layer does not change dramatically as the injection rate increases. Another observation is that the boundary layer grows very quickly close to the nozzle, in each picture. After about 5 diameters downstream of the nozzle the growth rate decreases dramatically.

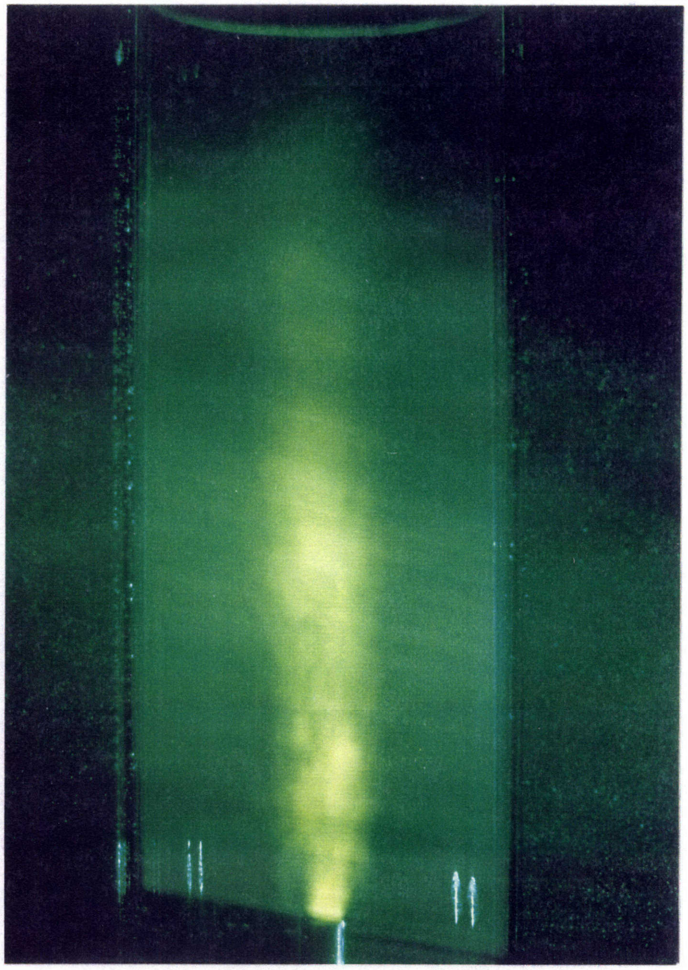

Figure 5.33: Longitudinal cross-section of the primary and secondary flows. The primary flow has been died with fluorescein sodium salt. U_j/U_{avg} is 1.13, the swirl number is 0.82, the average axial velocity is 2.37 m/s and the Reynolds number is 241,000.

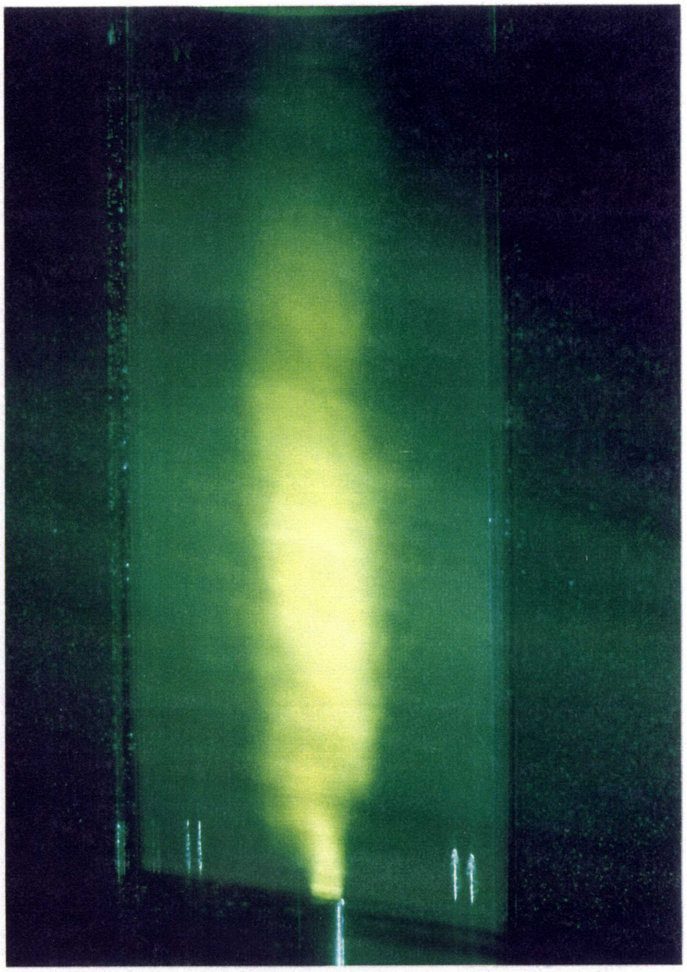

Figure 5.34: Longitudinal cross-section of the primary and secondary flows. The primary flow has been died with fluorescein sodium salt. U_j/U_{avg} is 2.82, the swirl number is 0.82, the average axial velocity is 2.37 m/s and the Reynolds number is 241,000.

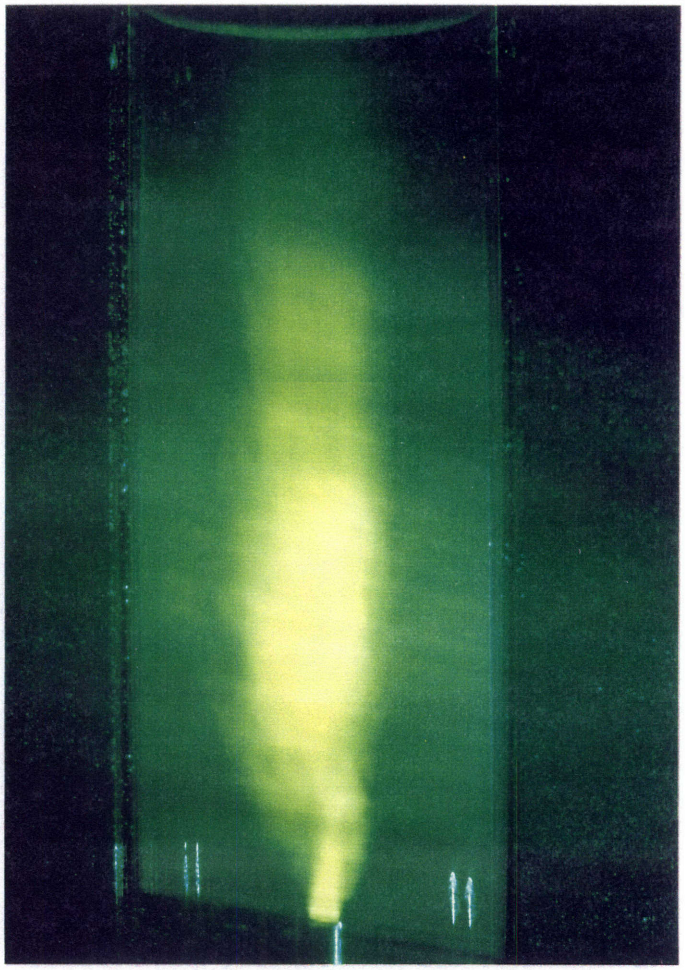

Figure 5.35: Longitudinal cross-section of the primary and secondary flows. The primary flow has been died with fluorescein sodium salt. U_j/U_{avg} is 3.95, the swirl number is 0.82, the average axial velocity is 2.37 m/s and the Reynolds number is 241,000.

5.2.3 Axial Cross-sections

Figures 5.36 to 5.39 are pictures of axial cross-sections at different axial positions and different injection rates. In every picture, U_j/U_{avg} is equal to 3.95. Once again, the swirl number is 0.82, the average velocity is 2.39 m/s and the Reynolds number is 241,000. The walls of the swirl chamber can be seen as the a solid dark green circle in each picture. The primary flow has been dyed with fluorescein sodium salt and appears yellow. These pictures are used to obtain some of the data in Figure 5.32. Therefore, refer to Figure 5.32 for the size of the jet boundary layer radius.

There are a couple of things to note in these figures. First, the absolute size of the test section in each photograph is different. This is because each axial cross-section is at a different distance from the camera. Nonetheless, the test section diameter remains constant, at 4 inches, and can be used as a scale in each photograph. Second, in Figure5.36, there is a yellow arm that extends from the primary flow. The arm extends in the counterclockwise direction. Third, the primary flow in Figures 5.37 and 5.38 seems cloudy. Finally, another arm can be seen extending from the primary flow in Figure 5.39. However, this time the arm extends in the clockwise direction.

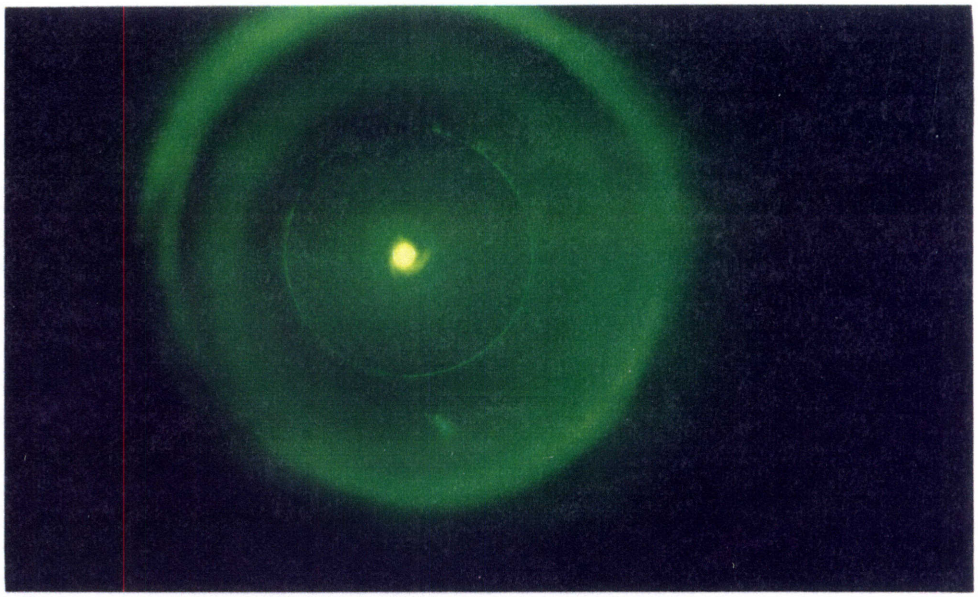

Figure 5.36: Axial cross-section of the primary and secondary flows. The primary flow has been died with fluorescein sodium salt. x/D_j is equal to 0.3, U_j/U_{avg} is 3.95, the swirl number is 0.82, the average axial velocity is 2.37 m/s and the Reynolds number is 241,000.

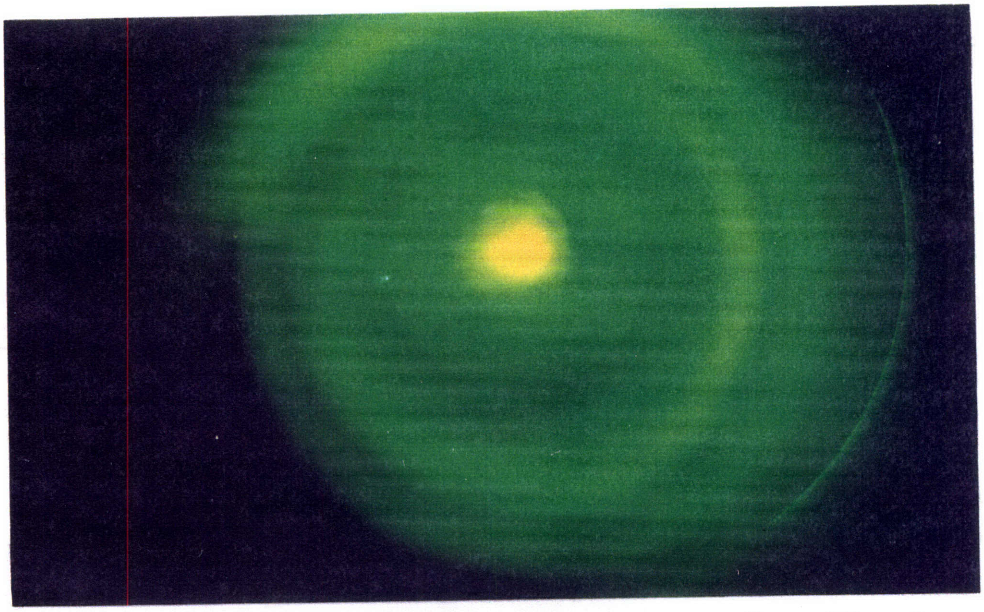

Figure 5.37: Axial cross-section of the primary and secondary flows. The primary flow has been died with fluorescein sodium salt. x/D_j is equal to 5.4, U_j/U_{avg} is 3.95, the swirl number is 0.82, the average axial velocity is 2.37 m/s and the Reynolds number is 241,000.

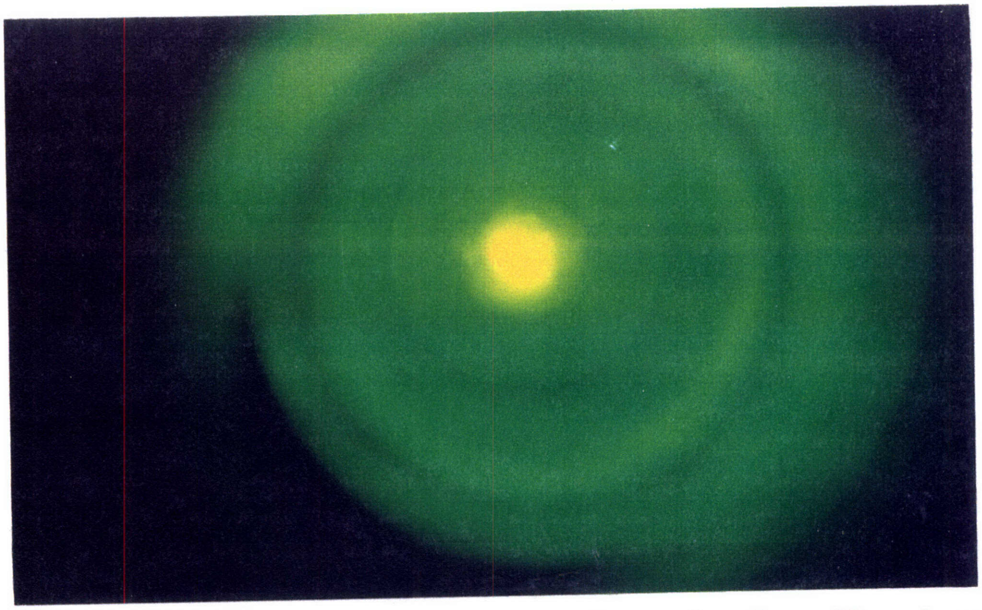

Figure 5.38: Axial cross-section of the primary and secondary flows. The primary flow has been died with fluorescein sodium salt. x/D_j is equal to 9.8, U_j/U_{avg} is 3.95, the swirl number is 0.82, the average axial velocity is 2.37 m/s and the Reynolds number is 241,000.

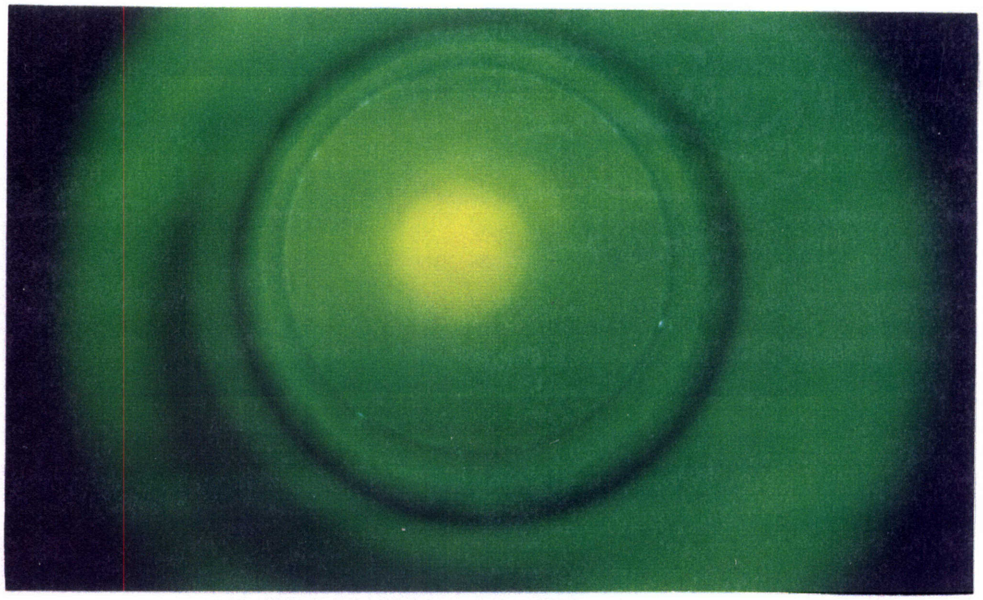

Figure 5.39: Axial cross-section of the primary and secondary flows. The primary flow has been died with fluorescein sodium salt. x/D_j is equal to 38.7, U_j/U_{avg} is 3.95, the swirl number is 0.82, the average axial velocity is 2.37 m/s and the Reynolds number is 241,000.

5.3 Particle Image Velocimetry Pictures

Figures 5.40 shows a PIV picture. The Nd:YAG laser has been double pulsed in this picture. The time between laser pulses is 0.5 ms. From the LDV measurements, it is know that the swirl number is 0.82, V_{avg} is 2.68 m/s, the Reynolds number is 241,000 and U_j/U_{avg} is 3.95.

Only the bottom left corner of the picture is used for analysis because of memory problems with the computer that runs the analysis program. Note that the distance between particle pairs is greatest at an r/D_j of about 2 to 3. Also, the distance between particles is smaller close to the wall and near the axis.

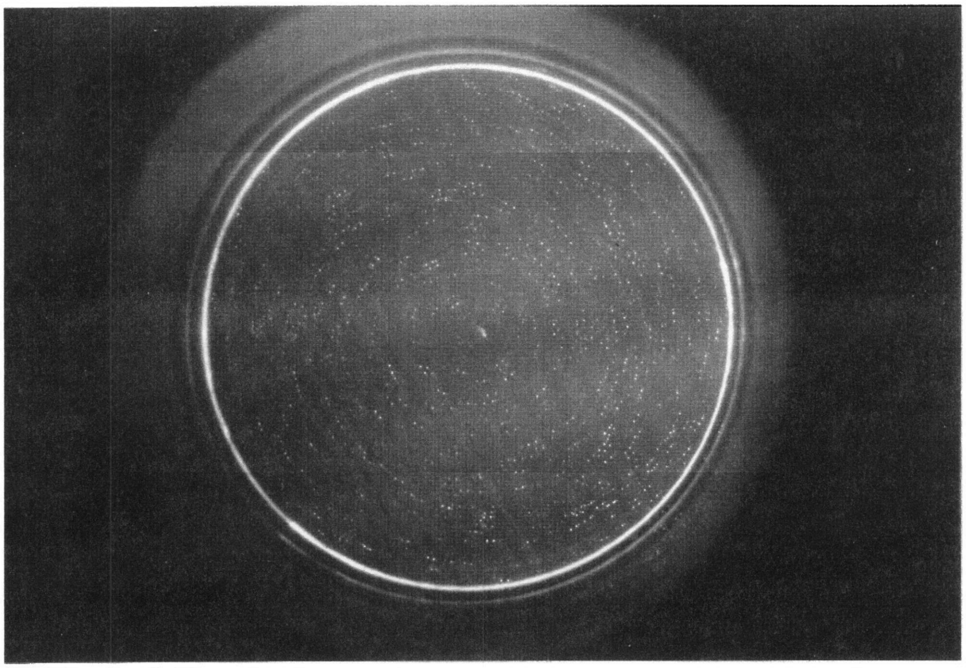

Figure 5.40: PIV picture of an axial cross-section at an x/D_j of 38.7.

The two-dimensional velocity profile obtained from Figure 5.40 is given in Figure 5.41. The axis of the test section is located in the upper left hand corner of the plot. The wall of the test section begins at an (X, Y) position of (0, 150). It then curves with the arrows until an (X, Y) position of (600, 750). The stray velocity vectors are due to an incorrect correlation between different particles. The empty space located at (200, 500) is caused by a dark spot on the photograph. Notice that the flow is rotating in the counter clockwise direction. This is consistent with the flow visualization results. The average tangential velocity vector measured from this two-dimensional profile is 2.7 m/s.

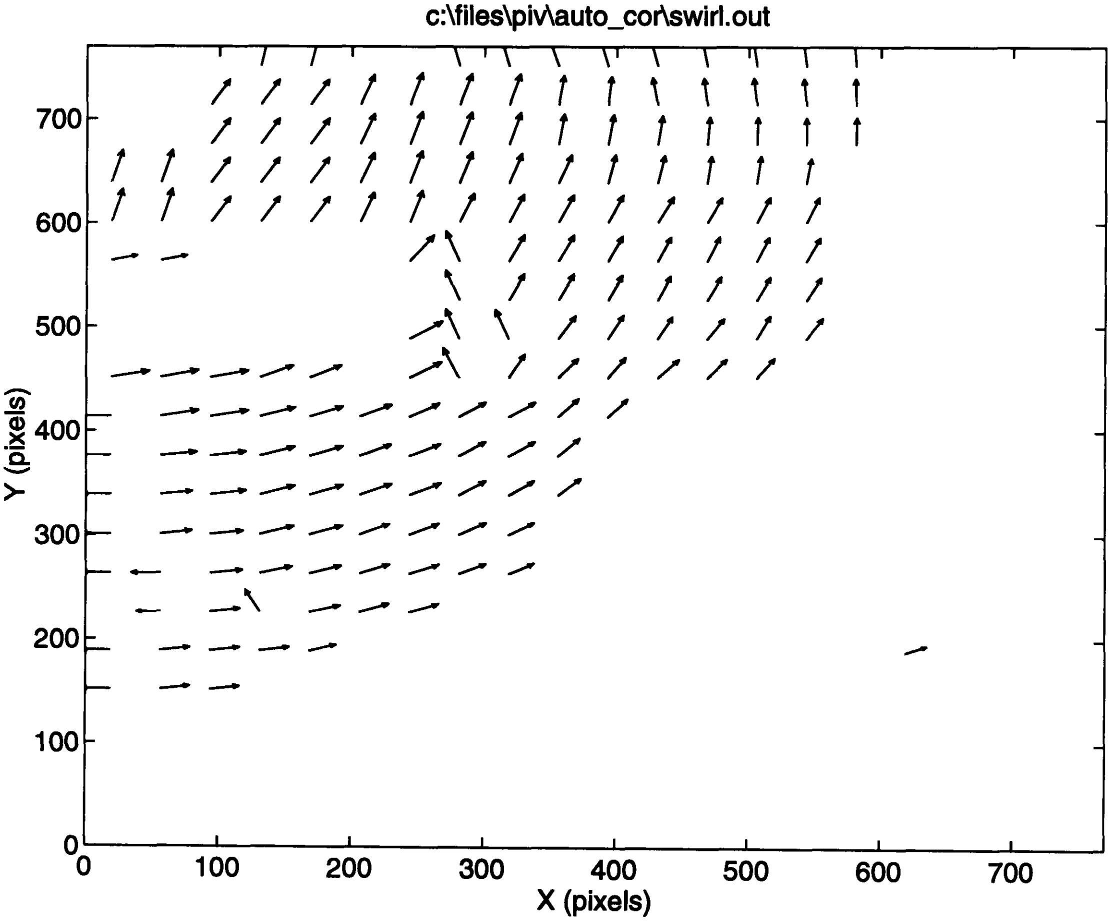

Figure 5.41: Two-dimensional axial velocity field of one quarter of the test section.

Chapter 6

Discussion

This chapter presents the findings of the research. Section 6.1 discusses the trends in the one-dimensional velocity profiles for different boundary conditions. Section 6.2 studies the results of the flow visualization pictures and discusses the mixing of the primary and secondary flows. Section 6.3 discusses the results of the PIV data.

6.1 One-Dimensional Velocity Profiles

This section presents the trends found in the one-dimensional velocity profiles as the swirl number, primary flow injection rate and axial position are varied. However, before the trends are shown in Section 6.1.2, the validity of the one-dimensional profiles is discussed and the data is compared to profiles obtained by previous researchers in a similar swirl chamber. After the trends have been discussed in Section 6.1.2, some unexpected findings in the velocity profiles are described in Section 6.1.3.

6.1.1 Validation of the One-dimensional Velocity Profiles

To check the validity of the LDV measurements, the conservation of mass is applied to the flow for each velocity profile. First, the secondary volume flow rate is calculated using the axial velocity profiles with no injection. The volume flow rate from the primary flow pump is then added to the secondary volume flow rate, thus giving the total volume flow rate. The average velocity of the combined flows is then calculated and compared to the measured average velocity. For a swirl number of 0.81, when the average velocity measured by the LDV system is compared to the average velocity calculated above, the average error for all axial positions and injection rates is 4.9%. For a swirl number of 0.59 the average error is 6.0%. For a swirl number of 0.51 the average error is 26.9%.

The large error for a swirl number of 0.51 may be due to the error in the numerical calculation of the average velocity from the axial velocity profiles. The trapezoidal rule is used to integrate the profiles and obtain the average velocity. However, because of the large primary flow injection rates, a denser velocity sampling may be needed. This large error also occurs for all swirl numbers close to the nozzle, where the effect of the primary flow injection dominates the flow and large velocity gradients are present.

If the large errors close to the nozzle are omitted from the averages, the average error in the comparison of the measured average velocity to the theoretical average velocity is: 2.8% for a swirl number of 0.81, 4.3% for a swirl number of 0.59 and 19.5% for a swirl number of 0.51. Therefore, the LDV data seems to obey the conservation of mass. The large errors in the comparison encountered close to the nozzle, and for large primary flow injection rates must be due to numerical integration.

Li and Tomita [15] performed an experiment on the degradation of swirl in a circular pipe.They used air as the working fluid in a vane type swirl chamber. They found the tangential velocity profile to be a Rankine's vortex, and the axial velocity profile to dip at the

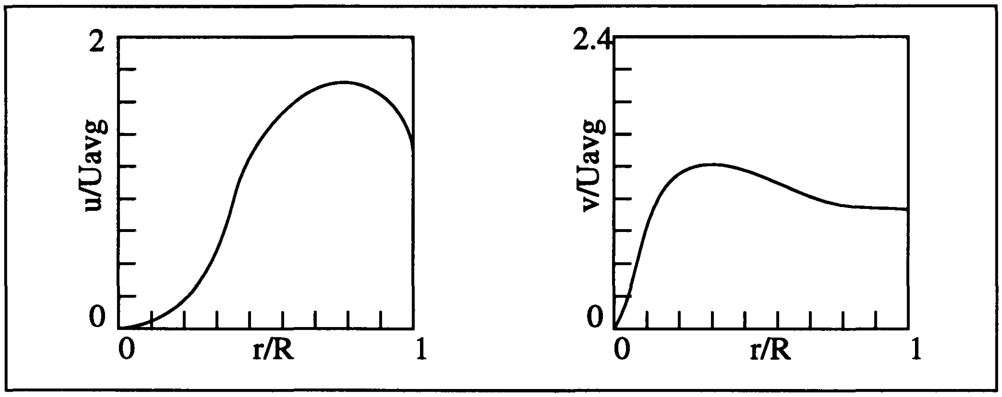

Figure 6.1: Sketches of axial and tangential velocity profiles reported by Li and Tomita [15]. The profiles are taken from a circular pipe with air as the working fluid. The swirl number is 0.58 and the Reynolds number is 125,000.

axis. The general shapes are sketched in Figure 6.1. These profiles are of the same shape as the profiles recorded in the MIT swirl chamber. The similarity in profiles is a good check for the validity of the LDV data.

One interesting difference in the above experiment is that Li and Tomita reported recirculation at a swirl number of 0.67. Recirculation has not occurred in the MIT swirl chamber, even at a swirl number of 0.82, which is above the critical swirl number of 0.6. Many researchers have pointed out that different swirl chambers produce different flow fields. The lack of recirculation in the swirl chamber at this super critical swirl number could be due to many mechanisms. First, the 90 degree turn the swirling flow encounters after the vane array could cause "secondary flows" that disrupt the formation of the recirculation zone. Second, recirculation may not have occurred because of the large acceleration the flow experiences after swirl has been imparted by the vanes. Finally, it may be that recirculation does not occur because water is used as the working fluid. If this is part of the reason, then compressibility effects could be important to the formation of the recirculation zone. The limited data obtained thus far is not enough to make valid assumptions about compressibility effects. More experiments should be run to look into the possibility that compressibility may be an important mechanism in the formation of the recirculation zone.

Finally, to validate that the flow in the test section is fully developed, axial velocity profiles are measured in the test section with a swirl number of 0.0. The results are presented in Figure 5.31. The axial velocity profile at every axial location is similar to fully developed flow in pipes. The profiles grow from zero velocity at the wall, then flatten off beyond the boundary layer due to the wall. The slight dip in the profile at the axis could be caused by the boundary layer due to the mandrel and the primary flow nozzle. One positive note is that the profiles in Figure 5.31 are similar at all axial locations, so any difference in the profiles with swirl are due to the swirl or injection, not the test section itself.

6.1.2 Flow Trends

The axial profiles, without injection, are similar to fully developed flow in pipes, except that the velocity decreases at an r/Dj of about 4 to 5. This form was common to every axial velocity profile. The decrease in velocity may be due to the negative pressure gradient that is set up along the axis because of the swirling flow. The dip in the profiles is not present when the axial velocity profiles were recorded with no swirl in the secondary flow, see Figure 5.31.

When the primary flow is injected, while the swirl number and axial distance remain constant, the axial velocity profile wanders from the shape of the profile with no injection, revealing two trends, see Figures 5.1 to 5.11. First, close to the axis, the velocity increases. The higher the primary flow injection rate, the higher the velocity close to the axis. Second, the velocity outside of the jet boundary layer decreases. However, this time, the higher the injection rate, the lower the velocity. The trend of the velocity increasing close to the axis and decreasing far away from the axis is a result of the conservation of mass. If the velocity close to the axis increases due to the primary flow injection, the velocity must decrease somewhere else, to conserve mass.

As the axial distance is increased, while the swirl number and primary flow injection rate remain constant, several trends can be seen in Figures 5.1 to 5.11. First, the jet boundary layer grows in the radial direction. The growth is a result of the shear forces exerted on the secondary flow by the primary flow. Second, the velocity at the axis decreases. The conservation of mass dictates that if the axial velocity increases in the radial direction due to the boundary layer growth, the velocity at the axis must decrease. Finally, the velocity outside of the boundary layer increases. This increase may also be a result of the conservation of mass and the decrease in velocity at the axis.

As the swirl number is increased, while the primary flow injection rate and axial distance remain constant, there seem to be no noticeable trends in the data, see Figures 5.23 to 5.30. This could be due to the small increase in swirl number between the three experiments. The swirl number only ranged from 0.51 to 0.82. The range of the swirl number may have to be larger to reveal any trends in the axial velocity profiles.

Let us now look at the trends in the tangential velocity profiles, Figures 5.12 to 5.22. The tangential velocity profiles, with and without injection, can be accurately modelled as a Rankine's vortex. This comes as no surprise because the Rankine's vortex is common to vane type swirlers. The first trend to note is that the tangential velocity profile never wandered from the Rankine's vortex model, despite changes in the swirl number, primary flow injection rate and axial position.

Second, the tangential velocity profiles are not affected by changes in the swirl number, or changes in the axial location. The similarity in the profiles for different axial locations may be explained by the fact that the distance between axial datapoints is less than the characteristic distance of decay for swirling flow in pipes. In other words, the distance travelled by the swirling flow in the axial direction may not be great enough for viscous losses to be observed. Li and Tomita [15] reported the characteristic length to be between 60 to 100 diameters.

Third, for the most part, a change in the primary flow injection rate does not affect the tangential velocity profiles. The explanation as to why the tangential velocity profiles do not change for different injection rates is not clear. Only four profiles, which will be discussed in the next paragraph seem to be affected by the primary flow injection rate.

A closer look at the tangential velocity profiles in Figures 5.12 and 5.13 reveals that the core of the Rankine's vortex shrinks in size for high injection rates. This shrinking of the core could be due to the large values of U_j/U_{avg}. You see, for the profiles with a core radius of around 2.5 nozzle diameters, the maximum injection rate corresponds to a U_j/U_{avg} of 3.93. Vanyo [18] wrote that the size of the core is affected by axial injection. However, there may be a critical injection rate that must be exceeded before the core will be affected. From the data, this critical value could be a U_j/U_{avg} between 3.93 and 5.76.

Why a critical injection rate needs to be exceeded before a change in the core size is noticed is not obvious. It could be due to the "secondary flows" in the test section. Shear forces from the primary flow entrain the secondary flow. This causes a radial flux of the secondary flow. As the secondary flow moves in radially, angular momentum must be conserved, so its angular velocity increases. It could be that the shear forces must be large to notice a change in the overall tangential velocity profile. Therefore, it may be that higher injection rates, $U_j/U_{avg} > 3.5$, produce a strong enough radial flow to observe a change in the tangential velocity profile.

6.1.3 Two Unexpected Results in the One-dimensional Velocity Profiles

For a swirl number of 0.82, a x/D_j of 5.4 and a U_j/U_{avg} of 2.82, the axial velocity close to the axis is greater than when U_j/U_{avg} is 3.95, see Figure 5.9. Several LDV runs were performed to validate these data points. This switching of the velocities seems counterintuitive. This is the only time that a slower injection rate produces a higher velocity than a faster injection rate. This could be a result of the interaction of the axial and tangential vorticity components defined in Section 2.1.3. There appears to be a sinusoidal oscillation of the velocity profiles at the axis. This should be studied in greater detail to make valid conclusions as to the cause of the oscillation. This oscillation could be a mechanism that affects the mixing of the primary and secondary flows. It could also be related to the oscillation of the mass transfer types discussed in Section 6.2.3.

By studying the axial velocity profiles in Chapter 5, it can be seen that the axial velocity at the axis of the swirl chamber, when there is no injection, increases for increasing x/D_j, if the swirl number is greater than 0.51. As a matter of fact, far downstream of the nozzle, Figure 5.11, the velocity at the axis is greatest when there is no injection. In other words, injection only slows down the flow at the axis far downstream. This increase in velocity at the axis can be explained with the aid of Bernoullis equation. This analyses was first performed by Batchelor in 1964 [20]. If a streamline is taken from before the test section to the core of the vortex, the pressure decreases. Therefore, using Bernoullis equation, the velocity must increase at the axis of the vortex core. Also, the stronger the swirl, the lower the pressure at the core, from equation 2.9. This decrease in pressure for higher swirl numbers causes the velocity along the axis to increase as seen in Figures 5.4 to 5.11. However, in Figure 5.11, the pressure at the axis could be increased by the injection of the primary flow, this would cause the axial velocity to decrease at the axis far downstream of the nozzle, which causes the axial velocity to be greatest when there is no injection.

6.2 Flow Visualization

The axial flow visualization pictures presented in Section 5.2 are used to quantify the rate of mixing of the primary and secondary flows. The rate of mixing can be quantified by measuring the growth of the primary flow jet boundary layer. The rate of mixing is discussed in Section 6.2.1. Additionally, two unexpected trends in the flow visualization pictures are discussed in Sections 6.2.2 and 6.2.3.

6.2.1 Rate of Mixing

The rate of mixing was quantified by measuring the growth of the primary flow jet boundary layer. The growth of the jet boundary layer is plotted in Figure 5.32. The plot shows that without swirl, the boundary layer grows linearly, as theory predicts [21]. The average error in a linear curve fit is 13%. This error could be due to the fact that a ruler was used to measure the area of the jet boundary layer, because the pictures with no swirl were to dark to digitize. With swirl, the boundary layer grows very quickly immediately after the nozzle. The growth rate then decreases sharply after an x/D_j of 10.

The most interesting result of the mixing rate measurements is that the two fluids mix faster when the secondary flow is swirled. The opposite occurs in burning, compressible experiments. The reason swirl increases the mixing is still unknown. It could be that the absolute velocity vector in the swirling flow is greater than the absolute velocity vector in the flow with no swirl, even though the average axial velocities are equal. The increase in the total velocity may increase the turbulent mixing in the swirling flow. In a compressible flow, the increase in turbulent mixing due to the increased velocity vector may be suppressed by the stratifying effects of the radial density gradient.

The increase in primary flow injection rate does affect the growth rate of the interface of the two fluids, when the secondary flow is swirled. The greater the injection rate, the faster the interface growth, particularly close to the nozzle exit. A change in the primary flow injection rate does not affect the mixing rate, when the secondary flow is not swirled.

6.2.2 Mass Transfer Transition

Close to the nozzle exit, less than one diameter downstream, the primary flow jet has no tangential velocity component, which creates large tangential velocity gradients between the primary and secondary flows. These velocity gradients may cause convection to be the primary mass transfer mechanism. This is observed in Figure 5.36, the yellow arm being torn off the jet reveals that the primary flow is being convected into the secondary flow. However, 5 to 10 diameters downstream of the nozzle, in Figure 5.37 and 5.38, the dyed jet seems cloudy, as if the primary flow is diffusing into the secondary flow. Finally, at 30 diameters downstream, in Figure 5.39, the yellow arm is being torn off the primary flow jet once again, signifying a transition back to convection.

This transition from convection to diffusion and back to convection is unexpected. The interaction of the axial and tangential vorticity components could once again be the cause. Close to the nozzle, the axial vorticity component seems to be large creating velocity gradients which cause the primary flow to be convected into the secondary flow. Further downstream the energy from the axial vorticity component could be transferred to the tangential vorticity component, reducing the velocity gradients and causing a transition to diffusion. The transition back to convection far downstream shows that the process may be sinusoidal. This switch in the strength of the vorticity components is similar to the oscillation of a pendulum and the conversion of potential energy to kinetic. Once again, this phenomena needs to be studied thoroughly before any solid conclusions can be made.

6.2.3 Reversal of Arms

The primary flow that is convected into the secondary flow, in Figure 5.36, forms an arm, visually similar to a sun flare, in a counter clockwise direction. Far downstream, in Figure 5.39, another arm is seen. However, this time the arm is convected in a clockwise direction. Once again, this switch in the direction of the arm is unexpected. It may be explained in the following way. Close to the nozzle, the radius of the primary flow jet boundary layer is 0.5 nozzle diameters. The boundary layer is well within the vortex core, which means the tangential velocity gradient is positive. In other words, the secondary flow has a larger tangential velocity component. Because the secondary flow is swirling in the counter clockwise direction, it may be tearing off part of the slower primary flow in the counter clockwise direction, creating the arm. Far downstream, the radius of the boundary layer is 3 nozzle diameters. The boundary layer has grown beyond the core of the vortex into the inviscid region, where the velocity decays as 1/r. The velocity gradient is now negative, so the primary flow has a larger tangential velocity component. The secondary flow may slow down the primary flow, creating an arm that lags behind the primary flow in the clockwise direction.

6.3 Particle Image Velocimetry

The particle image velocimetry systems works successfully. The results are given in Figure 5.41. The two-dimensional velocity field shows the instantaneous velocity distribution in one-quarter of the test section. The velocity vectors correctly track the swirling flow. By examining the magnitude of the vectors it can be seen that the velocity is a maximum at an r/D_j of about 2 to 3. The average tangential velocity measured from the picture is 2.7 m/s. This corresponds well with the LDV measurements.

Chapter 7

Conclusions

7.1 Accomplishments

As stated in Chapter 1, the goal of the thesis is to obtain a better understanding of the fundamental physics of the swirl mixing process within combustion chambers and how it differs from non-swirling processes. A swirl chamber is designed and constructed to simulate coaxial combustors. Using water as the working fluid, the swirl chamber is dynamically scaled to a wide range of combustion chambers. The swirl number can be adjusted from 0 to 1, the Reynolds number from 15,000 to 300,000 and the primary to secondary momentum flux ratio from 0 to 60. By using an incompressible fluid to simulate the primary and secondary flows, the determination of mixing rates is greatly simplified while still allowing accurate velocity measurements.

7.1.1 One-dimensional Velocity Profiles

One-dimensional, time averaged axial and tangential velocity profiles are measured during the mixing process using a laser Doppler velocimetry system. This data is used to investigate the changes in the velocity profiles for different swirl numbers, S, and primary flow injection rates, U_j, thus providing insight into the mechanisms which govern these complex flows. The swirl number is varied from 0 to 0.82, the non-dimensionalized primary flow injection rate varies from 0 to 8 and the non-dimensionalized axial distance varies from 0 to 30. All variables are nondimensionalized by the average axial velocity, U_{avg} and the primary flow nozzle diameter, D_j. The following phenomenon are observed in the LDV velocity profiles.

Close to the walls of the test section, the axial velocity profiles are similar to fully developed flow in pipes. The wall boundary layer extends about 0.5 to 1 nozzle diameters into the flow. At about 1 to 2 nozzle diameters from the wall, the axial velocity begins to decrease radially inward. It continues to decrease until the effect of the primary flow jet increases the axial velocity close to the axis. This decrease in the axial velocity appears to be a direct result of the radial pressure gradient present in the vortex core. The lowest pressure in a vortex occurs at the axis, the pressure then increases radially outward. The higher pressures produce a larger driving force, which may result in a higher velocity at larger radii. With the absence of swirl, the radial pressure gradient is not present. Therefore, the axial velocity profile should not decrease for radial distances less than 5 nozzle diameters from the nozzle exit. The measured axial velocity profile with no swirl demonstrates this.

Close to the axis, the axial velocity with injection is greater than the axial velocity without injection. Also, the axial velocity with injection is less than the axial velocity without injection for radial positions outside the primary flow jet boundary layer. This increase and decrease of the axial velocity may be a direct consequence of the conservation of mass.

By comparing the axial velocity profiles at different downstream positions, it is found that the measured primary flow jet boundary layer expands in the radial direction as the axial distance increases. The LDV measurements show that the radial growth is not linear with axial distance. The boundary layer grows quickly close to the nozzle, after about 10 nozzle diameters downstream the growth rate decreases sharply. The fast growth rate close to the nozzle may be due to the large shear layer set up because of the large radial velocity gradient near the nozzle. The shear layer creates a tangential vorticity component, which may contribute to the increase in boundary layer growth. Further downstream, where the mixing rate decreases, the radial velocity gradient decreases, which may be the cause of this decrease in mixing.

When the axial velocity profiles with no injection are compared at different axial positions, for a swirl number greater than 0.51, the axial velocity at the axis can be seen to increase with greater downstream distances. Batchelor [20] observed and explained a similar occurrence in his study of vortices shed from the end of aircraft wings. The same analysis may apply here. If a streamline is taken from before the entrance of the test section to the core of the vortex, the pressure decreases. Therefore, using Bernoullis equation, the velocity must increase along the axis of the vortex core. Also, the stronger the swirl, the lower the pressure at the core. This decrease in pressure for higher swirl numbers may further cause the velocity along the axis to increase.

Under all conditions, the tangential velocity profiles share the form of a Rankine's vortex, with a core of approximately 2 to 3 nozzle diameters in radius. The shape and magnitude of the tangential velocity profiles does not change despite variations in the swirl number, axial position and primary flow injection rate. Only four tangential velocity profiles had a core with a radius of 1 nozzle diameter. These four profiles may be influenced by the large shear layer caused by the high primary flow injection rate. The non-dimensionalized primary flow injection rate is over two times higher for these profiles, than for the profiles with a core of 2 to 3 nozzle diameters. The large shear layer between the primary and secondary flows may cause a large radial influx of the secondary flow; and, because the secondary flow is rotating, the conservation of angular momentum requires the tangential velocity of the secondary flow to increase as it moves in radially. This causes the vortex core to shrink. However, the reason the core only shrinks for profiles with high injection rates may be the result of an injection rate threshold which must be exceeded before the shear layer becomes strong enough for the tangential velocity profiles to be effected.

7.1.2 Rate of Mixing of the Primary and Secondary Flows

Measurements of the mixing of the primary and secondary flows are made for different swirl numbers, primary flow injection rates and axial distances. Measurements are taken for a swirl number of 0 and 0.82, while the non-dimensionalized primary flow injection rate varies from 0 to 8 and the non-dimensionalized axial distance varies from 0 to 30. The radial growth of the interface between the primary and secondary flows is measured by dying the primary flow with fluorescein sodium salt and photographing an axial cross-section of the flow created with an argon-ion laser. The size of the primary flow jet, at different axial distances, is measured from a digital copy of the photograph. The following effects swirl and injection rate have on the mixing are observed:

Swirl increases the rate of mixing between the primary and secondary flows at all axial positions, when compared to the no swirl mixing rate. This may be because the absolute velocity vector in the swirling flow is greater than the absolute velocity vector in the flow with no swirl, even though the average axial velocities are equal for the swirl and no swirl conditions. The increase in the total velocity may increase the turbulent mixing in the swirling flow. In compressible, burning experiments, for example Beer et al. [5], swirl decreases the mixing between the primary and secondary flows. They note that when the density increases radially outward within a swirling flow, a stable density stratification is formed which decreases the turbulent mixing. However, in the incompressible flow studied here, there is no radial density gradient to decrease the turbulent mixing.

As in the LDV velocity profiles, when swirl is present, the interface between the primary and secondary flows grows quickly close to the nozzle. At around 10 nozzle diameters downstream, the growth rate decreases sharply. This was discussed in section 7.1.1.

The absence of swirl produced a linear growth of the jet in the radial direction with increasing axial distances, and made the growth rate immune to changes in the injection rate. This corresponds to Abramovich's theory that the growth rate of a confined jet exhausted into another moving fluid should be linear [21].

7.1.3 Particle Image Velocimetry

The particle image velocimetry systems works successfully. PIV is performed with a swirl number of 0.82. The two-dimensional velocity field shows the instantaneous velocity distribution in one-quarter of the test section. The velocity vectors correctly represent the swirling flow. The velocity is a maximum at an r/D_j of about 2 to 3. The average tangential velocity measured from the profile is 2.7 m/s. This corresponds well with the LDV measurements.

7.2 Recommendations for Future Work

7.2.1 Experiments

The velocity profiles and flow visualization pictures provide insight into the fundamental mechanisms which govern the flows. However, because of the limited data, no solid conclusions can be made about these mechanisms. The author believes that studying these phenomena may result in a better understanding of how the fundamental mechanisms affect the mixing of the primary and secondary flows.

In Section 6.1.1, it is suggested that compressibility effects may be important to the formation of the recirculation zone because of the lack of recirculation for a super-critical swirl number in the test section. However, the data obtained in the thesis does not allow conclusions to be made about this possibility. Therefore, the lack of recirculation for super-critical swirl numbers in the test section should be examined more closely.

Section 6.1.3 discusses a switch in the velocity at the axis for different injection rates. However, this only occurs in Figure 5.9. If the interaction of the axial and tangential components of vorticity causes the switch, then similar experiments may lead to a better understanding of the interaction of the two vorticity components, which may be a fundamental mechanism that affects the mixing.

Section 6.1.3 also points out the increase in the velocity at the axis with no injection for swirl numbers above 0.51. Experiments should be performed on this phenomena to see if this affects the mixing of the primary and secondary flows.

Section 6.2.2 reveals the transition of the mass transfer of the primary into the secondary flow. This transition seems important to the mixing of the primary and secondary flows. More experiments should be run to see if this transition between convection and diffusion is a fundamental mechanism that affects the mixing of the two flows.

7.2.2 Improving the Swirl Chamber

The swirl chamber has been successfully designed and constructed. However, there are a few alterations that can be made. First, if the secondary pump is turned on when the valve to the swirl chamber is open, the transient pressure within the swirl chamber causes the o-ring between the large cylinder and lid to fail. This may be solved if a pressure release valve is installed in the swirl chamber. The large transient pressure can also be eliminated if a DC motor controller is installed in the secondary pump. Second, the reading from the pressure transducer which measures the pressure drop across the orifice plate has a sinusoidal oscillation. A low-pass filter has been built to reduce the oscillation, however, the noise persists. If the oscillation can be eliminated, higher accuracy velocity readings can be achieved. Third, the vanes currently have a rectangular cross-section. If the vanes are machined to have an aerodynamic cross-section, the efficiency of the vanes may improve, which may increase the swirl number range. Finally, some combustion chambers have diverging walls or a sudden expansion. It is suggested that a fixture be machined and mounted within the test section to model the divergence or sudden expansion in these combustion chambers.

7.2.3 Improving the PIV System

The particle image velocity system is very robust because of the control over the pulse spacing and number of pulses. However, there are galvanometers mounted on the laser that have the ability to bring another dimension to the system. First of all, a CCD camera can be synchronized with the firing of the laser. With the CCD camera, videos of the flow can be taken, with two or three pulses occurring for each frame. In other words, each video frame can capture a two-dimensional velocity field. Second, the galvanometers can be programmed to discretely sweep the laser sheet in the axial direction, with each video frame. In this way, consecutive video frames can capture the two-dimensional velocity fields at increasing axial distances. Therefore, three dimensional velocity movies of the flow can then be made. All of the equipment to build this system already exists in the lab.

References

[1] A. H. Legge, S. V. Krupa. *Air Pollutants and Their Effects on the Terrestrial Ecosystem,* pages 106-114. Wiley-Interscience Publication, 1986.

[2] A. C. Stern. *Air Pollution*, page 459. Academic Press, 1977.

[3] K. D. Kihm, N. Chigier, F. Sun. "Laser Doppler Velocimetry Investigation of Swirler Flowfields," *Journal of Propulsion and Power*, **VOL 6, NO. 4**, pages 364-374. 1989.

[4] H. W. Emmons, S. Ying. "The Fire Whirl," *Eleventh Symposium (International) on Combustion*, pages 475-478. The Combustion Institute: Pittsburgh, 1967.

[5] J. M. Beer, N. A. Chigier, T. W. Davies, K. Bassindale. "Laminarization of Turbulent Flames in Rotating Environments," *Combustion and Flame*, **16**, pages 39-45. The Combustion Institute, 1971.

[6] Lord Rayleigh. "On the Dynamics of Revolving Fluids," *Scientific Papers*, **6**, pages 341-349. Cambridge University Press, 1916.

[7] N. A. Chigier, J. M. Beer. *Journal of Basic Engineering*, **4**, page 788. 1964.

[8] N.A. Chigier, J. M. Beer, D. Grecov, K. Bassindale. "Jet Flames in Rotating Flow Fields," *Combustion and Flame*, 14, pages 171-180. The Combustion Institute, 1970.

[9] N. Syre, J. M. Beer. "Combustion in Swirling Flows: A Review," The Combustion Institute, 1974.

[10] J. L. Hapin. "Swirl Generation and Recirculation Using Radial Swirl Vanes," *International Gas Turbine and Aeroengine Congress and Exposition*, The American Society of Mechanical Engineers, 1993.

[11] N. Machii, K. Ogawa, M. Katsuki. "Turbulent Characteristics of a Swirling Flame for Gas Turbine Combustors," *ASME Cogen-Turbo*, pages 213-217. The American Society of Mechanical Engineers, 1993.

[12] S. A. Ahmed, A. S. Nejad. "Swirl Effects on Confined Flows in Axisymmetric Geometries," *Journal of Propulsion and Power*, **VOL 8, NO. 4**, pages 339-345. 1991.

[13] S. N. Singh, D. P. Agrawal, R. C. Malhotra, A. K. Raghava. "Effect of Swirl on Mixing of Co-axial Jets," *Aeronautical Journal*, pages 95-102. 1991.

[14] J. B. W. Kok, F. J. J. Rosendal, J. J. H. Brouwers. "LDA-Measurements on Swirling Flows in Tubes," *SPIE*, **2052**, pages 721-728. Laser Anemometry Advances and Applications, 1993.

[15] H. Li, Y. Tomita. "Characteristics of Swirling Flow in a Circular Pipe," *Transactions of the ASME*, **116**, pages 370-376. 1994.

[16] J. M. Beer, N. Chigier. *Combustion Aerodynamics*, page 107. Robert E. Krieger Publishing Company, Inc., 1983.

[17] A. K. Gupta, D. G. Lilley, N. Syred. *Swirl Flows*, page 2. Abacus Press, 1984.

[18] J. P. Vanyo. *Rotating Fluids in Engineering and Science*, page 170-172. Butterworth-Heinemann, 1993.

[19] E. A. Avallone, T. Baumeister III. *Marks' Standard Handbook for Mechanical Engineers*, pages 5-52. McGraw-Hill Book Company, 1987.

[20] G. K. Batchelor. "Axial Flow in Trailing Line Vortices," *Journal of Fluid Mechanics*, **20**, pp645-658. 1964.

[21] G. N. Abramovich. *The Theory of Turbulent Jets*, pages172-230. The MIT Press, 1963.

[22] R Dong, S. Chu, J. Katz. "Quantitative Visualization of the Flow within the Volute of a Centrifugal Pump. Part A: Technique," *Transactions of the ASME*, **VOL 114**, pages 390-403. September 1992.

Appendix A

Detailed CAD Drawings

A.1 Swirl Chamber

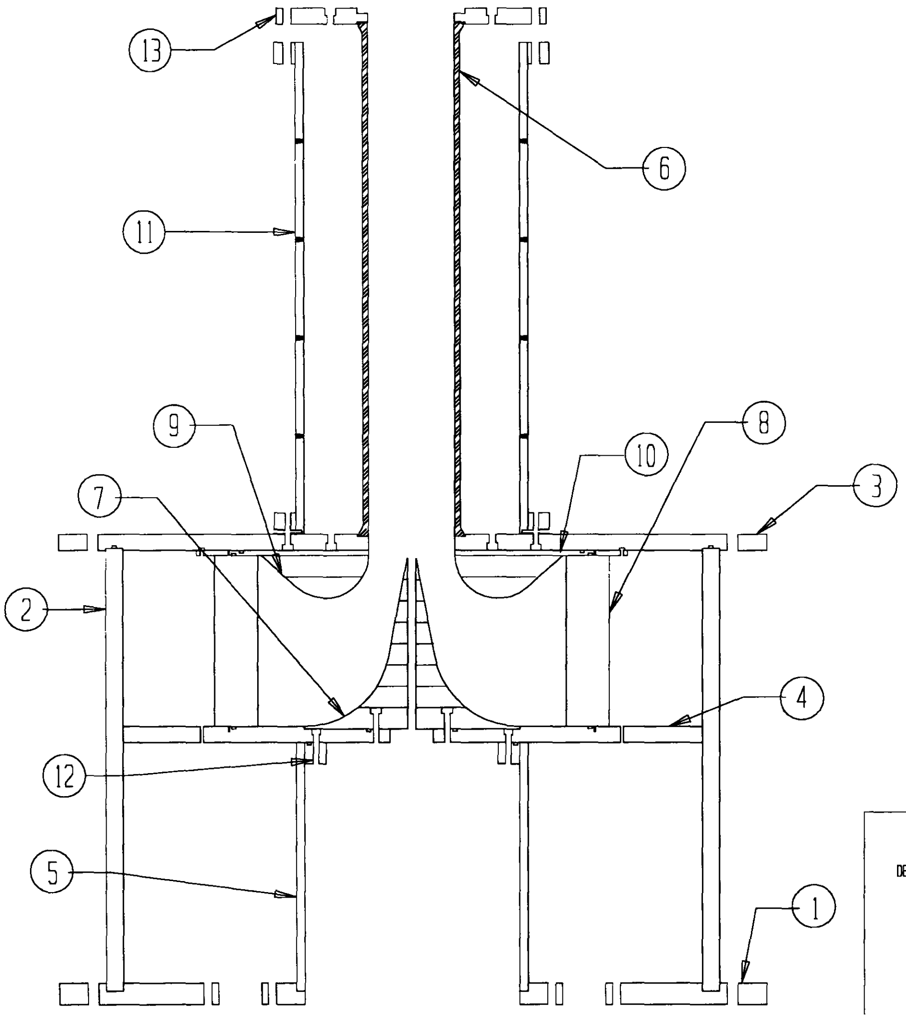

1.	Base
2.	Large Cylinder
3.	Lid
4.	Large Rib
5.	Small Cylinder
6.	Glass Test Section
7.	Mandrel
8.	Circular Vane Array
9.	Contour To Redirect Flow
10.	Vane Cover
11.	Viewing Reservoir
12.	Flange For Small Cylinder
13.	Test Section Support

PART #:

TOLERANCES

DECIMAL:

ANGULAR:

PROJECT: Swirl Chamber (MS Project at MIT)

PART NAME: Cross Section

MATERIAL: PVC

DRAWN BY: David Danitz

REVISION DATE: 3/14/94

SHEET 1 OF 1

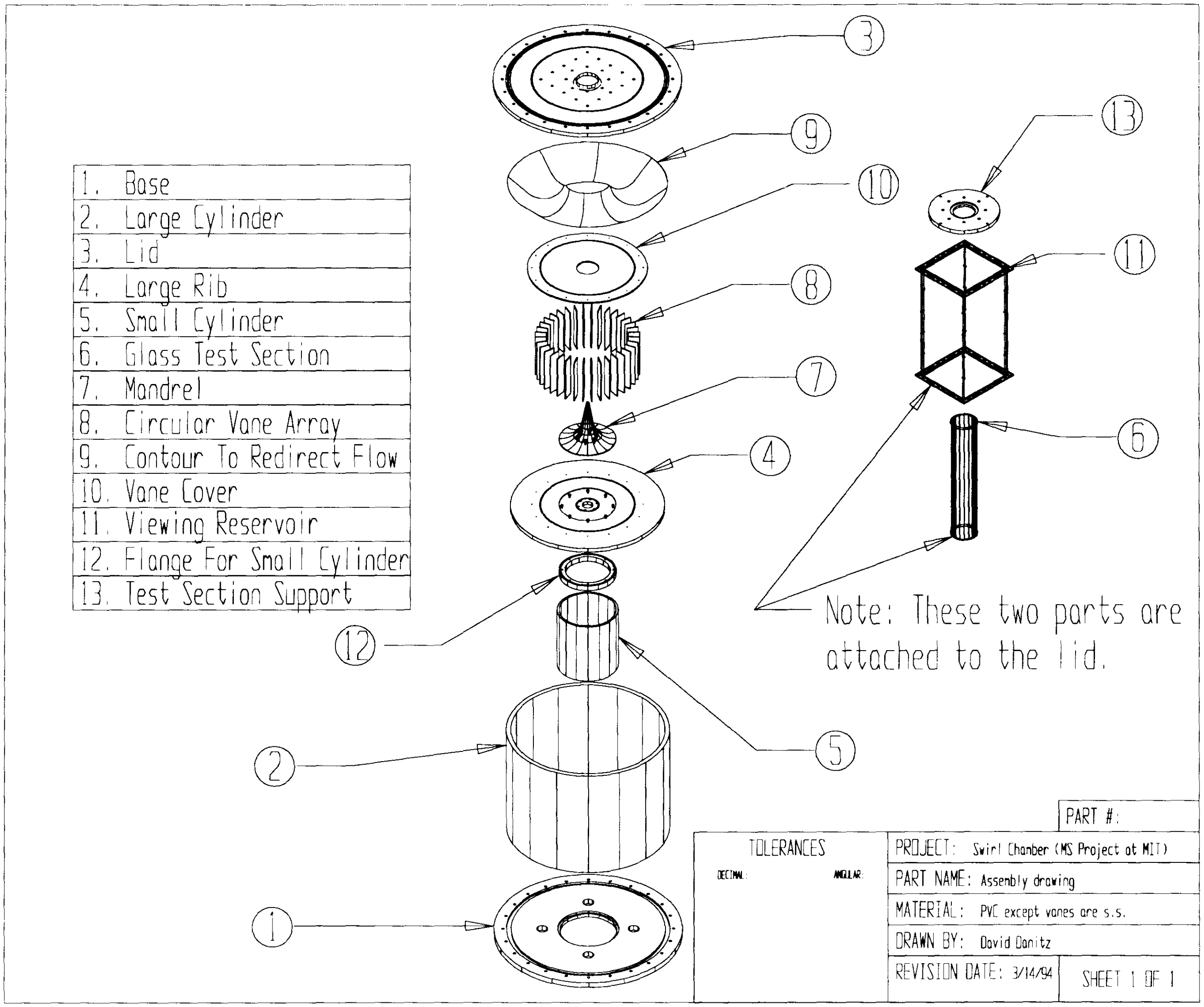

1.	Base
2.	Large Cylinder
3.	Lid
4.	Large Rib
5.	Small Cylinder
6.	Glass Test Section
7.	Mandrel
8.	Circular Vane Array
9.	Contour To Redirect Flow
10.	Vane Cover
11.	Viewing Reservoir
12.	Flange For Small Cylinder
13.	Test Section Support

Note: These two parts are attached to the lid.

PART #:

TOLERANCES

DECIMAL: ANGULAR:

PROJECT: Swirl Chamber (MS Project at MIT)

PART NAME: Assembly drawing

MATERIAL: PVC except vanes are s.s.

DRAWN BY: David Danitz

REVISION DATE: 3/14/94

SHEET 1 OF 1

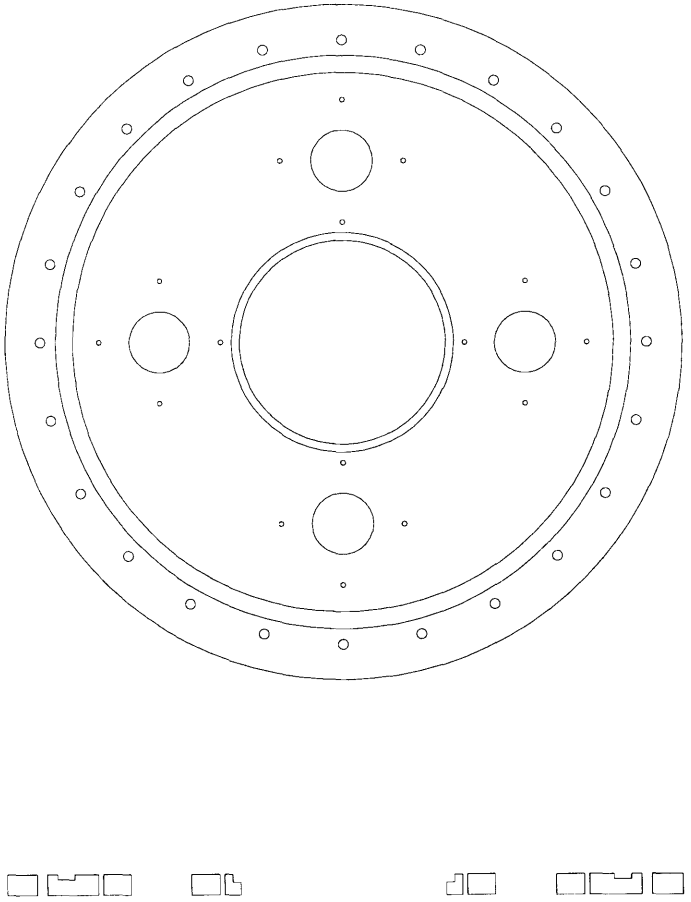

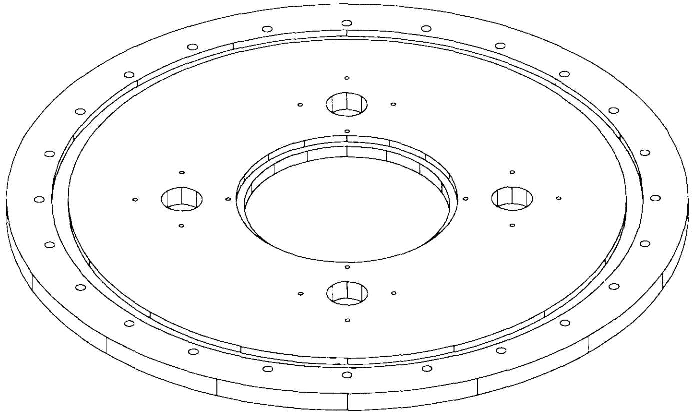

PART #: 1

TOLERANCES

DECIMAL:

X/X = +-1/32

.XX = +-.01

.XXX = +- .005

ANGULAR:

.X = +-.5 deg

X = +- 1 deg

PROJECT: Swirl Chamber (MS Project at MIT)

PART NAME: Base

MATERIAL: PVC

DRAWN BY: David Danitz

REVISION DATE: 3/14/94

SHEET 1 OF 4

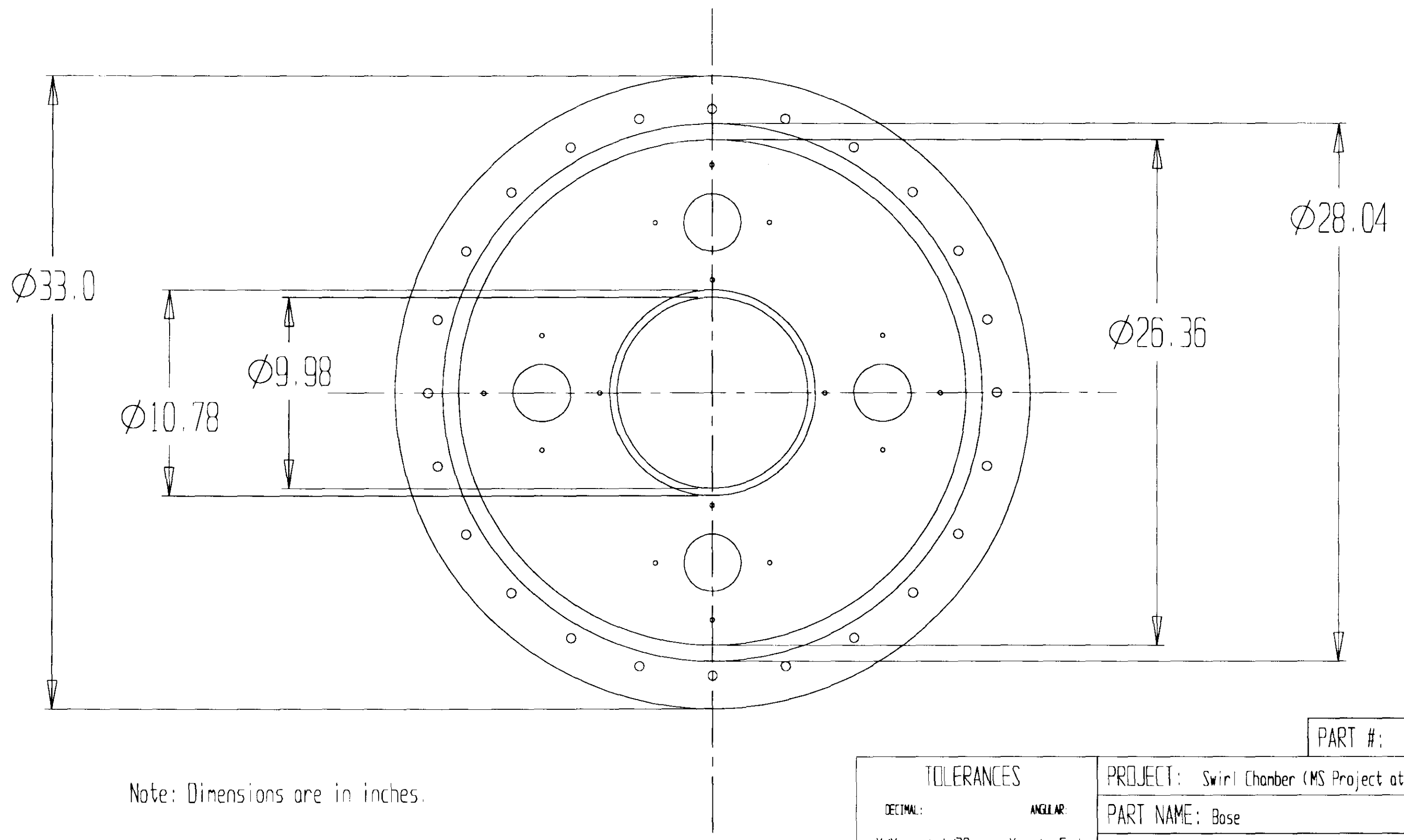

Note: Dimensions are in inches.

TOLERANCES

DECIMAL:	ANGULAR:
X/X = +-1/32	.X = +-.5 deg
.XX = +-.01	X = +- 1 deg
.XXX = +- .005	

	PART #: 1
PROJECT: Swirl Chamber (MS Project at MIT)	
PART NAME: Base	
MATERIAL: PVC	
DRAWN BY: David Danitz	
REVISION DATE: 3/14/94	SHEET 2 OF 4

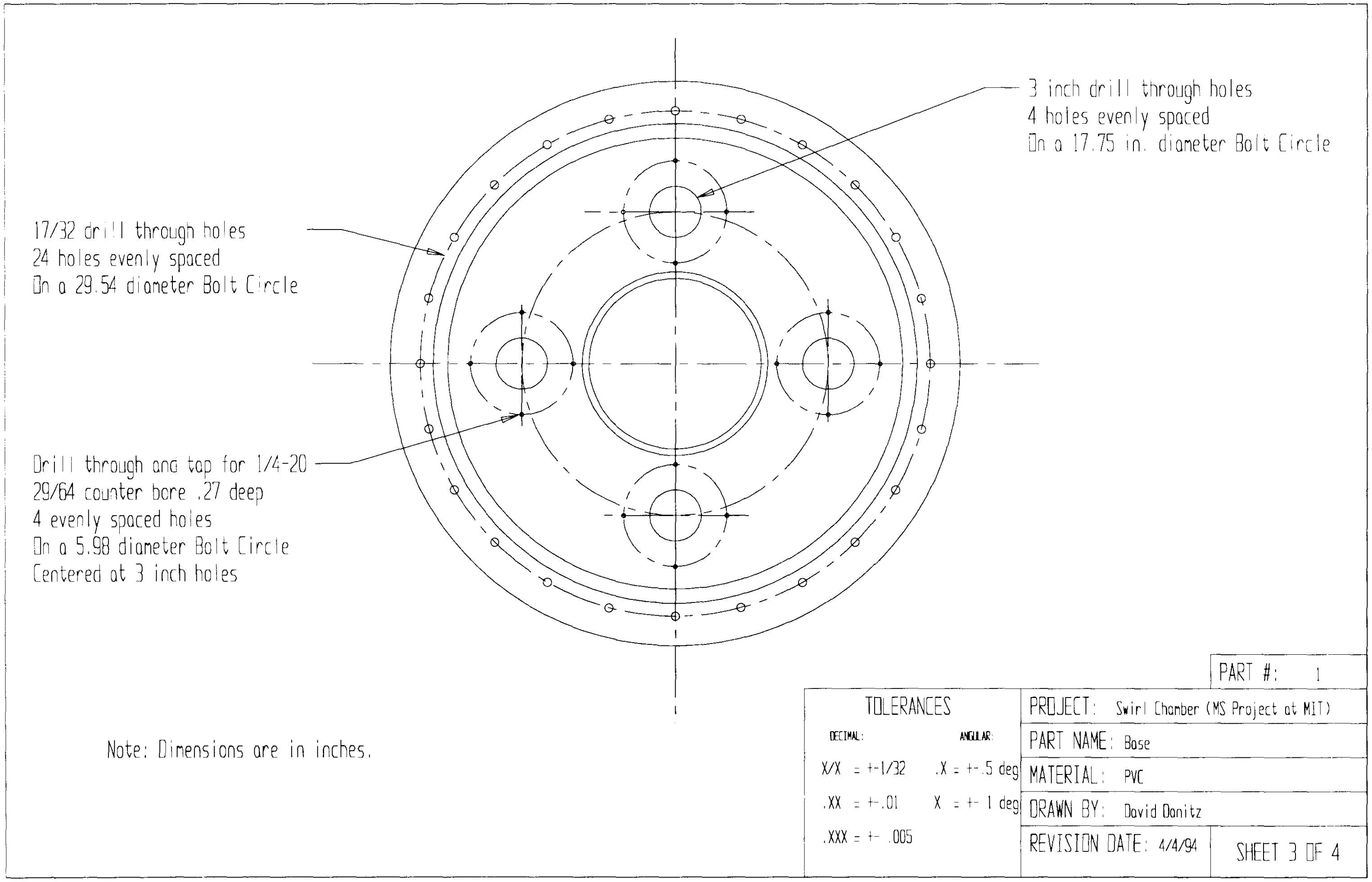
3 inch drill through holes
4 holes evenly spaced
On a 17.75 in. diameter Bolt Circle
17/32 drill through holes
24 holes evenly spaced
On a 29.54 diameter Bolt Circle
Drill through and tap for 1/4-20
29/64 counter bore .27 deep
4 evenly spaced holes
On a 5.98 diameter Bolt Circle
Centered at 3 inch holes
Note: Dimensions are in inches.
TOLERANCES
DECIMAL:
ANGULAR:
X/X = +-1/32
.X = +-.5 deg
.XX = +-.01
X = +-1 deg
.XXX = +-.005
PART #: 1
PROJECT: Swirl Chamber (MS Project at MIT)
PART NAME: Base
MATERIAL: PVC
DRAWN BY: David Danitz
REVISION DATE: 4/4/94
SHEET 3 OF 4

Note: Dimensions are in inches.

TOLERANCES

DECIMAL:	ANGULAR:
X/X = +-1/32	.X = +-.5 deg
.XX = +-.01	X = +- 1 deg
.XXX = +- .005	

PART #: 1

PROJECT: Swirl Chamber (MS Project at MIT)

PART NAME: Base

MATERIAL: PVC

DRAWN BY: David Danitz

REVISION DATE: 4/4/94

SHEET 4 OF 4

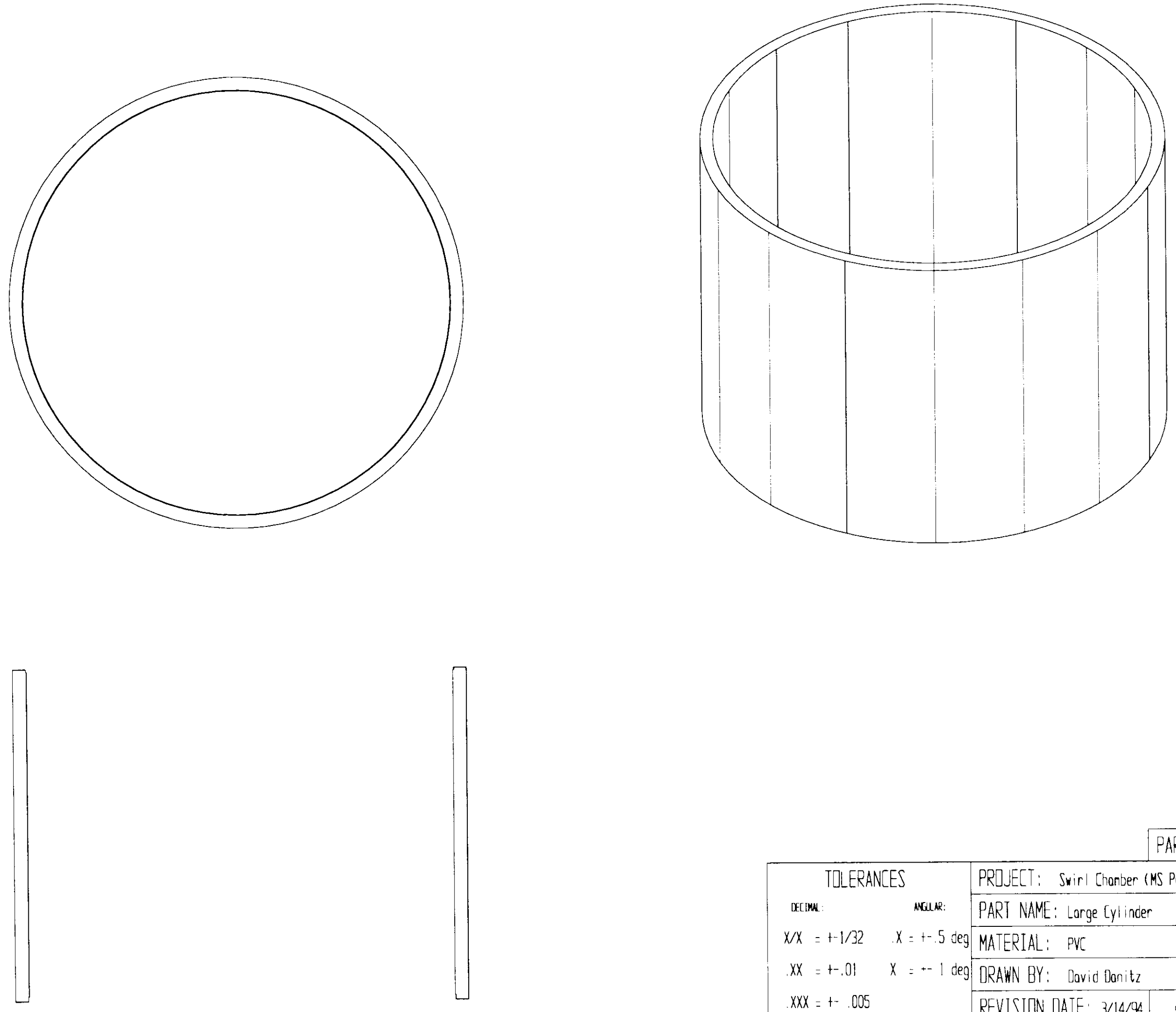

PART #: 2

TOLERANCES	
DECIMAL:	ANGULAR:
X/X = +-1/32	.X = +-.5 deg
.XX = +-.01	X = +- 1 deg
.XXX = +- .005	

PROJECT: Swirl Chamber (MS Project at MIT)

PART NAME: Large Cylinder

MATERIAL: PVC

DRAWN BY: David Danitz

REVISION DATE: 3/14/94

SHEET 1 OF 3

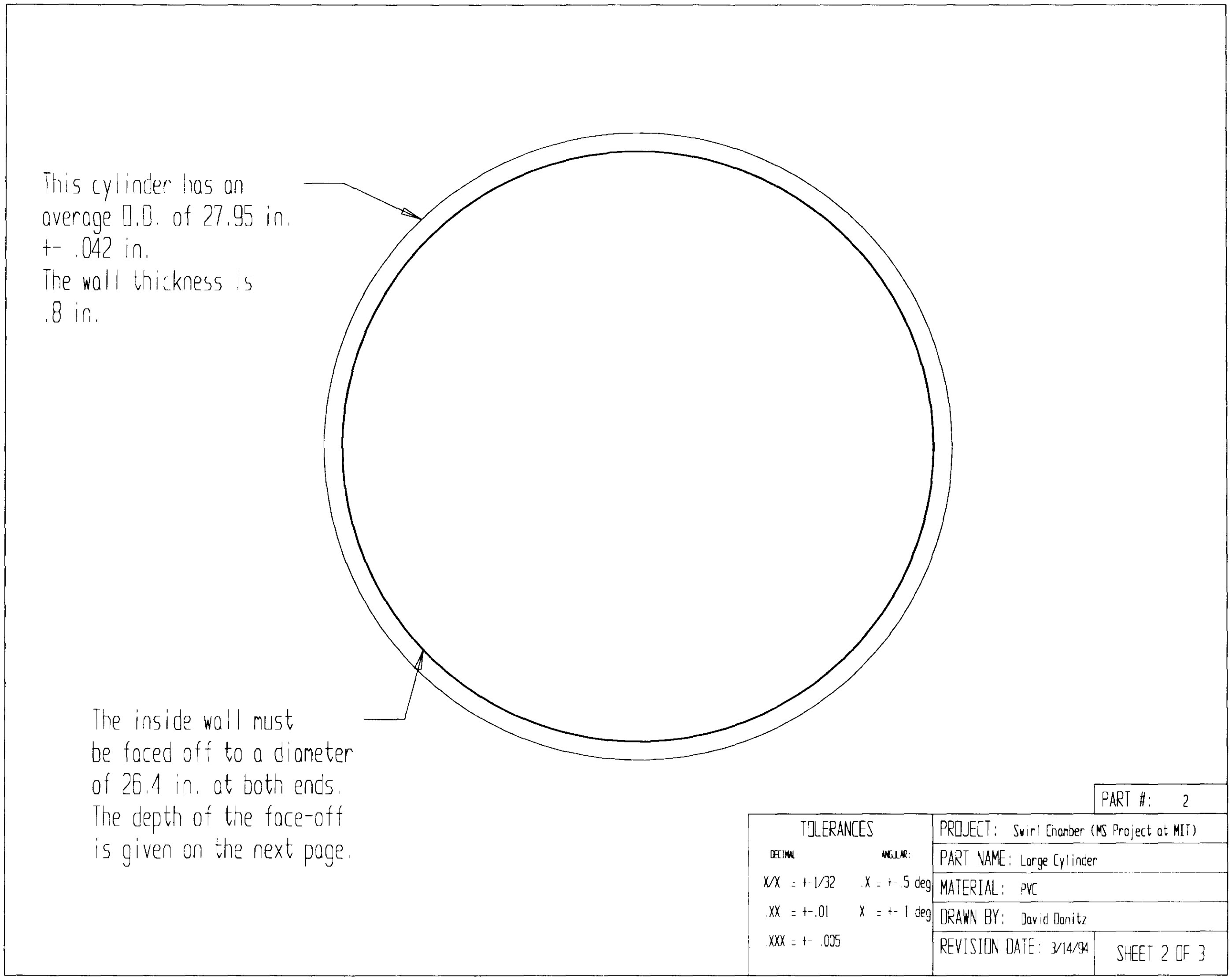

This cylinder has an
average O.D. of 27.95 in.
+- .042 in.
The wall thickness is
.8 in.

The inside wall must
be faced off to a diameter
of 26.4 in. at both ends.
The depth of the face-off
is given on the next page.

TOLERANCES
DECIMAL: ANGULAR:
X/X = +-1/32 .X = +-.5 deg
.XX = +-.01 X = +- 1 deg
.XXX = +- .005

PART #: 2
PROJECT: Swirl Chamber (MS Project at MIT)
PART NAME: Large Cylinder
MATERIAL: PVC
DRAWN BY: David Danitz
REVISION DATE: 3/14/94
SHEET 2 OF 3

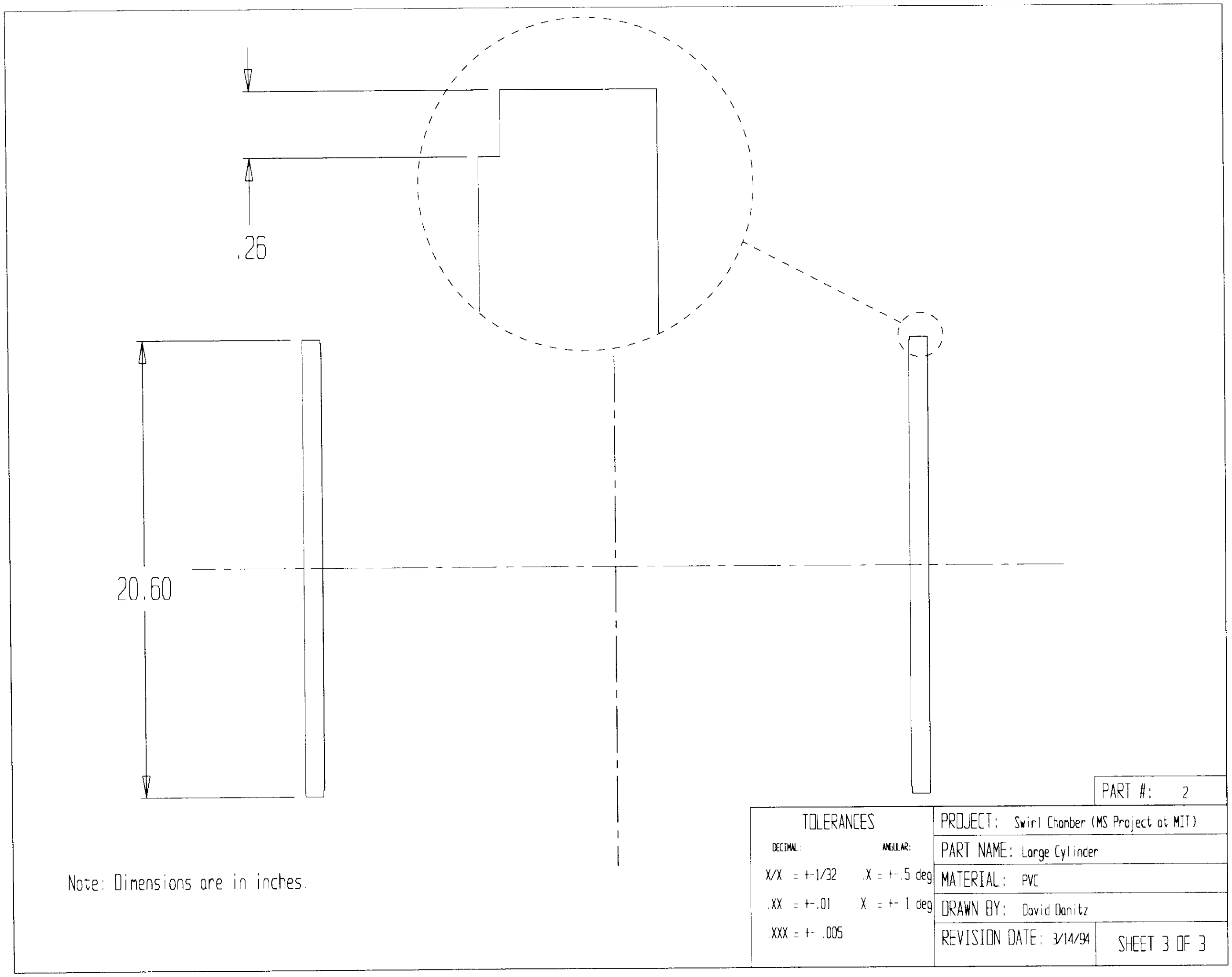
.26
20.60
Note: Dimensions are in inches.
TOLERANCES
DECIMAL:
ANGULAR:
X/X = +-1/32
.X = +-.5 deg
.XX = +-.01
X = +-1 deg
.XXX = +-.005
PART #: 2
PROJECT: Swirl Chamber (MS Project at MIT)
PART NAME: Large Cylinder
MATERIAL: PVC
DRAWN BY: David Donitz
REVISION DATE: 3/14/94
SHEET 3 OF 3

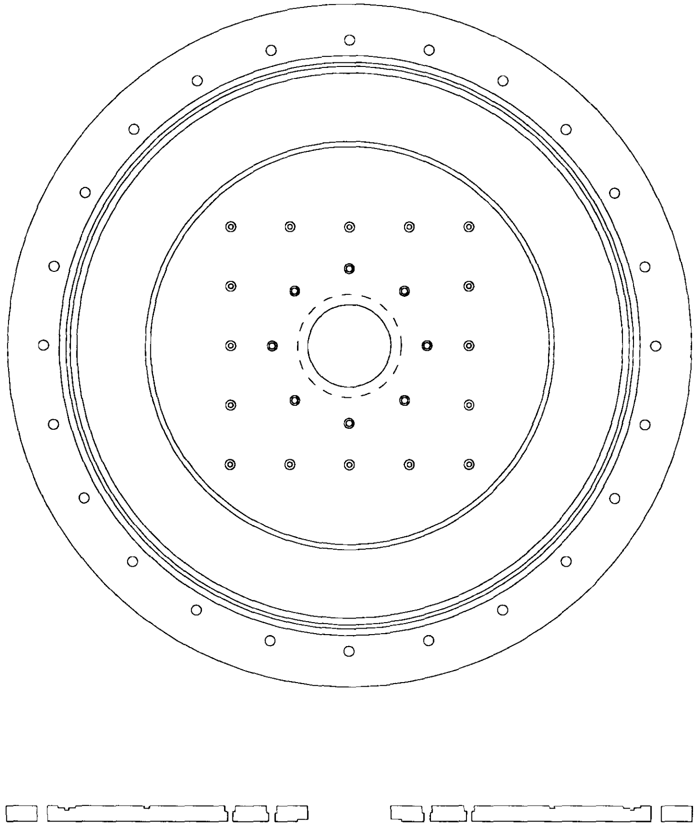

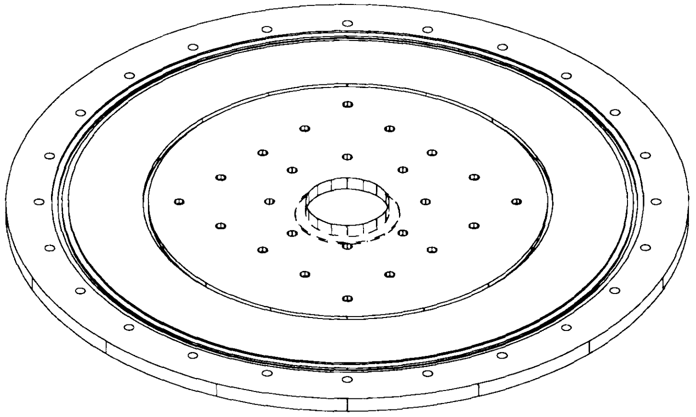

PART #: 3

TOLERANCES

DECIMAL:

X/X = +-1/32

.XX = +-.01

.XXX = +- .005

ANGULAR:

.X = +-.5 deg

X = +- 1 deg

PROJECT: Swirl Chamber (MS Project at MIT)

PART NAME: Lid

MATERIAL: PVC

DRAWN BY: David Danitz

REVISION DATE: 3/14/94

SHEET 1 OF 6

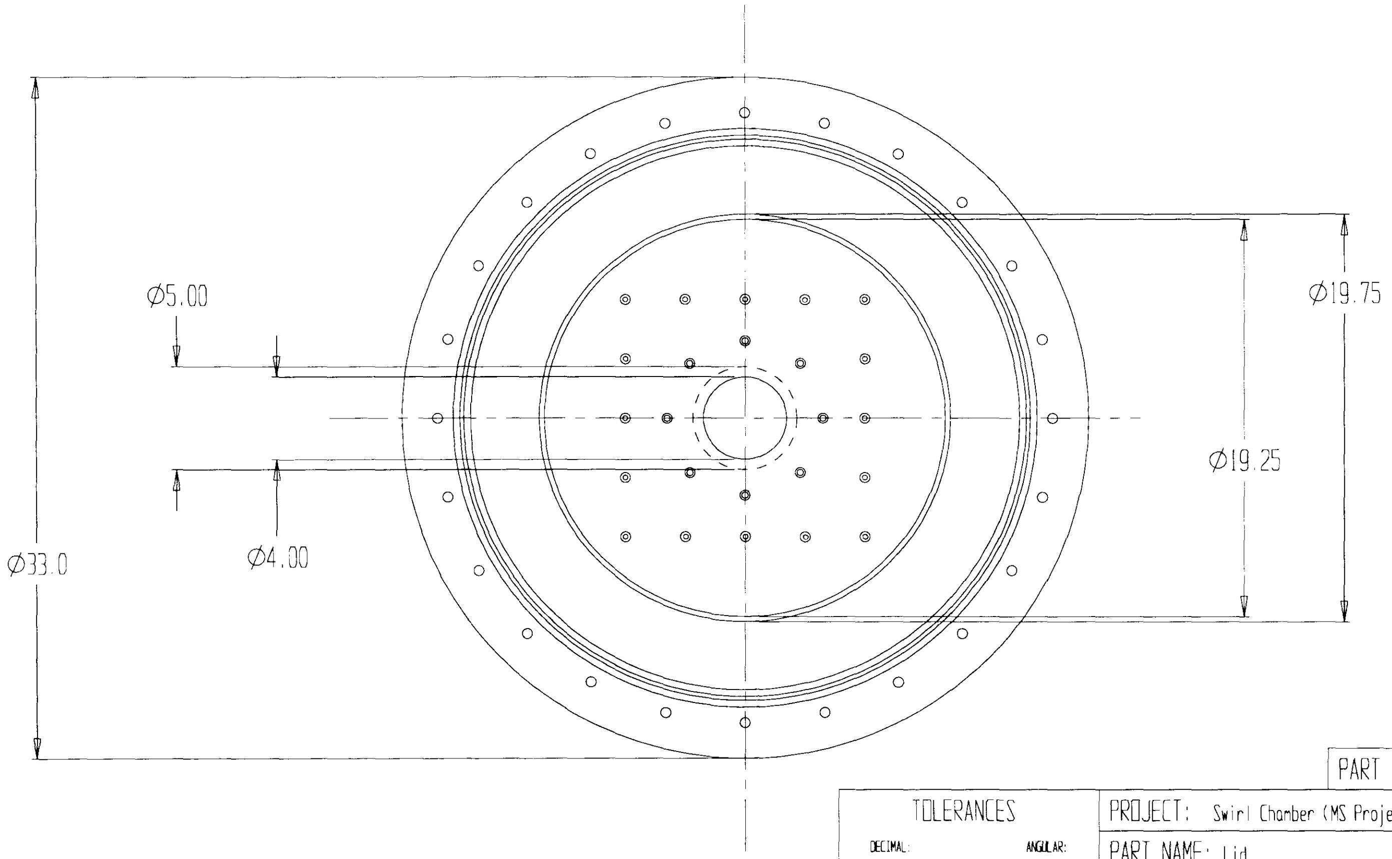

Note: Dimensions are in inches

TOLERANCES

DECIMAL:
X/X = +-1/32
.XX = +-.01
.XXX = +- .005

ANGULAR:
.X = +-.5 deg
X = +- 1 deg

PART #: 3
PROJECT: Swirl Chamber (MS Project at MIT)
PART NAME: Lid
MATERIAL: PVC
DRAWN BY: David Danitz
REVISION DATE: 3/14/94
SHEET 2 OF 6

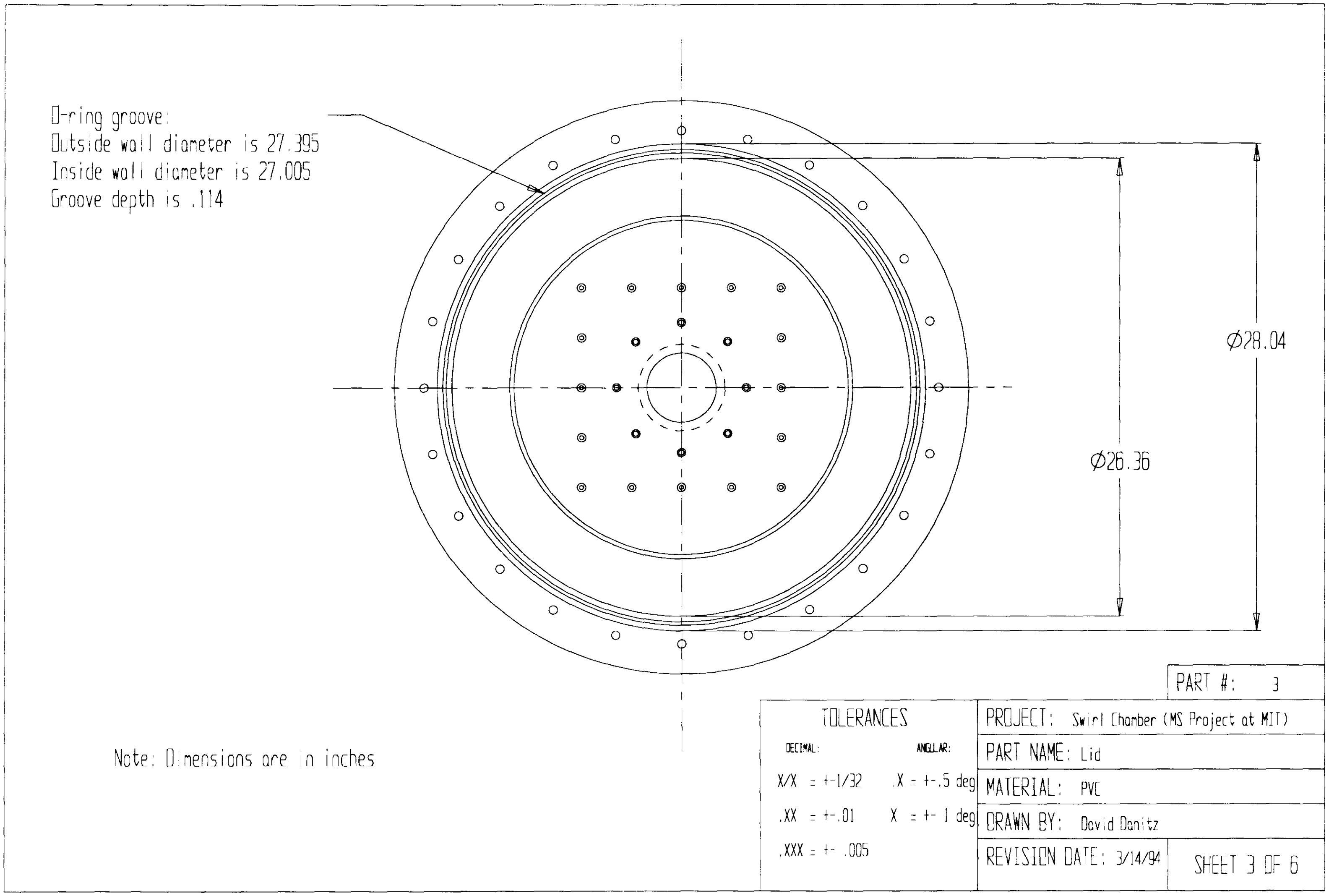
O-ring groove:
Outside wall diameter is 27.395
Inside wall diameter is 27.005
Groove depth is .114
Ø28.04
Ø26.36
Note: Dimensions are in inches
TOLERANCES
DECIMAL:
ANGULAR:
X/X = +-1/32
.X = +-.5 deg
.XX = +-.01
X = +- 1 deg
.XXX = +- .005
PART #: 3
PROJECT: Swirl Chamber (MS Project at MIT)
PART NAME: Lid
MATERIAL: PVC
DRAWN BY: David Danitz
REVISION DATE: 3/14/94
SHEET 3 OF 6

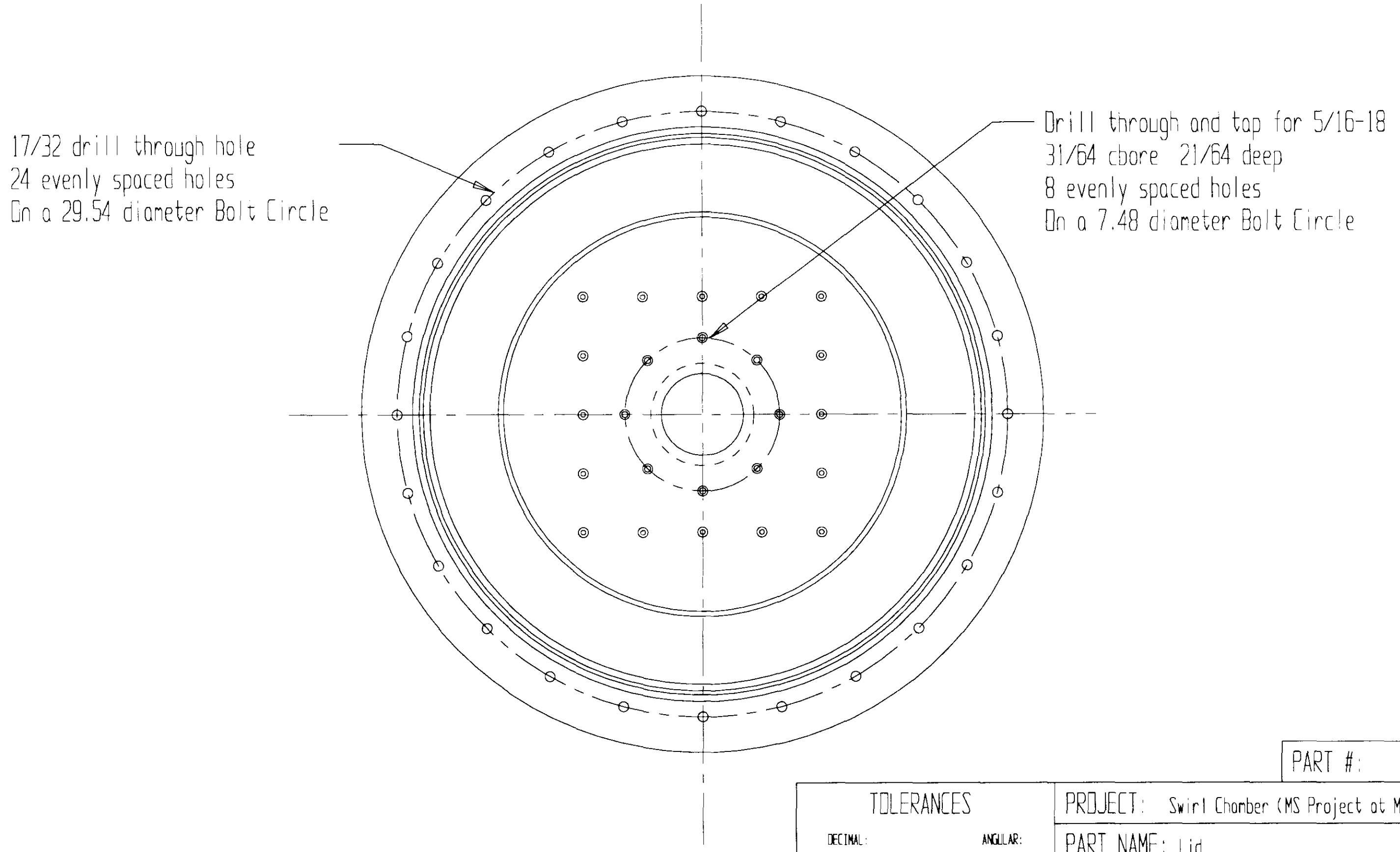

Note: Dimensions are in inches.

PART #: 3

TOLERANCES	
DECIMAL:	ANGULAR:
X/X = +-1/32	.X = +-.5 deg
.XX = +-.01	X = +- 1 deg
.XXX = +- .005	

PROJECT: Swirl Chamber (MS Project at MIT)

PART NAME: Lid

MATERIAL: PVC

DRAWN BY: David Danitz

REVISION DATE: 3/14/94

SHEET 4 of 6

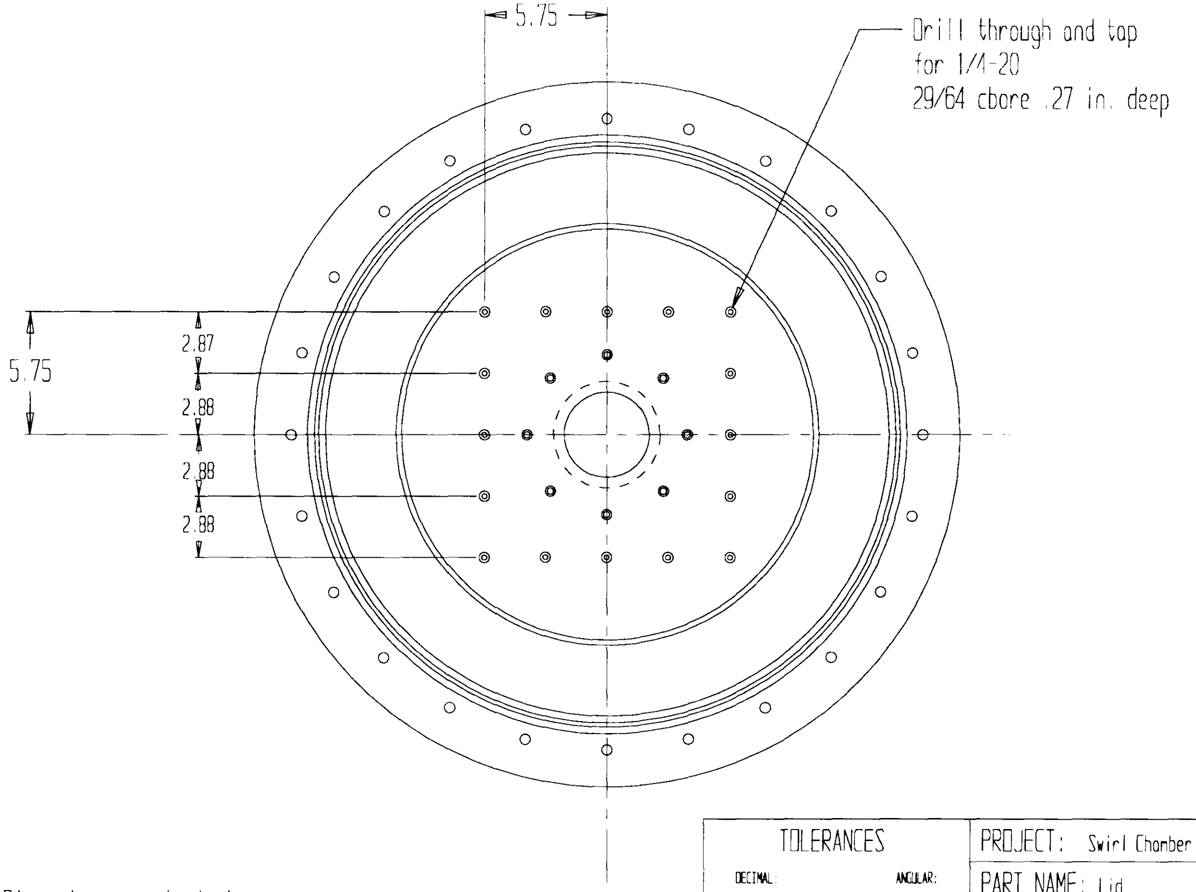

Note: Dimensions are in inches.

TOLERANCES

DECIMAL:
X/X = +-1/32
.XX = +-.01
.XXX = +- .005

ANGULAR:
.X = +-.5 deg
X = +- 1 deg

PART #: 3

PROJECT: Swirl Chamber (MS Project at MIT)

PART NAME: Lid

MATERIAL: PVC

DRAWN BY: David Danitz

REVISION DATE: 3/14/94

SHEET 5 of 6

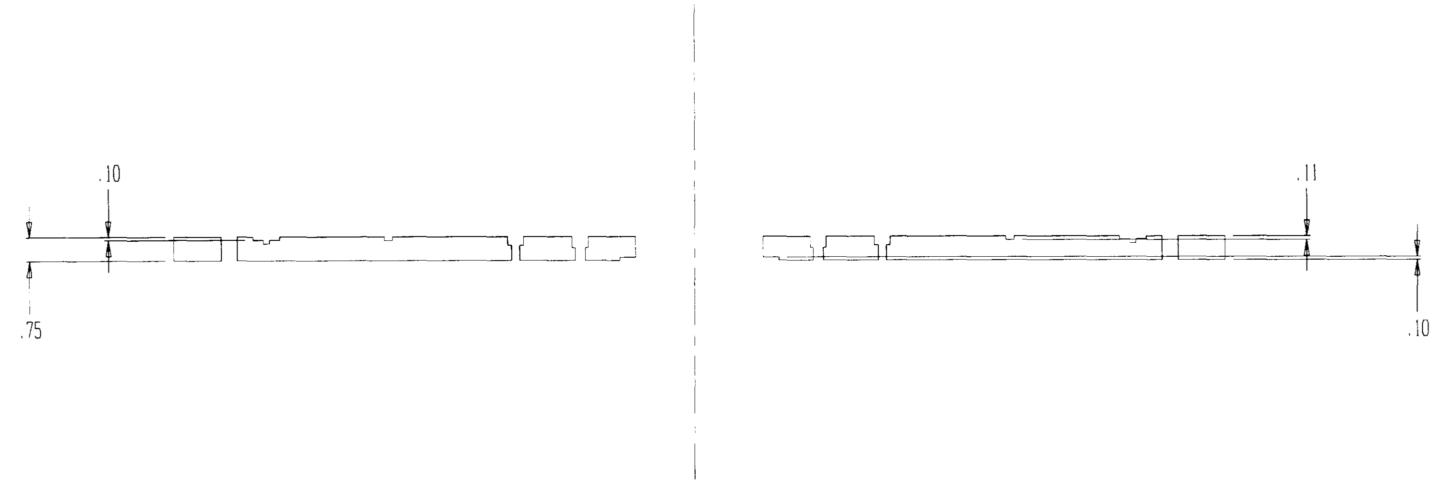

Note: Dimensions are in inches.

TOLERANCES

DECIMAL: ANGULAR:

X/X = +-1/32 .X = +-.5 deg

.XX = +-.01 X = +- 1 deg

.XXX = +- .005

PART #: 3

PROJECT: Swirl Chamber (MS Project at MIT)

PART NAME: Lid

MATERIAL: PVC

DRAWN BY: David Danitz

REVISION DATE: 3/14/94

SHEET 6 of 6

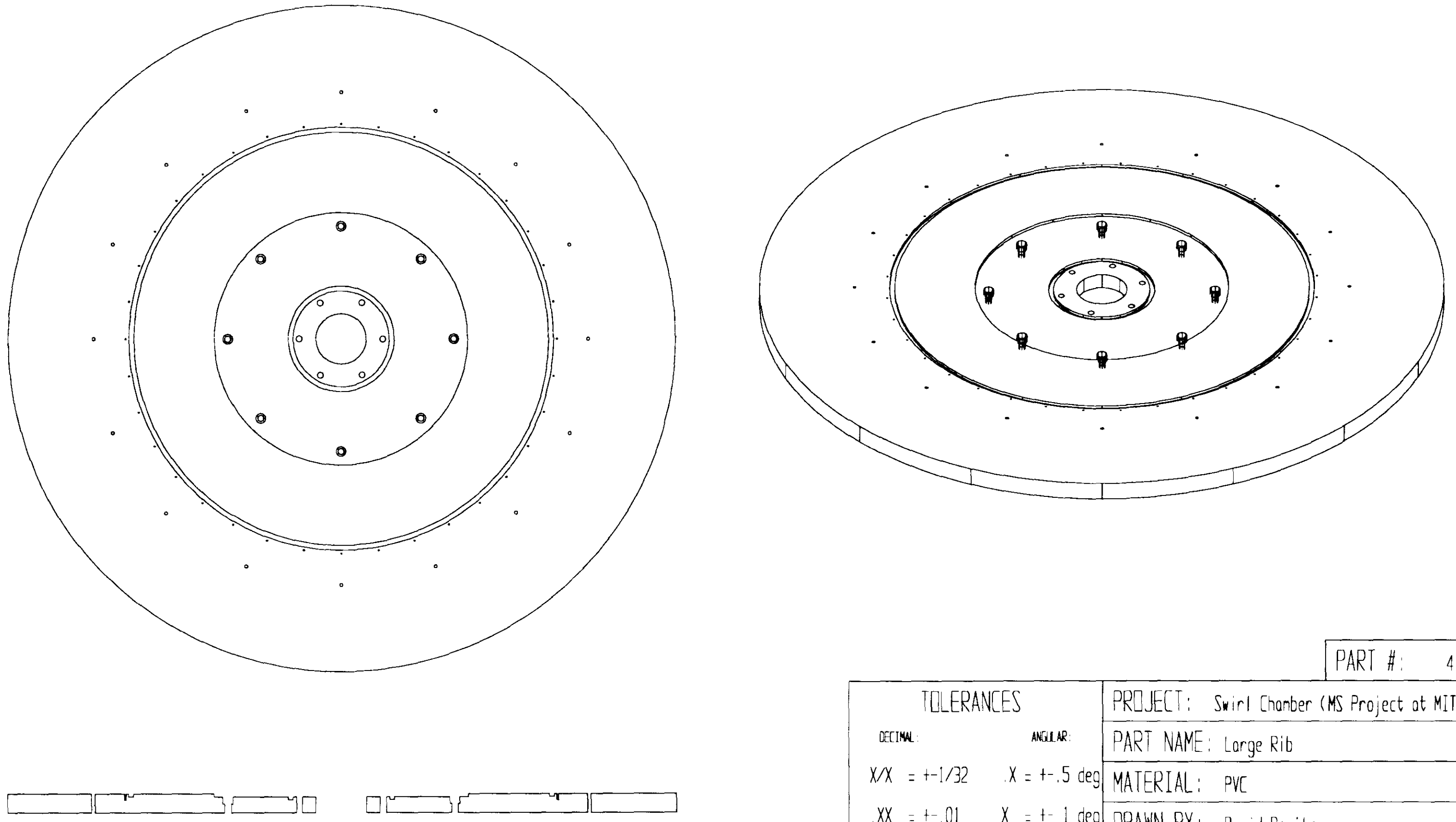

PART #: 4

TOLERANCES	
DECIMAL:	ANGULAR:
X/X = +-1/32	.X = +-.5 deg
.XX = +-.01	X = +- 1 deg
.XXX = +- .005	

PROJECT: Swirl Chamber (MS Project at MIT)

PART NAME: Large Rib

MATERIAL: PVC

DRAWN BY: David Danitz

REVISION DATE: 3/14/94

SHEET 1 OF 5

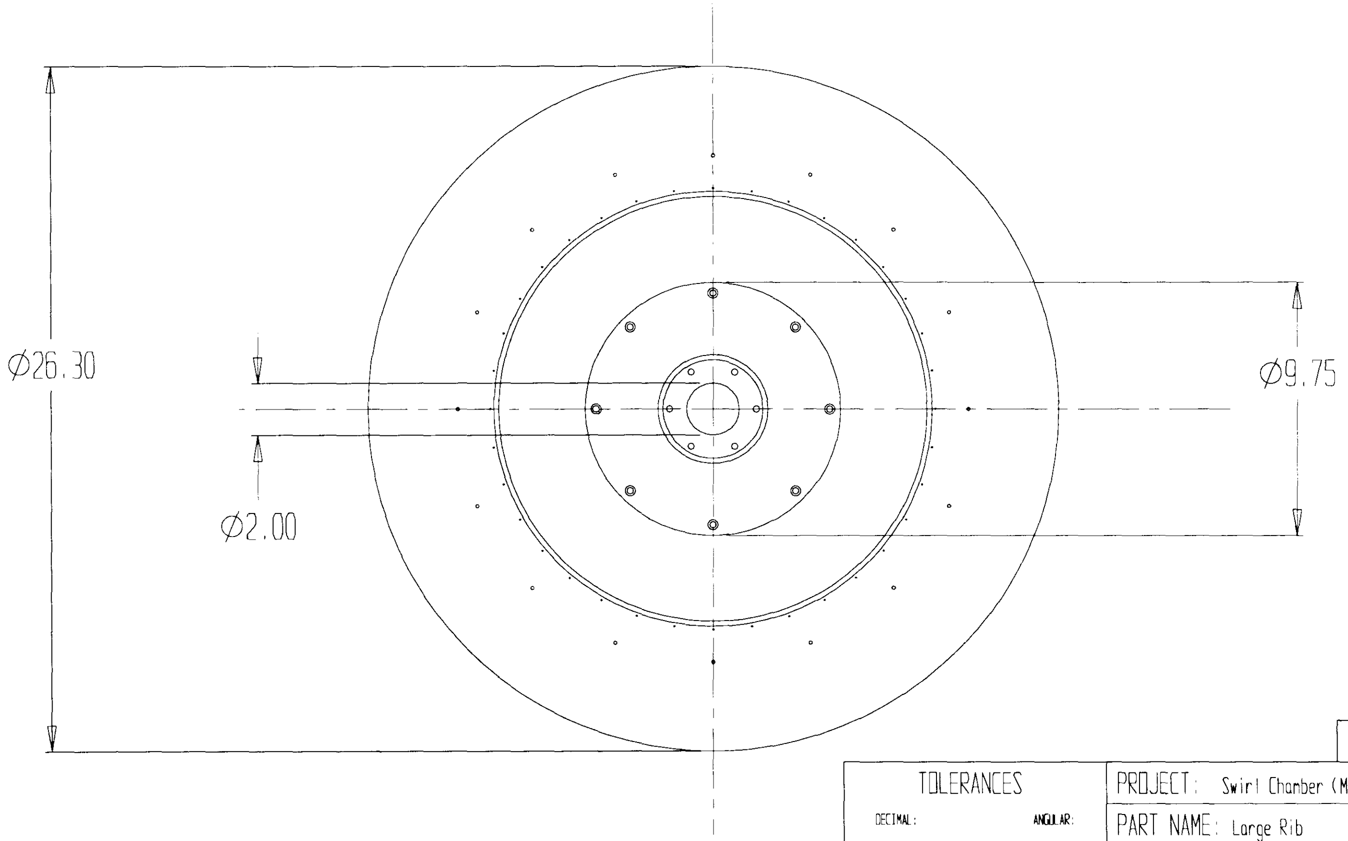

Note: Dimensions are in inches.

TOLERANCES

DECIMAL:
X/X = +-1/32
.XX = +-.01
.XXX = +- .005

ANGULAR:
.X = +-.5 deg
X = +- 1 deg

PART #: 4

PROJECT: Swirl Chamber (MS Project at MIT)

PART NAME: Large Rib

MATERIAL: PVC

DRAWN BY: David Danitz

REVISION DATE: 3/14/94

SHEET 2 OF 5

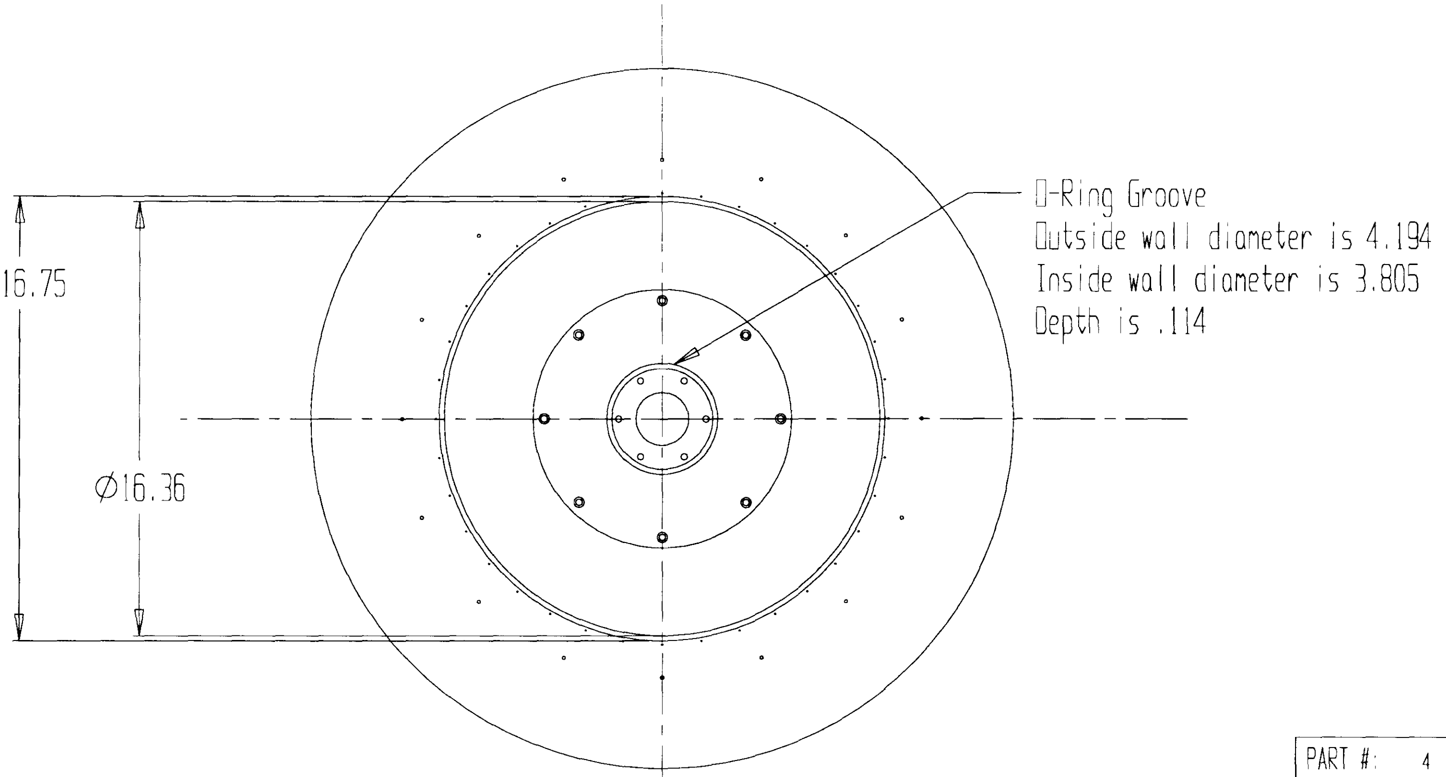

Note: Dimensions are in inches.

		PART #: 4	
TOLERANCES		PROJECT: Swirl Chamber (MS Project at MIT)	
DECIMAL:	ANGULAR:	PART NAME: Large Rib	
X/X = +-1/32	.X = +-.5 deg	MATERIAL: PVC	
.XX = +-.01	X = +- 1 deg	DRAWN BY: David Danitz	
.XXX = +- .005		REVISION DATE: 3/14/94	SHEET 3 OF 5

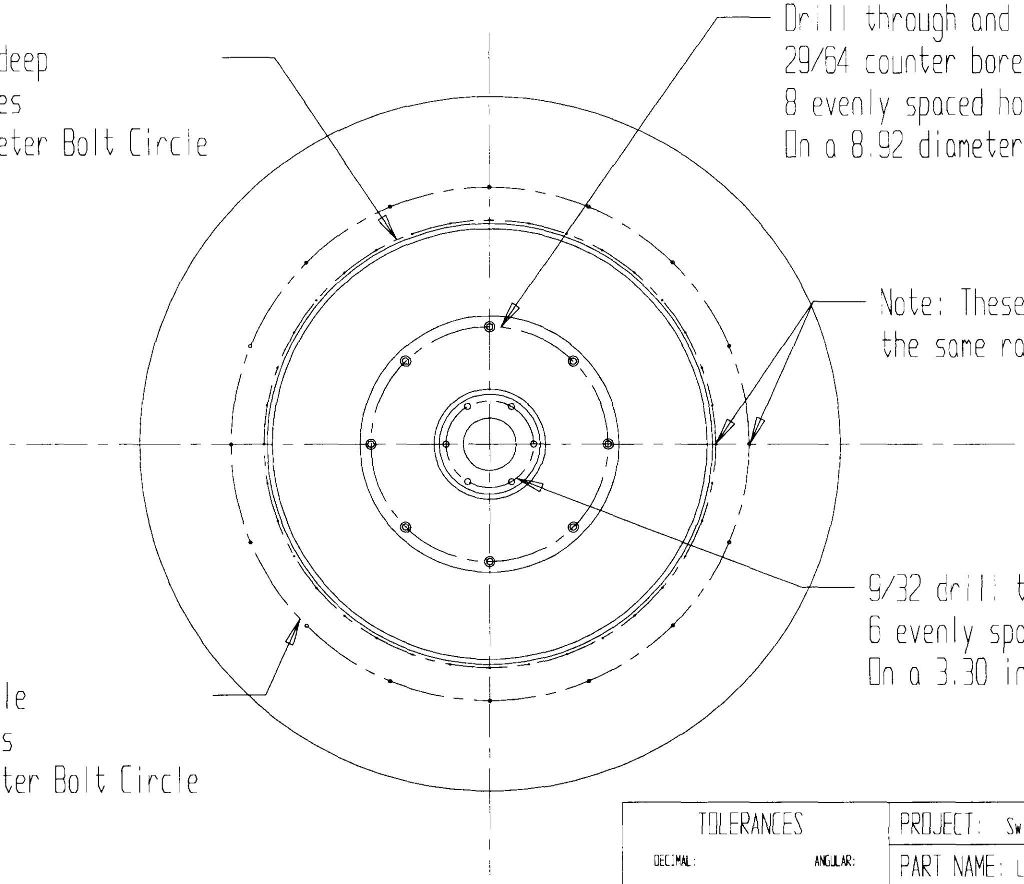

#51 drill hole 3/8 deep
36 evenly spaced holes
On a 17.00 inch diameter Bolt Circle

Drill through and tap for 1/4-20
29/64 counter bore .27 deep
8 evenly spaced holes
On a 8.92 diameter Bolt Circle

Note: These holes must be along the same radius.

9/32 drill through hole
6 evenly spaced holes
On a 3.30 inch Bolt Circle

5/32 drill through hole
16 evenly spaced holes
On a 19.50 inch diameter Bolt Circle

Note: Dimensions are in inches.

PART #: 4

TOLERANCES

DECIMAL:
X/X = +-1/32
.XX = +-.01
.XXX = +- .005

ANGULAR:
.X = +-.5 deg
X = +- 1 deg

PROJECT: Swirl Chamber (MS Project at MIT)
PART NAME: Large Rib
MATERIAL: PVC
DRAWN BY: David Danitz
REVISION DATE: 3/14/94
SHEET 4 OF 5

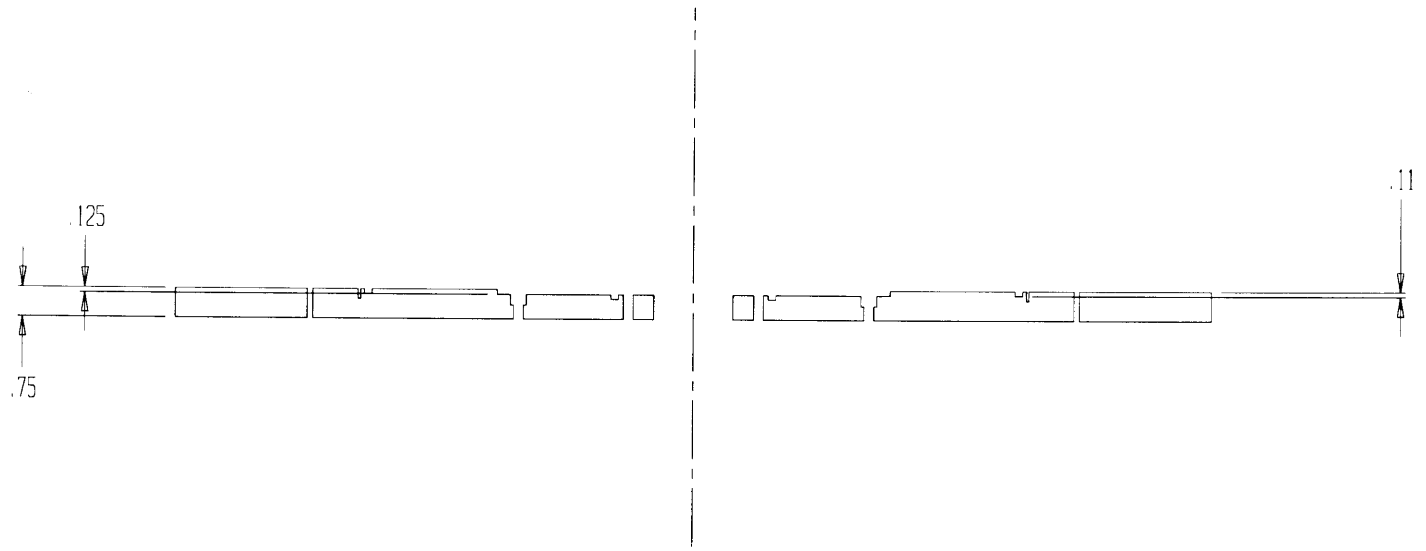

Note: Dimensions are in inches.

TOLERANCES

DECIMAL:	ANGULAR:
X/X = +-1/32	.X = +-.5 deg
.XX = +-.01	X = +- 1 deg
.XXX = +- .005	

	PART #: 4
PROJECT: Swirl Chamber (MS Project at MIT)	
PART NAME: Large Rib	
MATERIAL: PVC	
DRAWN BY: David Danitz	
REVISION DATE: 3/14/94	SHEET 5 OF 5

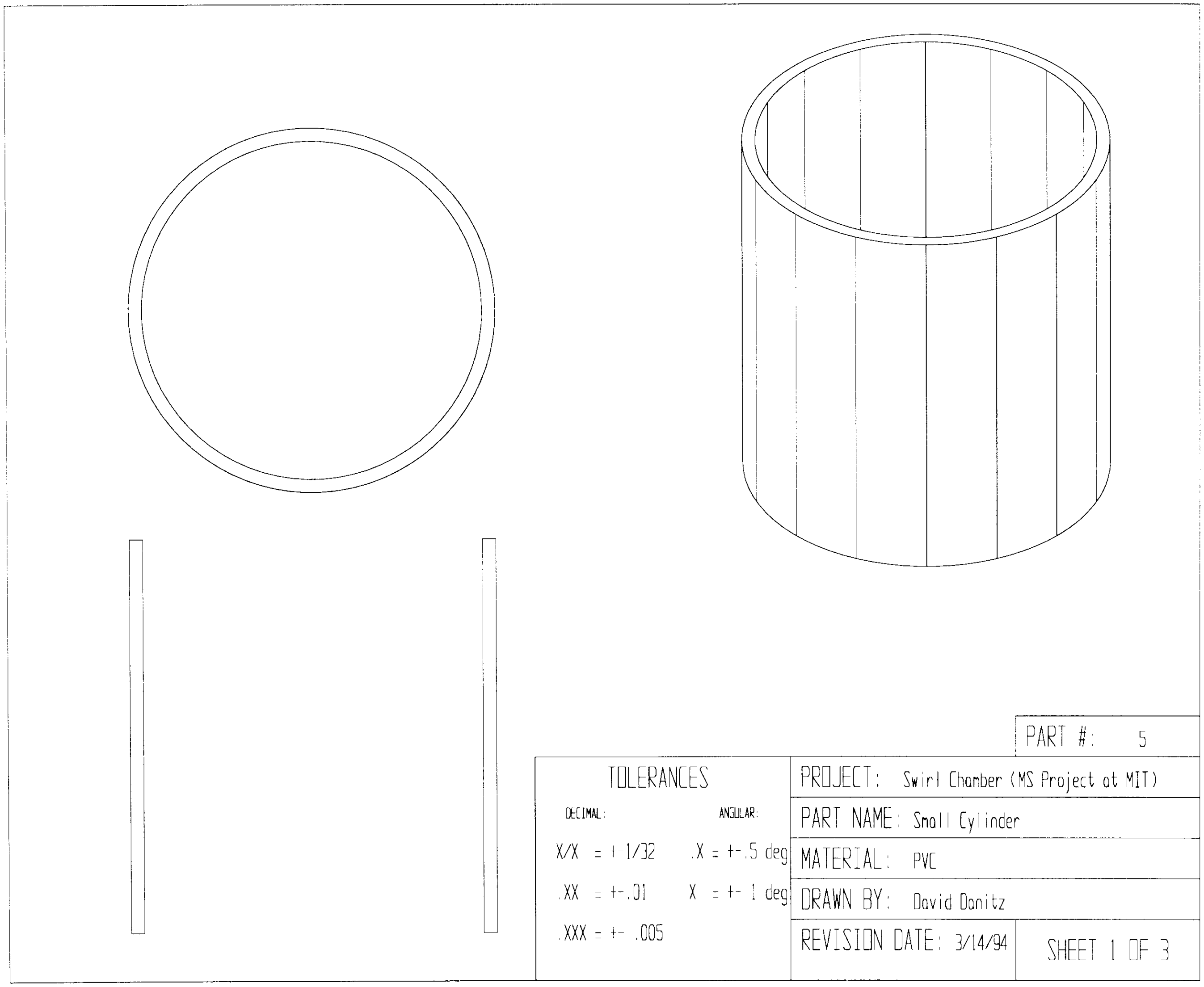

PART #: 5

PROJECT: Swirl Chamber (MS Project at MIT)

PART NAME: Small Cylinder

MATERIAL: PVC

DRAWN BY: David Danitz

REVISION DATE: 3/14/94

SHEET 1 OF 3

TOLERANCES

DECIMAL:	ANGULAR:
X/X = +-1/32	.X = +-.5 deg
.XX = +-.01	X = +- 1 deg
.XXX = +- .005	

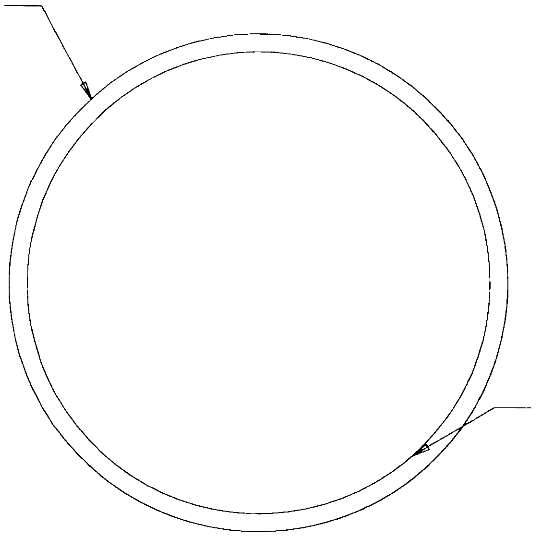

This cylinder has an
outside diameter of 10.75,
and an inside diameter of 9.976

The inside diameter must
be turned to 9.980.
The depth of the cut
is on the next page

TOLERANCES

DECIMAL:
X/X = +-1/32
.XX = +-.01
.XXX = +- .005

ANGULAR:
.X = +-.5 deg
X = +- 1 deg

PART #: 5
PROJECT: Swirl Chamber (MS Project at MIT)
PART NAME: Small Cylinder
MATERIAL: PVC
DRAWN BY: David Danitz
REVISION DATE: 3/14/94
SHEET 2 OF 3

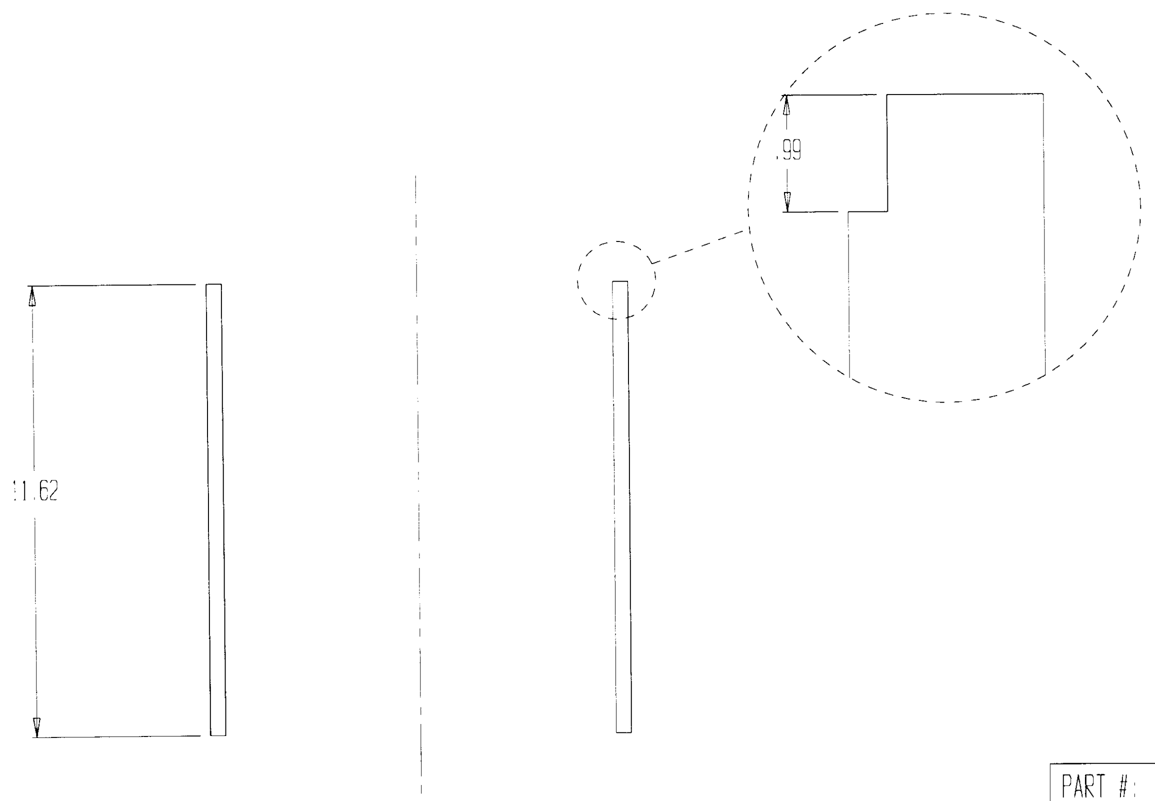

PART #: 5

TOLERANCES

DECIMAL:
X/X = +-1/32
.XX = +-.01
.XXX = +- .005

ANGULAR:
.X = +-.5 deg
X = +- 1 deg

PROJECT: Swirl Chamber (MS Project at MIT)
PART NAME: Small Cylinder
MATERIAL: PVC
DRAWN BY: David Danitz
REVISION DATE: 3/14/94

SHEET 3 OF 3

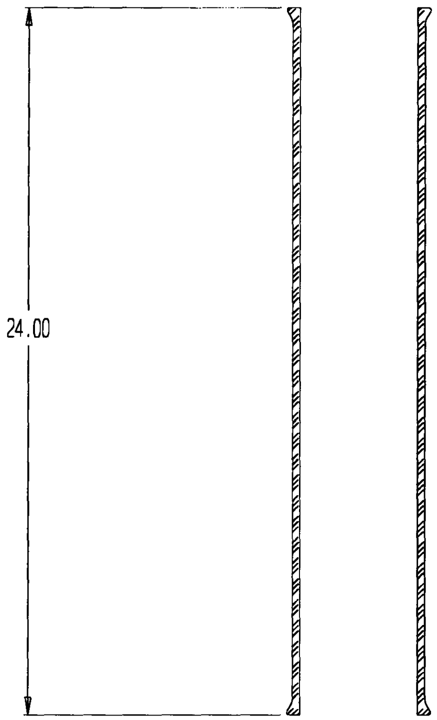

PART #: 6

TOLERANCES

DECIMAL: ANGULAR:

X/X = +-1/32 .X = +-.5 deg

.XX = +-.01 X = +- 1 deg

.XXX = +- .005

PROJECT: Swirl Chamber (MS Project at MIT)

PART NAME: Glass Test Section

MATERIAL: PVC

DRAWN BY: David Danitz

REVISION DATE: 3/14/94

SHEET 3 OF 3

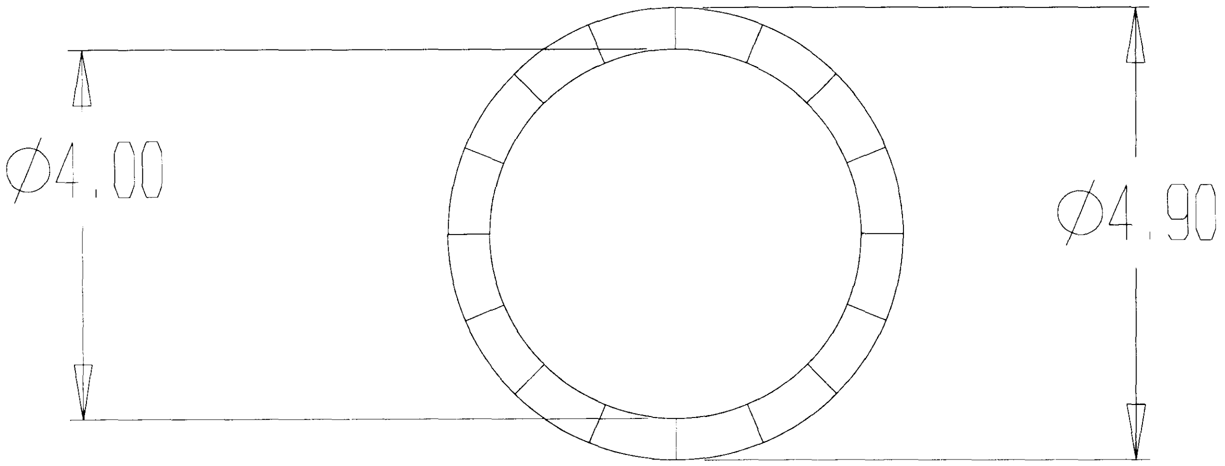

Note: Dimensions are in inches.

PART #: 6

TOLERANCES

DECIMAL:	ANGULAR:
X/X = +-1/32	.X = +-.5 deg
.XX = +-.01	X = +- 1 deg
.XXX = +- .005	

PROJECT: Swirl Chamber (MS Project at MIT)
PART NAME: Glass Test Section
MATERIAL: PVC
DRAWN BY: David Danitz
REVISION DATE: 3/14/94
SHEET 2 OF 3

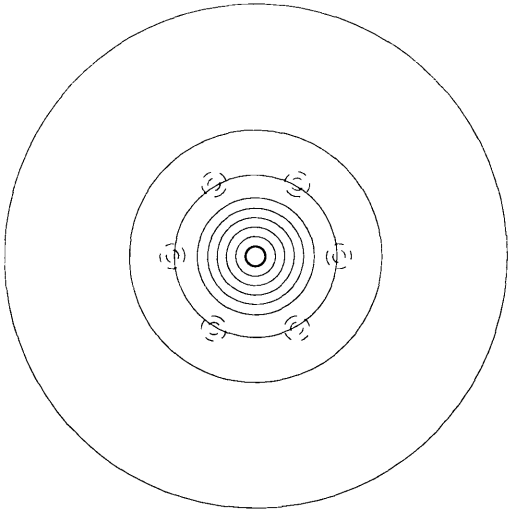

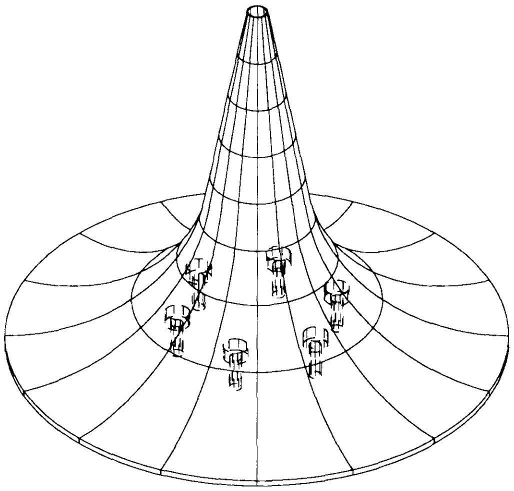

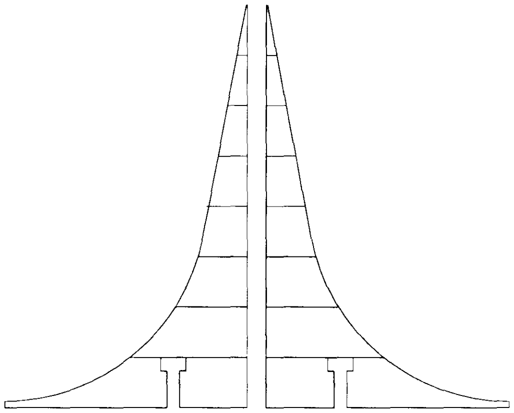

	PART #: 7
TOLERANCES	PROJECT: Swirl Chamber (MS Project at MIT)
DECIMAL: ANGULAR:	PART NAME: Center Mandrel
X/X = +-1/32 .X = +-.5 deg	MATERIAL: PVC
.XX = +-.01 X = +-1 deg	DRAWN BY: David Donitz
.XXX = +-.005	REVISION DATE: 3/14/94 SHEET 1 OF 3

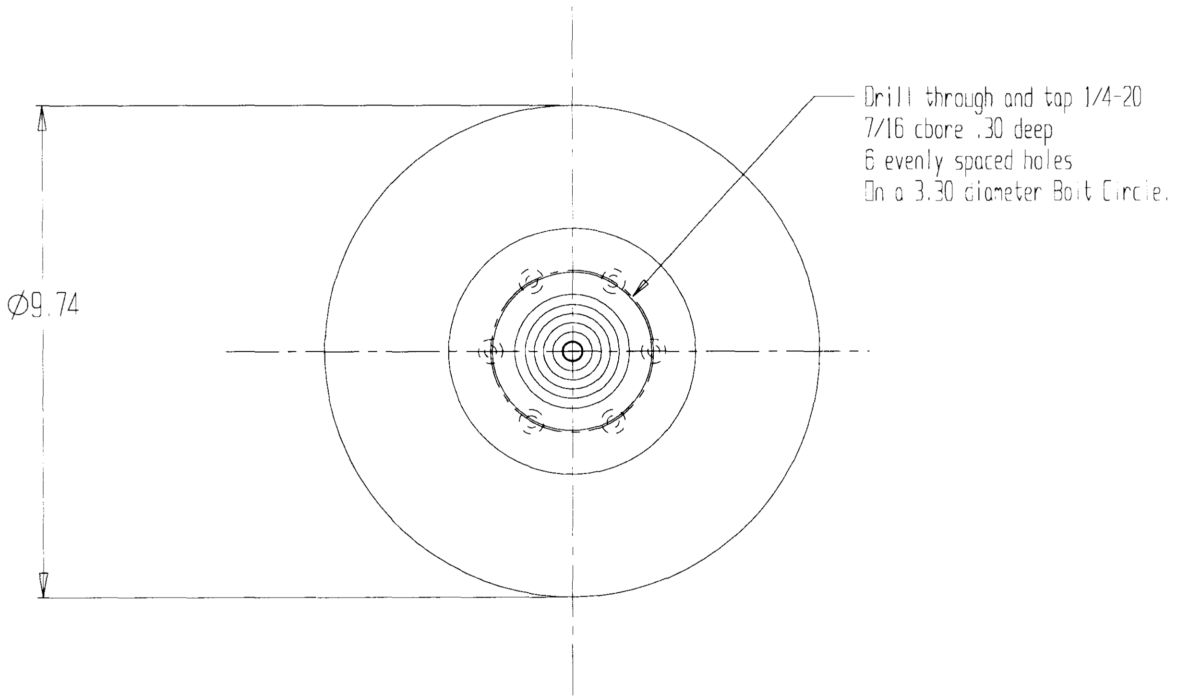

TOLERANCES

DECIMAL:
X/X = +-1/32
.XX = +-.01
.XXX = +- .005

ANGULAR:
.X = +-.5 deg
X = +- 1 deg

PART #: 7

PROJECT: Swirl Chamber (MS Project at MIT)

PART NAME: Center Mandrel

MATERIAL: PVC

DRAWN BY: David Donitz

REVISION DATE: 3/14/94

SHEET 1 OF 3

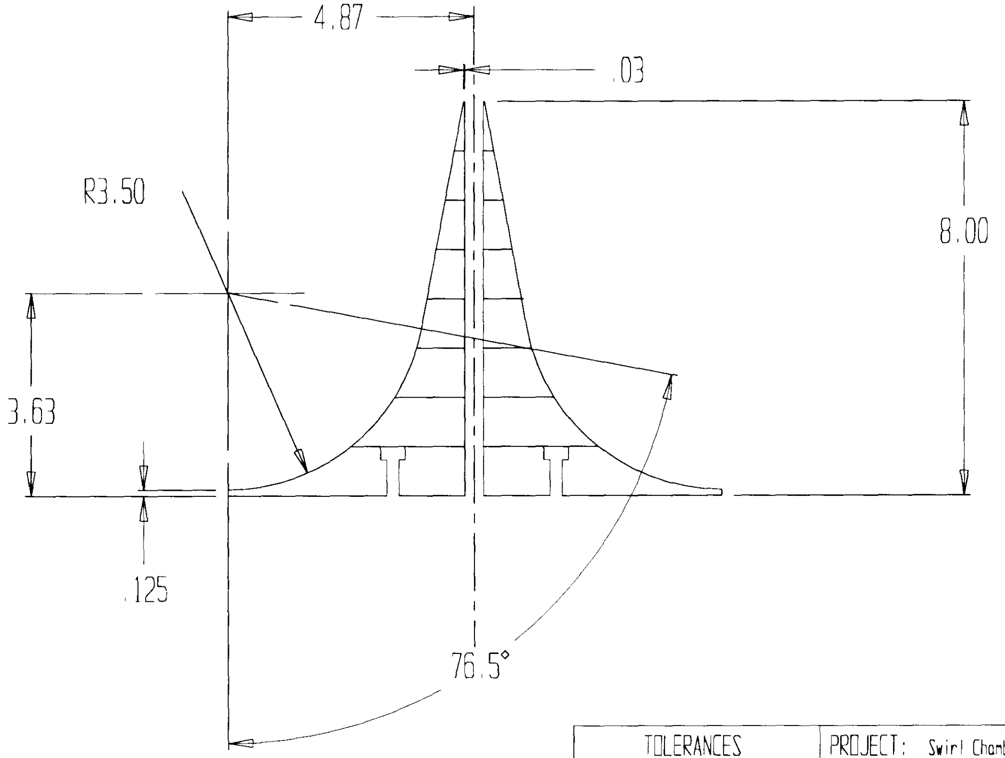

PART #: 7

TOLERANCES

DECIMAL:
X/X = +-1/32
.XX = +-.01
.XXX = +- .005

ANGULAR:
.X = +-.5 deg
X = +- 1 deg

PROJECT: Swirl Chamber (MS Project at MIT)

PART NAME: Center Mandrel

MATERIAL: PVC

DRAWN BY: David Danitz

REVISION DATE: 3/14/94

SHEET 3 OF 3

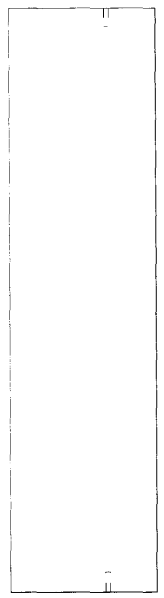

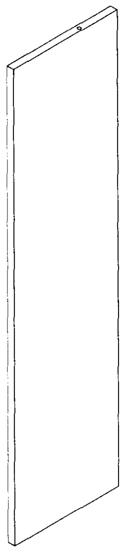

PART #: 8

TOLERANCES	
DECIMAL:	ANGULAR:
X/X = +-1/32	.X = +-.5 deg
.XX = +-.01	X = +-1 deg
.XXX = +- .005	

PROJECT: Swirl Chamber (MS Project at MIT)

PART NAME: Vane

MATERIAL: PVC

DRAWN BY: David Danitz

REVISION DATE: 4/1/94

SHEET 1 OF 3

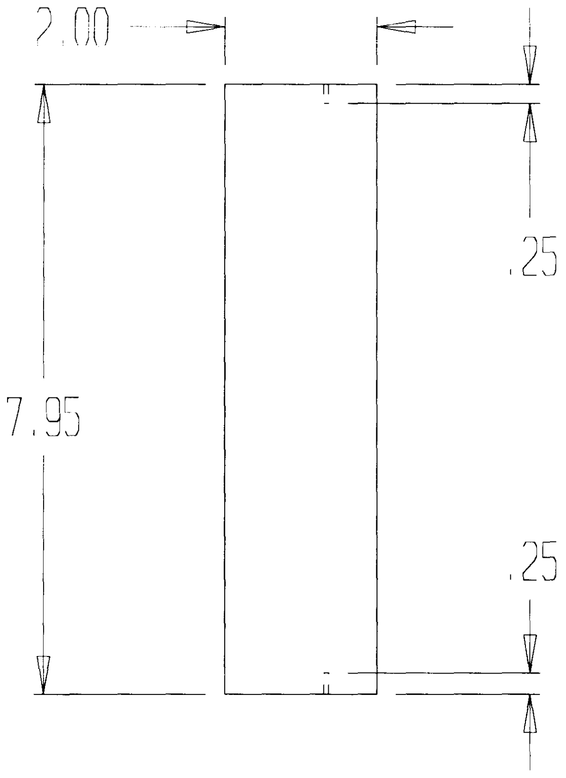

TOLERANCES

DECIMAL: ANGULAR

X/X = +-1/32 .X = +-.5 deg

.XX = +-.01 X _ +- 1 deg

.XXX = +- .005

PART #: 8

PROJECT: Swirl Chamber (MS Project at MIT)

PART NAME: Vane

MATERIAL: PVC

DRAWN BY: David Danitz

REVISION DATE: 4/1/94

SHEET 2 OF 3

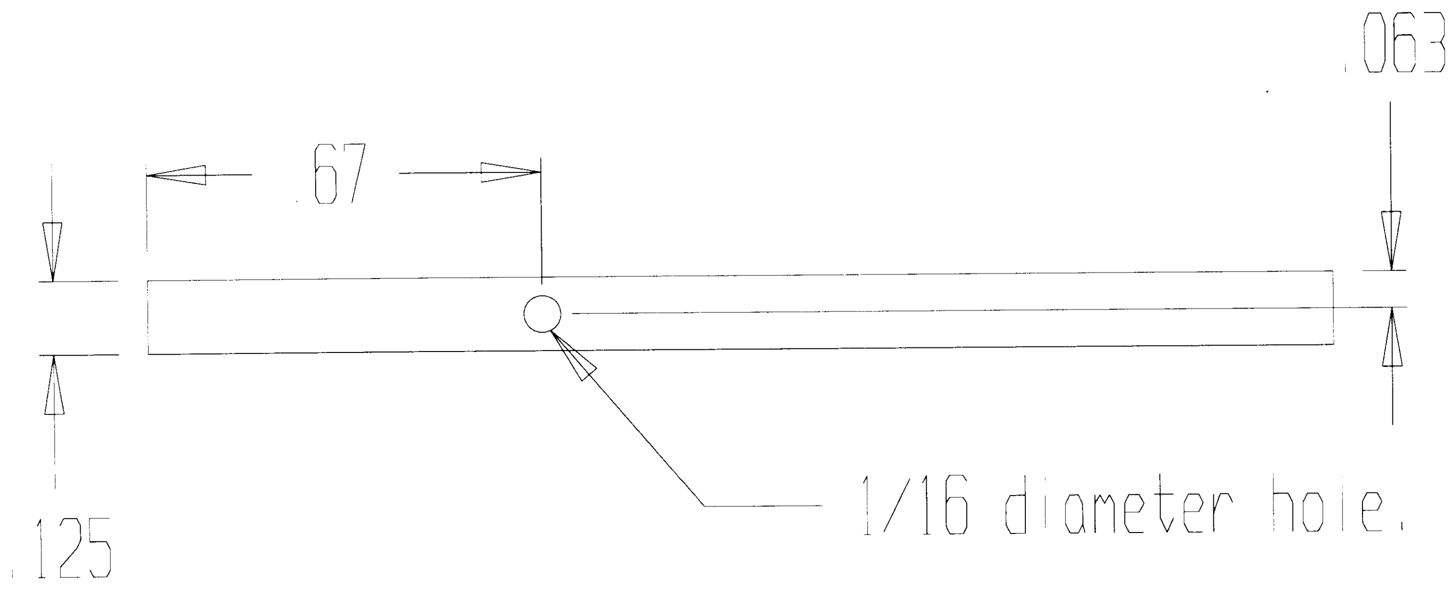

Note: Dimensions are in inches.

	PART #: 8
TOLERANCES	PROJECT: Swirl Chamber (MS Project at MIT)
DECIMAL: ANGULAR:	PART NAME: Vane
X/X = +-1/32 .X = +-.5 deg	MATERIAL: PVC
.XX = +-.01 X = +-1 deg	DRAWN BY: David Danitz
.XXX = +- .005	REVISION DATE: 4/1/94 SHEET 3 OF 3

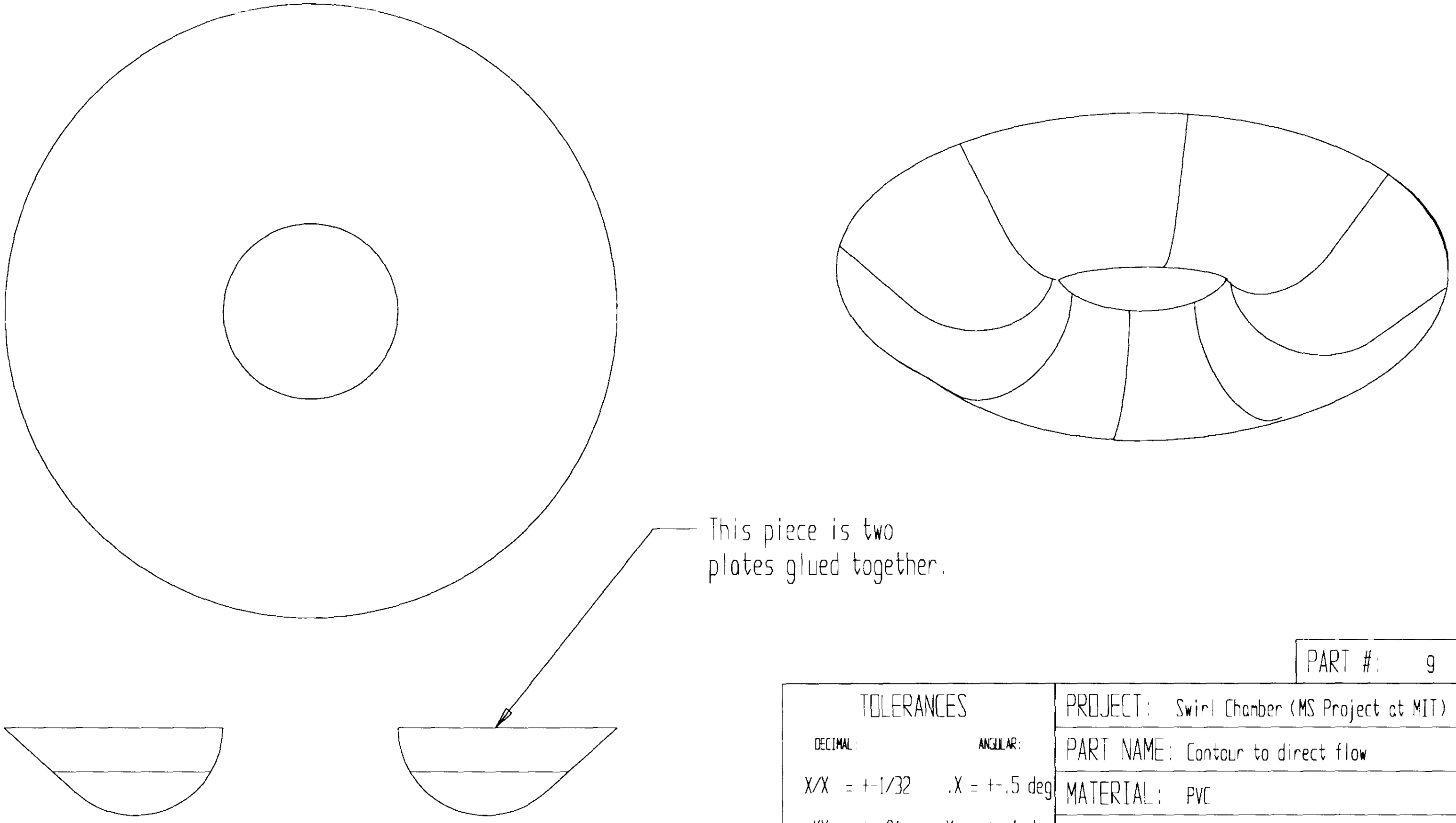

This piece is two plates glued together.

	PART #: 9
PROJECT:	Swirl Chamber (MS Project at MIT)
PART NAME:	Contour to direct flow
MATERIAL:	PVC
DRAWN BY:	David Danitz
REVISION DATE: 3/14/94	SHEET 1 OF 3

TOLERANCES

DECIMAL:	ANGULAR:
X/X = +-1/32	.X = +-.5 deg
.XX = +-.01	X = +- 1 deg
.XXX = +- .005	

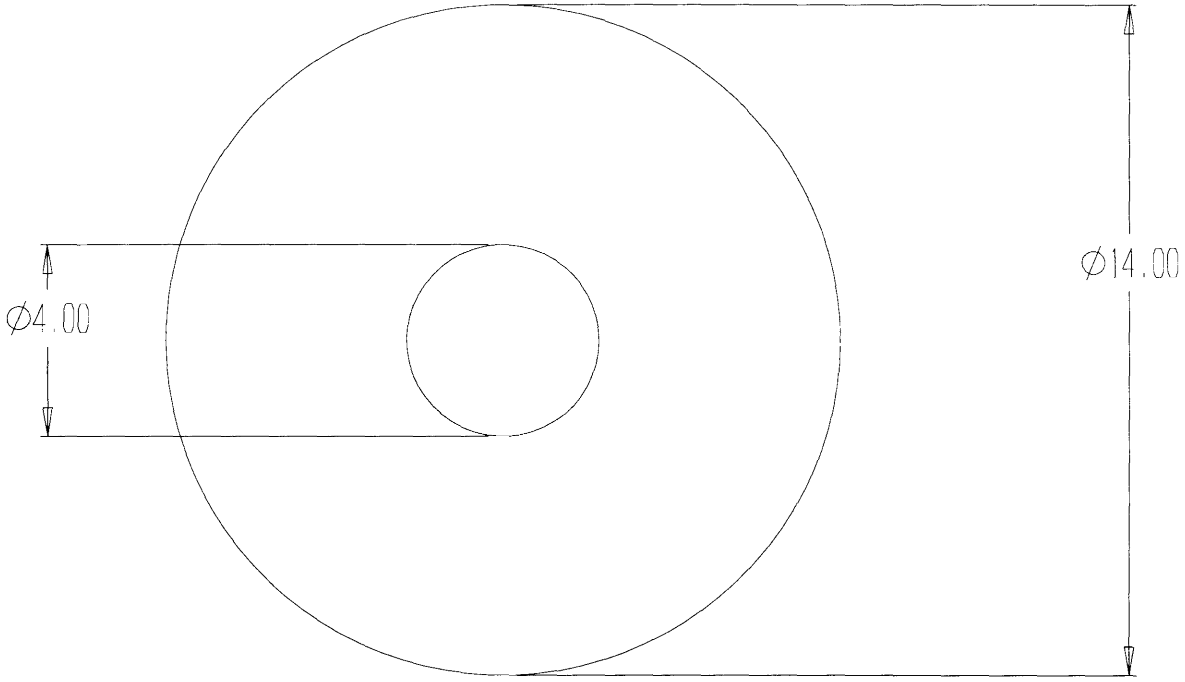

PART #: 9

TOLERANCES

DECIMAL: ANGULAR:

X/X = +-1/32 .X = +-.5 deg

.XX = +-.01 X = +- 1 deg

.XXX = +- .005

PROJECT: Swirl Chamber (MS Project at MIT)

PART NAME: Contour to direct flow

MATERIAL: PVC

DRAWN BY: David Danitz

REVISION DATE: 3/14/94

SHEET 2 OF 3

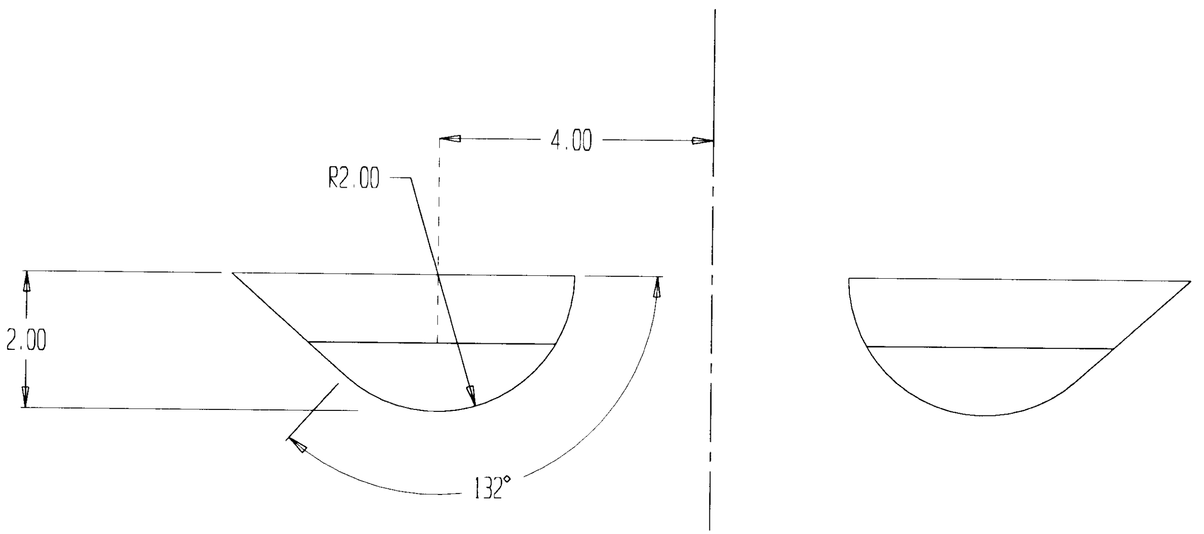

PART #: 9

PROJECT: Swirl Chamber (MS Project at MIT)

PART NAME: Contour to direct flow

MATERIAL: PVC

DRAWN BY: David Danitz

REVISION DATE: 3/14/94

SHEET 3 OF 3

TOLERANCES

DECIMAL:	ANGULAR:
X/X = +-1/32	.X = +-.5 deg
.XX = +-.01	X = +- 1 deg
.XXX = +- .005	

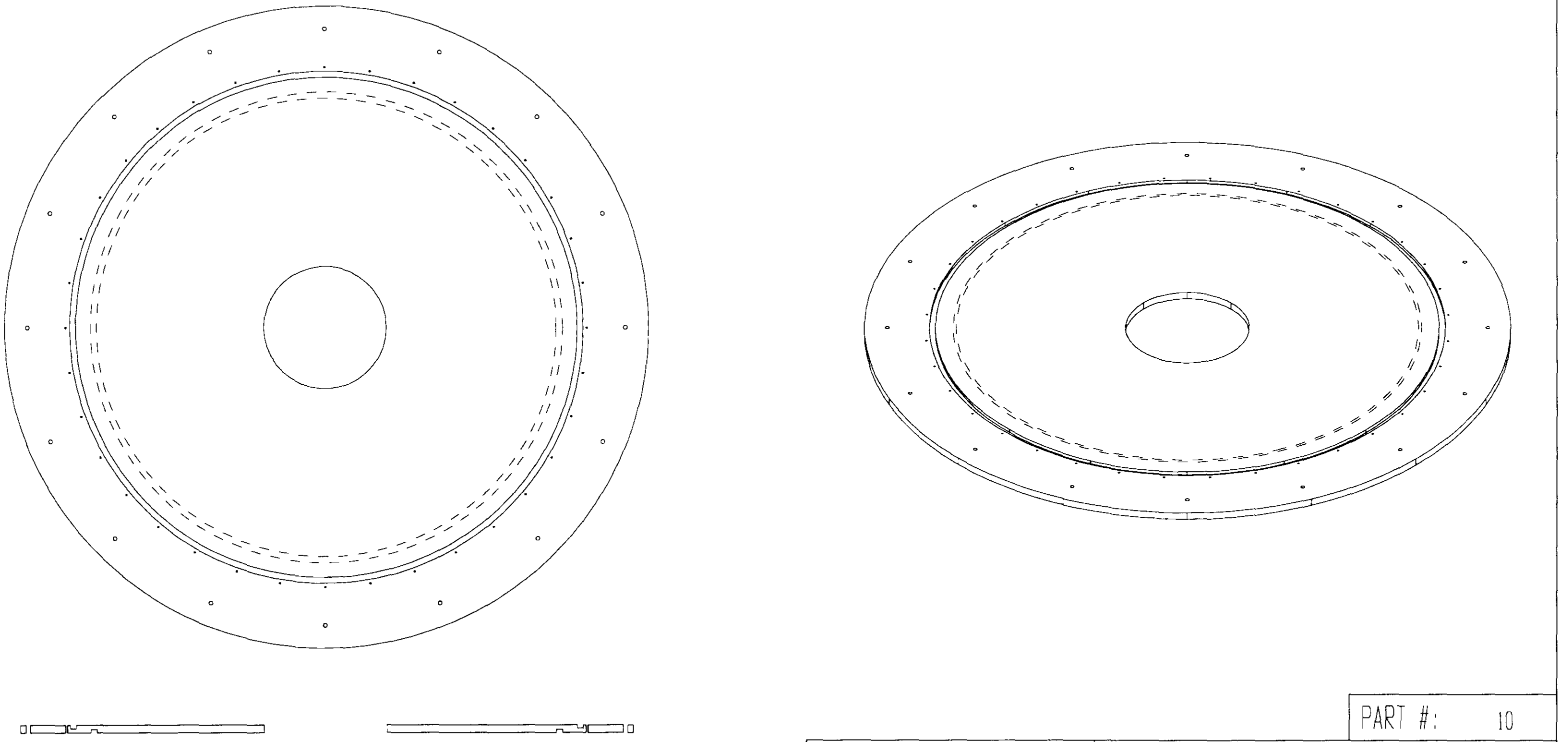

PART #: 10

TOLERANCES	
DECIMAL:	ANGULAR:
X/X = +-1/32	.X = +-.5 deg
.XX = +-.01	X = +-1 deg
.XXX = +- .005	

PROJECT: Swirl Chamber (MS Project at MIT)

PART NAME: Vane Cover

MATERIAL: PVC

DRAWN BY: David Danitz

REVISION DATE: 4/4/94

SHEET 1 OF 4

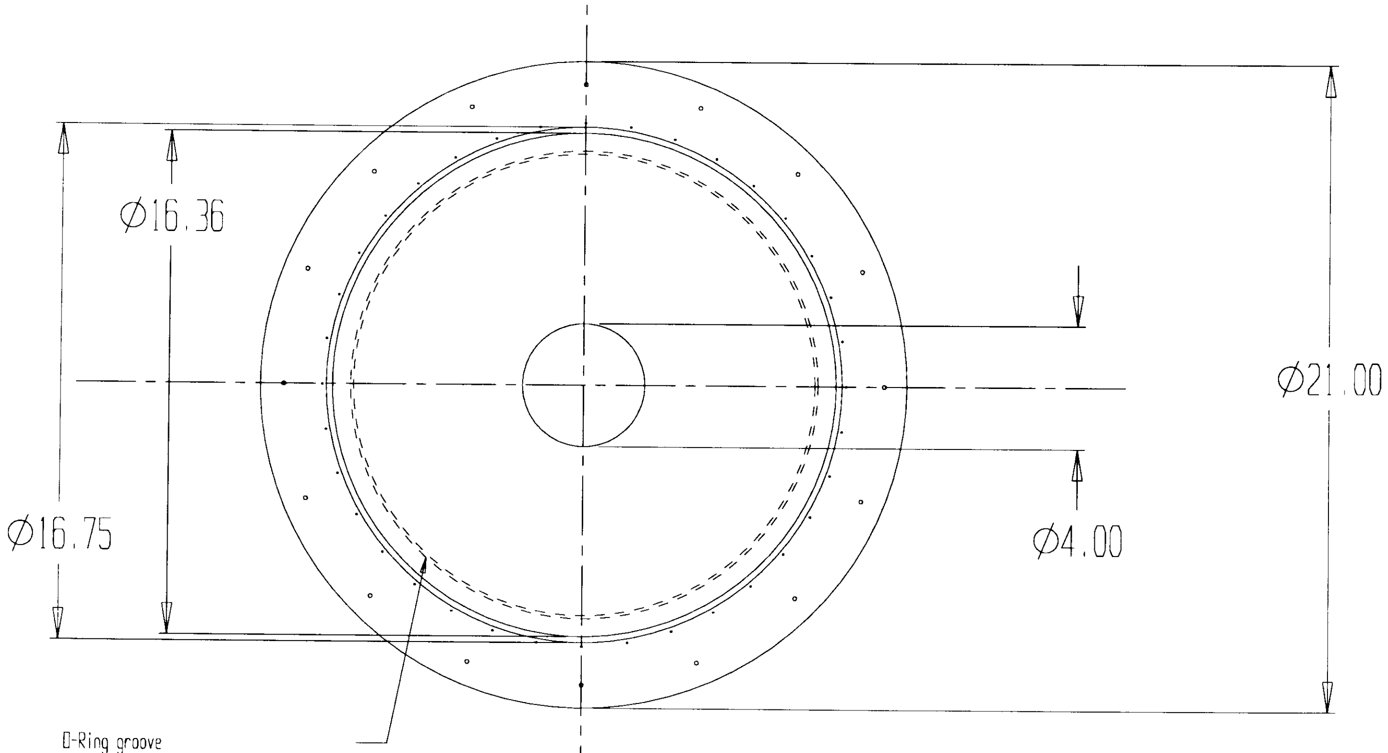

O-Ring groove
Outside wall diameter is 15.00
Inside wall diameter is 15.40
Depth is .10 in.
NOTE: O-Ring groove is on back side!

Note: Dimensions are in inches.

TOLERANCES

DECIMAL:	ANGULAR
X/X = +-1/32	.X = +-.5 deg
.XX = +-.01	X = +- 1 deg
.XXX = +- .005	

PART #: 10
PROJECT: Swirl Chamber (MS Project at MIT)
PART NAME: Vane Cover
MATERIAL: PVC
DRAWN BY: David Danitz
REVISION DATE: 4/4/94
SHEET 2 OF 4

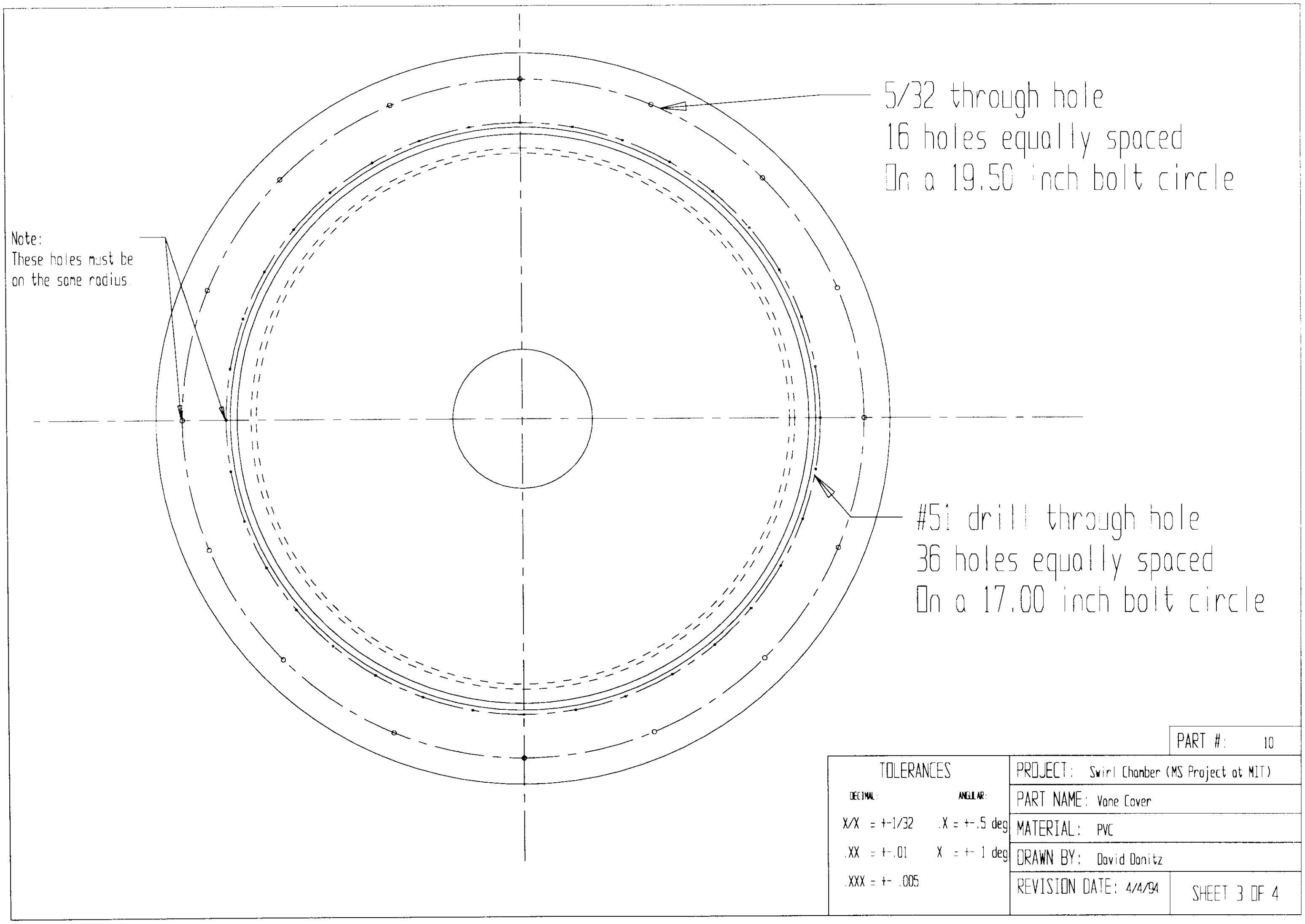
5/32 through hole
16 holes equally spaced
On a 19.50 inch bolt circle
#51 drill through hole
36 holes equally spaced
On a 17.00 inch bolt circle
Note:
These holes must be
on the same radius
PART #: 10
TOLERANCES
DECIMAL:
ANGULAR:
X/X = +-1/32
.X = +-.5 deg
.XX = +-.01
X = +- 1 deg
.XXX = +- .005
PROJECT: Swirl Chamber (MS Project at MIT)
PART NAME: Vane Cover
MATERIAL: PVC
DRAWN BY: David Danitz
REVISION DATE: 4/4/94
SHEET 3 OF 4

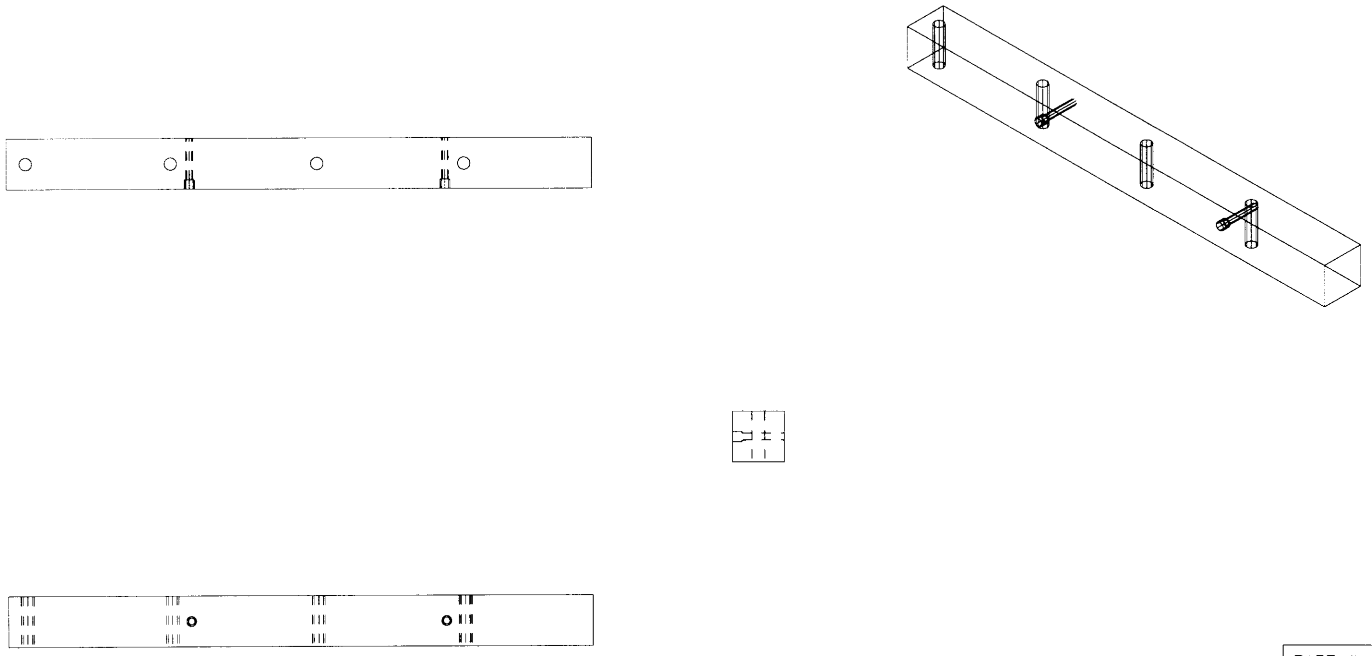

PART #: 11a

TOLERANCES		
DECIMAL:	ANGULAR:	
X/X = +-1/32	.X = +-.5 deg	PROJECT: Swirl Chamber (MS Project at MIT)
.XX = +-.01	X = +- 1 deg	PART NAME: Viewing Reservoir Base
.XXX = +- .005		MATERIAL: Clear Acrylic
		DRAWN BY: David Danitz
		REVISION DATE: 4/1/94

SHEET 1 OF 4

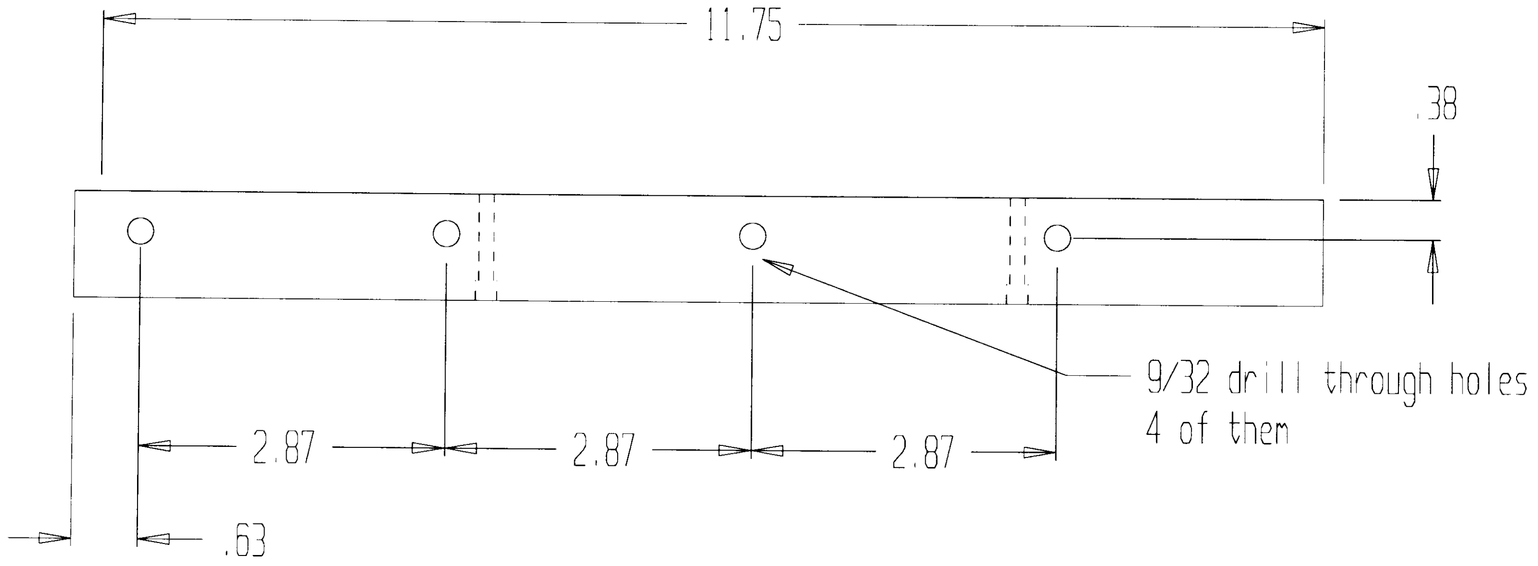

Note: All dimensions are in inches.

TOLERANCES

DECIMAL:
X/X = +-1/32
.XX = +-.01
.XXX = +-.005

ANGULAR:
.X = +-.5 deg
X = +-1 deg

PART #: 11a

PROJECT: Swirl Chamber (MS Project at MIT)

PART NAME: Viewing Reservoir Base

MATERIAL: Clear Acrylic

DRAWN BY: David Danitz

REVISION DATE: 4/1/94

SHEET 2 OF 4

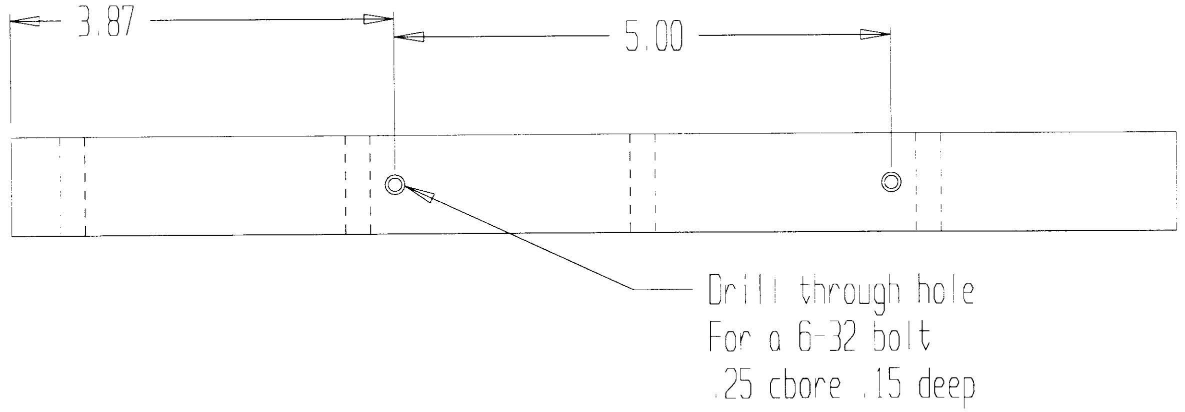

Note: All dimensions are in inches.

TOLERANCES

DECIMAL:
X/X = +-1/32
.XX = +-.01
.XXX = +- .005

ANGULAR:
.X = +-.5 deg
X = +- 1 deg

PART #: 11a
PROJECT: Swirl Chamber (MS Project at MIT)
PART NAME: Viewing Reservoir Base
MATERIAL: Clear Acrylic
DRAWN BY: David Donitz
REVISION DATE: 4/1/94
SHEET 3 OF 4

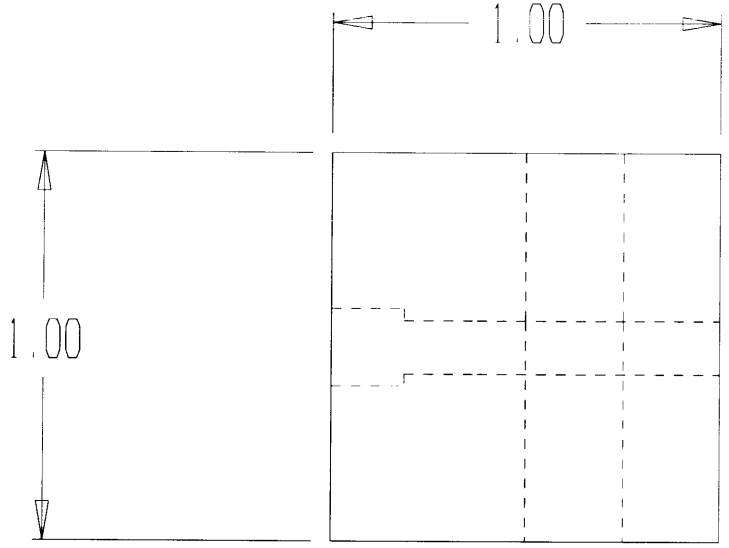

Note: All dimensions are in inches.

TOLERANCES

DECIMAL: ANGULAR:

X/X = +-1/32 .X = +-.5 deg

XX = +-.01 X = +- 1 deg

.XXX = +- .005

PART #: 11a

PROJECT: Swirl Chamber (MS Project at MIT)

PART NAME: Viewing Reservoir Base

MATERIAL: Clear Acrylic

DRAWN BY: David Danitz

REVISION DATE: 4/1/94

SHEET 4 OF 4

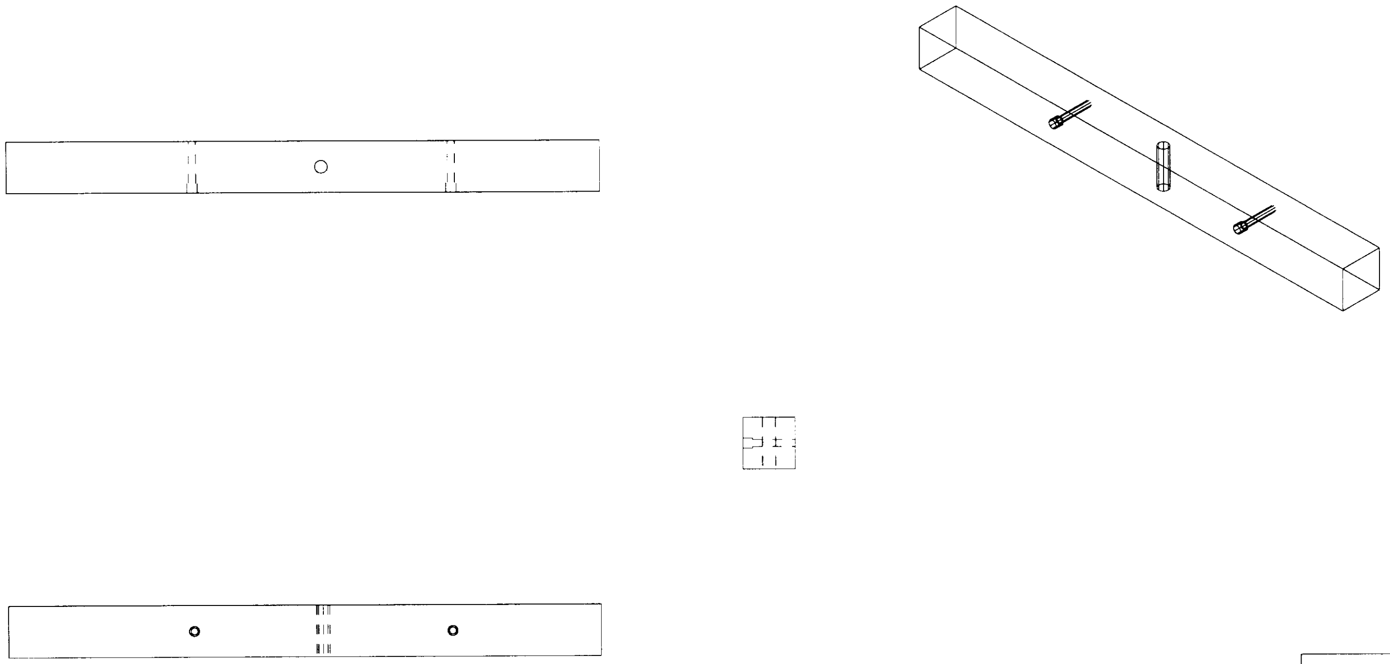

		PART #: 11b
TOLERANCES	PROJECT: Swirl Chamber (MS Project at MIT)	
DECIMAL: ANGULAR:	PART NAME: Viewing Reservoir Base	
X/X = +-1/32 .X = +-.5 deg	MATERIAL: Clear Acrylic	
.XX = +-.01 X = +- 1 deg	DRAWN BY: David Danitz	
.XXX = +- .005	REVISION DATE: 4/1/94	SHEET 1 OF 2

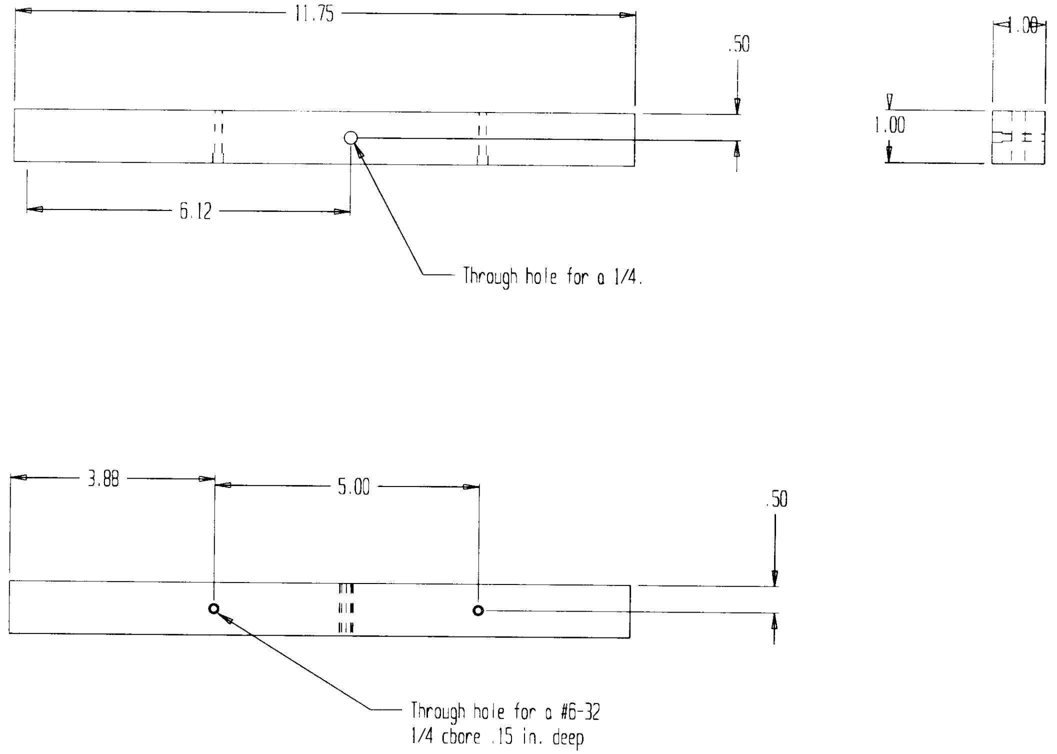

Through hole for a 1/4.

Through hole for a #6-32
1/4 cbore .15 in. deep

Note: Dimensions are in inches.

TOLERANCES

DECIMAL:	ANGULAR:
X/X = +-1/32	.X = +-.5 deg
.XX = +-.01	X = +- 1 deg
.XXX = +- .005	

PART #: 11b
PROJECT: Swirl Chamber (MS Project at MIT)
PART NAME: Viewing Reservoir Base
MATERIAL: Clear Acrylic
DRAWN BY: David Danitz
REVISION DATE: 4/1/94
SHEET 2 OF 2

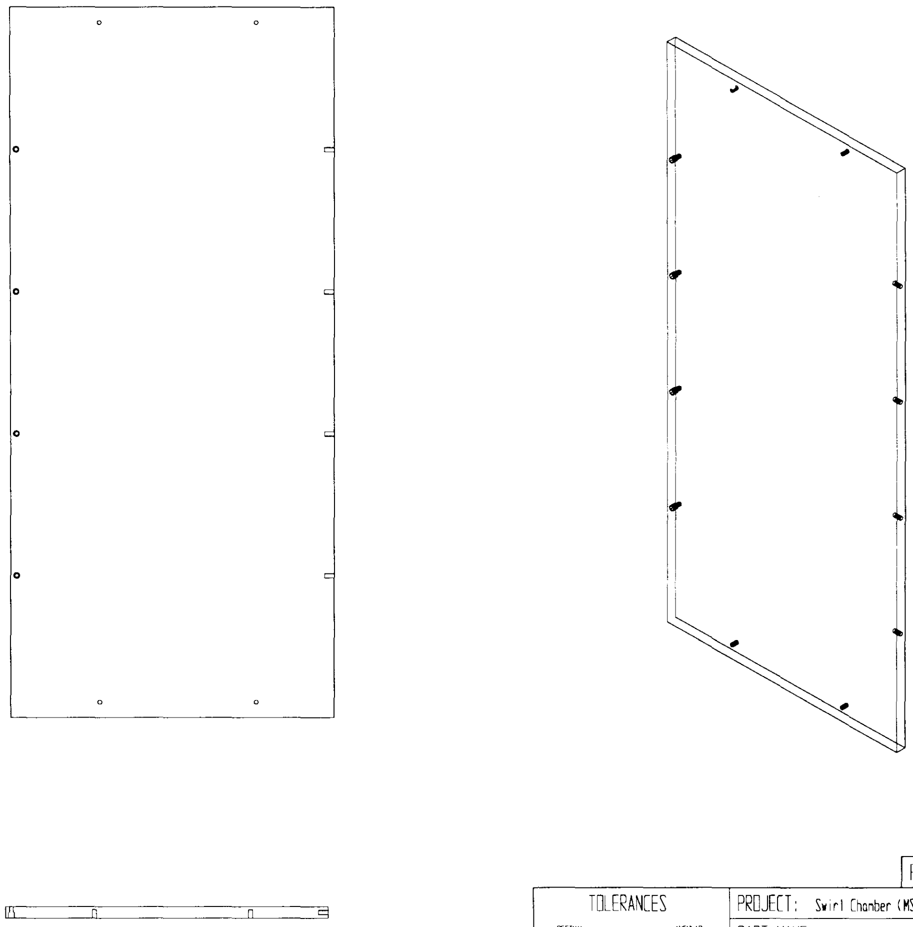

PART #:	11c

TOLERANCES

DECIMAL:	ANGULAR:
X/X = +-1/32	.X = +-.5 deg
.XX = +-.01	X = +-1 deg
.XXX = +- .005	

PROJECT: Swirl Chamber (MS Project at MIT)

PART NAME: Side viewing panels

MATERIAL: Clear acrylic

DRAWN BY: David Danitz

REVISION DATE: 4/1/94

SHEET 1 OF 3

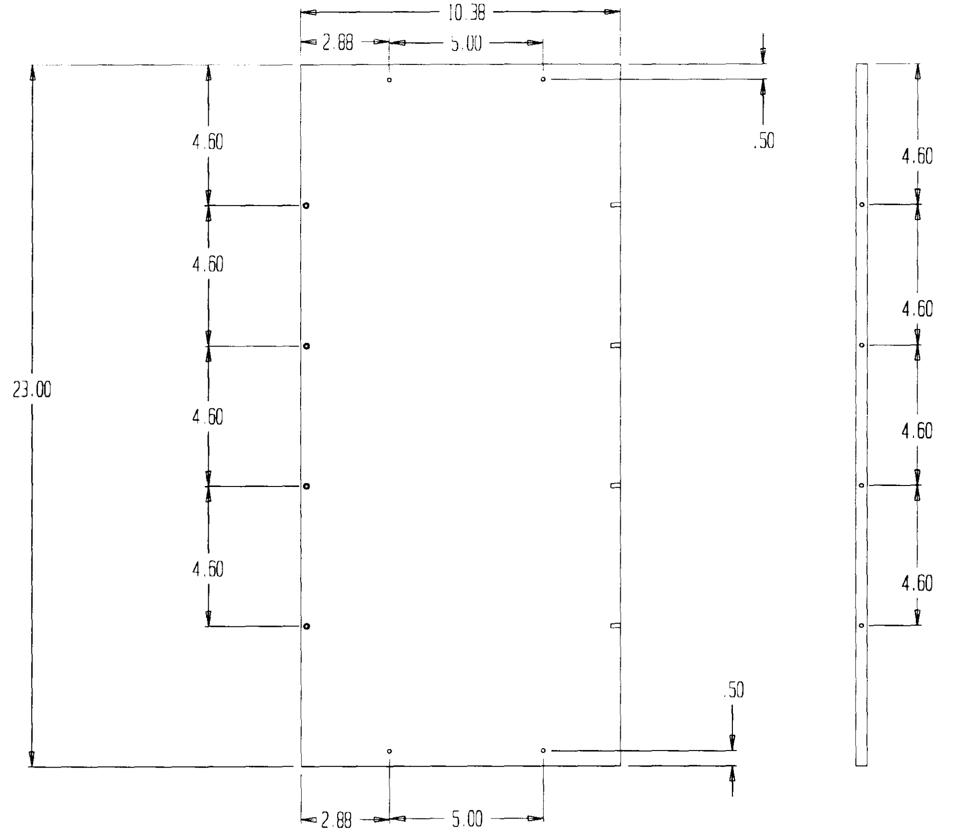

Note: Dimensions are in inches.

PART #: 11c

TOLERANCES

DECIMAL:
X/X = +-1/32
.XX = +-.01
.XXX = +- .005

ANGULAR:
.X - +-.5 deg
X = +- 1 deg

PROJECT: Swirl Chamber (MS Project at MIT)
PART NAME: Side viewing panels
MATERIAL: Clear acrylic
DRAWN BY: David Danitz
REVISION DATE: 4/1/94
SHEET 2 OF 3

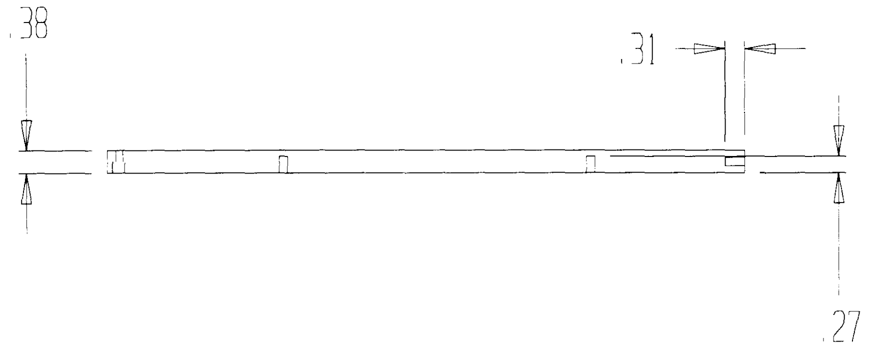

Note: Dimensions are in inches.

TOLERANCES
DECIMAL: ANGULAR:
X/X = +-1/32 .X = +-.5 deg
.XX = +-.01 X = +-1 deg
.XXX = +- .005

PART #: 11c
PROJECT: Swirl Chamber (MS Project at MIT)
PART NAME: Side viewing panels
MATERIAL: Clear acrylic
DRAWN BY: David Donitz
REVISION DATE: 4/1/94
SHEET 3 OF 3

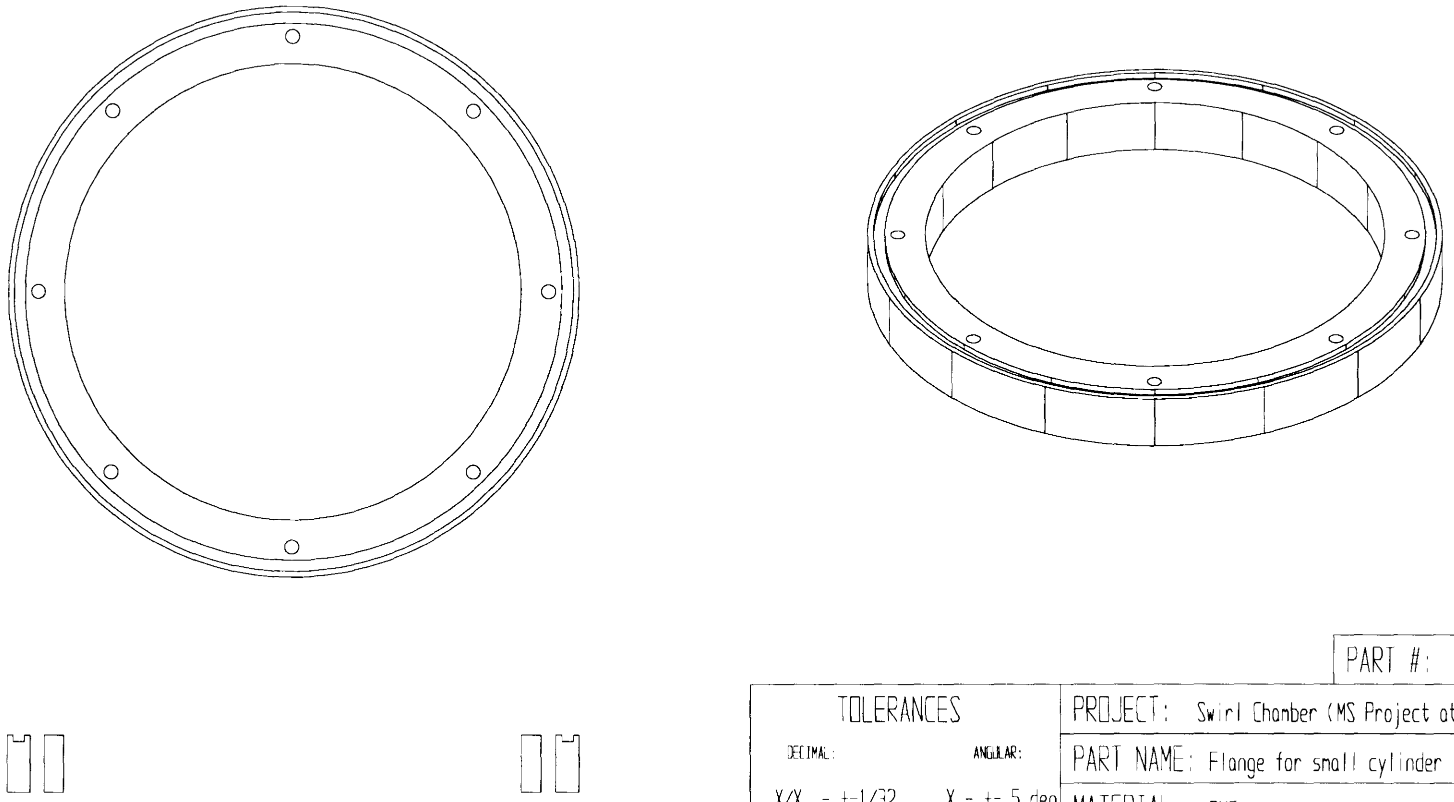

		PART #: 12
TOLERANCES	PROJECT: Swirl Chamber (MS Project at MIT)	
DECIMAL: ANGULAR:	PART NAME: Flange for small cylinder	
X/X = +-1/32 .X = +-.5 deg	MATERIAL: PVC	
.XX = +-.01 X = +- 1 deg	DRAWN BY: David Danitz	
.XXX = +- .005	REVISION DATE: 3/14/94	SHEET 1 OF 3

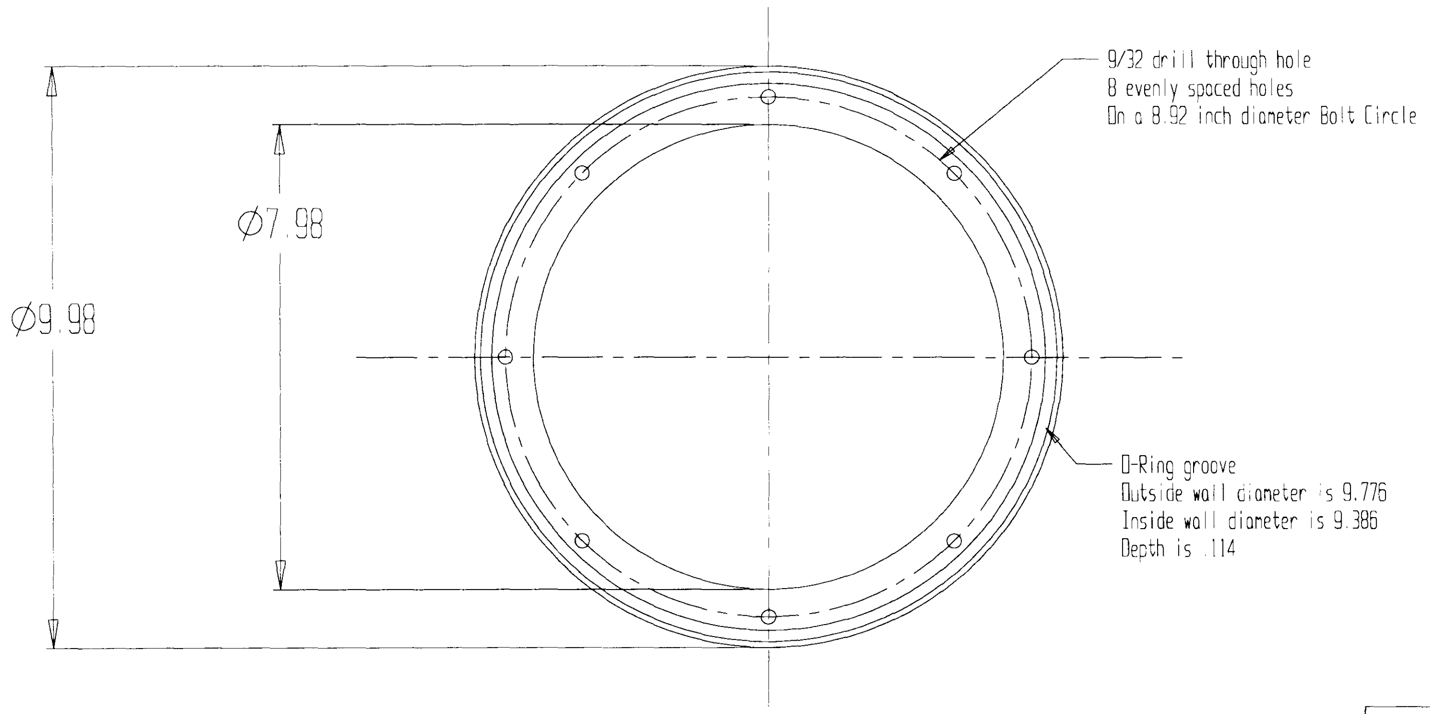

PART #: 12

TOLERANCES

DECIMAL:

X/X = +-1/32

.XX = +-.01

.XXX = +- .005

ANGULAR:

.X = +-.5 deg

X = +- 1 deg

PROJECT: Swirl Chamber (MS Project at MIT)

PART NAME: Flange for small cylinder

MATERIAL: PVC

DRAWN BY: David Danitz

REVISION DATE: 3/14/94

SHEET 2 OF 3

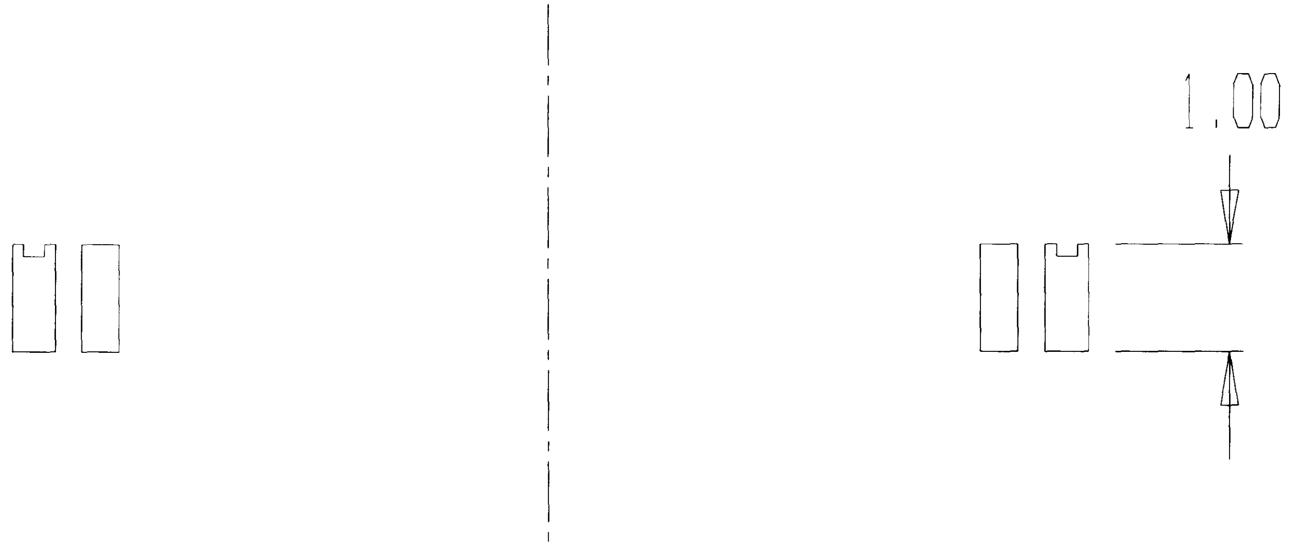

Note: Dimensions are in inches.

TOLERANCES

DECIMAL:		ANGULAR:	
X/X	= +-1/32	.X	= +-.5 deg
.XX	= +-.01	X	= +- 1 deg
.XXX	= +- .005		

PART #: 12

PROJECT: Swirl Chamber (MS Project at MIT)

PART NAME: Flange for small cylinder

MATERIAL: PVC

DRAWN BY: David Danitz

REVISION DATE: 3/14/94

SHEET 3 OF 3

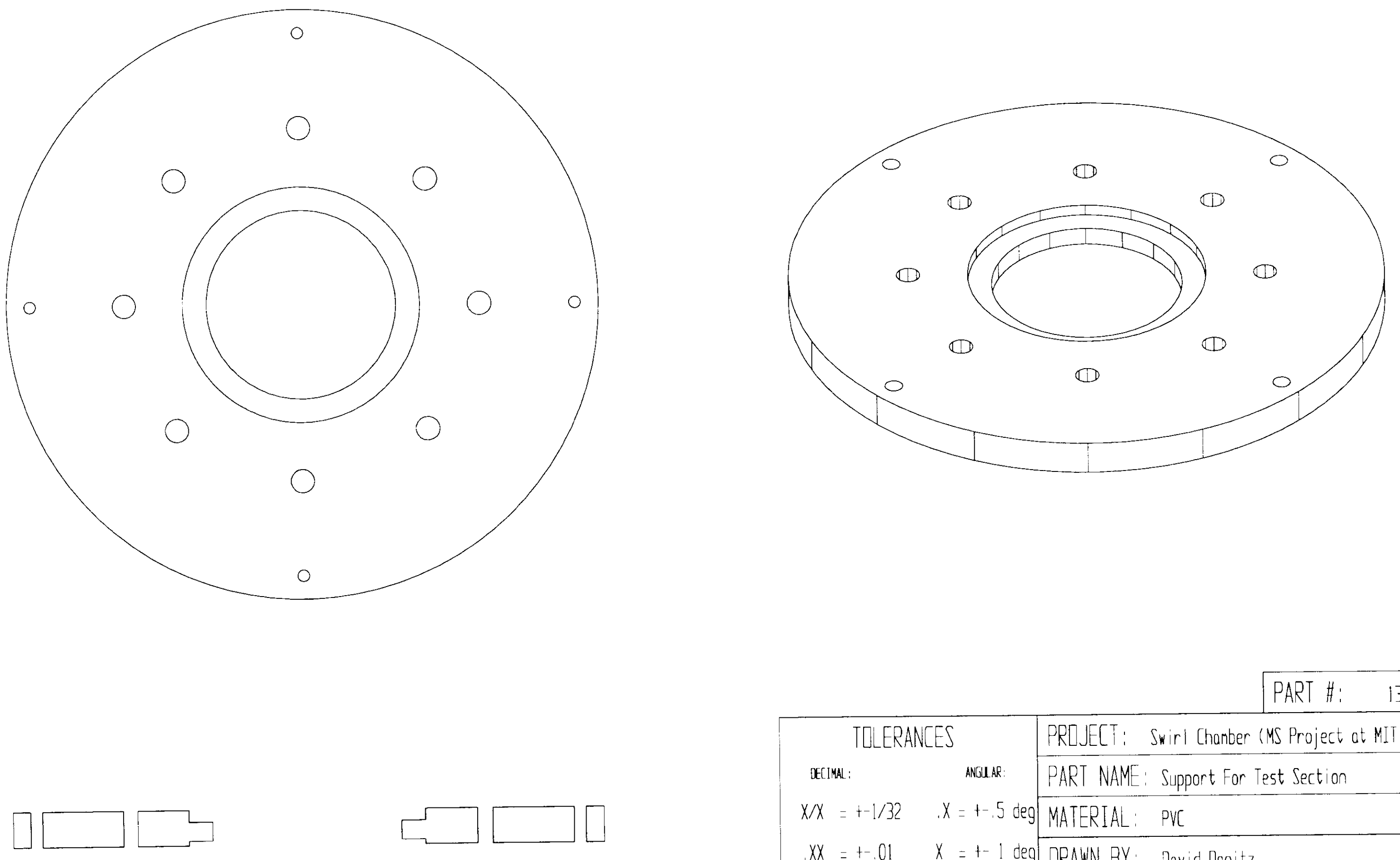

	PART #: 13
TOLERANCES	PROJECT: Swirl Chamber (MS Project at MIT)
DECIMAL: ANGULAR:	PART NAME: Support For Test Section
X/X = +-1/32 .X = +-.5 deg	MATERIAL: PVC
.XX = +-.01 X = +-1 deg	DRAWN BY: David Danitz
.XXX = +- .005	REVISION DATE: 3/31/94 SHEET 1 OF 4

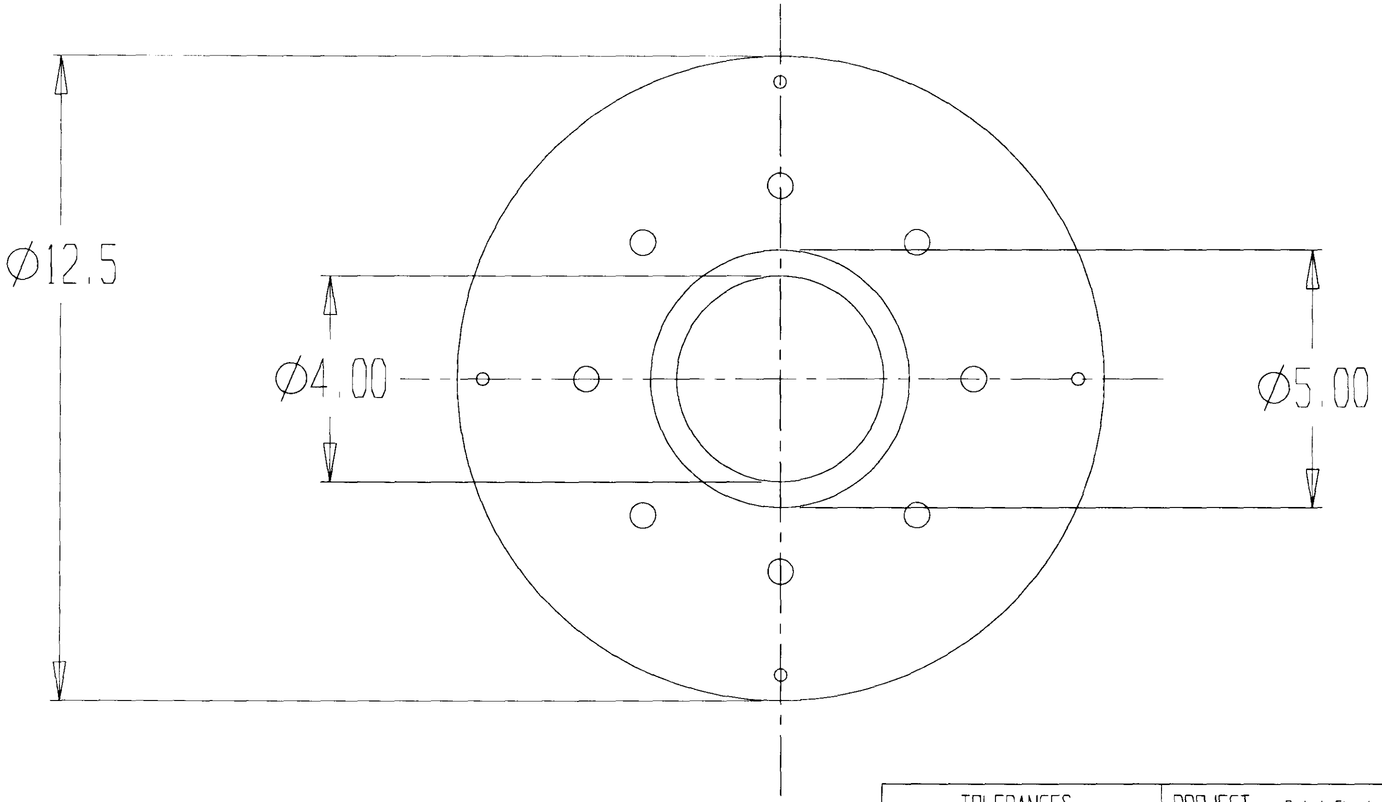

Note: dimensions are in inches.

PART #: 13

TOLERANCES		
DECIMAL:	ANGULAR:	PROJECT: Swirl Chamber (MS Project at MIT)
X/X = +-1/32	.X = +-.5 deg	PART NAME: Support For Test Section
.XX = +-.01	X = +- 1 deg	MATERIAL: PVC
.XXX = +- .005		DRAWN BY: David Danitz
		REVISION DATE: 3/31/94

SHEET 2 OF 4

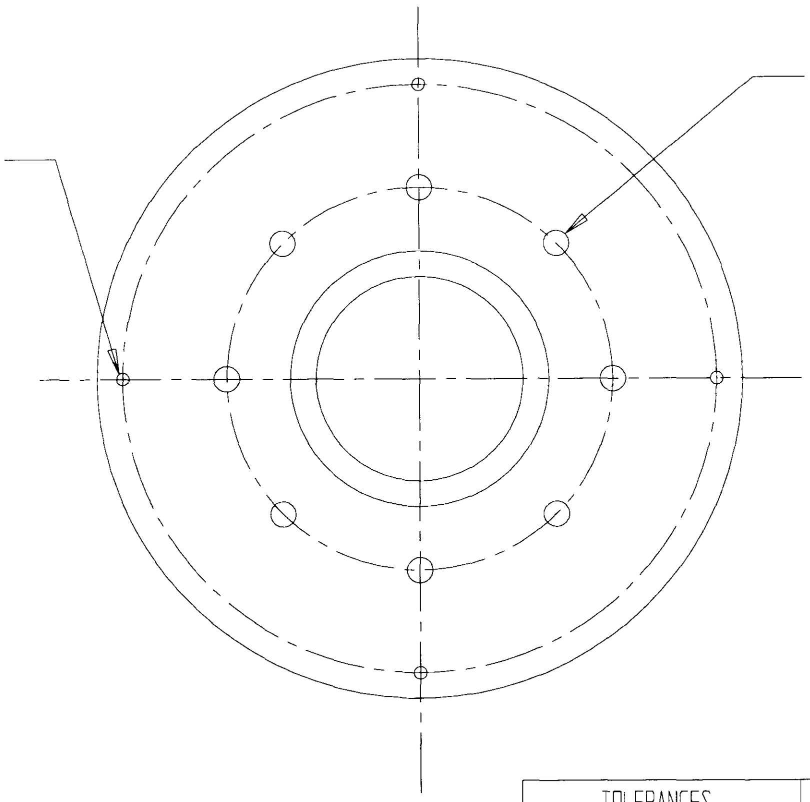

1/4 drill through hole
4 evenly spaced holes
On a 11.5 inch Bolt Circle

Drill through hole for
A 5/16 bolt
8 evenly spaced holes
On a 7.48 diameter Bolt Circle

Note: Dimensions are in inches.

TOLERANCES

DECIMAL:	ANGULAR:
X/X = +-1/32	.X = +- 5 deg
.XX = +-.01	X = +- 1 deg
.XXX = +- .005	

PART #: 13

PROJECT: Swirl Chamber (MS Project at MIT)
PART NAME: Support For Test Section
MATERIAL: PVC
DRAWN BY: David Danitz
REVISION DATE: 3/31/94
SHEET 3 OF 4

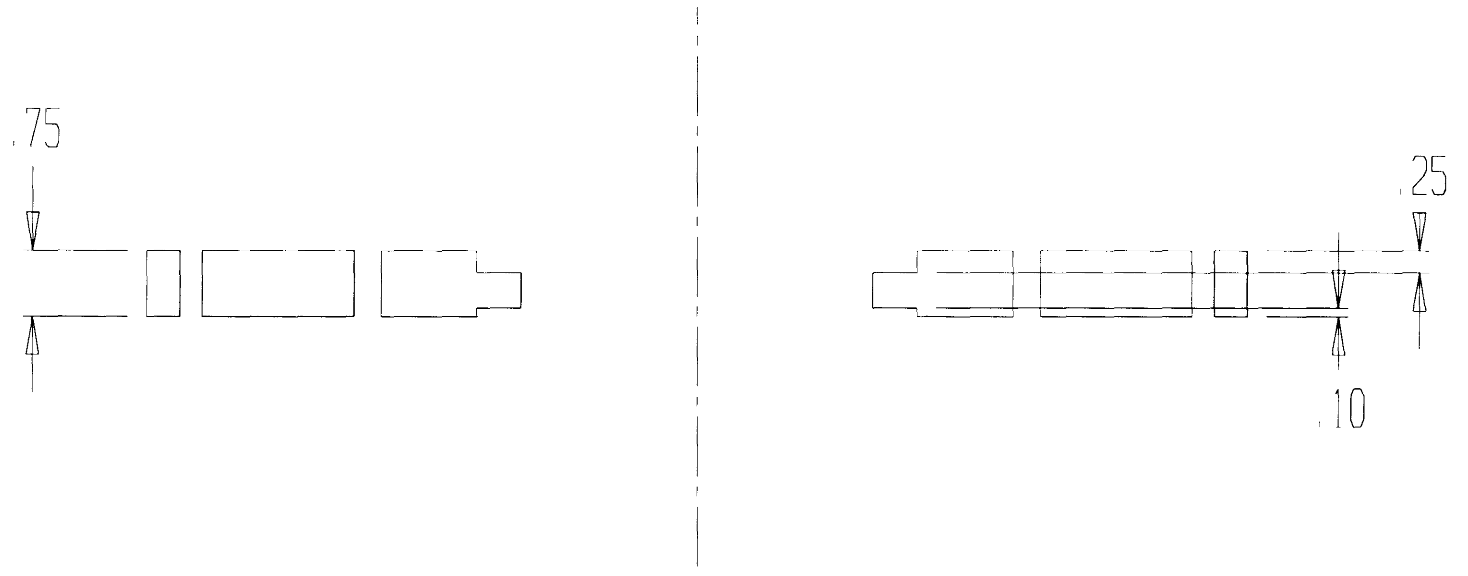

Note: Dimensions are in inches.

TOLERANCES

DECIMAL:	ANGULAR:
X/X = +-1/32	.X = +-.5 deg
.XX = +-.01	X = +- 1 deg
.XXX = +- .005	

PART #: 13

PROJECT: Swirl Chamber (MS Project at MIT)

PART NAME: Support For Test Section

MATERIAL: PVC

DRAWN BY: David Danitz

REVISION DATE: 3/31/94

SHEET 4 OF 4

A.2 Nd:YAG Laser

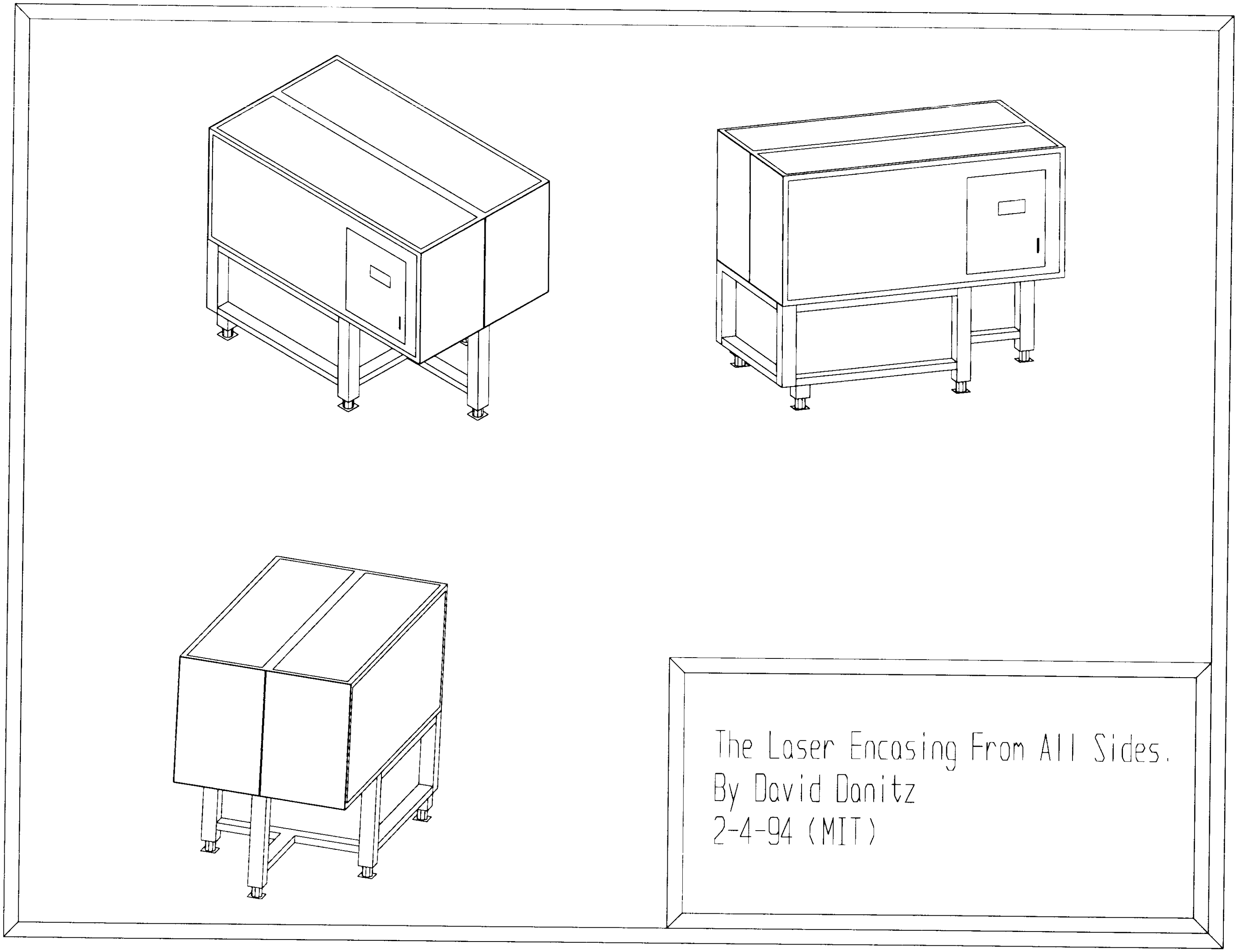

The Laser Encasing From All Sides.
By David Danitz
2-4-94 (MIT)

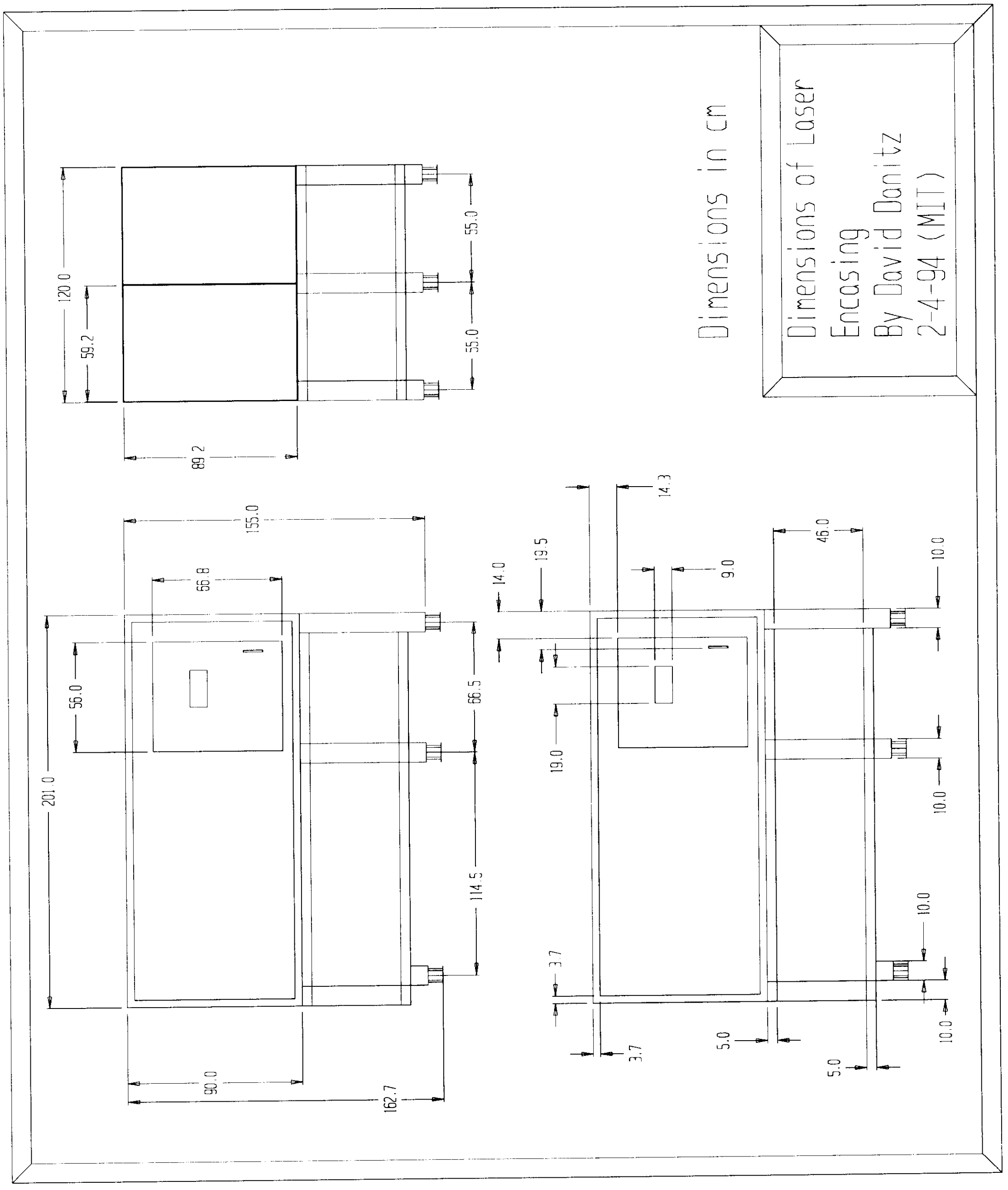
Dimensions of Laser
Encasing
By David Danitz
2-4-94 (MIT)
Dimensions in cm
120.0
59.2
55.0
55.0
89.2
155.0
66.8
56.0
201.0
66.5
114.5
90.0
162.7
14.0
19.5
9.0
14.3
46.0
10.0
19.0
10.0
10.0
3.7
3.7
5.0
5.0
10.0

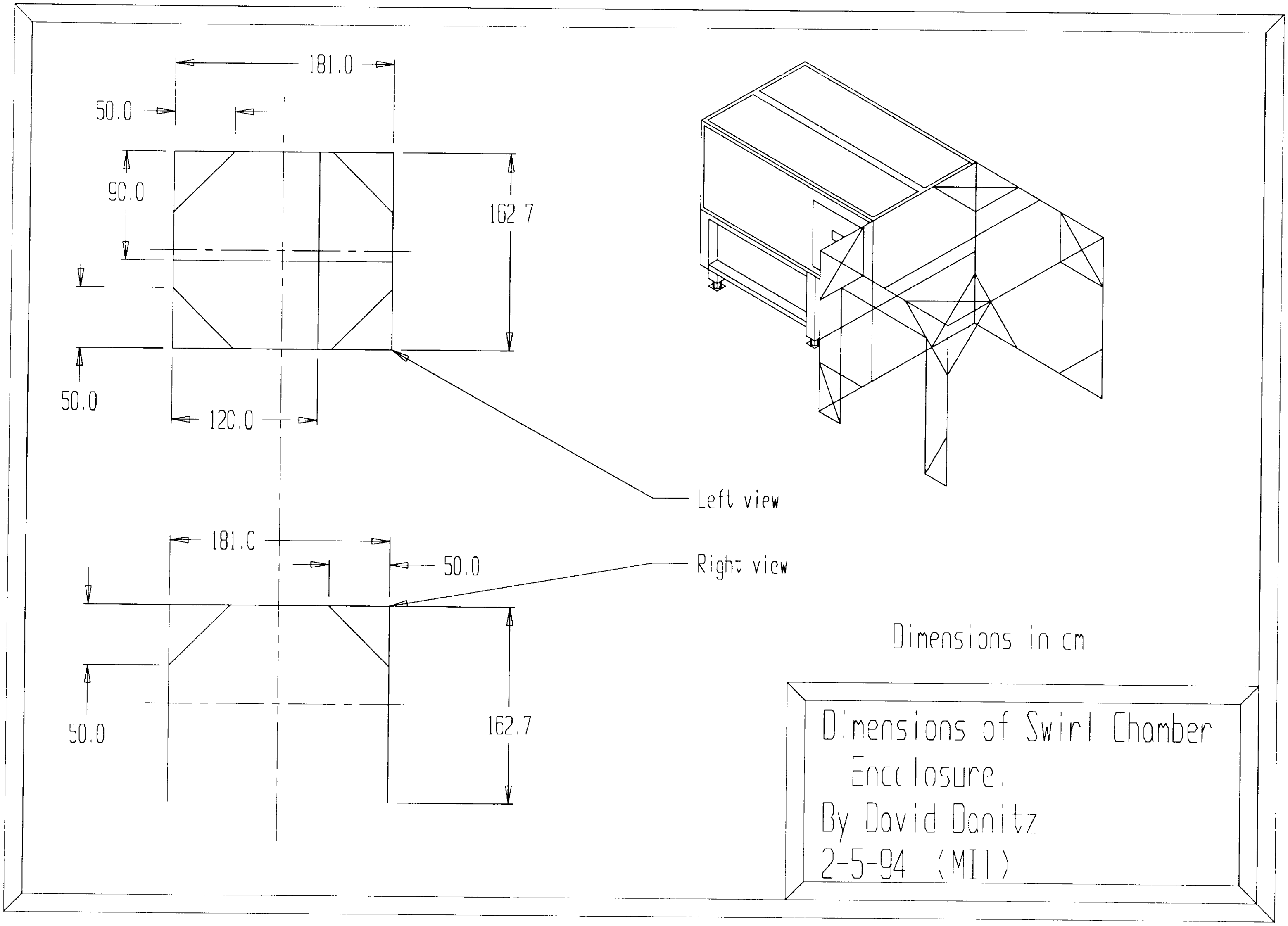

Dimensions in cm

Dimensions of Swirl Chamber
Encclosure.
By David Danitz
2-5-94 (MIT)

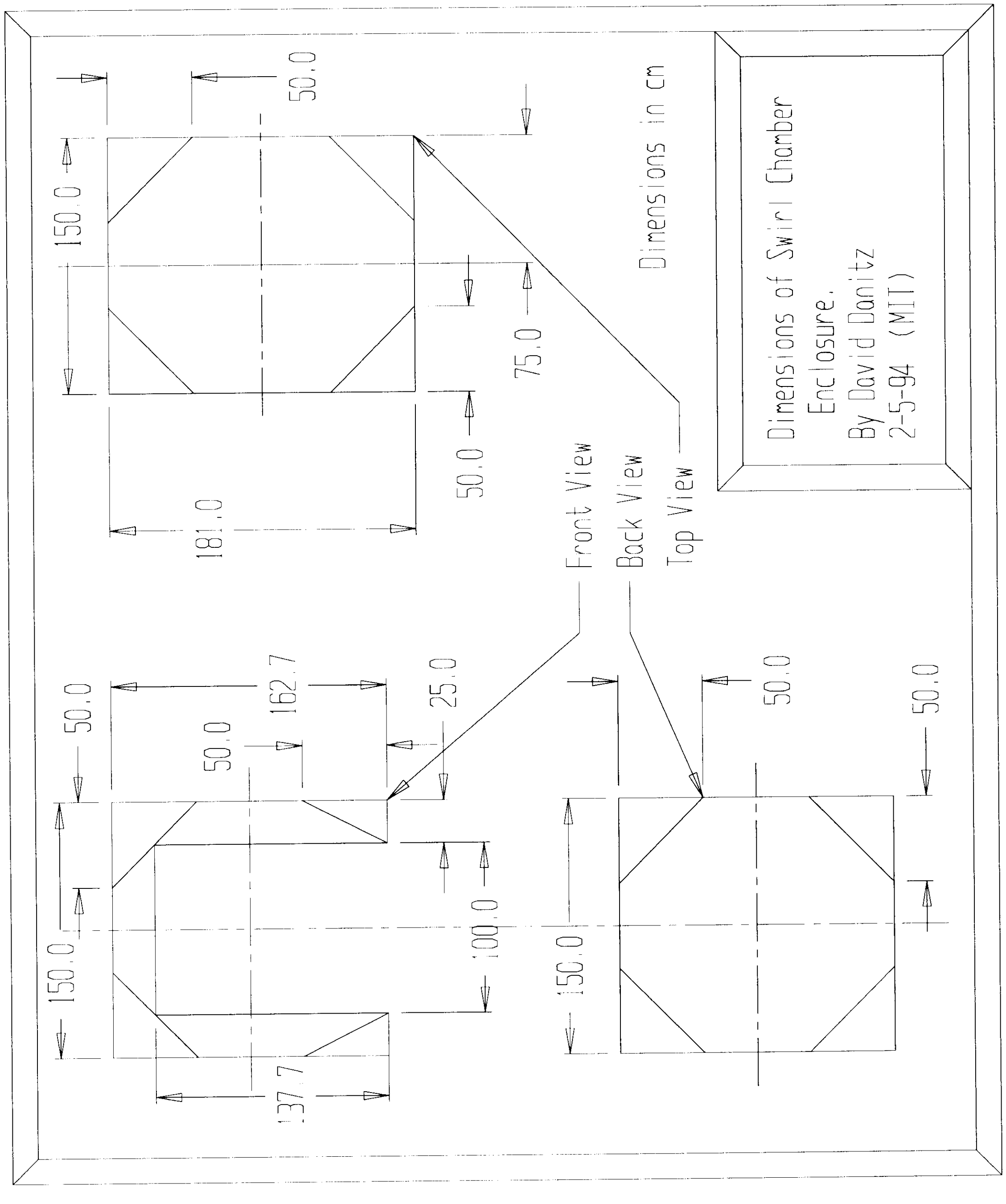
Dimensions of Swirl Chamber
Enclosure.
By David Danitz
2-5-94 (MIT)
Dimensions in cm
Front View
Back View
Top View
150.0
50.0
75.0
50.0
181.0
50.0
150.0
50.0
162.7
25.0
50.0
100.0
137.7
150.0
50.0
50.0

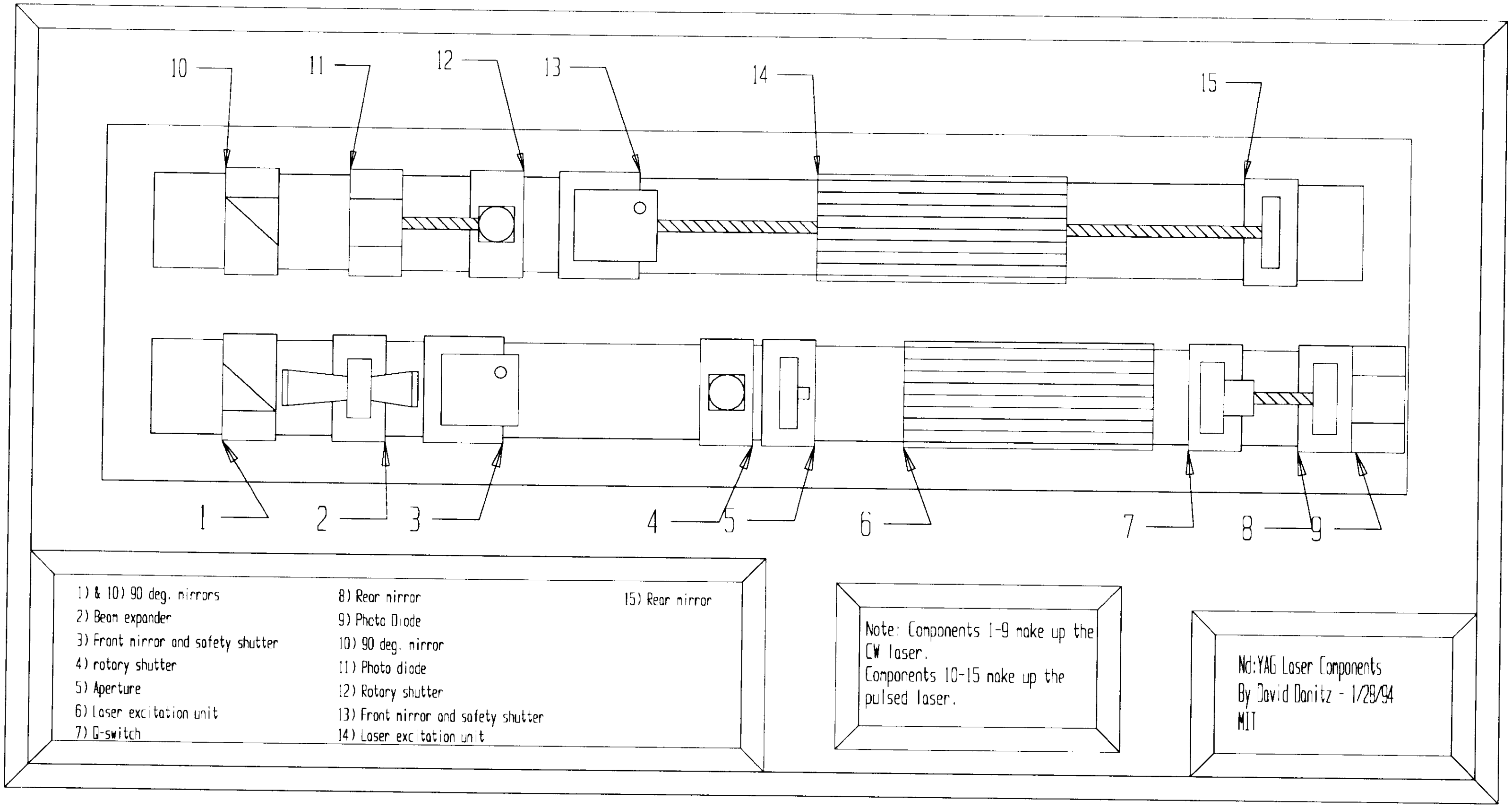
10
11
12
13
14
15
1
2
3
4
5
6
7
8
9
1) & 10) 90 deg. mirrors
2) Beam expander
3) Front mirror and safety shutter
4) rotary shutter
5) Aperture
6) Laser excitation unit
7) Q-switch
8) Rear mirror
9) Photo Diode
10) 90 deg. mirror
11) Photo diode
12) Rotary shutter
13) Front mirror and safety shutter
14) Laser excitation unit
15) Rear mirror
Note: Components 1-9 make up the CW laser.
Components 10-15 make up the pulsed laser.
Nd:YAG Laser Components
By David Danitz - 1/28/94
MIT

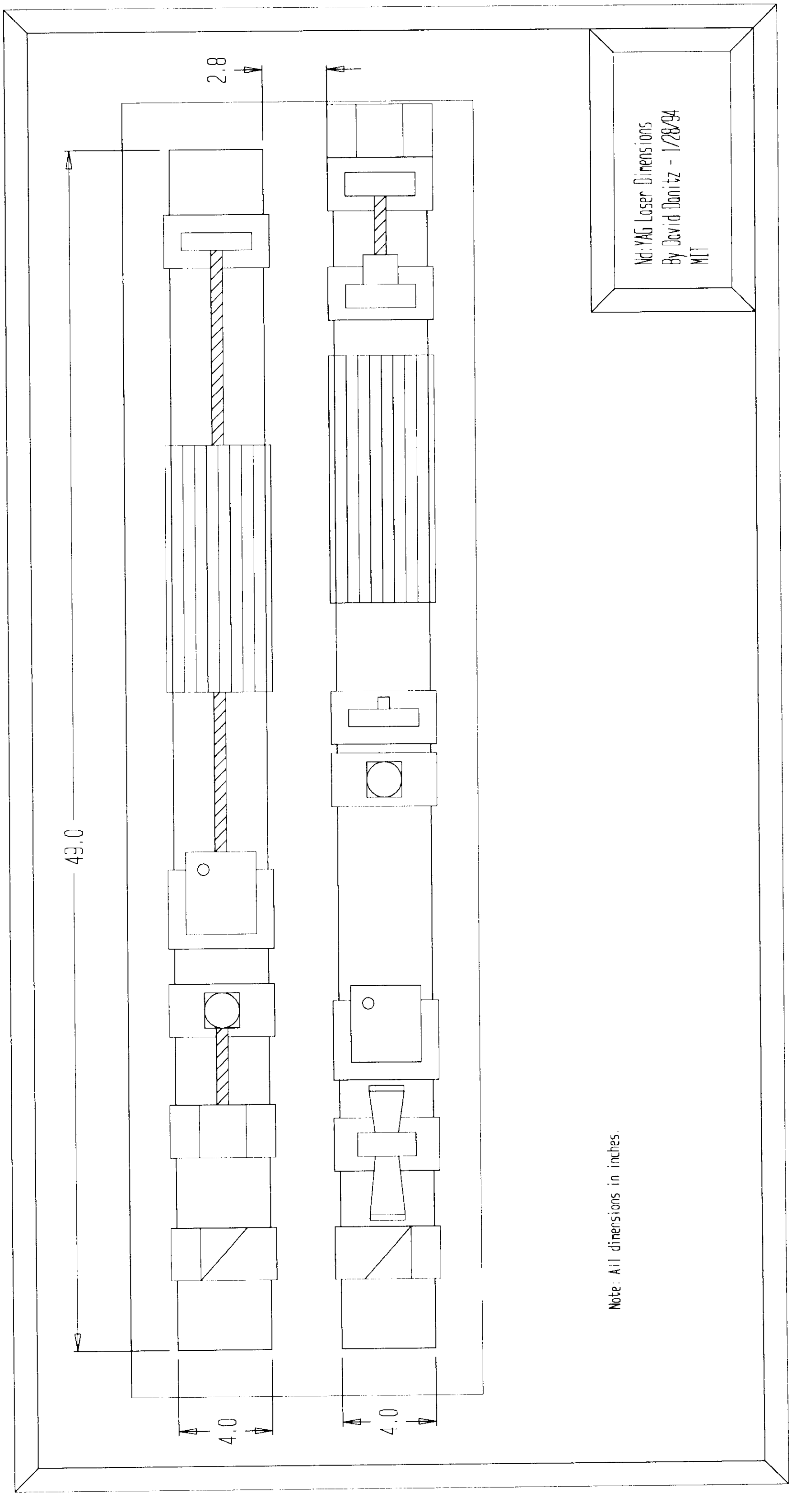
Nd:YAG Laser Dimensions
By David Danitz - 1/28/94
MIT
Note: All dimensions in inches.
2.8
49.0
4.0
4.0

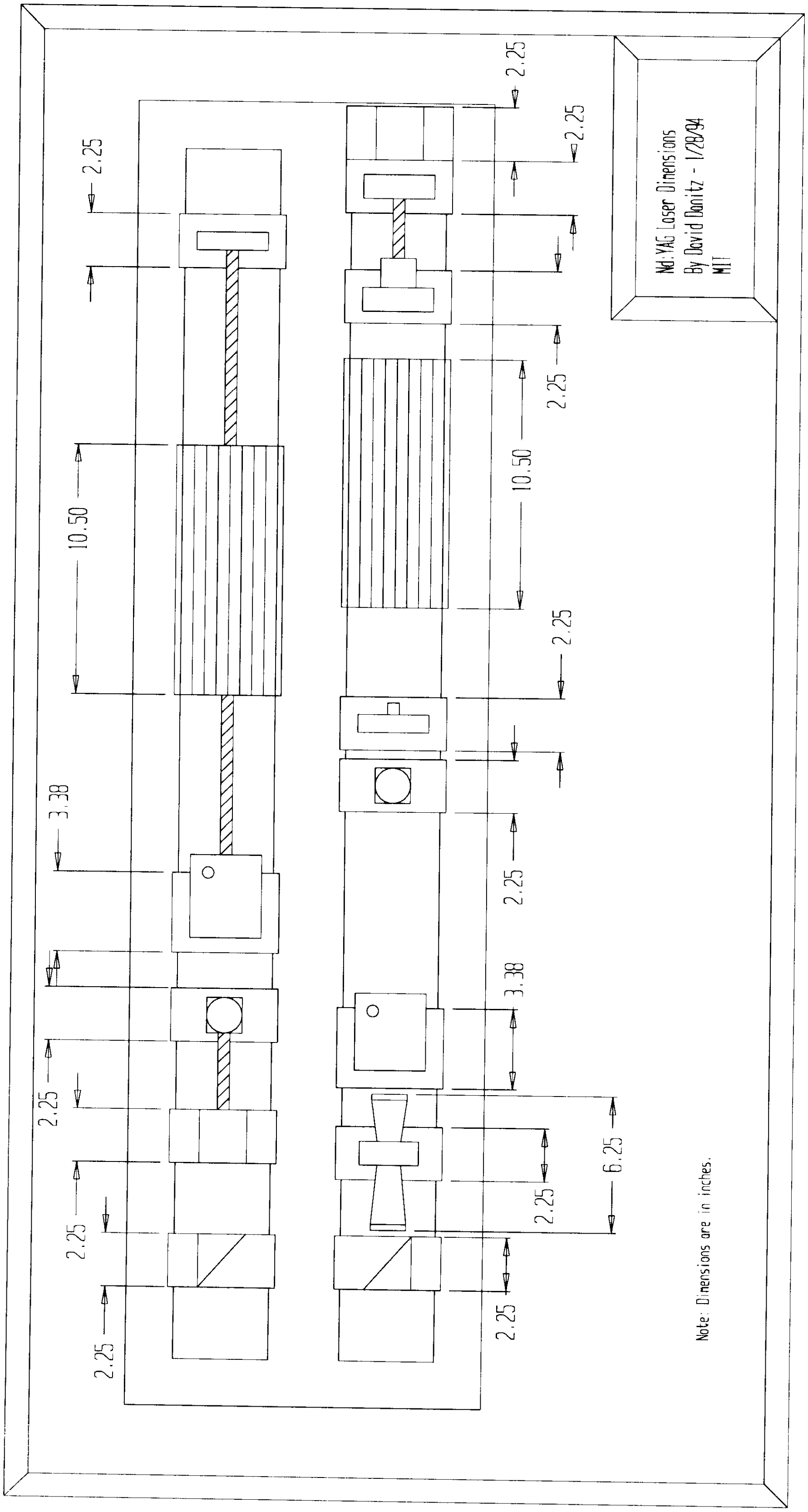
Nd:YAG Laser Dimensions
By David Danitz - 1/28/94
MIT
Note: Dimensions are in inches.
2.25
2.25
2.25
10.50
2.25
2.25
3.38
2.25
2.25
2.25
10.50
2.25
3.38
6.25
2.25
2.25
2.25

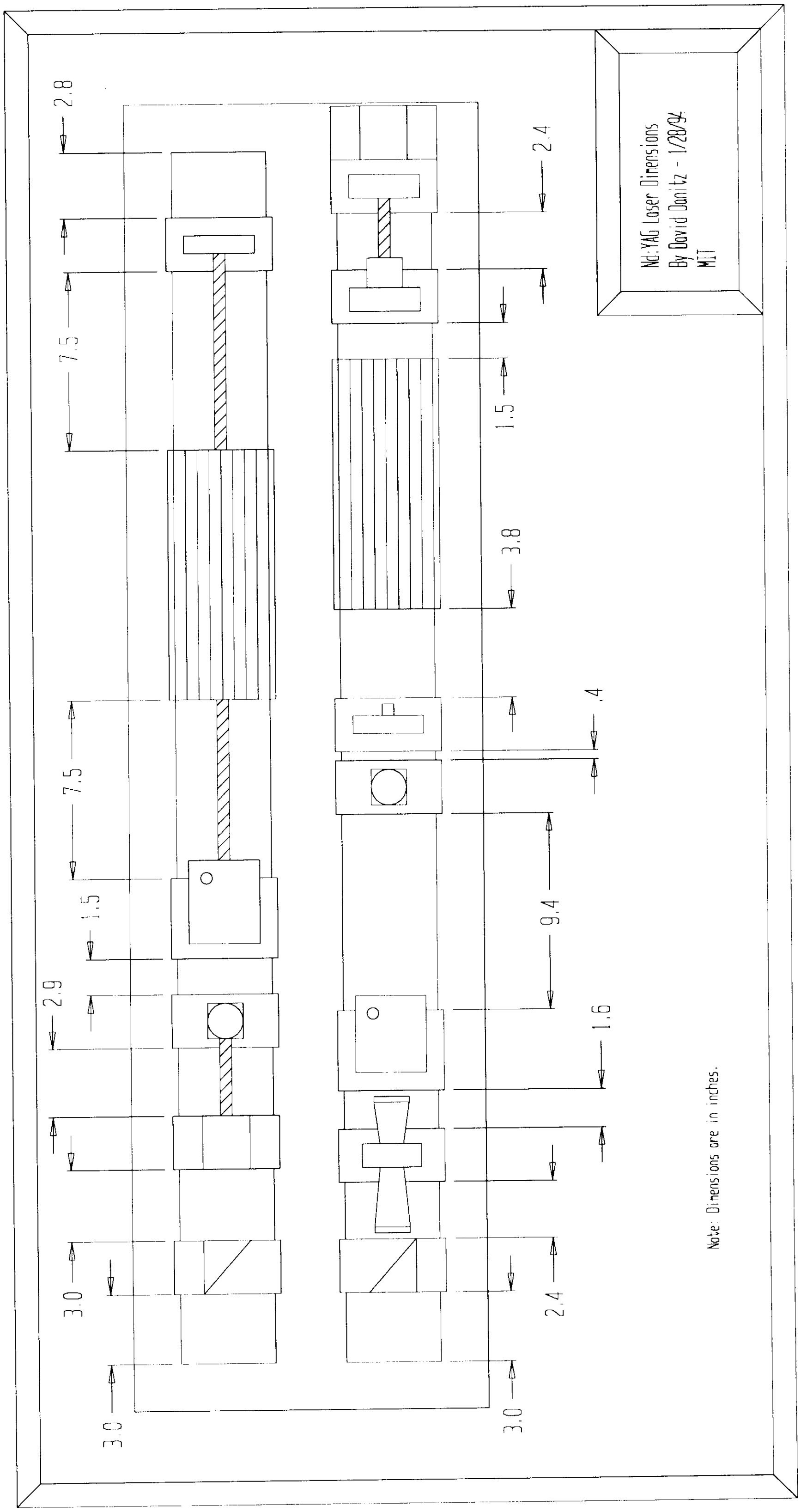
Nd:YAG Laser Dimensions
By David Danitz - 1/28/94
MIT
Note: Dimensions are in inches.
2.8
7.5
7.5
1.5
2.9
3.0
3.0
2.4
1.5
3.8
.4
9.4
1.6
2.4
3.0

Appendix B

Construction of the Swirl Chamber

B.1 Parts Machined by the Author

In order to maintain a tight budget, several of the swirl chamber parts were machined in-house at the MIT student machine shop. Pictures of these parts are given in Figures C.1 to C.9. Poly vinyl chloride (PVC) was used for all parts except the optical viewing reservoir, which was made from clear acrylic. Most parts were machined using a milling machine or a lathe. A few of the more interesting points of the construction are mentioned here. First, the large cylinder was made from a piece of a 15 ft PVC sewer pipe. A 2 ft length was cut off and machined to the proper dimension with a 3 ft lathe. Second, the mandrel consists of eight pieces of 1 in. thick PVC glued together. A rough cone was constructed with the 1 in. pieces. The cone was then machined on a lathe using a tool bit mounted on a swiveling arm. Finally, the secondary flow reservoirs are made from the remaining 13 ft of sewer pipe. The pipe was cut in half and end plates were machined on the 3 ft lathe.

Figure B.1: Parts 1 and 2: the base and the large cylinder.

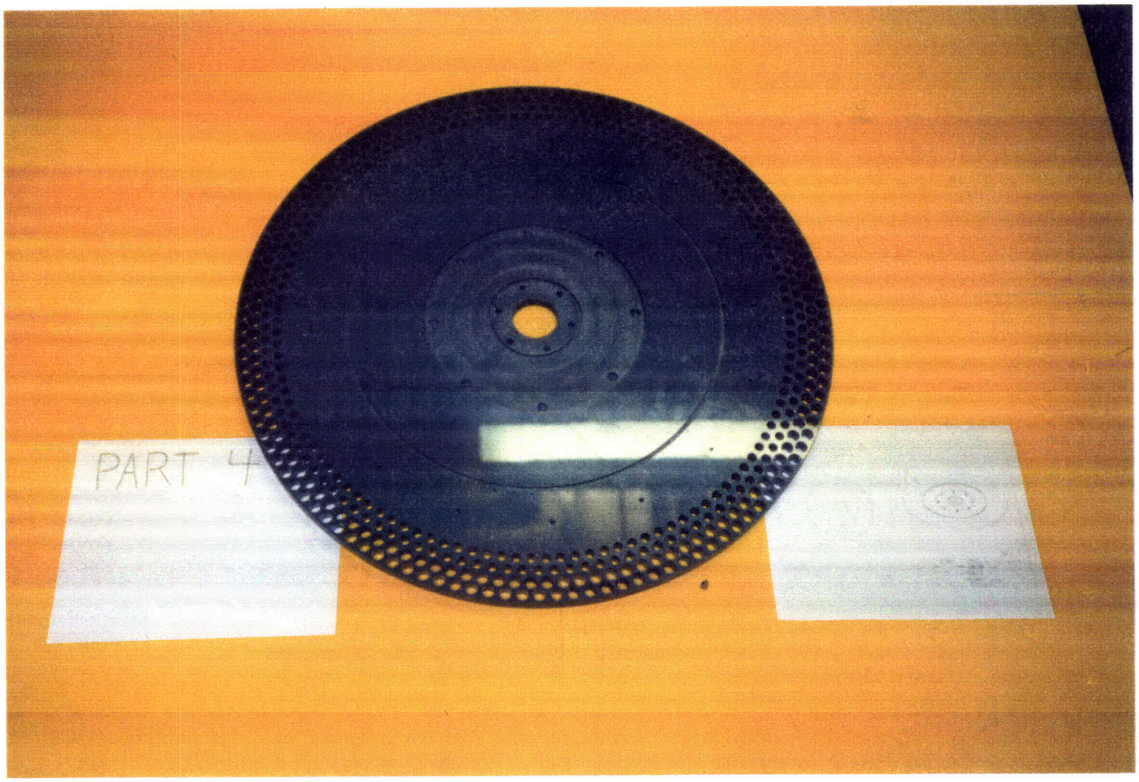

Figure B.2: Part 4: The large rib.

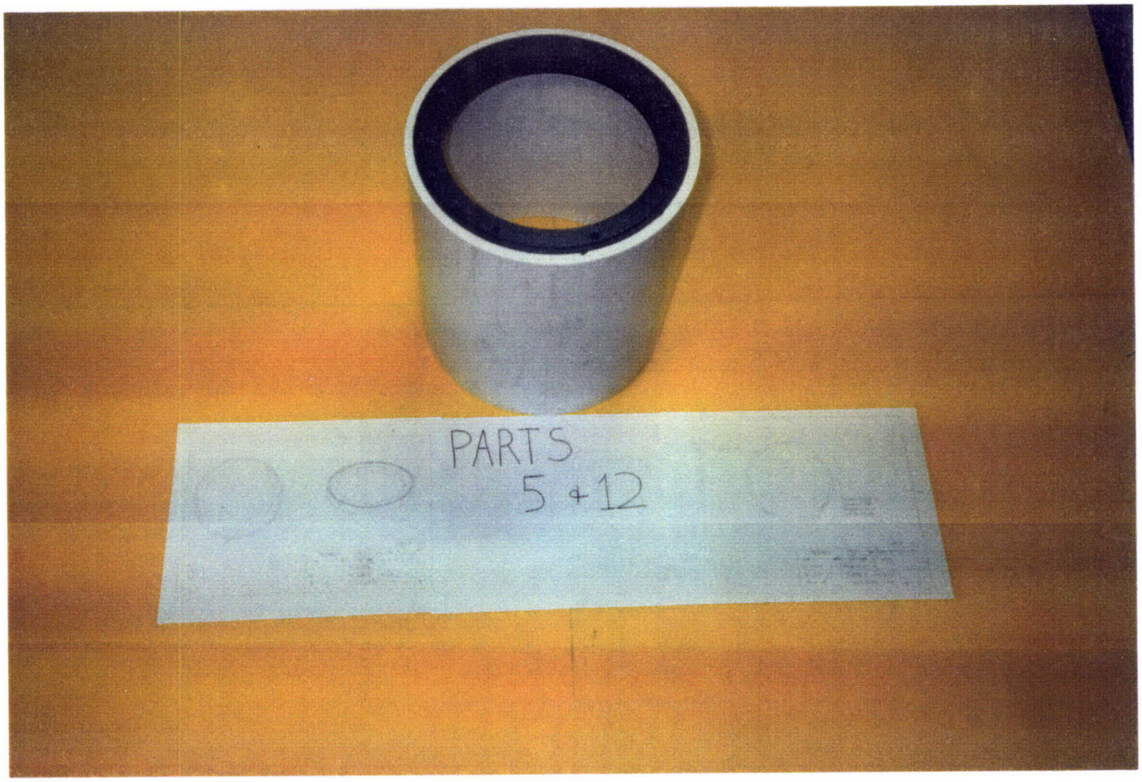

Figure B.3: Parts 5 and 12: The small cylinder and the flange.

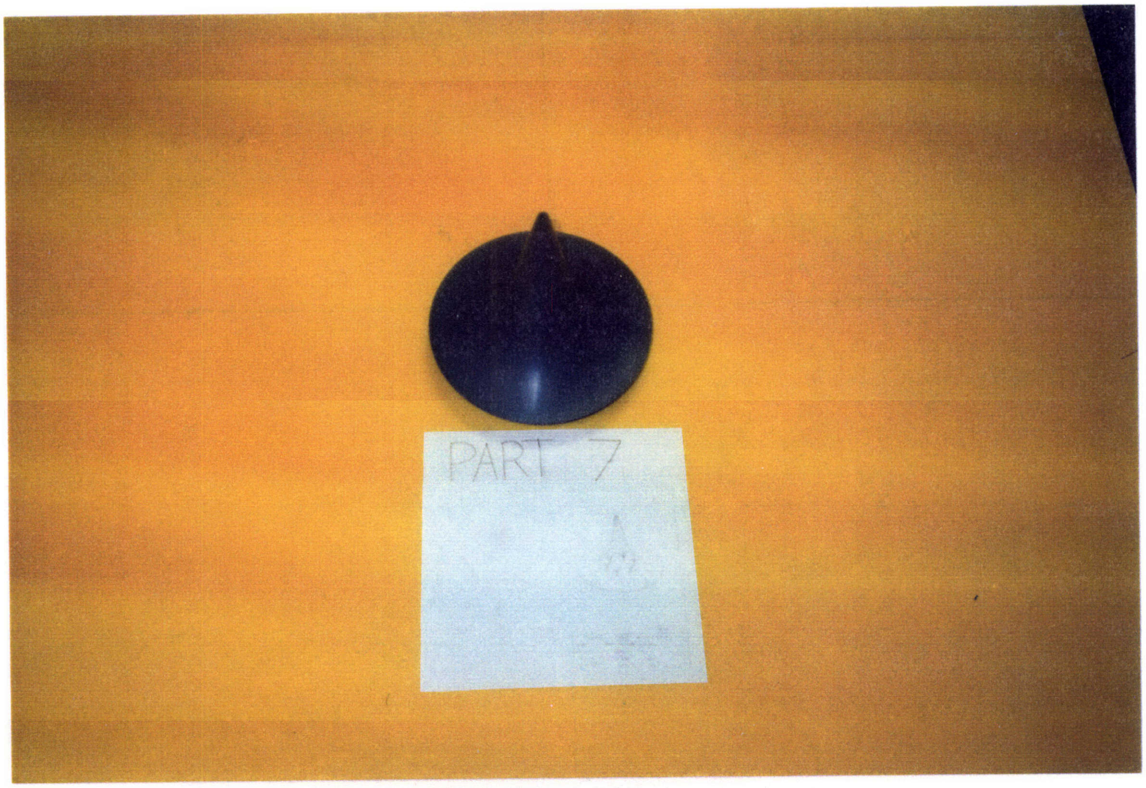

Figure B.4: Part 7: The mandrel.

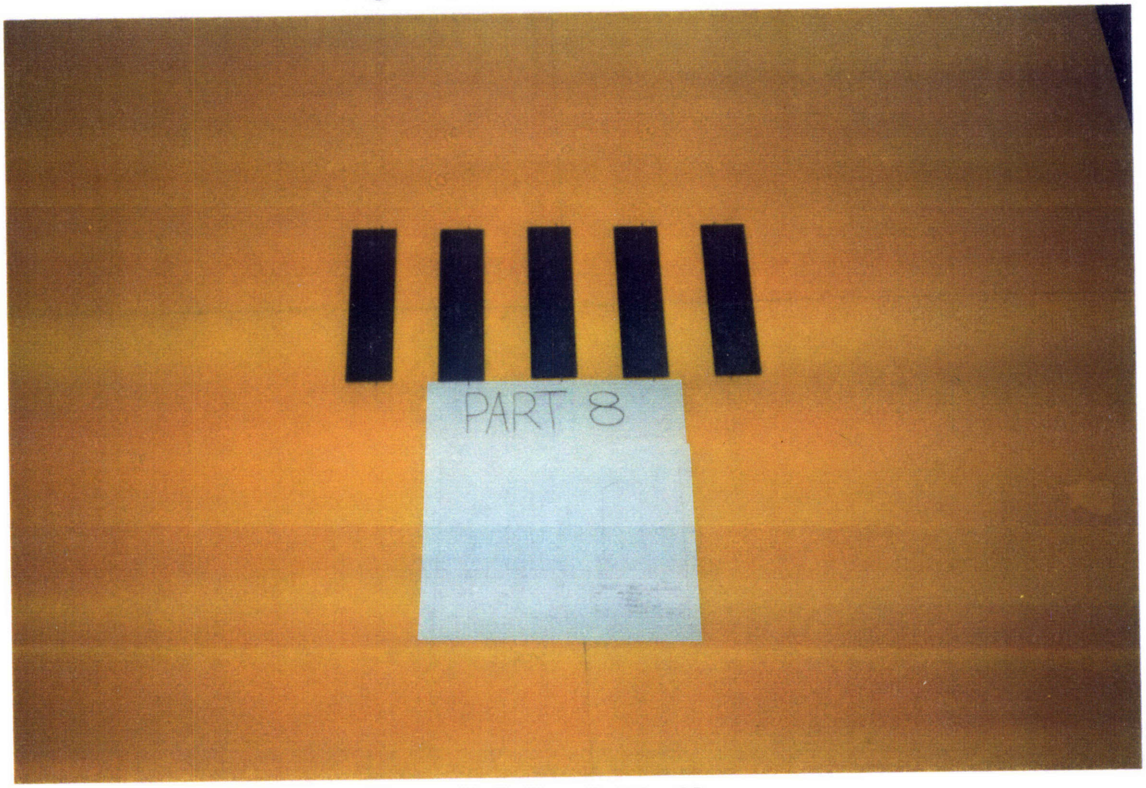

Figure B.5: Part 8: The Vanes.

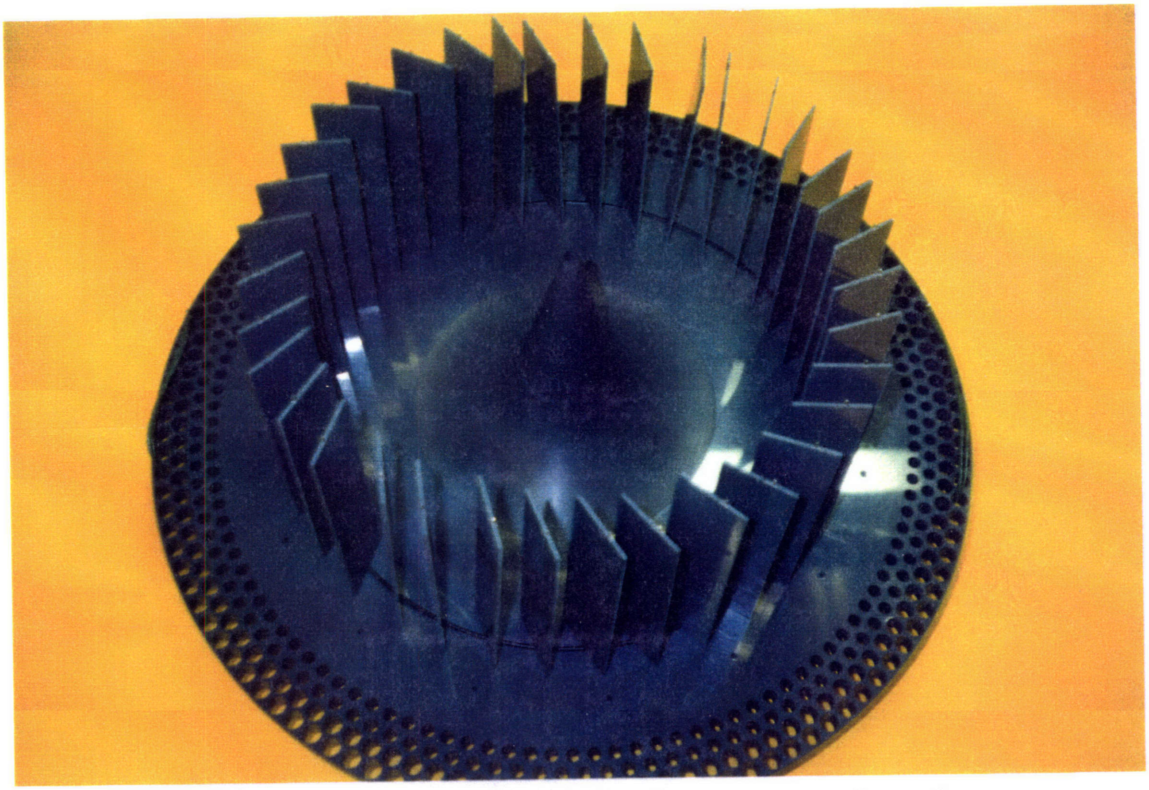

Figure B.6: The large rib, mandrel and vanes mounted together.

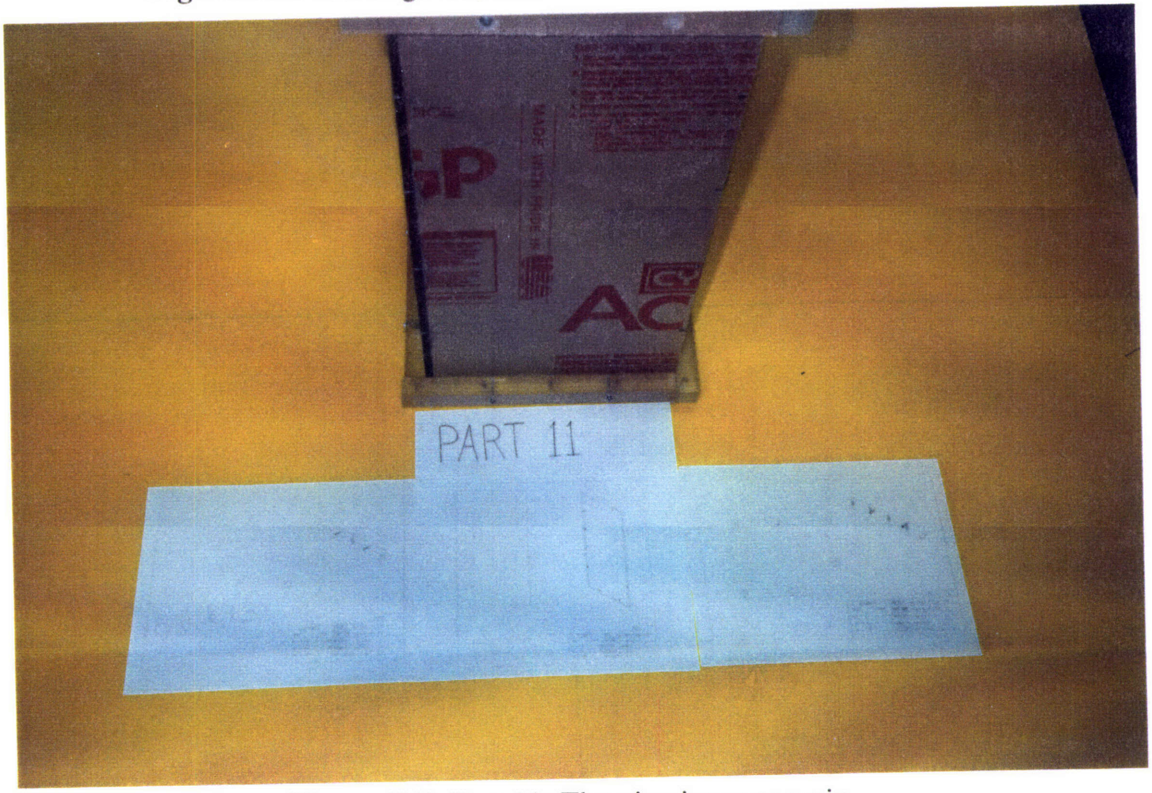

Figure B.7: Part 11: The viewing reservoir.

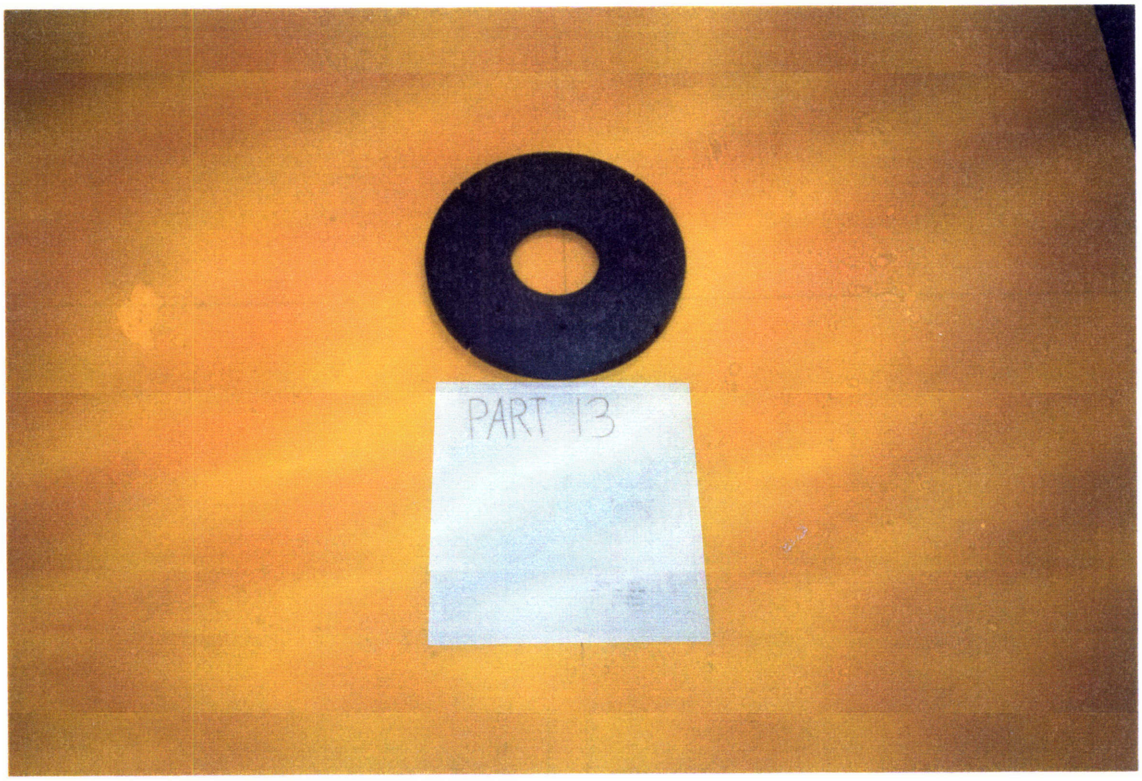

Figure B.8: Part 13: The test section support.

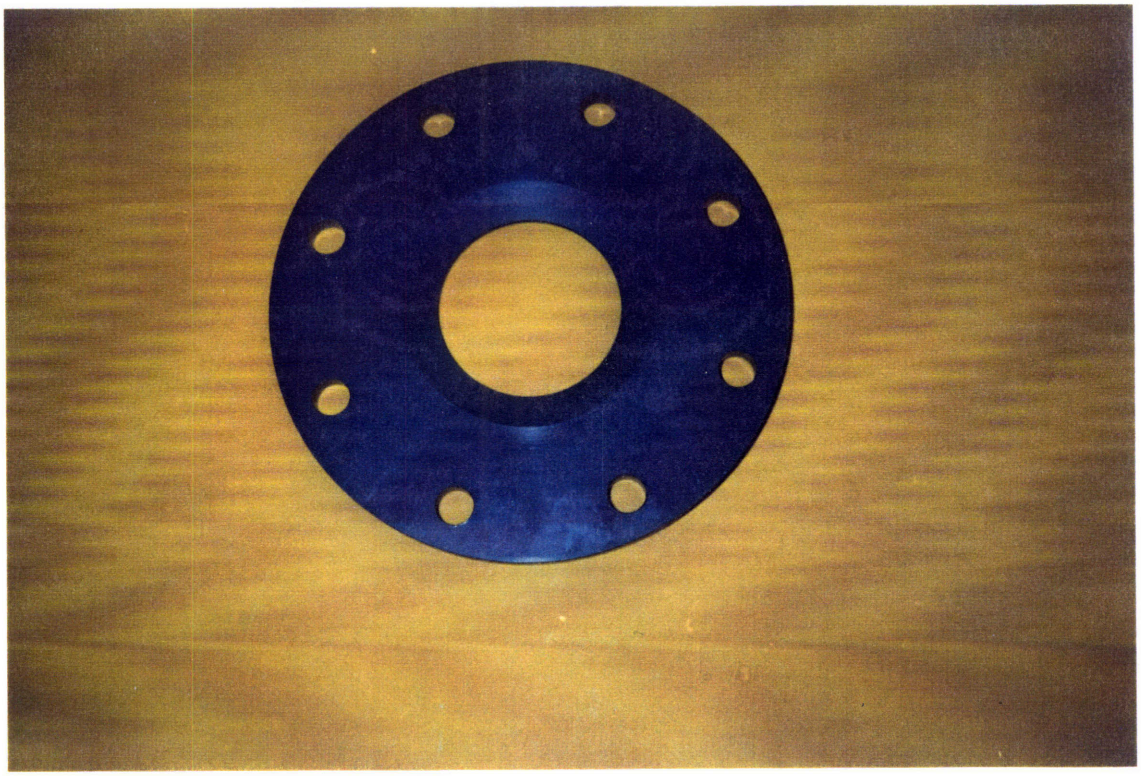

Figure B.9: The orifice plate.

B.2 Parts Machined by Outside Shop

The following parts were machined by a local machine shop.

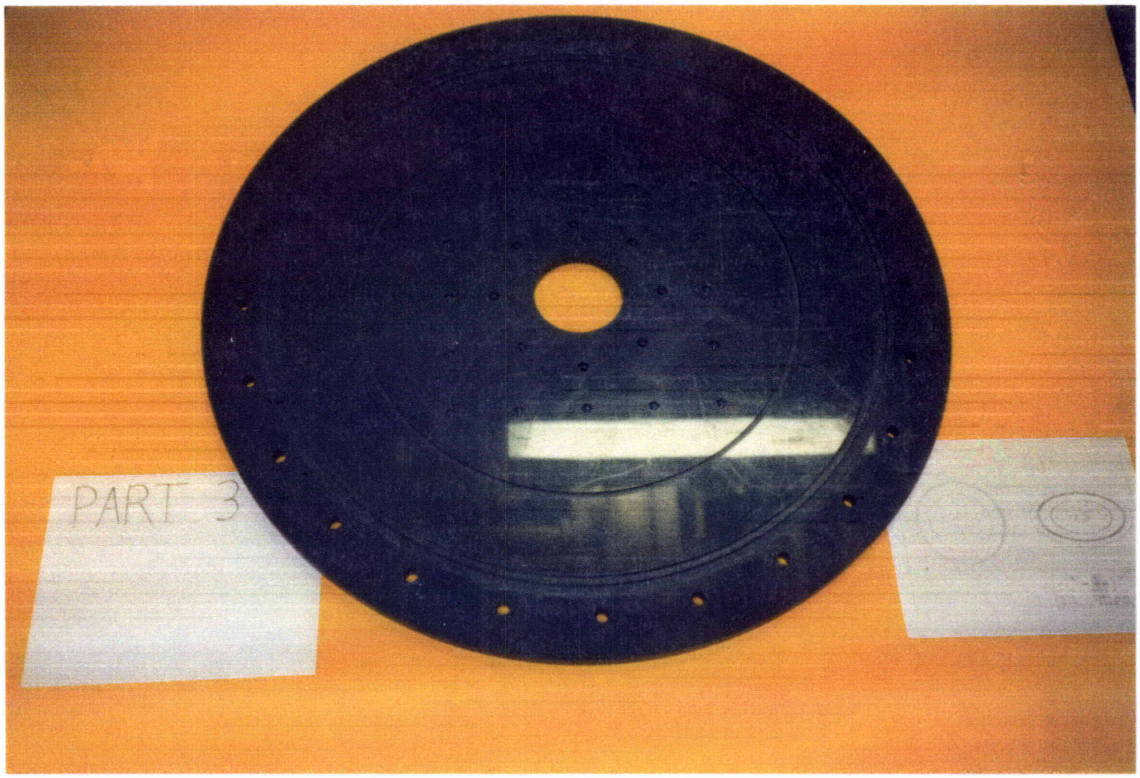

Figure B.1: Part 3: The lid.

Figure B.2: Part 9: The contour to redirect flow.

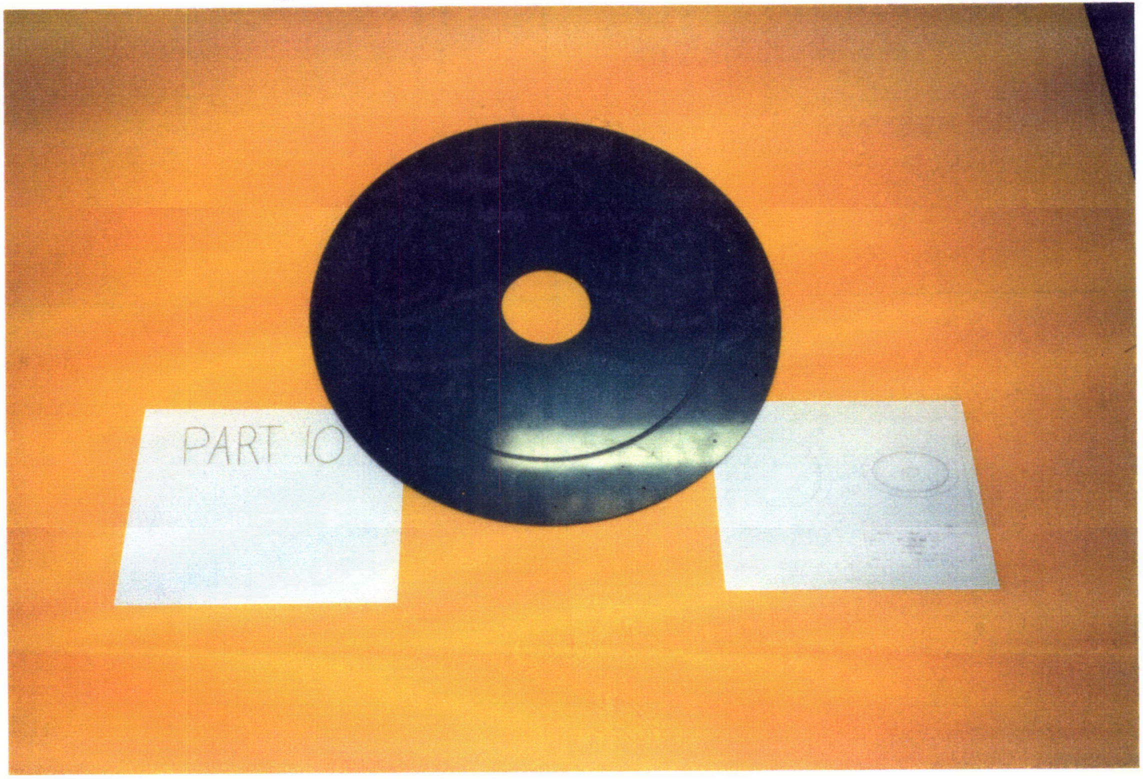

Figure B.3: Part 10: The vane cover.

Appendix C

Supplements to the PIV System

C.1 Hardware

The CAD drawings of the mount for the cylindrical lens and the galvanometer head extender are given on the following pages.

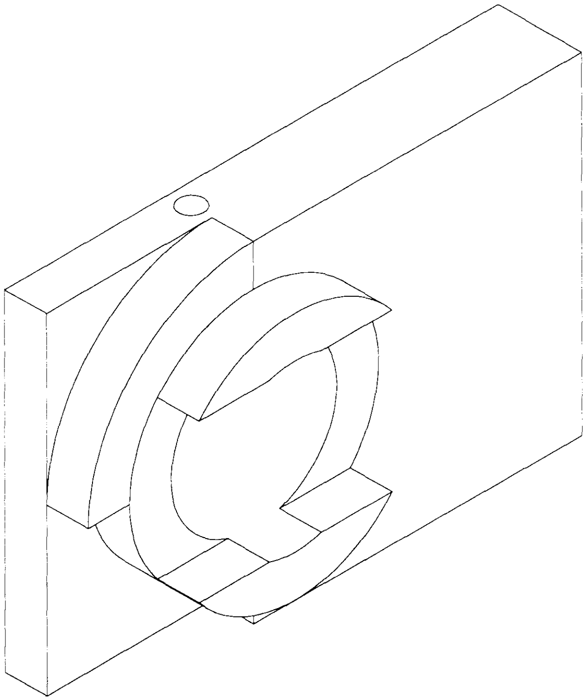

PART #:

TOLERANCES

DECIMAL:

X/X = +-1/32

.XX = +-.01

.XXX = +- .005

ANGULAR:

.X = +-.5 deg

X = +- 1 deg

PROJECT: Cylindrical Lens Mount (MS Project at MIT)

PART NAME: Lens Mount & Rotator (CYLENSO.PTN)

MATERIAL: Aluminun

DRAWN BY: David Danitz

REVISION DATE: 9/13/94

SHEET 1 OF 3

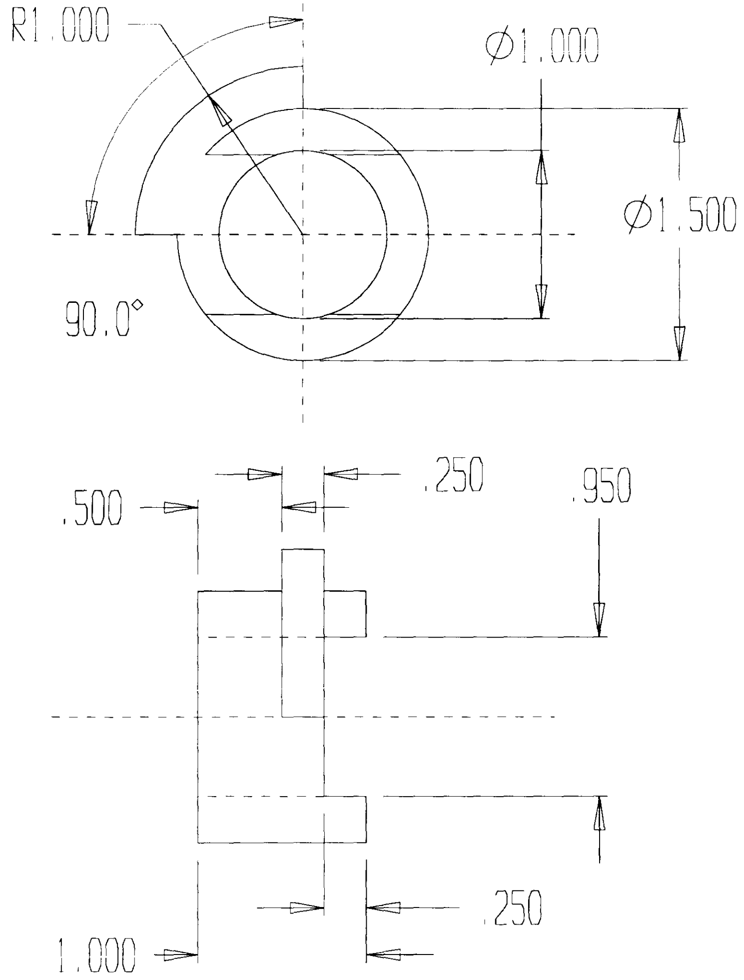

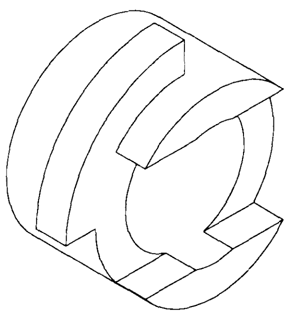

Note: Place set screws on
flat surfaces to hold lens
in place.

PART #: 1

TOLERANCES

DECIMAL: ANGULAR:

X/X = +-1/32 .X = +-.5 deg

.XX = +-.01 X = +- 1 deg

.XXX = +- .005

PROJECT: Cylindrical Lens Mount (MS Project at MIT)

PART NAME: Rotator (CYLENS1.PTN)

MATERIAL: Aluminum

DRAWN BY: David Danitz

REVISION DATE: 9/13/94

SHEET 2 OF 3

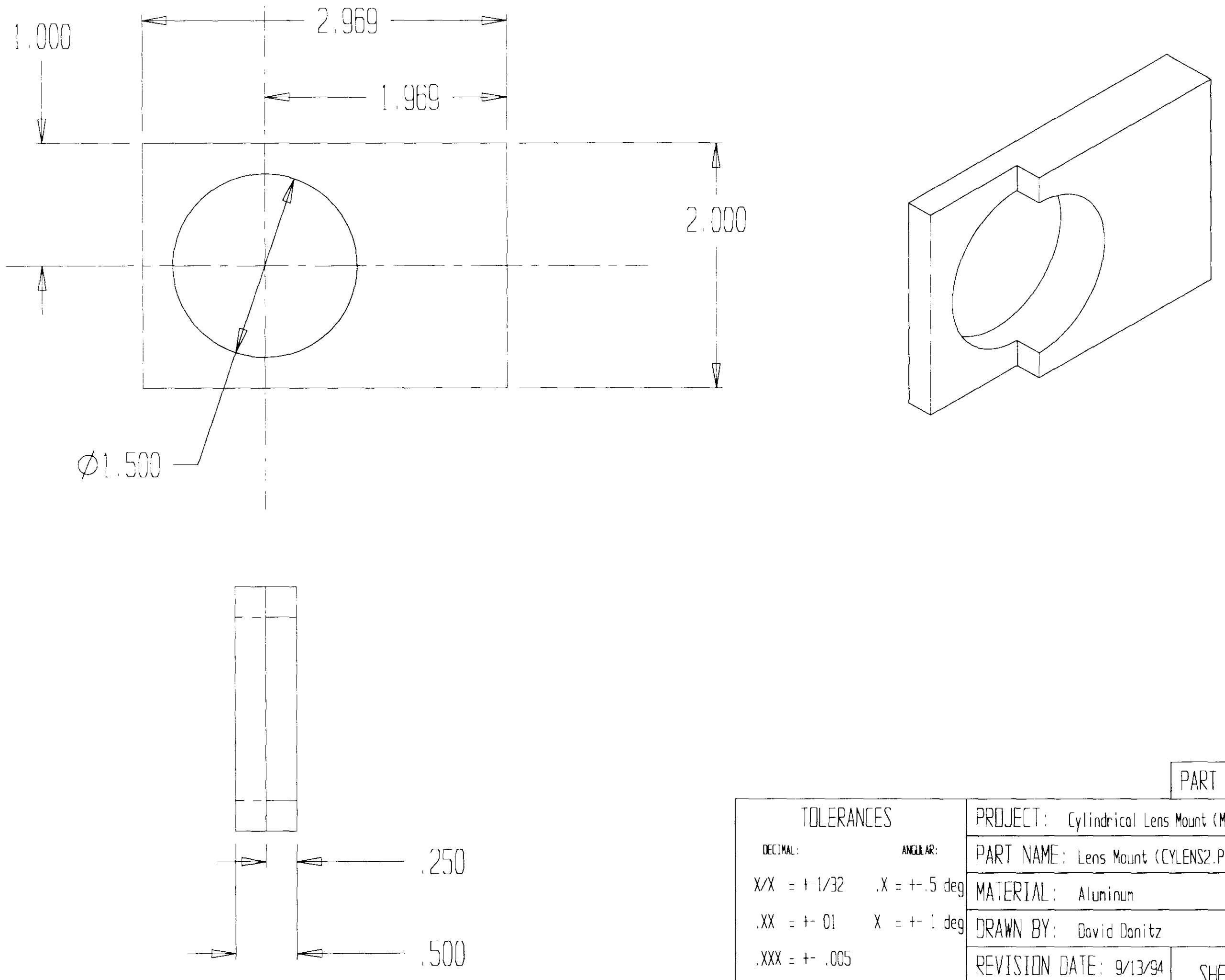

PART #: 2

TOLERANCES

DECIMAL:
X/X = +-1/32
.XX = +- 01
.XXX = +- .005

ANGULAR:
.X = +-.5 deg
X = +- 1 deg

PROJECT: Cylindrical Lens Mount (MS Project at MIT)
PART NAME: Lens Mount (CYLENS2.PTN)
MATERIAL: Aluminum
DRAWN BY: David Danitz
REVISION DATE: 9/13/94

SHEET 3 OF 3

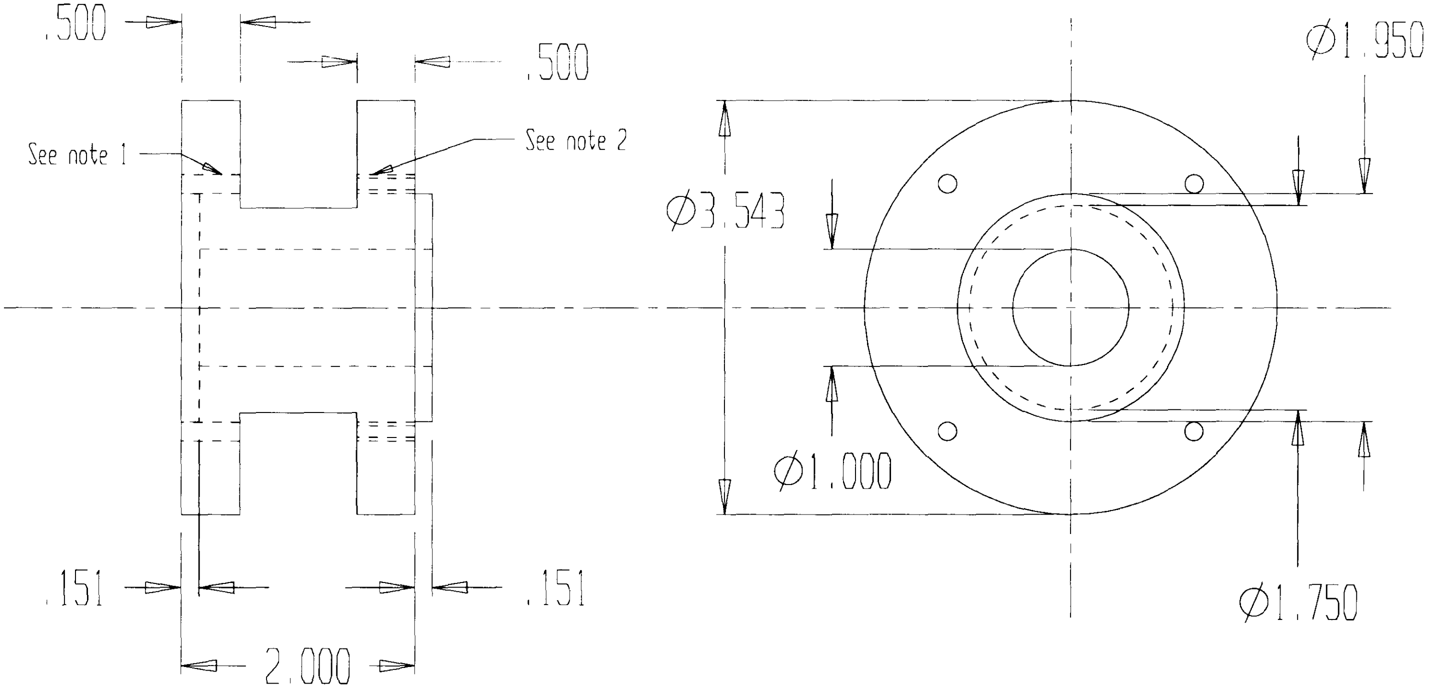

Note 1: Four evenly spaced through holes on a 2.995 in. bolt circle.

Note 2: Four evenly spaced holes, drill through and tap with 6-32 on a 2.995 in. bolt circle.

TOLERANCES		
DECIMAL:	ANGULAR:	
X/X = +-1/32	.X = +-.5 deg	
.XX = +-.01	X = +- 1 deg	
.XXX = +- .005		

PART #:

PROJECT: Laser Conversion (MS Project at MIT)

PART NAME: Galvanometer Mount Extender (LASREXT.PTN)

MATERIAL: Aluminum

DRAWN BY: David Danitz

REVISION DATE: 9/13/94

SHEET 1 OF 1

C.2 Laser Timing Program

The timing program written by Professor Hart is initiated by typing “laser” at the c:\ prompt on the IBM PS2. The program is written in Pascal. The main purpose of the program is to control the CTM-05 timing card. All four timers are set with the program. The first timer corresponds to the length of the Nd:YAG laser pulse. The other three timers control the spacing between the three pulses. Because of the robustness of the program and timing circuit, any combination the spacing between laser pulses can be accomplished at the touch of a button.

```
{$R-}
{$I-}
{$B+}
{$S+}
{$N-}
{$L tpctm5}
{$M 65500,16384,655360}

Program QSwitch;

(*********************************************************************)
(*                          QSwitch.PAS                              *)
(*     Q-Switch Timing program for the CTM-05 Timer/Counter Board    *)
(*                       D.P. Hart  07/14/94                         *)
(*********************************************************************)

uses CRT;   {unit declaration, contains readkey, clrscr and gotoxy
functions}

type
 parray = array [0..15] of integer;

var   key          :  char;
      base_address:  integer;
      params       :  parray;
      mode,flag    :  integer;
      result       :  integer;
      Num_Pulses   :  integer;
      counter,i    :  integer;
      delay        :  array[1..5] of word;
      count        :  array [1..5] of word;
```

```
      term_on_err :  boolean;

function tp_ctm5(var mode:integer; var params:parray; var
flag:integer):integer;external;

{********************  procedure to report errors *******************}

Procedure report_error;
Begin
   clrscr;
   writeln;writeln;writeln;
   writeln('     CTM-05 error # ',result,' has occurred');
   writeln('     as a result of the following parameters');
   writeln;
   writeln('     params[0] = ',params[0]);
   writeln('     params[1] = ',params[1]);
   writeln('     params[2] = ',params[2]);
   writeln('     params[3] = ',params[3]);
   writeln('     params[4] = ',params[4]);
   writeln('     params[5] = ',params[5]);
   writeln;
   writeln('  DO NOT OPERATE LASER UNTIL THIS IS FIXED!!');
   writeln;
   write('  press any key to continue ...');
   key := readkey;
   term_on_err := true; {jump out of program on error}
End;

{**********************************************************************}

  {Initializes the ctm-05 driver with the address of the board, this
must be done before
   any other calls are made to the driver }

Procedure setmode0;
Begin
   mode := 0;
   flag := 0;
   params[0] := base_address;    {I/O base address}
   params[1] := 1;      {Fout divider ratio of 1}
   params[2] := 11;     {Fout source = F1 (1MHz)}
   params[3] := 0;      {compare 2 disabled}
   params[4] := 0;      {compare 1 disabled}
   params[5] := 0;      {time of day disabled}
   result := tp_ctm5(mode, params, flag);

{**********************************************************************}

{ Set the ctm-05 counter mode registers using a for
  loop to increment through the registers }

Procedure setmode1;

{We will set the counters to retriggerable one-shots (Mode R in the
```

```
Am9513 handbook)}

Begin
   For counter := 1 to 4 do
   Begin
      mode := 1;
      flag := 0;
      params[0] := counter;{counter to initialize}
      params[1] := 6;      {active high edge gating}
      params[2] := 0;      {count on rising edge}
      params[3] := 11;     {input from F1}
      params[4] := 1;      {enable special gate - retriggerable}
      params[5] := 0;      {reload from load register}
      params[6] := 1;      {count repetitively}
      params[7] := 0;      {binary count - not sure about this - load in
binary value?}
      params[8] := 0;      {count down}
      params[9] := 5;      {active low terminal count pulse}
      result := tp_ctm5(mode, params, flag);
      If(result <> 0) then
      Begin
         gotoxy(10,9);
         writeln('   error initializing counter ',counter);
         report_error;
      End;
   End;
End;


{*******************************************************************}

{ procedure load_and_arm uses: mode 2 to disarm all 5 counters, mode 3
  to load them, then mode 2 to arm them }

Procedure load_and_arm;

Begin

   mode := 2;
   params[0] := 6;            { disarm selected counters }
   for counter := 1 to 4 do
      params[counter] := 1;   { select all counters }
   result := tp_ctm5(mode, params, flag);
   If (flag <> 0) then
   Begin
      writeln('    error disarming counters ');
      writeln;
      report_error;
   End;

   mode := 3;                    { load counter }
    For counter := 1 to 4 do
   Begin
      params[0] := counter;         {counter number }
```

```
      params[1] := delay[counter];  { load desired delay }
      result := tp_ctm5(mode, params, flag);
      If (flag <> 0) then
      Begin
         writeln('    error loading counter ',counter);
         writeln;
         report_error;
      End;
   End;

   mode := 2;        { arm all counters }
   params[0] := 3;   { arm and load }
   For counter := 1 to 4 do
      params[counter] := 1;   { select all counters }
   result := tp_ctm5(mode, params, flag);
   If (flag <> 0) then
   Begin
      writeln('    error arming counters ');
      writeln;
      report_error;
   End;
End;

{***********************************************************************}

Procedure Announce;
Begin


   clrscr;
   gotoxy(1,18);
   writeln;
   writeln('  System Parameters:');
   writeln('    Laser Pulse Width = ',Delay[1],' usec.');
   writeln('    Number of Pulses = ',Num_Pulses);
   for i:=1 to Num_Pulses do
   writeln('    Delay #',i,' = ',Delay[i+1],' usec.');
   gotoxy(1,1);
   writeln;writeln;writeln;
   writeln('   Nd:YAG Q-Switch Laser Timing Program - Version 1.0, 7/16/
94');
   writeln('   Uses CTM-05 Counter/Timer Board for pulsed laser control.
');
   writeln;writeln;
   writeln('         F1:  Run system test');
   writeln('         F2:  Set laser pulse width');
   writeln('         F3:  Set number of pulses');
   writeln('         F4:  Set pulse delays');
   writeln('         F5:  Activate timer');
   writeln('         F10: Exit Program - Return to DOS');
   writeln;
   write('    Command: ');
```

```
End;
{**********************************************************************}

Procedure  Pulse_Number;
Begin

      clrscr;

     Repeat
      gotoxy(5,5);
      write('Enter the number of pulses per laser flash [1-3]: ');
      Read(Num_Pulses);
     Until (Num_Pulses>=1) and (Num_Pulses<=3);

For i:=Num_Pulses to 3 do Delay[i+1]:=25000;  {insure pulse delays are
set correctly}

Announce;

end;

{**********************************************************************}

Procedure Laser_Pulse_Width;
begin

     Delay[1]:=Delay[1];

     clrscr;

   Repeat
      gotoxy(1,5);
      write('  Enter the length of the laser flashlamp pulse in usec.
[200-20000]: ');Readln(Delay[1]);
     Until (Delay[1]>=200) and (Delay[1]<=20000);
                           {0.2ms is the minimum flashlamp pulse
length 20ms the maximum}

   clrscr;
   writeln;writeln;writeln;
   writeln('   Make sure the laser pulse width is set to less then,
',Delay[1],' usec.');
   writeln;
   writeln('   Check laser voltage - BE CAREFUL NOT TO BURN OPTICS BY
OPERATING AT TOO');
   writeln('                         HIGH OF ENERGY LEVEL!!! ');
   writeln;
   writeln('   The maximum average power output is 10 watts - ');
   writeln('     monitor laser power meter to verify');
   writeln;
   writeln;
   write('    press any key to continue ...');
   key := readkey;
```

```
For i:=1 to Num_Pulses do              {insure that all pulse delays are
set correctly}
  If Delay[i+1]>Delay[1] then Delay[i+1]:=Delay[1];

   Delay[1]:=Delay[1];

Announce;

end;

{*********************************************************************}

procedure Pulse_Delays;
begin

  clrscr;

For i:=2 to Num_Pulses+1 do
  Begin

      writeln;

   Repeat
      gotoxy(3,i+3);
      write('  Enter the delay of laser pulse #',i-1,' in usec. [1-
',Delay[1],']: ');
      Read(Delay[i]);
   Until (Delay[i]>=1) and (Delay[i]<=Delay[1]);

   end;

Announce;

End;


{*********************************************************************}

Procedure OpenScreen;
Begin
   clrscr;
   writeln;writeln;writeln;writeln;
   writeln(' This program uses the CTM-05 Timer/Counter Board to control
the Nd:YAG ');
   writeln(' KD*P Q-Switch.  ');
   writeln;
   writeln(' ** Remember **');
   writeln('          Connect the laser trigger pulse output to the
timer');
   writeln('          and turn on the HV supply.');
   writeln;
   writeln(' CAUTION!!!! - Do NOT operate the laser unless you know
EXACTLY');
   writeln('          what you are doing.  Improper operation can result
```

```
in damage ');
   writeln('         to the Pockels Cell and the CD*A frequency-
doubler.');
   writeln;writeln;
   write('   press any key to continue ...');
   key := readkey;
End;

{*********************************************************************}

Procedure System_Test;
Begin

   Num_Pulses:=0;
   delay[1]:=25000;  {set for 25ms to ensure stored energy isn't
dumped }
   delay[2]:=25000;  {set for no pulse output on counters 2-4}
   delay[3]:=25000;
   delay[4]:=25000;

   setmode1;          {Set up the counters to the correct operating
modes }
   load_and_arm;      {Load the counters with the pulse delays and
enable them }


   clrscr;
   Writeln;writeln(' SYSTEM TEST');
   writeln;writeln;writeln;
   writeln('  This is a test sequence to insure that the system is
functional. ');
   writeln('  If this test fails, damage can occur if laser operation is
continued. ');
   writeln;
   writeln('  Set the laser to MINIMUM voltage with a SINGLE 1ms
pulse.');
   writeln;
   write('  press any key to continue ...');
   key := readkey;

   If (term_on_err <> false) Then
    begin
     clrscr;
     writeln;writeln;writeln;
     writeln('  An error has occured.  DO NOT OPERATE LASER!');
     writeln;writeln;
     write('      press any key to continue ...');
     key := readkey;
    end
   else
    begin
     clrscr;
     Writeln;writeln(' SYSTEM TEST');
     writeln;writeln;writeln;
```

```
     writeln('  Set the laser power meter to "Energy Per Pulse". ');
     writeln('  Fire the laser and observe the output power meter. ');
     writeln('  If ANY output power is observed, DISCONTINUE ALL USE
OF THE LASER!  ');
     writeln;
     write('  press any key to continue ...');
     key := readkey;
   end;

Announce;

End;

{*******************************************************************}

Procedure Activate_Timer;

Begin

   setmode1; {Set up the counters to the correct operating modes }
   load_and_arm; {Load counters with the pulse delays and enable them}

  If (term_on_err <> false) Then
    begin
     clrscr;
     writeln;writeln;writeln;
     writeln('  An error has occured.  DO NOT OPERATE LASER!');
     writeln;
     write('  press any key to continue ...');
     key := readkey;
    end
   else
    begin
     clrscr;
     writeln;writeln;writeln;
     writeln('  The system is now active.  ');
     writeln('  It will control the Pockels Cell from the laser Trig.
Pulse');
     writeln;writeln;

     gotoxy(1,18);
     writeln;
     writeln('   System Parameters:');
     writeln('     Laser Pulse Width = ',Delay[1],' usec.');
     writeln('     Number of Pulses = ',Num_Pulses);
     for i:=1 to Num_Pulses do
     writeln('     Delay #',i,' = ',Delay[i+1],' usec.');

    Repeat
     gotoxy(1,9);
     write('  press F10 to deactivate ...');
     key := readkey;
    Until Ord(key)=68;
```

```
   end;

   mode := 2;
   params[0] := 6;            { disarm selected counters }
   for counter := 1 to 4 do
      params[counter] := 1;   { select all counters }
   result := tp_ctm5(mode, params, flag);
   If (flag <> 0) then
   Begin
      clrscr;
      writeln('    error disarming counters ');
      writeln;
      report_error;
   End;

Announce;

End;

{****************** main program ***********************************}

Begin

   term_on_err := false;  {initialize error toggle}

   OpenScreen;            {Opening warning message}

   base_address := 768;   {location of counter/timer board in computer}

   setmode0;              {initialize counter/timer board }
   If(result <> 0) then   {check to see if all is well }
      report_error;

   System_Test;            {Always check to make sure the laser system
                          is working correctly}
                          {Optics can burn if Q-Switch fails to function}

   Laser_Pulse_Width;      {set the initial parameters}
   Pulse_Number;
   Pulse_Delays;
   Activate_Timer;

Repeat

   key:=Readkey;
   Case ord(key) of
      59: System_Test;         {F1 entered}
      60: Laser_Pulse_Width;   {F2 entered}
      61: Pulse_Number;        {F3 entered}
      62: Pulse_Delays;        {F4 entered}
      63: Activate_Timer;      {F5 entered}
   end; {case}

 Until ord(key)=68;    {exit program when F10 is entered}
```

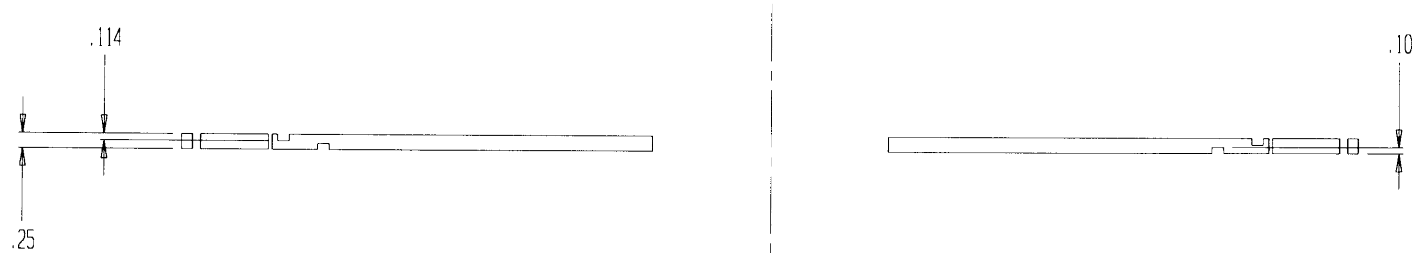

Note: Dimensions are in inches.

TOLERANCES

DECIMAL: ANGULAR:

X/X = +-1/32 .X = +-.5 deg

.XX = +-.01 X = +-1 deg

.XXX = +-.005

PART #: 10

PROJECT: Swirl Chamber (MS Project at MIT)

PART NAME: Vane Cover

MATERIAL: PVC

DRAWN BY: David Danitz

REVISION DATE: 4/4/94

SHEET 4 OF 4

```
   mode := 2;
   params[0] := 6;            { disarm selected counters }
   for counter := 1 to 4 do
      params[counter] := 1;   { select all counters }
   result := tp_ctm5(mode, params, flag);
   If (flag <> 0) then
   Begin
      writeln('    error disarming counters ');
      writeln;
      report_error;
   End;

End.   {Thats all folks!}
```